LORE Approach for Phased Array Measurements and Noise Control of Landing Gears

Patricio A. Ravetta

Dissertation submitted to the faculty of the Virginia Polytechnic Institute and State University in partial fulfillment of the requirements for the degree of

Doctor of Philosophy
in
Mechanical Engineering

Ricardo Burdisso, Chair
Wing Ng, Co-Chair
Marty Johnson
Alfred Wicks
Mehdi Khorrami
Robert Stoker

November 28th, 2005
Blacksburg, Virginia

Keywords: Aeroacoustics, Phased Array, Landing Gear Noise, Noise Control Devices, Beamforming, Deconvolution

LORE Approach for Phased Array Measurements and Noise Control of Landing Gears

Patricio A. Ravetta

ABSTRACT

A novel concept in noise control devices for landing gears is presented. These devices consist of elastic membranes creating a fairing around the major noise sources. The purpose of these devices is to reduce wake interactions and to hide components from the flow, thus, reducing the noise emission. The design of these fairings was focused on the major noise sources identified in a 777 main landing gear. To find the major noise sources, an extensive noise source identification process was performed using phased arrays. To this end, phased array technologies were developed and a 26%-scale 777 main landing gear model was tested at the Virginia Tech Stability Wind Tunnel.

Since phased array technologies present some issues leading to misinterpretation of results and inaccuracy in determining actual levels, a new approach to the deconvolution of acoustic sources has been developed. The goal of this post-processing is to "simplify" the beamforming output by suppressing the sidelobes and reducing the sources mainlobe to a small number of points that accurately identify the noise sources position and their actual levels. To this end, the beamforming output is modeled as a superposition of "complex" point spread functions and a nonlinear system of equations is posted. Such system is solved using a new 2-step procedure. In the first step an approximated linear problem is solved, while in the second step an optimization is performed over the nonzero values obtained in the previous step. The solution to this system of equations renders the sources position and amplitude. The technique is called: noise source Localization and Optimization of Array Results (LORE). Numerical simulations as well as sample experimental results are shown for the proposed post-processing.

Dedicated to the people I love:
my family… and you…

Acknowledgements

First of all I would like to acknowledge my advisor, Dr. Ricardo Burdisso, for being a great advisor in research as well as in life, for understanding and helping, for giving me opportunities to grow as a person and as a researcher. Thank you.

I would also like to express my gratitude to my co-advisor, Dr. Wing Ng, for giving me solutions and a helping hand every time I needed them, in academics and in everyday life.

I am thankful to the Committee members, Dr. Mehdi Khorrami, Dr. Robert Stoker, Dr. Marty Johnson, and Dr. Alfred Wicks for guiding and helping me every time they had the chance, for encouraging me in my research, and most of all for becoming an important part of my life.

My most sincere gratitude to Dr. Sergio Preidikman for guiding me in my first steps in graduate research and becoming a great friend. It is also because of him that I have the chance to be here.

All this time in this place far from home would have not been easy without the support of many friends that I got to know here in the U.S. My sincere gratitude to Leonardo and Beatriz, Diego, Juan Carlos and Laura, Paula, Hugo and Fulvia, Marcos and Rosana, Virgilio and Tatiana, Kai, Jim and Maria Stone, Jorge and Maria, Sebastian and Cecilia, Santiago, Cemil and all the friends that I might be forgetting in this words, but will always be in my thoughts.

I can not forget about my friends back at home: Marcos, Eugenio, Alvaro, Alejandro, Natalia, Daniela, and many more that were always there for me and understood why I am here, even when I did not. Gracias…

I also can not forget about you my angel, I never will… You know you have been the sweetest thing in my life. Thank you for sharing your dreams with me and for loving me despite the distance and all the difficulties.

And last, but most important, thanks to my family. I would not be here if it were not for each and every one of them supporting and helping me to grow up as a person. Thanks for your love.

Thank you God for making my dreams come true, for being always with me providing me strength, and for giving me the chance to share my life with all these beautiful people.

Table of Contents

Index of Figures

Page

Index of Tables

Page

Chapter 1

Introduction

Due to the development of quieter turbofan engines for civil transportation, the engine noise component of the total aircraft emission has been significantly reduced in the past years. This has lead to a situation where airframe noise has become an important noise source in commercial aircrafts. Airframe noise is defined as the noise generated as a result of the airframe moving through the air. While at take-off engines still are the dominant noise source, airframe noise is as important as the engine noise on approach due to the engines operating at low thrust. In such condition, the deployed high lift devices and landing gears are the dominant noise sources. The importance of airframe noise is expected to increase with the development of even higher bypass ratio engines that will further reduce jet noise.

The main problem is that when approaching the airport for landing, aircrafts need to fly a few miles at low altitude. Figure 1.1 [1] shows typical Instrument Landing System (ILS) approaches with some reference altitudes and distances. The normal ILS approach is used to save fuel, reduce noise and facilitate air traffic controllers speed control, while basic ILS approach is used during training and normal line operation [1]. Since cities are continuously expanding, many airports that were away from population are now embedded in highly populated areas. This is especially true in Europe and Japan as illustrated in Figure 1.2. Therefore, commercial transport has an even more significant impact on community noise.

In this sense, strict noise regulations are imposed by aviation authorities (U.S. Federal Aviation Authority, Joint Aviation Authority, International Civil Aviation Authority, and the European Union). Furthermore, some airports (John Wayne, London Heathrow) are already imposing stricter regulations in order for aircrafts to operate in them. Thus, there is a clear need to further reduce noise levels in future years. The reduction of airframe noise is being sought by both industry and government agencies. Past and on-going programs to reduce airframe noise

include: STAR (Subsonic Transportation Aeroacoustic Research), QAT (Quiet Aircraft Technologies), RAIN (Reduction of Airframe and Installation Noise), AST (Advanced Subsonic Technology), QTD (Quiet Technology Demonstrator) and QTD II.

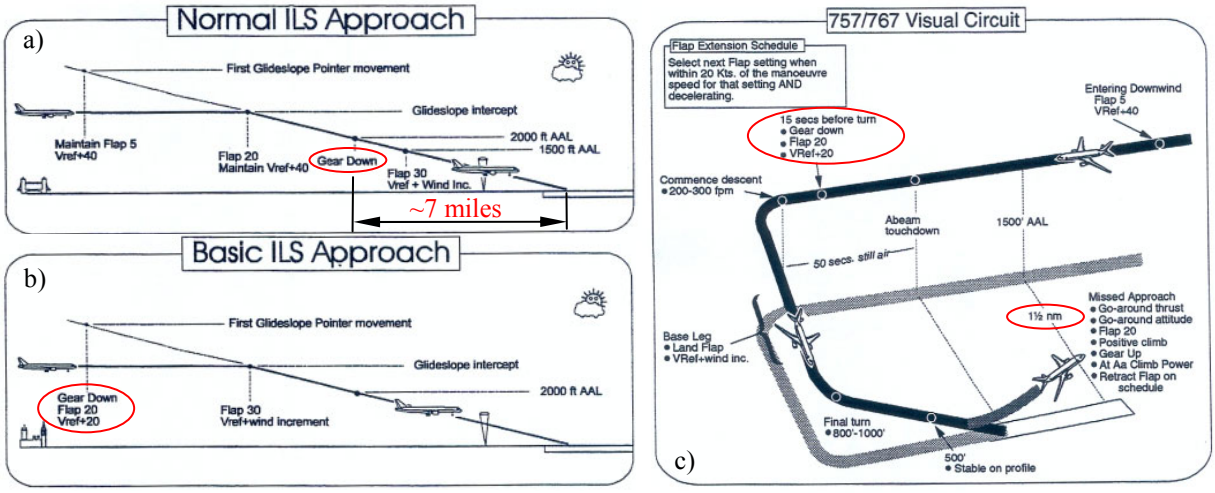

Figure 1.1: a), b) Instrument landing system (ILS) approach paths and c) schematic of visual circuit for a 757/767 from operations manual [1]

Figure 1.2: Example of airports embedded in highly populated areas [2]

1.1 Literature Review

Given the nature of this work, the literature review section is divided in 3 sub-sections:

- Airframe and Landing Gear Noise,
- Phased Array Technologies, and
- Problems in Phased Array Measurements.

1.1.1. Airframe and Landing Gear Noise

Many studies have been conducted over the past years, mainly to identify airframe noise sources. Most of the work presented in the literature has been performed by NASA [3,4], Boeing [5-8], and European organizations or companies [9-13] such as ONERA, DLR, Airbus and Messier-Dowty. As mentioned before, the high-lift devices and landing gears have been found to be the most significant noise sources. The relative level between these components was found to be dependent on the size of the aircraft. Thus, noise from high-lift devices is likely to dominate for medium size aircraft while landing gear noise seems more of a problem for high capacity aircrafts [14]. Figure 1.3 shows a Boeing 777 with gears deployed and high lift devices in approach configuration. Figure 1.4 shows some noise source identification results obtained by Stoker et al. [8] in a full-scale test. These results show significantly dominant noise sources in the above mentioned airframe components, i.e. red spots indicating high noise levels. Since this configuration was used to measure airframe noise, engines were set to idle, i.e. engine noise does not appear as a dominant noise source in these maps.

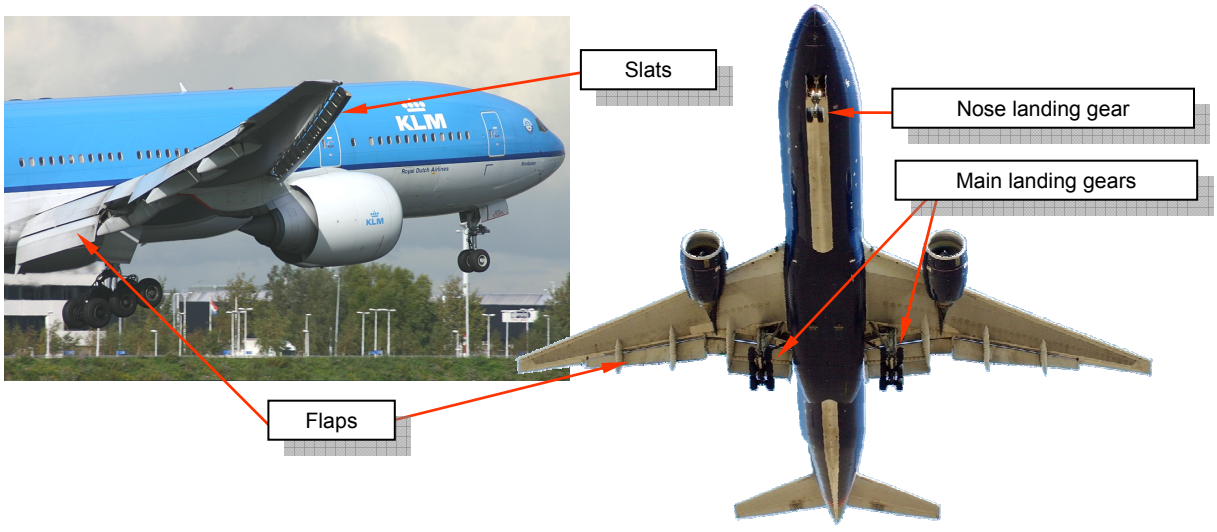

Figure 1.3: Main airframe noise components in approach and landing configuration [2]

Research on airframe noise started in the 1970's [15-17]. They were focused on the airplane as a whole system, i.e. no breakdown into components. These early studies rendered some basic insight into radiation and noise source generation mechanisms. These studies were both theoretical and experimental. However, noise prediction was not detailed or accurate. This is

related mainly to the lack of understanding of the flow and noise generation mechanisms around the complexities of the landing gear and other components. Predictions accounting for the potential interaction effect between components are even more complex [10]. However, these early studies determined that an aircraft in its landing approach configuration generated noise levels almost 10 dB higher than in cruise configuration.

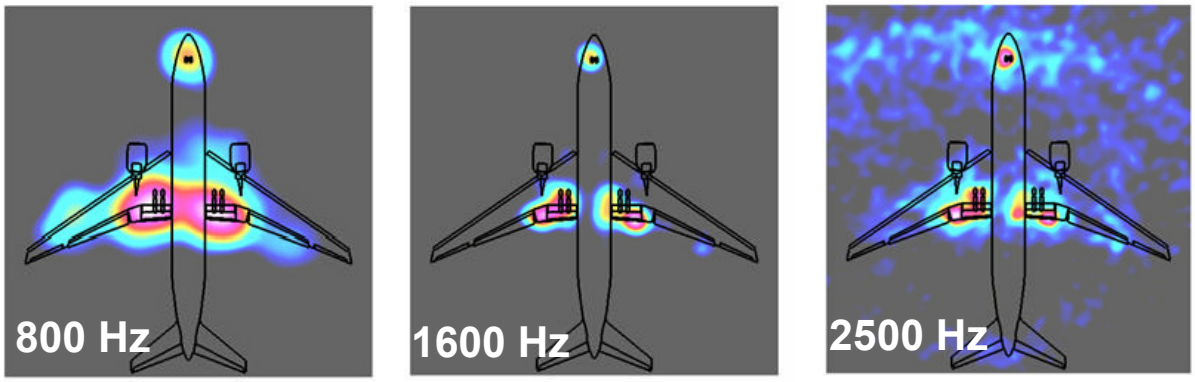

Figure 1.4: Full-scale flight test noise source identification on a 777 aircraft in approach configuration performed by Stoker et al. [8] showing the landing gears as main noise sources at different frequencies.

As pointed out in the literature [18], the current era of airframe noise research is characterized by studies focused on the components of airframe noise. In this sense, different models and configurations have been used for these studies in terms of type of aircraft, scale, and detail level of the landing gear.

In the particular case of landing gears, acoustic emission is not considered in its design process. Thus, its shape and structure were defined with the sole purpose of supporting the dynamic load during landing. Another design constraint is the ease of inspection and maintenance. For this reason, hydraulic lines and electrical wiring, among other components, are exposed to the flow; thus, making the design "poor" from the aerodynamic point of view.

Most of the work in the literature shows tests performed using low fidelity landing gear models. However, work by Stoker and Sen [7] on a 6.3% semi-span model of a 777 aircraft showed that when using a high fidelity model the noise levels coming from the landing gear were significantly increased as compared to the low fidelity gear. This increase in noise was particularly evident between 1 and 2 kHz which is an important frequency range for airplane noise certification. To overcome this issue, Jaeger et al. [19] tested many configurations of an

isolated high fidelity 26%-scale 777 main landing gear model at the NASA Ames 7- by 10-feet wind tunnel and established a potential noise reduction of about 6 dB using aerodynamic fairings and careful design of major components. They also presented a comparison of integrated levels for different configurations. Figure 1.5a and b show some results from this work.

In most recent work, Stoker et al. [8] found some discrepancies when scaling between wind tunnel results and flight test data. These differences were attributed to details of the model, Reynolds number and phased array processing effects. To avoid scaling issues, Dobrzynski et al. [14,20] tested full-scale 4- and 6-wheels Airbus 340 main landing gear as well as nose gears. In terms of noise control devices design, Dobrzynski et al. [21] found that using streamlined fairings a realistic noise reduction potential of 3 dB can be achieved. Figure 1.5c shows some of the fairings tested.

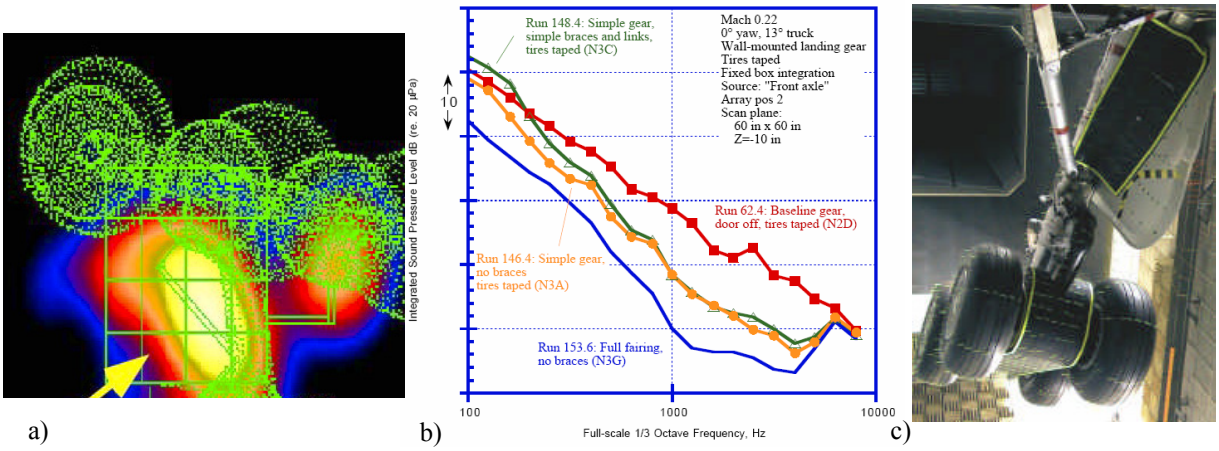

Figure 1.5: Previous work on landing gear noise. a) noise source identification and b) integrated spectra results for a 777 main landing gear [19], and c) wind tunnel test of noise control concepts [21]

As indicated by Dobrzynski et al. [21], one of the key limitations for testing is usually the prohibitive cost associated with wind tunnel and/or flight tests which in terms constraint the number of test configurations. To avoid this problem, researchers are taking the first step into landing gear noise prediction using large scale computation and acoustic analogy [22] of often simplified, low detail gears. In these studies, the surface pressure data from an unsteady CFD calculation is used, i.e. near-field data. The far-field noise can then be predicted using the Ffowcs Williams-Hawkings equations [23] for different observer positions. Figure 1.6 shows the simplified gear model, the perturbation pressure, and an instantaneous view of the vorticity from

the work by Lockard and Khorrami. Flow computations of high-lift devices such as flaps and slats received considerable attention in the past years. Noise predictions for these components are also available in the literature [24-26]. However, given the high complexity of the model and the flow field, this approach is not practical for landing gears with the current computational resources.

Other approaches used to predict the noise from landing gears is the use of semi-empirical models [10,27], components-based approaches [28,29], directivity patterns [30], and statistical models [31]. Component-based approaches have also been implemented for airframe noise without modeling the landing gear [32]. Reasonably accurate models are claimed by all the methods, but most of them under-predict the landing gear noise by 7 or more EPNLdB (Effective Perceived Noise Levels) [31]. These approaches also give a poor prediction at high frequencies since the details are usually not modeled. In other cases, the problem is that the predictions are accurate only for some observer angles [28]. The reason for some of these discrepancies is not clear.

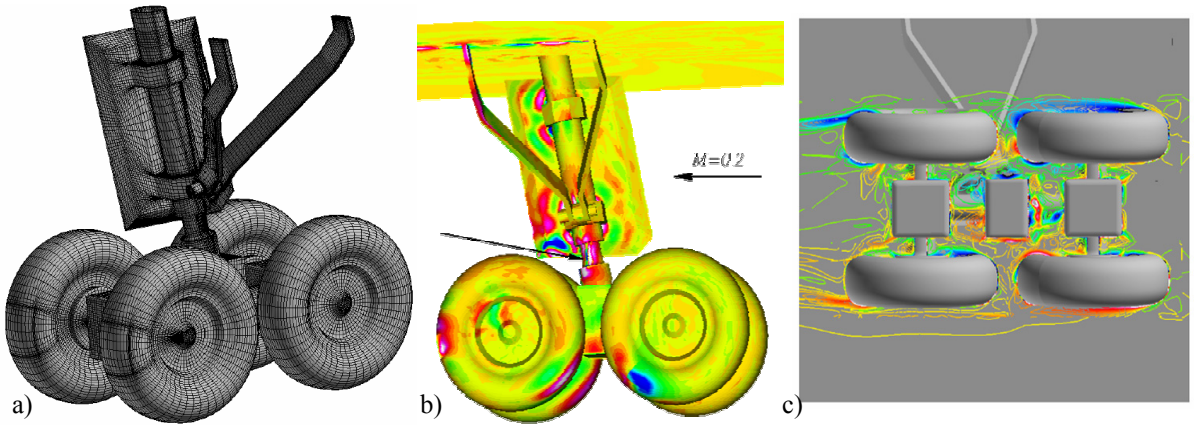

Figure 1.6: a) Simplified landing gear model used for noise prediction using CFD and acoustic analogy [23], b) perturbation pressure, and c) an instantaneous view of the vorticity from CFD results.

Another problem with landing gear noise is that the results from one test can not be extrapolated or generalized to other landing gear with the necessary accuracy. In the case of wind tunnel tests, this has been attributed to the lack of complexity in the models and the difference in Reynolds number. In the case of extrapolating to full-scale results, the working conditions like local flow velocity, components interaction, and difference in such complex geometries makes it very difficult to estimate. Some attempts in this sense were proposed by Dobrzynski [10]. To this

end, a semi-empirical relation for the overall noise dependant on gear size and number of axles was proposed.

Another problem that makes predictions difficult is that the noise radiated from the landing gear is modified by the local environment, i.e. diffraction/reflection on the wing, stowing cavity effects, convective amplification and local flow velocity variations [19].

Since these modeling efforts are still in their early stages, testing of scaled models still seems to be the best way to accomplish noise reduction efforts in the near future.

Another approach being studied to reduce the impact on community noise is the modification of the landing approach procedures [33]. One such procedure is the Continuous Descent Approach (CDA) which is based on avoiding the leveled flight shown in Figure 1.1. Reductions of 3 to 6 dB in peak A-weighted noise levels were observed using this approach. As reported in the study, the challenge for the development of new CDA procedures is in the integration with air traffic systems for use during highly congested traffic conditions. This issue is related to the minimum required distance between aircraft in approach for landing.

1.1.2. Phased Array Technologies

As mentioned before, in aeroacoustics it is very important to accurately determine the level and position of the most significant noise sources. Thus, it is desired to have a “tool” to quantify the contribution of each component to the overall noise signature, and maybe more importantly to aid in the design of a localized noise control device. In a later stage, the efficiency of such noise control device could also be studied using the same approach.

As indicated in the literature [34-38], wind tunnels are very difficult environments for acoustic measurements. In closed wall wind tunnel, this is mostly related to the fact that the background noise of the tunnel interferes with the actual noise from the model being studied. In many cases, the background noise can exceed the noise levels from the model. The background noise is usually related to the unsteadiness in the boundary layer, noise from the fan, turning vanes, turbulence screens, and other tunnel components.

If the time history from a single microphone were to be used for aeroacoustic measurements, only changes in the overall noise would be determined. In fact, the noise from the model could

be completely below the background noise levels. Even using microphones close to the "suspected" noise sources would be difficult given the complexity of the models. In addition, this technique would be very time consuming.

Starting in the 1970's, Grosche and Kendall [39, 40] developed the use of acoustic mirrors to localize and in some cases quantify the noise from models in an open jet tunnel. An acoustic mirror is a microphone fixed at the focal point of a large concave elliptical mirror, this is the reason it is also known as elliptical mirror. The idea is to measure the noise from other focal point, in this case, in the region of interest of the source. The problem is that to scan distributed sources, the system needs to be mechanically operated. Since the size of the mirrors for measurements at low frequencies is excessively large, moving this type of structures is not trivial. These systems are still being used, particularly in "large" facilities [41]. This is related to the fact that the mirror should be placed in the far-field of the acoustic source being measured; thus, only possible in such large facilities.

Another technology that has "invaded" the aeroacoustic world is the so called microphone phased array. It is based on the idea of using a number of microphones in a known pattern to identify the wave fronts from sources in the scanning field. Thus, detecting "surfaces" with the same phase and relating them to the sources distribution. One of the biggest advantages is that the signal to noise ratio (SNR) is increased with the number of sensors in the array. This is accomplished by the use of cross-correlation between the microphones, and thus being able to separate spatially incoherent noise over the array sensors.

Unlike elliptical mirrors, microphones arrays do not need to be moved to "scan" the acoustic field. In turn, a single set of data is taken and then "steered" electronically by post processing the signals on the microphones; thus, significantly reducing the acquisition time when compared to elliptical mirrors. Such array steering is accomplished by assuming a propagation model for the noise sources. The most common model is spherical spreading, i.e. monopole sources. With this assumption, the output of the array at any point in space can be determined by delay and sum of the signals in the microphones. Such delay is given by the propagation time from the source to each of the sensors. The algorithm used to steer the array assuming monopole sources is known as conventional beamforming. If sources in the far field were to be analyzed, these iso-surfaces would be "straight" over the array, i.e. plane waves.

The beamforming processing can be done either in time or frequency domain. The latter one

offers many advantages when testing given the availability of special techniques; for this reason it was selected and used in the present work. These approaches are equivalent in the sense that time shifts in the time domain correspond to phase delays in the frequency domain.

In the frequency domain approach, a matrix containing the auto- and cross-spectra of the microphones is used. Such matrix is known as the cross-spectral matrix (CSM). The processing of the array signals renders, at each frequency of interest, the power level for each point of a given scanning grid in space or for each direction of arrival (DOA). Thus, the array renders a scalar quantity related to the sum of the product of the array response with the source distribution. This relationship is called the source-receiver model and will be used in this work extensively. In the case of a single source in the scanning field, the pattern will produce a maximum level that is the square of the sound pressure radiated from the source times a factor related to the free-space Green's function to account for distance to the source. With this procedure, the same peak level that a single source will produce on a single omni-directional microphone is rendered.

Phased array technologies were first developed for sonar and radar applications as early as World War II for the detection of submarines [42,43]. The first application of an array for aeroacoustic measurements was in 1975, by Soderman and Noble [44]. They used a linear array to measure turbofan noise. Using time delay they were able to reject undesired noise. The first use of a 2D array was performed by Brooks et al. [45] to measure noise from a helicopter scale-model. They used phase delay and sum in the frequency domain. According to the literature [37], Dougherty and Underbrink used 2D arrays since late 1980's in the Boeing LSAF (Low-Speed Aeroacoustic Facility) open jet tunnel, and in the Ames 7- by 10-ft closed jet tunnel. Their arrays were designed to give useful results for a wide range of frequencies. They tested many real aeroacoustic sources using conventional beamforming and the MUSIC algorithm [46]. They also quantified the spectra from multiple or distributed sources using integration of the levels in the maps and normalizing that result using the integrated source level for a single source.

Most recently, phased arrays are common practice in most aeroacoustic tests. These situations include the measurement of noise from trailing edge of an airfoil, turbofan engines, high lift devices, landing gears, and full airplane configurations. In addition to model-scale examinations in wind tunnels, microphone arrays are being used to examine full-scale noise sources of current production aircraft [8,11]. As reported by Stoker [18], this is useful because

even though a new airplane configuration undergoes significant amounts of wind tunnel testing, unexpected noise sources can still appear in production. Phased arrays can also be used as a research tool to gain insight into the physical mechanism causing the noise, i.e. understanding of flow physics [18].

1.1.3. Problems in Phased Array Measurements

As seen in the previous section, the implementation of phased arrays is very useful in aeroacoustics. However, there are many problems related mainly to the interpretation of results. As mentioned before, conventional beamforming assumes monopole sources, and thus the directivity pattern would be expected to be that of spherical iso-surfaces. Thus, regardless of the position of the array in space with respect to the source, it should be able to recover the same output. Note that this is not true in the case of dipoles, quadrupoles, extended, or distributed sources, typical of many aeroacoustic sources. Moving sources may also present some directivity pattern. Furthermore, the sources can be correlated. The extent to which the monopole assumption is true will determine whether the array gives a true measure of the noise source under study [35].

In general, the investigation of the strengths of the noise sources is a much more difficult problem than determining their locations. As addressed in the literature [11,47], the interpretation of phased array results is still difficult due to the occurrence of several effects including:

- sidelobes (pattern, levels),
- array limited resolution related to its geometry (angles, distance, layout, size),
- coherence loss during propagation to the array (attenuation, atmospheric effects),
- reflections contaminating the maps (hard wall tunnels),
- source region characteristics (spatial extent, directivity pattern, coherence),
- Doppler-shifted frequency (in the case of moving sources),
- signal processing (microphone shading, interpolation method in de-Dopplerization).

Particularly in closed jet wind tunnel testing, the sidelobes and reflections can highly

contaminate the maps. Furthermore, sidelobes associated with the reflections can also be a problem. Remember that in closed wall wind tunnel testing the background noise levels could be of the order of the noise from the model being investigated. These problems clearly complicate the determination of the position and absolute source levels from phased array measurements. Many studies addressed some of these issues using integration. However, as reported in the literature [47], integration does not work in "all" cases, i.e. in trailing edge noise. Mainly because integration assumes that sources are incoherent, while in trailing edge noise there is a correlation length. Another problem is that airfoil noise is usually of low level when compared to the background noise of the tunnel. This issue is addressed in the literature for sources extended in one direction by Oerlemans and Sijtsma [47]. In this work, they determined the coherence level between different sources and applied the spatial source coherence to identify mirror sources in a closed wind tunnel. They also were able to estimate the spanwise coherence length in trailing edge measurements in the small anechoic tunnel at the National Aerospace Laboratory (NLR). Their results were satisfactory in terms of absolute spectra as long as the sources were not too close to the boundaries of the integration box.

Horne et al. [48] investigated the effect of source coherence of two monopole sources in the response of the phased array. They found that both peak and integrated response levels varied significantly as a function of phase and coherence level between the two sources. As will be shown in following chapters, if multiple incoherent sources are scanned, the levels in the maps are no longer the actual acoustic pressure radiated by the sources. For the particular case of coherent sources, the beamforming output depends on the case. If there is incoherent noise contaminating the signals, the results may also be affected due to a small number of averages. This can also occur if there is some spatial coherence of the noise over the array.

In the case of high background noise environments, the removal of such noise using Diagonal Removal (DR) beamforming is a must to get good results. But, as reported in the literature, applying DR affects the integration results [49,50].

As reported by Brooks and Humphreys [35], array size is also relevant in terms of integrated spectra levels. In their work, they conclude that integrated noise source levels are retrievable and levels are independent of array size as long as certain experimental and processing criteria are met. However, in general, large arrays render substantially decreased levels when compared to small arrays. They also found that integrated levels depend in part on source distribution when

DR is applied and that extended sources are subject to substantial measurement error for large arrays. They clearly state that accounting for a distributed source is a significant issue. However, in their study the sources were relatively small with intense levels compared to other sources. The problem is that, in general, a small array cannot resolve and separate the details of distributed sources while a large array is suitable to separate noise sources but not for directivity measurements.

The problem of reflections is also addressed in the literature. Some efforts have been proposed to eliminate reflections based on the image method [51,52]. In this case, the steering vector is modified to account for a given number of source images/reflections. This highly increases the computational time needed for the beamforming. Another work proposes measuring the steering vectors in-situ [53]. Thus, moving a source inside the tunnel and calculating the steering vector. This procedure is also very time consuming and involves more "expensive" testing time.

Another approach could be to determine the Green's functions for the wind tunnel test section and use them in the steering vectors. In this way, all reflections would be accounted for. However, the number of modes used in the expansion at high frequency might actually degrade the results. Furthermore, Green's functions become more sensitive at high frequency to the actual wind tunnel geometry.

The suppression of sidelobes in a beamforming map is one of the keys to aid in the process of noise source identification. In this sense, a new technique called DAMAS [54] (Deconvolution Approach for the Mapping of Acoustic Sources) was presented in 2004 and has shown a breakthrough in array processing. In this technique, Brooks et al. model the cross-spectral matrix (CSM) and obtain an inverse problem in which the power of the noise sources is solved for. Since the resulting modeled CSM is not invertible, a Gauss-Seidel iterative scheme is used. However, as mentioned in the original work, the required computational time and some other restrictions limit the current capabilities of this approach. Figure 1.7a shows simulations of the iterative scheme applied to a monopole source at the center of the scanning grid. The upper left figure shows the output of the conventional beamforming and the other three figures are results for different iteration numbers. As can be seen convergence is obtained in a relatively small number of iterations. If the source is not in a grid point, the results are not accurate, i.e. rendering many artificial sources like shown in Figure 1.7b. For more complex sources like the ones in

Figure 1.7c and d, a large number of iterations is needed. Furthermore, for some frequencies the convergence is not reached even for 5000 iterations. This issue is attributed to the relation between grid spacing and beamwidth and is explained in detail in the same work. Also, this approach was reported to show very good agreement when applied to calibrated noise sources in terms of recovering the actual power of the sources.

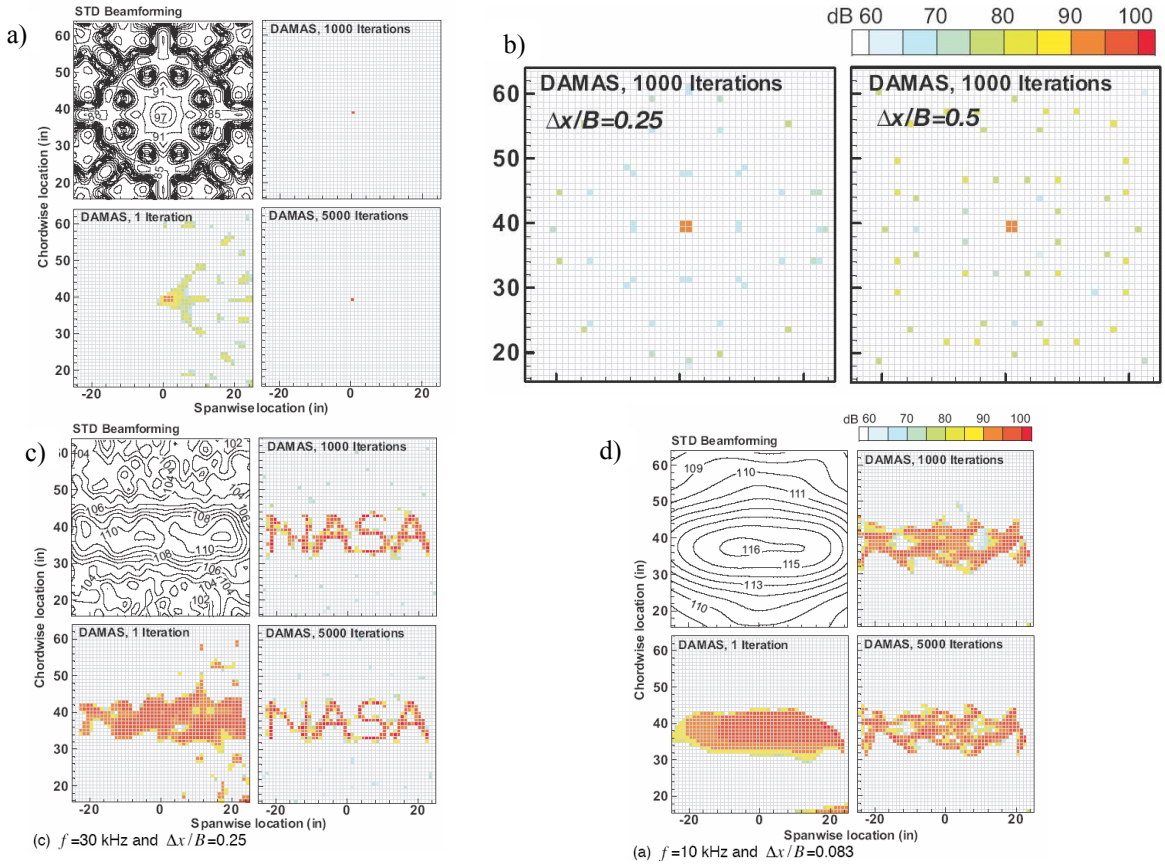

Figure 1.7: Application of DAMAS approach for a monopole source a) in the center of the grid, and b) "off-center". c),d) Results for more complex sources distributions [54] showing the accuracy dependence with beamwidth

In 2005, Dougherty [55] developed extensions to DAMAS using regularization techniques based on the Wiener filter [56] and Gaussian low-pass filters. However, these approaches also are limited. In fact, as mentioned by the author:

- it does not appear to be possible to estimate microphone spectra by integrating the source map resulting from Wiener filter deconvolution,

- DAMAS2 and DAMAS3 restrict the point spread function to a translationally-invariant, convolutional form. This is a common assumption in optics and radio astronomy, but may be a serious limitation in aeroacoustic beamforming,
- there are limitations in terms of the source region, i.e. it needs to be small compared with the distance between the array and the source,
- the applicability of the convolutional form can be extended to larger sectors but the use of special coordinates is needed.

Also in 2005, Brooks et al. [57] extended DAMAS to 3-dimensional cases. In this case, the scanning grid was defined according to the characteristics of the array used, i.e. they are not regular grids. The results showed that the application to 3D cases presents many challenges. Thus, they are considered successful as a first step into this type of cases.

1.2 Objectives of This Work

As suggested in the literature, it is still important to clearly identify the noise sources, quantify their contribution to the overall noise emission, and develop and test practical noise control devices. Such implementation of practical noise control devices for the landing gear is generally constrained by many non-acoustic considerations such as weight, available space, accessibility to the gear components for inspection and maintainability, and so forth. Thus, it is critically important to identify the gear components that are mostly responsible for the flyover noise emissions. In this way, the design of noise control devices can be focused to those identified gear components.

As part of NASA project “Revolutionary Airframe-Noise Modeling and Noise Reduction Concepts,” aeroacoustic measurements of a 26%-scale 777 main landing gear model were performed at the Virginia Tech (VT) Stability Wind Tunnel. The main objectives were the noise source identification and design of noise control devices. As mentioned before, the state-of-the-art technology for noise source identification is the use of microphones phased arrays. Due to the excessive cost of the instruments and the data acquisition system required, the implementation of this technology was restricted to governmental agencies (NASA, DLR) and big companies such

as Boeing and Airbus. During the past years, with the financial support of NASA Langley Research Center, this technique was developed at Virginia Tech. As a result, a 32-element phased array was first constructed and the computer codes to process the data were developed. In a second stage of the project, a 63-element phased array was implemented. With these technologies, the noise emission reduction potential of selected gear components was investigated by individually removing gear components. The results were also used to provide some insight into the noise generation mechanism of some parts. This task was possible since the landing gear model is an assembly of a large number of individual parts. Due to the large number of results from the many configurations tested, only illustrative examples of the results are presented in this work.

In a later stage, a new concept in noise control devices was developed, designed and tested. These devices were constructed using elastic membranes and showed a great noise reduction potential. The results from devices for the braces, main strut, lower truck, cable harness, and torque link are presented in this work.

During the development of the mentioned tasks, phased array technologies were used extensively. For such reason, some of the issues mentioned before showed up regarding beamforming. As stated before, one of those problems is to clearly identify the noise sources position and levels from the beamforming maps, especially for complex sources distributions and when some sources are at or under the array SNR, i.e. which can be confused with sidelobes. Motivated by the DAMAS approach presented by Brooks et al. and in an effort to overcome some of the issues mentioned in their work, a new modeling technique was developed. The idea is to use an “image processing-like” approach to identify the noise sources from the beamforming maps. Thus, recognizing patterns in the beamformed output and relating them to the noise sources that would produce that map. The technique is referred here as noise source Localization and Optimization of Array Results (LORE). Numerical simulations as well as experimental results using LORE will be presented in this work.

1.3 Contributions

The key contributions of this work include:

1. ***A detailed noise source identification on a Boeing 777 main landing gear:*** In this sense, the main noise sources were found for different array positions, classified and summarized in a single Sound Pressure Level (SPL) vs. frequency plot.
2. ***Study on noise generation mechanisms and potential noise reduction:*** This was accomplished by removing components and analyzing its effect on the beamforming output of the new configuration when compared to the baseline configuration.
3. ***A new concept of elastic membrane-based noise control devices is presented:*** In this sense, devices were designed for the major noise sources taking into account most of the non-acoustic constraints. The basic and "flight" concepts were tested on the 26%-scale 777 main landing gear model. The results show very promising noise reduction potential.
4. ***Modeling and post-processing technique for phased array results:*** A new modeling and post-processing technique for beamforming in aeroacoustic testing is developed. The goal is to eliminate from the beamforming maps all the sidelobes, thus, rendering a map where only the actual noise sources and their levels are present. The model is based in the complex form of the point spread function and is derived from the source-receiver model. The resulting nonlinear model of the beamforming output is solved with a new approach. This 2-step procedure first solves an approximated problem and then optimizes the results. In the present work, a least squares formulation with non-negativity constraints is used to solve the approximated problem. The multidimensional optimization of the results from the previous step is achieved using the downhill simplex method developed by Nelder and Mead.

1.4 Organization

This dissertation is organized in seven chapters and four appendixes as follows:

- Chapter 1 provides an introduction and literature review and also describes the objectives and major contributions of this work to the field of aeroacoustics.
- Chapter 2 is dedicated to the theory and development of phased array technologies. In this sense, the conventional beamforming algorithm is derived from the basic idea of delay and sum of signals. This chapter also introduces the concepts of spatial aliasing, beamforming in frequency bands, diagonal removal beamforming, and integration of beamforming maps. A detailed theoretical derivation for the array calibration procedure is also presented using the source-receiver model. The design process of the VT 32-element single arm modified-spiral array is described.
- In Chapter 3, the experimental setup used in the tests is presented. The array instrumentation and data acquisition systems are described. The main characteristics of the 26%-scale 777 main landing gear model used in this work and the main features of the VT Stability wind tunnel are also depicted. This chapter also presents details on the installation of the phased array in the wind tunnel as well as some preliminary testing.
- Chapter 4 describes the methodology and results for the noise source identification process. The resulting full-scale noise source ID results are shown for 3 different array positions. A repeatability study is shown comparing results from different test entries. This study is performed in terms of noise sources relative levels, position and overall integrated spectra. The effect of components removal and how it can be used to gain insight into the physics behind the noise generation is also shown in this chapter. In particular, some conclusions regarding noise generation mechanisms are outlined for the braces and lock links.
- In Chapter 5, the concept, design process and experimental testing of a series of noise control devices is presented. These noise control devices use a new concept based on elastic membrane fairings. Devices were designed for the braces, main strut, cable harness, torque link and lower truck. Beamforming maps as well as integrated spectra are used to quantify the noise reduction for each device as well as their combination.

- Chapter 6 introduces a new post-processing technique for beamforming results. A detailed theoretical derivation is given for the new modeling proposed. A "new" solution approach for the resulting system of nonlinear equations is proposed. Several numerical simulations as well as experimental results were analyzed and are presented.
- Chapter 7 summarizes the conclusions from this work and describes the future work.
- Appendix A describes the algorithm for solving least squares problems with non-negativity constraint used in the first step of the LORE approach.
- Appendix B describes the multidimensional optimization chosen for step 2 of LORE. The method is based on the downhill simplex method developed by Nelder and Mead.
- Appendix C shows the DAMAS modeling approach and some "extra" derivations that enables a direct comparison with the LORE modeling proposed in this work. To this end, analytical and "visual" approaches are used to compare both models to results from actual beamformed maps.
- Appendix D explains the formulation to extrapolate the test results to full-scale levels and frequencies accounting for flow speed, scale, frequency resolution, and distance to the model.

Chapter 2

Phased Array Technologies

During the last few years, phased array technologies have been widely used in aeroacoustic testing. The main purpose of this chapter is to provide the reader with some background in terms of the physical concepts, assumptions and vocabulary behind conventional beamforming. The definitions and derivations presented in this chapter will also help understand the details of the post-processing technique proposed in Chapter 6. A detailed explanation is also given for procedures used in most phased array measurements, such as: array calibration, beamforming with diagonal removal, and integration of array results.

2.1 Beamforming Algorithm

As mentioned before, the raw data from the microphones must be processed using a beamforming algorithm. The beamforming process can be performed either in the time or the frequency domain [58]. In this work, the frequency domain approach was used. The beamforming process assumes monopole sources located at every point in the desired scanning grid, i.e. spherical spreading. The monopole equation rendering the complex pressure at a distance r of a monopole source is given by:

$$p(r,t) = \frac{A}{r} e^{-i(\omega t - kr)} \tag{2. 1}$$

where:

r is the distance from the observer to the source,

$p(r,t)$ is the acoustic pressure at a distance r from the source at time t,

A is the amplitude of the noise source,

$\omega = 2\pi f$ is the angular frequency of the source, and

k is the wavenumber corresponding to the frequency f.

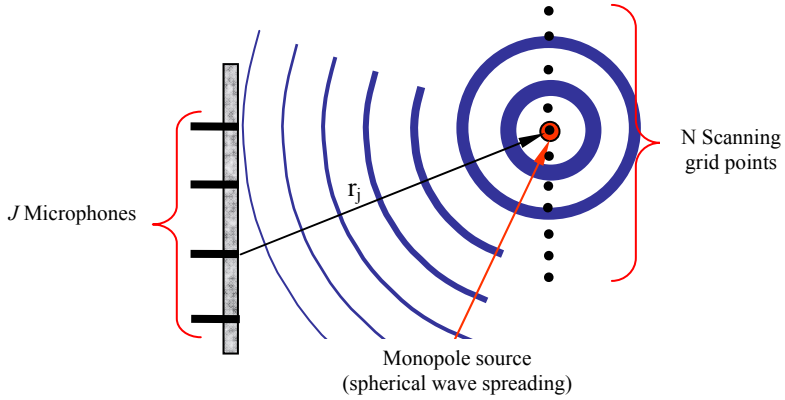

Figure 2.1: Schematic of a phased array measurement showing the scanning grid, the microphones position and the wave propagation for a single monopole source.

Then, assuming spherical spreading, the acoustic pressure P at any point n in the acoustic field can be obtained with the delay and sum of the signals in the J sensors of the array as:

$$P_n = \frac{1}{J}\sum_{j=1}^{J} w_j^* p_j \qquad (2.\ 2)$$

where:

p_j is the frequency-domain pressure at microphone j,

w_j is a weighting factor used to render the actual source level at point n, and

$*$ indicates complex conjugate.

Arranging the signals and weighting factors in a vector of length J, this yields:

$$P_n = \frac{\vec{w}^{\dagger}\vec{p}}{J} \qquad (2.\ 3)$$

where:

$\vec{w}$ is the weighting vector, also called steering vector, and

$\dagger$ indicates the Hermitian, i.e. complex conjugate transpose.

The so called steering vector is used to "steer" the phased array to a particular point in the

grid by giving to each signal the correct phase delay and amplitude corrections. The weight vector has to be such that unit gain is found for unit sources in the assumed direction, thus:

$$\vec{w}^{\dagger}\vec{C} = 1 \tag{2. 4}$$

where $\vec{C}$ is the array propagation vector for a monopole source in free-field, whose components are given by the free-space Green's function:

$$C_j(\vec{x}_n) = \frac{e^{-ik\left|\vec{x}_n - \vec{x}_j\right|}}{4\pi\left|\vec{x}_n - \vec{x}_j\right|} = \frac{e^{-ikr_j}}{4\pi r_j} \tag{2. 5}$$

where:

$\vec{x}_n$ are the coordinates of the grid point where the array is being steered to, and

$\vec{x}_j$ are the coordinates of microphone *j*.

The factor 4π is usually neglected since the calibration of the array output will take care of this constant. Then, in order to satisfy equation 2.4 and to maximize the beamforming output, the steering vector is chosen parallel to the propagation vector. This is:

$$\vec{w}(\vec{x}) = \frac{\vec{C}(\vec{x})}{\left\|\vec{C}(\vec{x})\right\|} \tag{2. 6}$$

As mentioned before, the components of the steering vector include the theoretical phase delay for each microphone with respect to the scanning point as well as corrections in amplitude due to distance to the point as given by the monopole equation.

Since the mean squared value (*msv*) of the acoustic pressure is given by:

$$msv = \frac{pp^{\dagger}}{2} \tag{2. 7}$$

Then, the beamforming output of the array, i.e. the estimated mean squared value of the pressure, at point *n* is:

$$b_n = \frac{1}{2J^2} w_n^{\dagger}\, \vec{p}\, \vec{p}^{\dagger} w_n = \frac{\vec{w}_n^{\dagger} G\, \vec{w}_n}{J^2} \tag{2. 8}$$

where *G* is the *J* by *J* cross-spectral matrix (CSM) at the frequency of interest.

When dealing with experimental data, the CSMs contain the averaged cross-spectra between all microphones in the off-diagonal elements and the averaged auto-spectra of the microphones in the diagonal terms. Thus:

$$G_{ij}(f) = \frac{\langle p_i(f)\, p_j^*(f) \rangle}{2}$$
$$G_{ii}(f) = \frac{\langle p_i(f)\, p_i^*(f) \rangle}{2} \qquad (2.9)$$

where:

$p_i(f)$ is the Fourier transform of the signal at microphone *i*, and

$\langle \cdot \rangle$ indicates average over *K* time blocks, thus:

$$\langle p_i(f)\, p_j^*(f) \rangle = \frac{1}{K} \sum_{k=1}^{K} p_{i,k}(f)\, p_{j,k}^*(f) \qquad (2.10)$$

where $p_{j,k}(f)$ is the Fourier transform of the *k*-th block of the signal at microphone *j*.

Using the beamforming algorithm, if the array is focused at an actual noise source, the microphone signals will add constructively resulting into a large beamforming output. If a source is not present at that point in space, the signals add destructively yielding a lower beamforming output. The same procedure is performed for each frequency of interest over a set of grid points.

After the beamforming process is completed, the maximum lobe (mainlobe) indicates the actual position of the sources at each scanning frequency as shown in Figure 2.2b. In this figure the levels were cutoff 20 dB below the mainlobe level for ease of visualization. The signal to noise ratio (SNR) is determined by the difference between the mainlobe and the sidelobes, i.e. lobes not associated with a source but resulting from the spatial aliasing effects due to the discrete nature of the array. The spatial aliasing is explained in the following section. In beamforming it is common to define the "spot size" representing the source location as the region 3dB down from the maximum SPL as shown in Figure 2.2a. The spot size determines the spatial resolution or beamwidth (BW) of the array, which as mentioned before, depends on the array characteristics. The beamwidth of an array is usually expressed as a function of the wavelength and the distance to the source by determining the constant *k* in the expression:

$$BW_Z = k\lambda \tag{2. 11}$$

where:

Z is the distance to the source in the direction normal to the array,

k is a constant dependant on the array characteristics, and

λ is the wavelength.

If more than one noise source is present at the same scanning frequency, they can also be "identified". However, precaution must be taken to avoid confusing noise sources with sidelobes associated to louder noise sources. Knowing the theoretical and/or experimental SNR of the array and the behavior of the sidelobes is helpful to differentiate noise sources from sidelobes, i.e. if the SNR is about 10 dB, lobes close to that level can not be associated to actual noise sources.

The beamforming algorithm can also be derived using the source-receiver model, as will be shown in following sections.

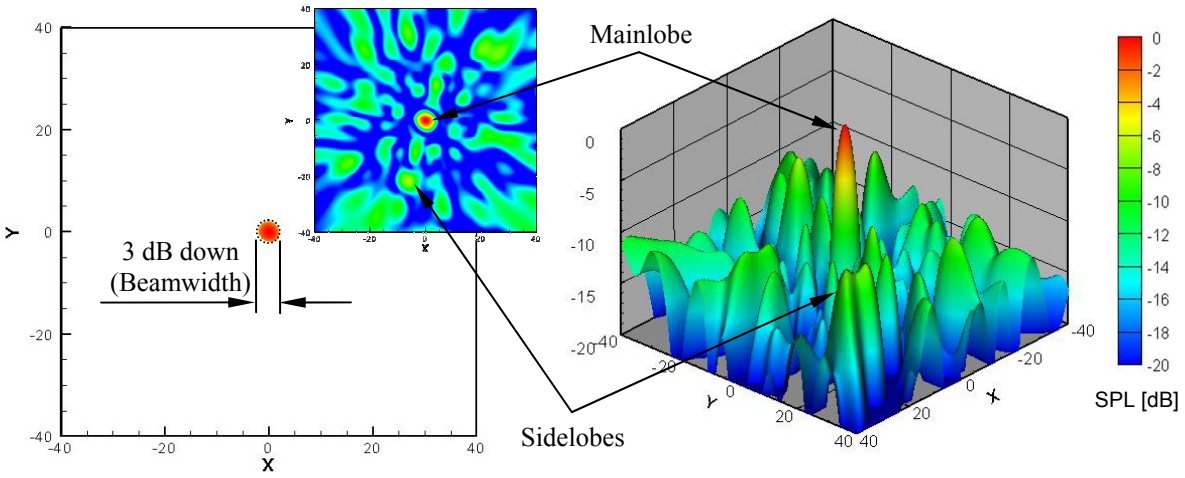

Figure 2.2: Typical beamforming output for a single source showing the mainlobe, sidelobes and beamwidth using 2D and 3D contour plots.

2.2 Spatial Aliasing - Sidelobes

The presence of sidelobes in the beamforming maps is related to spatial aliasing. Due to the discrete number of sensors, the "region" of the array is spatially undersampled. Spatial aliasing is analogous to aliasing in the time domain. Temporally undersampling a time domain signal will result in the inability to distinguish between multiple frequency components. A discrete number of sensors in an array results in inability to distinguish between multiple directions of propagation, i.e. the direction of arrival of the waves becomes ambiguous. To avoid aliasing in the time domain it is common to use analog or digital filtering. In the spatial domain, there is not a practical procedure that would filter directional components that alias into the adequately sampled directional region [59]. As the Nyquist rate is used in the time domain, it may be applied in the spatial domain by sampling at an interval not to exceed one-half wavelength. However, this is limited by the number of sensors and the usually broad range of frequencies that needs to be analyzed.

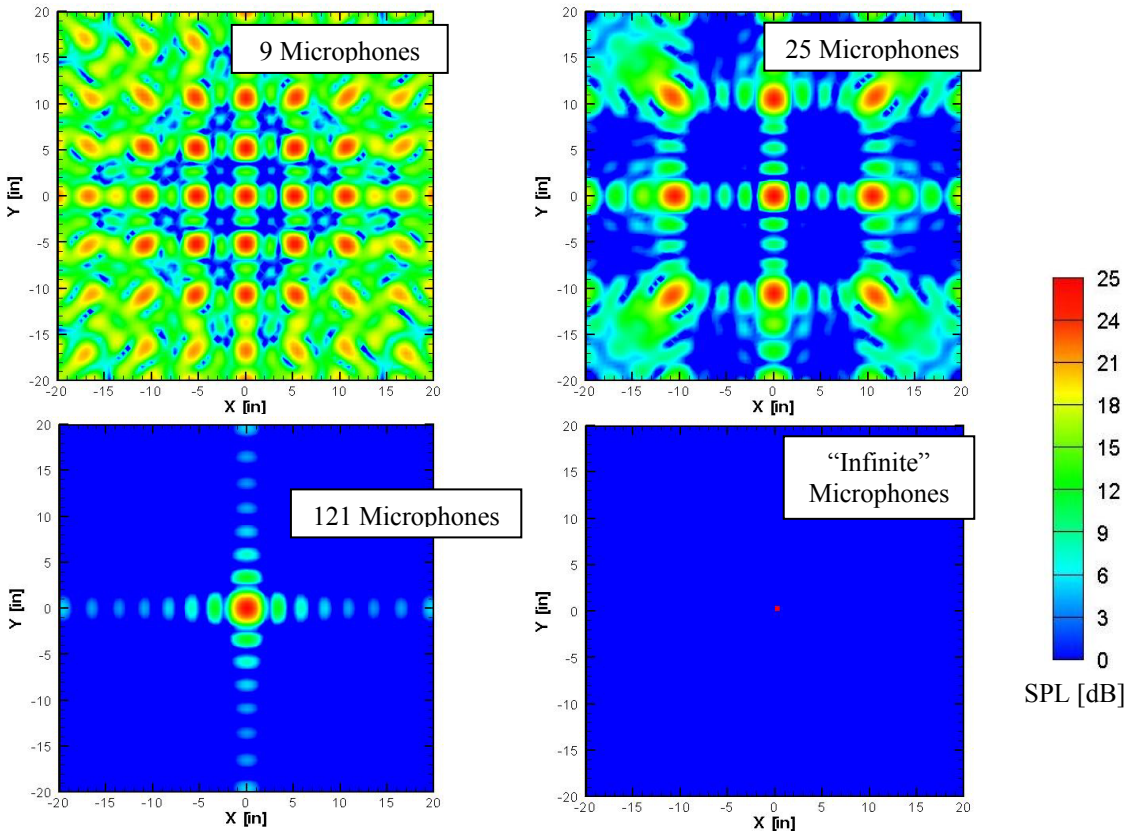

Figure 2.3: Aliasing effects as a function of number of sensors using a square array (schematic)

Figure 2.3 shows an example of the spatial aliasing effect on the beamforming output as a function of the number of microphones in the array. In this case, square arrays of microphones were numerically simulated with a single monopole source at the grid center. As can be seen, as the number of microphones increases, the sidelobes are reduced in level and number. This is related to the capability of the array of determining more accurately the direction of arrival of the wave, and thus, reducing the ambiguity. In the extreme case of an infinite number of sensors, the array output would not show sidelobes, i.e. it would only render the *msv* of the pressure at the source position.

2.3 Beamforming in 1/12th Octave Frequency Bands

In this work, the beamforming results are presented in 1/12th octave frequency bands. The center, upper and lower frequencies are obtained from the following general expressions for *1/bth* octave bands using *b=12*. The center frequency of the *n*-th frequency band is given by:

$$f_{c_n} = h^n \tag{2. 12}$$

The lower frequency of the *n*-th frequency band is:

$$f_{l_n} = \frac{f_{c_n}}{2^m} \tag{2. 13}$$

and the upper frequency of the *n*-th frequency band is:

$$f_{u_n} = f_{c_n} 2^m \tag{2. 14}$$

where:

$$h = 2^{1/b} \quad \text{and} \quad m = \frac{1}{2b} \tag{2. 15}$$

The beamforming maps in 1/12th octave bands can then be obtained in two ways:

1. beamforming at each frequency spectral line and adding the power in the maps for all the frequencies in a band, or

2. adding the spectral content in the CSMs in each frequency band and using them to beamform.

In the second approach, the computational time is significantly reduced and it was used in this work. The center frequency of the band is used to compute the steering vectors. As reported in the literature [58], this processing is valid as long as the analysis bandwidth is a small fraction of the central frequency, so that the phase is well defined in the steering vector.

2.4 Array Calibration

As seen before, the beamforming algorithm uses the steering vector to give the correct phase delay to each microphone. Then, errors are introduced in the beamformed output if the microphones are not phase matched. Furthermore, the cabling as well as the errors in the actual spatial location of the microphones may also affect the relative phase in the signals. In order to account for errors in the relative phase between the microphones, a calibration of the array is required. It can also be proven that the calibration will reduce the effect of the error in the positioning of the microphones [59] but it will not be derived here.

For the calibration of the array, an anechoic chamber test is performed using a single speaker driven with white noise. As a result of this test, a calibration matrix is generated for each frequency spectral line and then used as an input in the beamforming code. As will be shown next, these diagonal calibration matrices contain the phase delay and magnitude corrections for each microphone needed to correct the results. These corrections are then used to correct the data from an actual scanning of any complex source.

The following derivation will show how to obtain the error in the relative phase between the microphones. Basically, the calibration procedure uses the experimental data signals from a single source and compares them to the theoretical phase delay given by the steering vector.

Using the source-receiver model, the narrowband signal at microphone *j* can be expressed as the superposition of the sound from the sources distribution as:

$$u_j = \int C_j\left(\vec{x}_s\right) s\left(\vec{x}_s\right) d\vec{x}' \tag{2. 16}$$

where:

$s(\vec{x}_s)$ is the Fourier transform of the amplitude of a source at $\vec{x}_s$, and

$C_j(\vec{x}_s)$ is the *j*-th component of the array propagation vector, defined in equation (2.5).

Arranging the signal and the array response for all the microphones in vectors:

$$\vec{u}(t) = \int \vec{C}(\vec{x}_s) s(\vec{x}_s) d\vec{x}_s \tag{2. 17}$$

Then, the CSM at a particular frequency can be expressed as:

$$G = \vec{u}(t)\vec{u}^{\dagger}(t) \tag{2. 18}$$

Assuming for $s(\vec{x}_s)$ the simplest source distribution, i.e. a single point source at $\vec{x}''$, the source distribution can be written as:

$$s(\vec{x}_s) = a(\vec{x}'')\delta(\vec{x}_s - \vec{x}'') \tag{2. 19}$$

where:

$a(\vec{x}'')$ is the amplitude of the source, and

$\delta(\vec{x}_s - \vec{x}'')$ is the Dirac's delta function.

Then, the signal at the microphones due to a single source at $\vec{x}''$ is:

$$\vec{u}(t) = \int \vec{C}(\vec{x}_s) a(\vec{x}'')\delta(\vec{x}_s - \vec{x}'') d\vec{x}_s \tag{2. 20}$$

where the solution to the integral is given by:

$$\int \vec{C}(\vec{x}')\delta(\vec{x}' - \vec{x}'') d\vec{x}' = \vec{C}(\vec{x}'') \tag{2. 21}$$

Then, the narrowband signal at the *J* microphones is given by:

$$\vec{u}(t) = a(\vec{x}'')\vec{C}(\vec{x}'') \tag{2. 22}$$

Then, the CSM due to a single monopole source at $\vec{x}''$ is given by:

$$G = \left[a(\vec{x}'')\vec{C}(\vec{x}'') \right] \left[a(\vec{x}'')\vec{C}(\vec{x}'') \right]^{\dagger} \tag{2. 23}$$

Rearranging terms, the CSM can be written as:

$$G = \vec{C}(\vec{x}'')\vec{C}(\vec{x}'')^{\dagger} \left| a(\vec{x}'') \right|^2 \tag{2. 24}$$

To simplify the following derivation, lets suppose that $\left| a(\vec{x}'') \right|^2 = 1$. With this simplification, the components of the matrix *G* are just being scaled by a factor. It will be proven now that such *G* has only one nonzero eigenvalue. Since the CSM matrix for a single source is obtained as:

$$G = \left[\vec{C}(\vec{x}'')\vec{C}(\vec{x}'')^{\dagger} \right] \tag{2. 25}$$

The rows of *G* are a linear combination of the vector $\vec{C}(\vec{x}'')$, in the same way the columns of *G* are a linear combination of the vector $\vec{C}^{\dagger}(\vec{x}'')$. Then, there is only one linearly independent row, and thus rendering a single nonzero eigenvalue. To prove that $\vec{C}(\vec{x}'')$ is the eigenvector associated to λ, the only nonzero eigenvalue of *G*, the definition of eigenvector can be used to write:

$$G\ \vec{C}(\vec{x}'') = \lambda \vec{C}(\vec{x}'') \tag{2. 26}$$

If $\vec{C}(\vec{x}'')$ is an eigenvector, this expression should be satisfied. Then, using the CSM for a single source given by equation (2.24):

$$\left[\vec{C}(\vec{x}'')\vec{C}(\vec{x}'')^{\dagger} \right] \vec{C}(\vec{x}'') = \lambda \vec{C}(\vec{x}'') \tag{2. 27}$$

Re-arranging terms, this can be written as:

$$\vec{C}(\vec{x}'') \left\| \vec{C}(\vec{x}'') \right\|^2 = \lambda \vec{C}(\vec{x}'') \tag{2. 28}$$

Then, $\vec{C}(\vec{x}'')$ is an eigenvector of *G* associated to the only nonzero eigenvalue $\lambda = \left\| \vec{C}(\vec{x}'') \right\|^2$.

Including the time average of $\left|a\left(\vec{x}''\right)\right|^2$ in the formulation would render the same eigenvector (when normalized) while the eigenvalue will be scaled by such factor. The normalized eigenvector, $\vec{v}_{cal}$, corresponding to the dominant eigenvalue of the calibration CSM, is then taken as the correct expression of the normalized propagation vector, thus:

$$\vec{v}_{cal} = \frac{\vec{C}\left(\vec{x}_s\right)}{\left\|\vec{C}\left(\vec{x}_s\right)\right\|} \tag{2. 29}$$

where the components of $\vec{C}\left(\vec{x}_s\right)$ are complex numbers given by:

$$\left(\vec{C}\left(\vec{x}_s\right)\right)_j = \alpha_j + i\beta_j \tag{2. 30}$$

and can be written in complex exponential form as:

$$\left(\vec{C}\left(\vec{x}_s\right)\right)_j = \frac{e^{ik\varphi_j}}{q_j}, \quad \text{with: } q_j = \frac{1}{\sqrt{\alpha^2+\beta^2}}, \quad \varphi_j = \frac{\tan^{-1}\left(\beta/\alpha\right)}{k} \tag{2. 31}$$

Then, each component of $\vec{v}_{cal}$ will be of the form:

$$\left(\vec{v}_{cal}\right)_j = \frac{\left(\vec{C}\left(\vec{x}_s\right)\right)_j}{\left\|\vec{C}\left(\vec{x}_s\right)\right\|} = \frac{e^{ik\varphi_j}}{q_j\sqrt{\sum_{j=1}^{J}\frac{1}{q_j^2}}} = \frac{e^{ik\varphi_j}}{\hat{q}_j} \tag{2. 32}$$

Since the components of the theoretical normalized propagation vector for a source at $\vec{x}_s$ are given by:

$$\left(\vec{v}_{theory}\right)_j = \frac{\left(\vec{C}_{theory}\left(\vec{x}_s\right)\right)_j}{\left\|\vec{C}_{theory}\left(\vec{x}_s\right)\right\|} = \frac{e^{ik\left|\vec{x}_j-\vec{x}_s\right|}}{\left|\vec{x}_j-\vec{x}_s\right|\sqrt{\sum_{j=1}^{J}\frac{1}{\left(\vec{x}_j-\vec{x}_s\right)^2}}} = \frac{e^{ik\left|\vec{r}_j\right|}}{\left|\vec{r}_j\right|\sqrt{\sum_{j=1}^{J}\frac{1}{\vec{r}_j^{\,2}}}} = \frac{e^{ik\left|\vec{r}_j\right|}}{\hat{r}_j} \tag{2. 33}$$

Then, to find the difference between the measured and the theoretical normalized propagation vectors, the following expression is used for each microphone:

$$\frac{\left(\vec{v}_{cal}\right)_j}{\left(\vec{v}_{theory}\right)_j} = \frac{e^{ik\varphi_j}}{\hat{q}_j}\frac{\hat{r}_j}{e^{ik|\vec{r}_j|}} = \frac{\hat{r}_j}{\hat{q}_j}e^{ik\left(\varphi_j - |\vec{r}_j|\right)} \tag{2. 34}$$

This expression has a correction for the amplitude given by $\hat{r}_j/\hat{q}_j$ and a phase difference or correction given by $k\left(\varphi_j - |\vec{r}_j|\right)$. Then, the calibrated signal for microphone *j* is obtained by:

$$p_{cal_j} = \left[\frac{\left(\vec{v}_{cal}\right)_j}{\left(\vec{v}_{theory}\right)_j}\right]^* p_j = \frac{\hat{r}_j}{\hat{q}_j}e^{-ik\left(\varphi_j - |\vec{r}_j|\right)}p_j \tag{2. 35}$$

Arranging this calibration factors in the diagonal of a matrix, D_{cal_i}, it yields:

$$D_{cal} = diag\left(\frac{\left(\vec{v}_{cal}\right)_1}{\left(\vec{v}_{theory}\right)_1}, ..., \frac{\left(\vec{v}_{cal}\right)_J}{\left(\vec{v}_{theory}\right)_J}\right) \tag{2. 36}$$

Then, the correction to each component of the CSM can be obtained using:

$$G_{cal_{ij}} = \left(D^*_{cal_{ii}}\ p_i\right)\left(p^*_j\ D_{cal_{jj}}\right) = D^*_{cal_{ii}}\ G_{ij}\ D_{cal_{jj}} \tag{2. 37}$$

Thus, the calibrated CSM is obtained by pre- and post-multiplying the CSM with the diagonal calibration matrix as:

$$G_{cal} = D^{\dagger}_{cal}\ G\ D_{cal} \tag{2. 38}$$

As mentioned in the previous section, the beamforming is performed adding the CSMs in each band. However, the calibration must be applied to the narrowband CSMs, i.e. before adding them.

In "real life" cases, the cross-spectral matrix may be contaminated with noise from other sources in the field or noise in the microphones signal. As will be proven later in this chapter, the uncorrelated noise in the signals only affects the elements in the diagonal of the CSM. So, the CSM in the calibration test actually is of the form:

$$G = \vec{C}(\vec{x}'')\vec{C}(\vec{x}'')^{\dagger}\left|a(\vec{x}'')\right|^2 + g\ \mathbf{I}_J \tag{2. 39}$$

where:

$\mathbf{I}_J$ is the $J \times J$ identity matrix, and

g is an uncorrelated noise term, assumed to be the same at all the microphones for simplicity.

In this case, the approach developed before using the largest eigenvalue and its associated eigenvector will still give a good approximation to the actual propagation vector if g is not too significant. Usually it is suggested to get at least a factor of ten between the first and second eigenvalues of G to render a good calibration. This might be accomplished by driving the speaker loud enough.

The quality of the signals in the calibration test can be assessed by analyzing the coherence between the microphones as a function of frequency. For each frequency spectral line, the coherence can be defined in terms of the auto- and cross-spectra of the signals as:

$$\gamma^2 = \frac{G_{ij}G_{ji}}{G_{ii}G_{jj}} \tag{2. 40}$$

where $G_{ij}(f)$ and $G_{ii}(f)$ are given in equations (2.9).

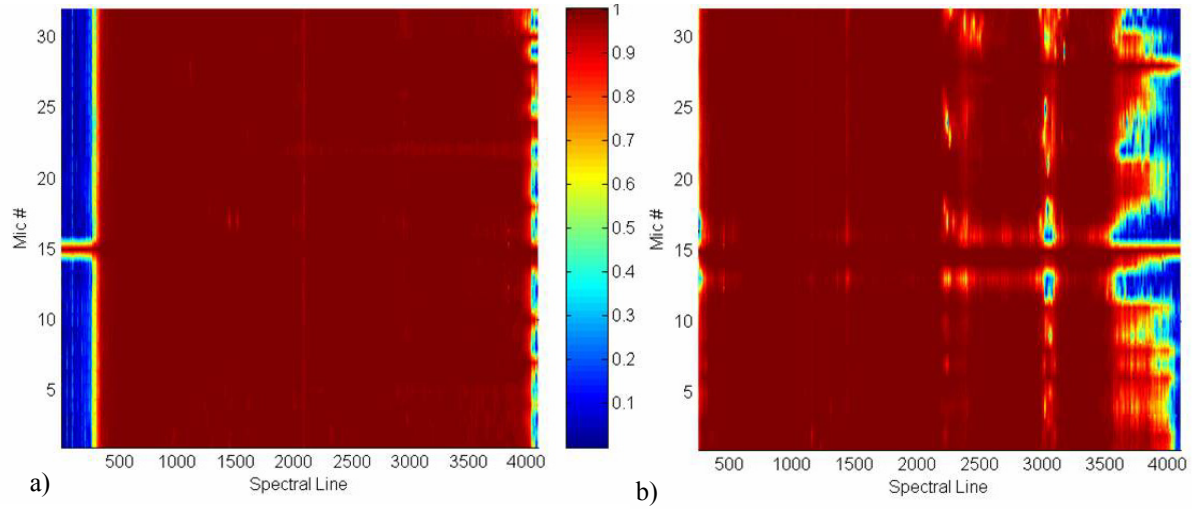

Figure 2.4: Microphones coherence as a function of frequency for a) "good" calibration and b) "poor" calibration data for a 32-element array using microphone 15 as reference.

The coherence gives a measure of the uncorrelated content in the signals, i.e. a coherence factor close to 1 indicates a low uncorrelated content. Figure 2.4a shows the coherence for a 32-element array using sensor 15 as reference. In this case, it can be seen that the coherence is very good over all the frequency range of interest. Thus, remembering that this array was not designed for very low frequency. Figure 2.4b shows the example of a "poor" calibration, resulting in low coherence at mid to high frequencies.

2.5 Removal of Flow Noise - Diagonal Removal Beamforming

Testing in a closed-wall wind tunnel presents some difficulties that might not be present in an anechoic facility. One of them is usually related to the self-noise of the microphones flush-mounted in the tunnel walls. Furthermore, if the wind tunnel facility was not intended for aeroacoustic measurements, the background noise levels could be significant, i.e. noise related to the fan, supporting struts, turning vanes, etc. Thus, the levels corresponding to the model being measured could be well below the background noise of the facility.

Another problem is that in closed-jet tunnels the sound passes through the boundary layer before reaching the sensor or the shear layer in the case of open-jet tunnels. In both cases there is a loss of spatial coherence leading to lower estimated levels than the actual ones [60]. One of the advantages of testing in a closed test section is the possibility of accurate measurements of the acoustic source position because of the absence of spreading shear layer [36].

Two methods are commonly used in aeroacoustic testing to reduce the microphones self-noise and the effect of background noise. One of them consists of recessing the array behind a Kevlar cloth like proposed by Jaeger et al. [61]. This approach was implemented for this work and will be explained in Chapter 3.

The second approach is to remove the uncorrelated noise by removing the diagonal elements of the CSM, i.e. zeroing them. These terms are associated with the auto-spectra of the microphones and include the "total" power in each signal. It can be shown that diagonal removal (DR) is useful and it does not significantly impact the beamforming output in the follow up analysis. As seen in equations (2.9) and (2.10), the frequency domain averaged auto-spectra for a signal X can be written as:

$$G_{xx} = \frac{1}{2K}\sum_{k=1}^{K} X_k(f) X_k^*(f) \tag{2. 41}$$

Suppose that the signal X is composed by a coherent signal with amplitude A plus some uncorrelated noise m, thus the single-sided spectrum is given by:

$$X(f) = A(f) + m(f) \tag{2. 42}$$

Then, the expected value of the autospectrum is:

$$\begin{aligned} E[G_{xx}] &= \frac{1}{2}E[XX^*] = \frac{1}{2}E\left[\left(A(f)+m(f)\right)\left(A(f)+m(f)\right)^*\right] \\ &= \frac{1}{2}E\left[AA^* + mm^* + Am^* + A^*m\right] \end{aligned} \tag{2. 43}$$

Since the expected value is "equivalent" to take an infinite number of averages, for uncorrelated content it will render a zero value. Given that A and m are uncorrelated, the expected value of their product is zero, and the auto-spectra can be written as:

$$G_{xx} = \frac{A^2}{2} + \sigma^2 \tag{2. 44}$$

where σ^2 is the mean square value (*msv*) of the uncorrelated noise in the signal.

Then, the diagonal terms of the CSM account for the correlated power of the signal plus the *msv* of the uncorrelated noise. It can also be shown that the cross-spectrum is not affected by the uncorrelated noise. Suppose the case of two signals of the form previously introduced:

$$X(f) = A(f) + m(f)\ , \qquad Y(f) = B(f) + n(f) \tag{2. 45}$$

where:

A(f) and *B(f)* represent correlated content, and

m(f) and *n(f)* represent uncorrelated content.

Then the cross-spectrum is defined as:

$$G_{xy} = \frac{1}{2K}\sum_{k=1}^{K} X_k(f)\,Y_k^*(f) \tag{2.46}$$

Thus, the expected value of the cross-spectrum is given by:

$$\begin{aligned} E\left[G_{xy}\right] &= \frac{1}{2}E\left[XY^*\right] = \frac{1}{2}E\left[\left(A(f)+m(f)\right)\left(B(f)+n(f)\right)^*\right] \\ &= \frac{1}{2}E\left[AB^* + mn^* + An^* + B^*m\right] \\ &= \frac{1}{2}E\left[AB^*\right] \end{aligned} \tag{2.47}$$

So, the cross-spectrum of the signals is given by:

$$G_{xy} = \frac{AB^*}{2} \tag{2.48}$$

As can be seen, the cross-spectrum of the microphones does not contain the power of the uncorrelated signals like in the auto-spectrum.

Then, by removing the diagonal components of the CSM "all" the uncorrelated noise is removed, but correlated data is also removed. However, this procedure is helpful in "cleaning" the beamforming maps and has been widely applied in most aeroacoustic applications. A sample of beamforming synthesized data (without uncorrelated noise) is shown in Figure 2.5 for processing with and without diagonal removal. As can be seen, in the absence of uncorrelated noise, the map is "cleaner". Another reason for having a map that looks "cleaner" is that the CSM is no longer positive-definite. Thus, the beamforming output can render negative values for some scanning points. Since logarithmic scale is used in the plots, the negative values were replaced with a value close to zero, i.e. 1×10^{-16}. Note also that the peak value at the source is almost the same in both cases. As suggested by Dougherty [59], the differences in the mainlobe levels can be adjusted by adding to the map the following quantity:

$$\mu = 10\ \log\left(\frac{J}{J-1}\right) \tag{2.49}$$

where J is the number of microphones.

This result can also be reached analyzing the fact that J out of the J^2 components of the CSM are being zeroed. So, the relation between the total number of nonzero components for each case can be written as:

$$\frac{J^2}{J^2-J}=\frac{J}{J}\frac{J}{(J-1)}=\frac{J}{J-1} \tag{2. 50}$$

that would render the same correction factor given by equation 2.49.

As reported in the literature [47,[49,50], the fact that the CSM is no longer positive-definite when the DR is applied, also affects the integrated levels, i.e. they are less reliable.

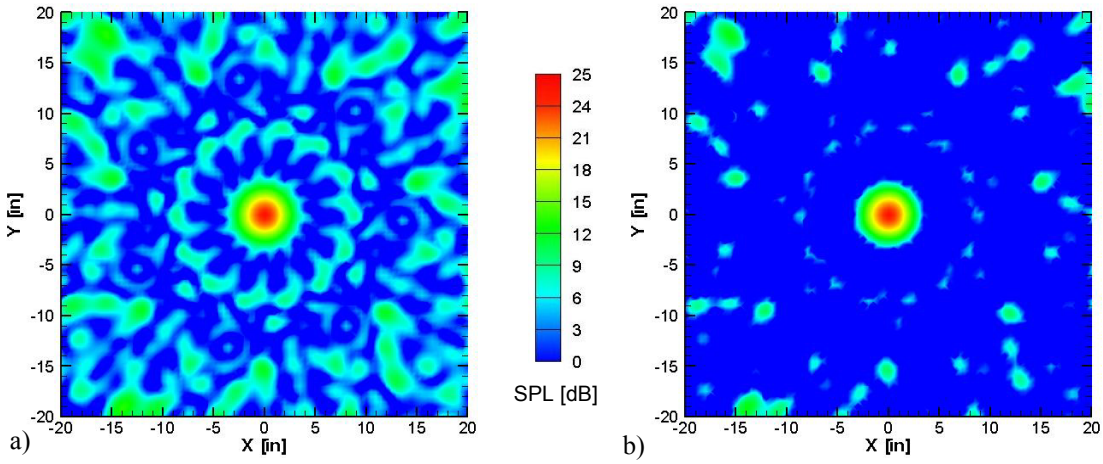

Figure 2.5: Beamforming simulation for a single source without background noise a) without using DR, and b) using DR. (15 kHz)

If instead of synthesized signals actual measured data is used, more significant differences can be found. In this case beamforming results for a source immersed in the flow of a closed wall wind tunnel are presented. Figure 2.6 shows the results obtained without and with DR. As can be seen, at this particular frequency the source is loud enough such that even in the presence of uncorrelated noise it can be clearly identified. When the DR is used, the map is significantly "cleaned". Thus, these results are "similar" to the ones obtained with synthesized data.

If the same case is analyzed for a higher frequency, where the source level is about 20dB lower, the results shown in Figure 2.7 are obtained. As can be seen in Figure 2.7a, beamforming without DR the dynamic range is only of about 2 dB and nothing can be said about the source. However, using DR the results are drastically improved and the source can be clearly identified

as seen in Figure 2.7b. These results also suggest that the uncorrelated noise at this particular frequency is significant when compared to the actual source level.

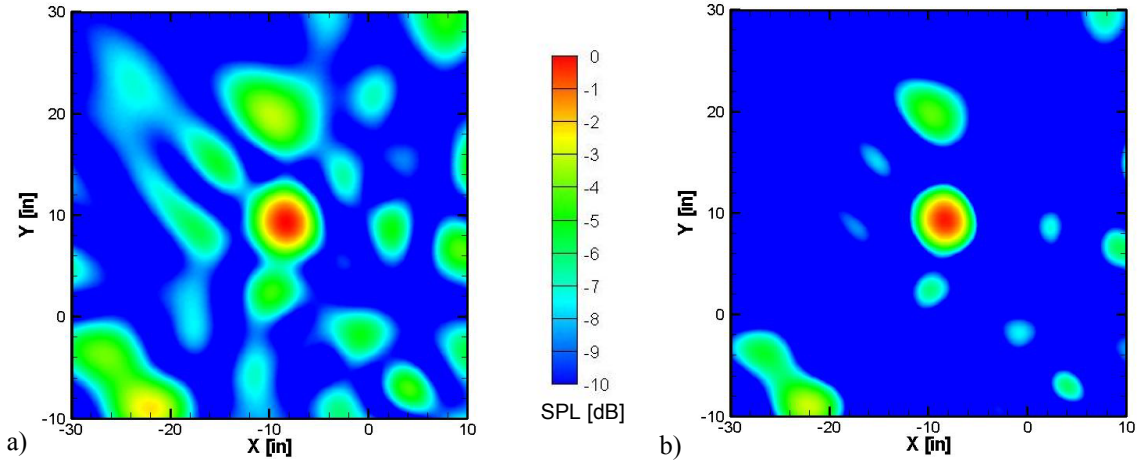

Figure 2.6: Beamforming of experimental data for a single loud source a) without DR, and b) with DR. (5.2 kHz)

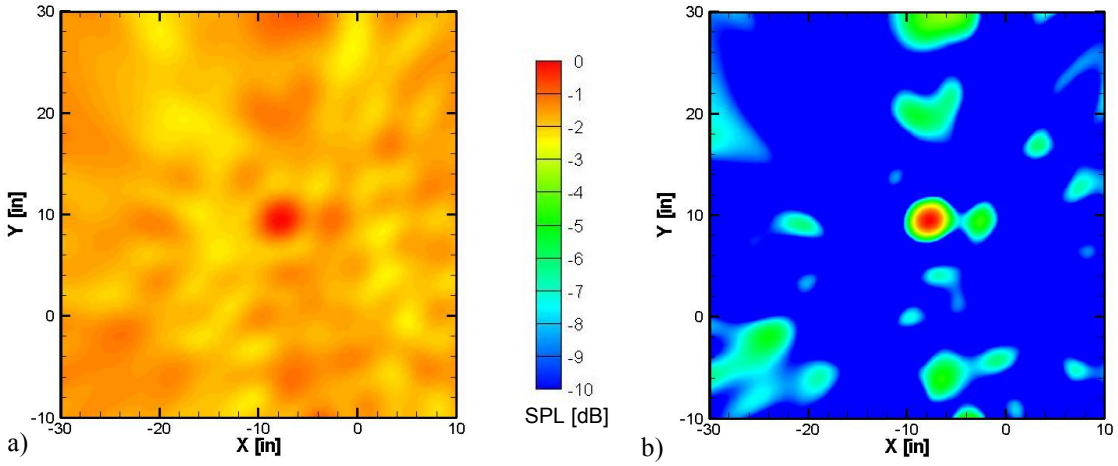

Figure 2.7: Beamforming of experimental data for a single source with levels close to the background noise a) without DR, and b) with DR (6.1 kHz)

2.6 Integration of the Beamforming Maps

As mentioned in Chapter 1, obtaining accurate quantitative results from phased array measurements is not trivial. One way to quantify the results would be to calculate a single value

for each region of interest at every frequency. In this way, a spectrum can be rendered for each component under study.

The most frequently used procedure to determine the spectrum levels from phased array measurements is the integration of the beamforming map. Thus, for every frequency, the beamforming output over a region is added to obtain a single value. The integrated level I is then obtained as:

$$I(V,f)=\int_{V} b(f,\vec{x})\; d\vec{x} \tag{2. 51}$$

where:

V is an integration volume enclosing the noise source being quantified, and

$b(f,\vec{x})$ is the beamforming output at point $\vec{x}$ for frequency f.

However, note that with this approach the contribution from the sidelobes from the source being quantified are being added, and eventually, the sidelobes from other noise sources in the scanning field are also added. Notice also that changing the integration volume will change the integral output as a consequence of adding a different number of points. To account for these problems, two corrections proposed in the literature [59] are used in this work. The first one attempts to eliminate the sidelobes from the integration and consists of integrating only the levels of the volume V that are within a given threshold from the peak level of the region. Usually this quantity is closely related to the array theoretical SNR, that as seen before, determines the relative level between the mainlobe and the worst sidelobe.

The second one accounts for the number of points being integrated and the array response using a normalization factor. This factor relates the integration output to the one obtained from beamforming a single source at the scanning grid center. As explained in Chapter 1, this is an effort to obtain the actual levels of the sources as would be measured by a single microphone.

Since there is a discrete number of points in the domain of integration, the normalized integrated spectra at frequency f can be written as:

$$I_{norm}(V,f)=\frac{\sum_{n} b_n(f)}{\zeta(f)}, \qquad b_n > b_{\max}-\delta \tag{2. 52}$$

where:

$b_{\max}$ is the maximum value in the beamforming map,

δ is a threshold set by the user, related to the array SNR, and

ζ is the normalization factor given by:

$$\zeta(f) = \int_V p_0(\vec{x}, \vec{x}_0)\, d\vec{x}, \qquad p_0 > p_{\max} - \delta \tag{2. 53}$$

where:

$\vec{x}_0$ are the coordinates of the center of the integration volume V, and

$p_0(\vec{x}, \vec{x}_0) = \left|\vec{w}^{\dagger}(\vec{x})\vec{C}(\vec{x}_0)\right|^2$ is the array point spread function (***psf***) for a source at $\vec{x}_0$.

A detailed definition and derivation of the array point spread function (***psf***) is given in Chapter 7, where it will be shown that it renders the beamforming map for a single source. This normalization of the integrated spectra by the ***psf*** should also eliminate the influence of the array shape. Thus, comparisons of the integrated spectra could be performed for data acquired with (somewhat) different arrays. However, as reported by Brooks et al. [35] and detailed in Chapter 1, many factors affect the possibility of such comparison.

Chapter 3

Experimental Setup

The experimental setup used in the tests of the landing gear model is presented in this chapter. The array instrumentation, data acquisition systems, main characteristics of the 26%-scale 777 main landing gear model used in this work and the main features of the VT Stability wind tunnel are described. This chapter also presents details on the installation of the phased array in the wind tunnel as well as some preliminary testing of the phased array.

3.1 Phased Array Instrumentation and Data Acquisition

The research presented in this work was performed in 2 main phases. For this reason, results using 2 different phased arrays are presented. The first series of tests was performed using a phased array developed at Virginia Tech consisting of 32 PCB microphones type 130B10. The design was a single arm modified spiral. A picture of the array and the positioning of the microphones are shown in Figure 3.1. The beamwidth of this array, at a plane 36" parallel to it, is characterized by $BW_{36"} = 1.48\ \lambda$. Its worst sidelobe is about 6 dB below the mainlobe at high frequencies, i.e. 20 kHz. Figure 3.2 shows simulated beamforming results for a single source at the grid center, in a plane 36" parallel to the array, at 5, 10 and 25 kHz. In addition to the phased array, a linear array of 10 Panasonic WM-60AY Electret microphones with the conditioner circuit developed and tested by NASA [62] was used to determine the radiation directivity in the first series of tests.

In the second phase, a 63-element array was developed using Panasonic Electret microphones. The pattern of this array was an equal-aperture multi-arm spiral designed for VT by J. Underbrink and R. Stoker from the Boeing Co. Figure 3.3 shows the array and the positioning of

the sensors. The array response is shown in Figure 3.4. The beamwidth of this array for a plane at 36" is given by $BW_{36"} = 2.45\,\lambda$, and the SNR is about 10 dB at high frequencies.

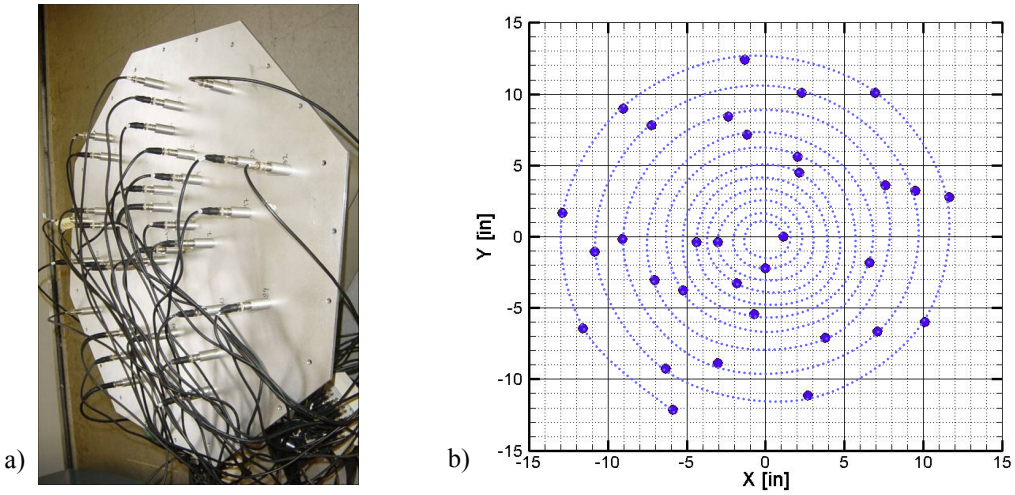

Figure 3.1: 32-element single-arm spiral VT phased array. a) Picture of the array, and b) microphones position.

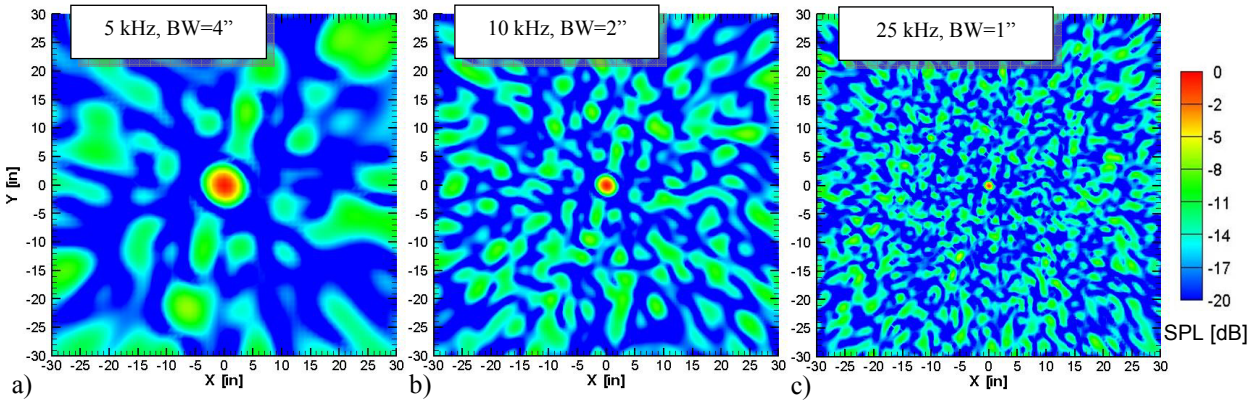

Figure 3.2: 32-element phased array response for a) 5, b) 10 and 25 kHz in a plane 36" from the array.

The acoustic data was acquired using an Agilent multi-channel data acquisition system. The collected data included the time histories for the phased array microphones and, if present, the 10 microphones of the linear array. All channels were acquired simultaneously at a sampling frequency of 51.2 kHz. In each data acquisition 25 blocks of 16384 samples were taken. However, in the beamforming process, the CSMs were obtained averaging 50 blocks of 8192 samples. The software for the data acquisition is VEE Pro based. The beamforming code was developed at Virginia Tech using Intel Fortran Compiler 7 and Intel Math Kernel Library 6. The

data visualization and analysis was performed using Tecplot®.

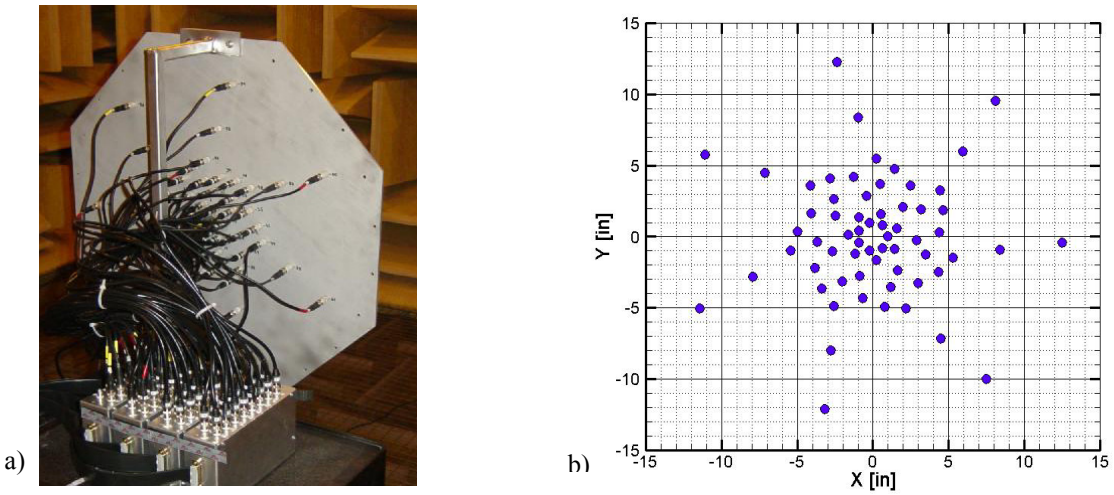

Figure 3.3: 63-element multi-arm spiral VT phased array. a) Picture of the array, and b) microphones position.

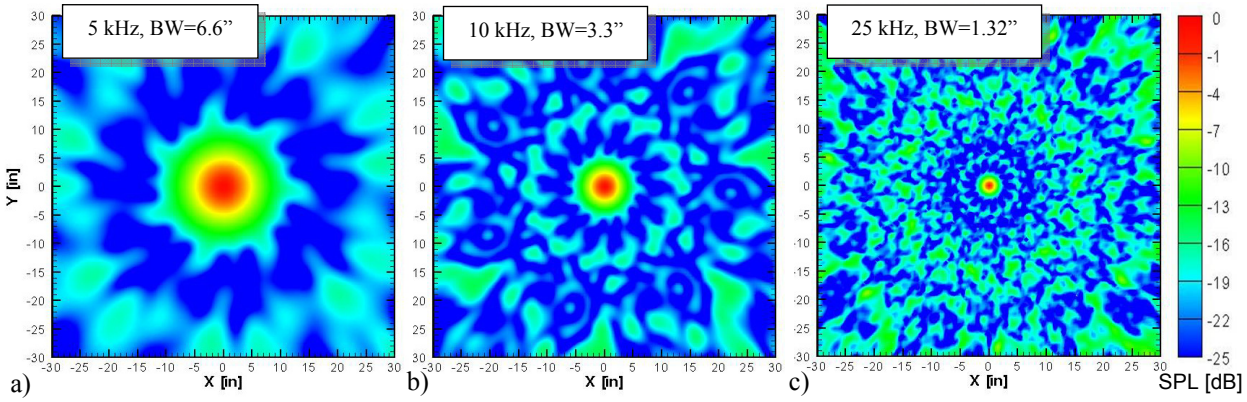

Figure 3.4: 63-element phased array response for a) 5, b) 10 and 25 kHz in a plane 36” from the array.

For each configuration the beamforming results for forty-five 1/12th octave bands, from band number 132 through 176, were computed. These bands correspond to center frequencies from 2 kHz to 25 kHz model scale. However, the low-pass filter of the data acquisition system was set to about 20 kHz. The microphones used in the phased array were found to be reliable only up to about 20 kHz in terms of levels. As reported by Humphreys et al. [62], the microphones response is not flat above this frequency. However, as long as the phase is matched, the beamforming maps should still be accurate in terms of identifying noise sources.

3.2 High Fidelity 26%-scale 777 Main Landing Gear Model

The high fidelity 26%-scale 777 main landing gear model used in this study was originally tested under the STAR (Subsonic Transport Aeroacoustic Research) program using a semi-span model of the 777 at the NASA Ames 40- by 80-ft wind tunnel [63]. The isolated gear model was also evaluated under the AST (Advance Subsonic Transport) and QAT (Quiet Aircraft Technology) programs at the NASA Ames 7- by 10-ft wind tunnel [19]. The model is shown in Figure 3.5a and b in the actual landing position. However, for these tests, the model was mounted on the floor of the wind tunnel test section, i.e. these pictures are upside down.

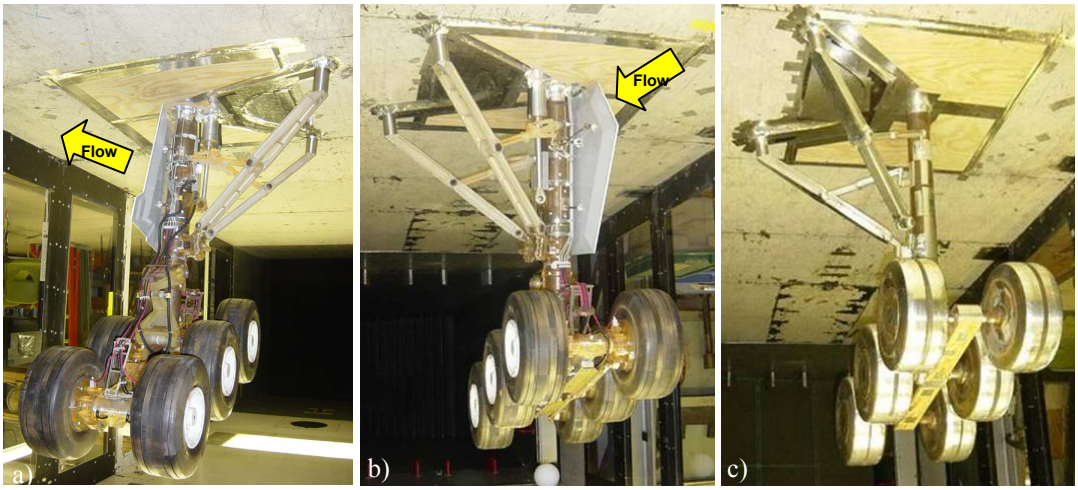

Figure 3.5: High fidelity 26% scale 777 main landing gear model, a) rear and b) front views. c) Low fidelity configuration obtained by removing all the details.

This high fidelity model features all the major gear components: strut, braces, torque link, cable harnesses, lock links, main door, and wheels. It also includes most of the details found in the original landing gear, including: oleo lines, cables, wheel hubs, brakes cylinders, hydraulic valves. Pictures of the full scale landing gear are shown in Figure 3.6.

The main structure of the model is made of steel and aluminum and the details are mostly made in stereo lithography up to an accuracy of 3mm in full-scale. The main differences with the actual landing gear are that: the wheel hubs do not have the openings that allow air to flow freely through the wheels, a smaller door located close to the wing and attached to the main door is not in the model, and the wing cavity was not modeled. For the low detail configuration, all the details can be removed yielding a “clean” or low fidelity configuration as shown in Figure 3.5c.

Figure 3.6: Pictures of the actual 777-200 main landing gear. a) [2], b),c) and d) courtesy of The Boeing Co.

3.3 Virginia Tech Wind Tunnel Facility

The experiments presented in this work were conducted at the Virginia Tech Stability Wind Tunnel shown in Figure 3.7. The Virginia Tech Stability Wind Tunnel was originally built at the NACA Langley Aeronautical Laboratory in 1940. The wind tunnel was donated to Virginia Tech in 1958. The facility is a continuous, closed jet, single return, subsonic wind tunnel with a 24 foot long square test section of 6- by 6-ft. The test section is not treated acoustically. The tunnel is powered by a 600 hp DC motor driving a 14 ft propeller providing a maximum speed of about 280 km/h for the empty wind tunnel ($M \simeq 0.23$). New propeller blades were installed and the motor overhauled in 1996. The propeller drives the flow first through an air exchange tower, where the pressure and temperature are equalized to atmosphere, and then to an 18- by 18-ft settling chamber. The settling chamber houses seven anti-turbulence screens, each with an open area ratio of 0.6 and separated about 6 in. Flow exiting the screens is accelerated to test speed through a 9:1 symmetric contraction. The dense anti-turbulence screens and large contraction ratio result in a flow through the empty test section that is both closely uniform and of low turbulence intensity.

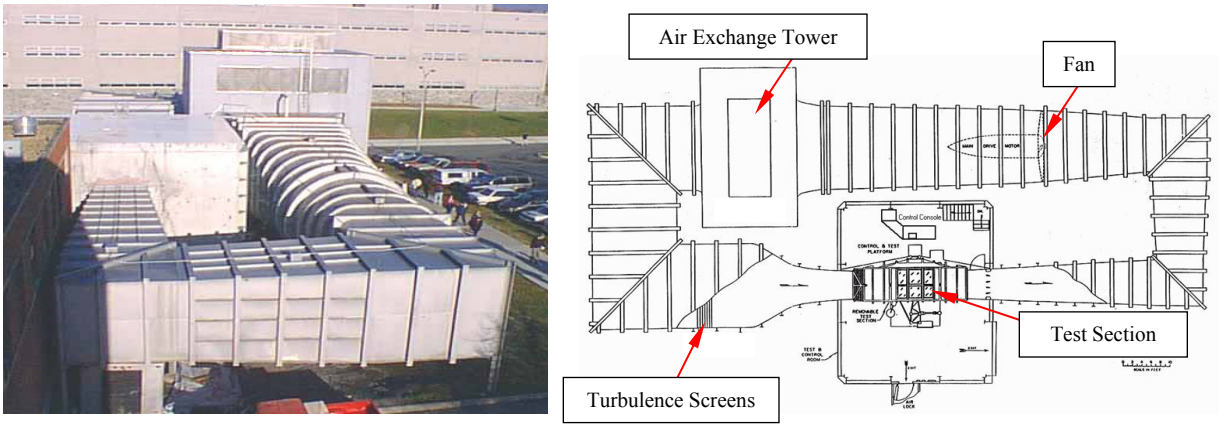

Figure 3.7: Picture and schematic of the Virginia Tech Stability Wind Tunnel.

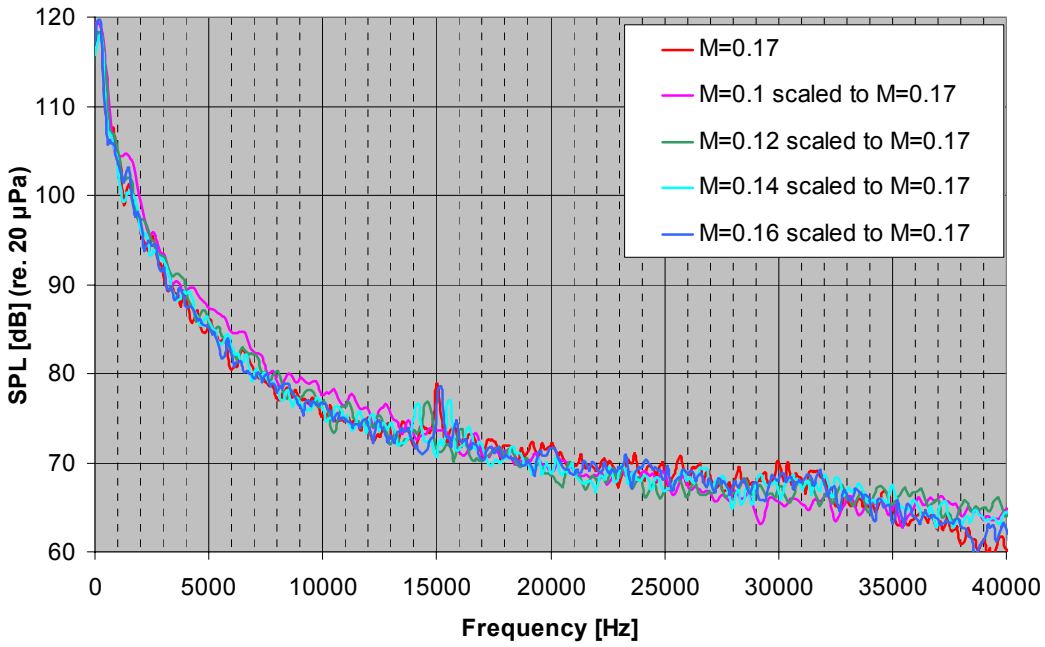

Figure 3.8: Extrapolation of landing gear noise for different test speeds to M=0.17 using the assumption of a modified dipole type source, i.e. V^6 scaling. Measurements obtained using a single in-flow microphone.

Since it was desired to run the tunnel at the same flow speed for all gear configurations tested, the maximum speed achievable in the wind tunnel with the baseline high fidelity landing gear was determined to be around Mach 0.17. A concern related to this matter was the blockage effect, i.e. area of the model relative to the test section area. The blockage was estimated to be about 9% using the model frontal area. However, given the complexity of the model, the actual blockage was obtained experimentally. To his end, a test was performed using a Pitot probe

upstream the model, i.e. at the beginning of the test section, and traversing the Pitot probe at the plane of the landing gear as indicated in Figure 3.9a. The flow velocity profile at the model position shown in Figure 3.9b was used to determine the blockage. As can be seen, close to the tunnel wall the flow speed is about 5.5% higher than the free-stream velocity measured with the probe upstream. Closer to the model, the flow change is about 6.5% higher relative to the normalized free stream velocity. The comparison of such measurements was used to establish a blockage of about 6%. This value is lower than the 10% suggested, so blockage effects were determined not to be an issue.

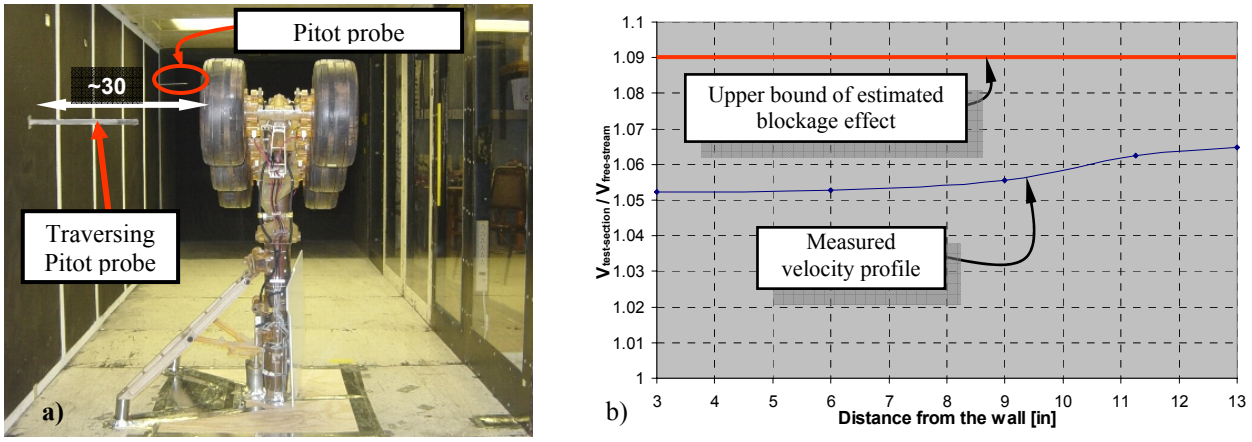

Figure 3.9: Measurement of blockage. a) Experimental setup and b) velocity profile in the model area.

Since the actual approach/landing speed of this aircraft is about Mach 0.22, i.e. higher than the maximum speed achievable in the tunnel, a correction for flow speed should be applied to extrapolate the model-scale test results to full-scale. As reported in the literature [14], for the landing gear case this extrapolation is in agreement with the assumption of a dipole type source, i.e. according to the flow speed to the sixth power (V^6). In order to determine the accuracy of this extrapolation for the test setup presented in this work, different wind tunnel speeds were tested. From these results it was found that the noise spectra scaled very well with the sixth power of the flow velocity. The extrapolation of results for different speeds to Mach 0.17 is shown in Figure 3.8. For this test a single ¼" B&K microphone was located inside the test section downstream the model. To avoid the noise generated by the flow fluctuations in the microphone diaphragm, a B&K nose cone was used.

3.4 Arrays Installation

For aircraft certification purposes, the noise emitted by the aircraft towards an observer in the flyover path is the most important component. However, if only a phased array in the flyover position were used for the measurements, most of the noise sources would not be identified accurately since they would be shielded by the truck and wheels. Hence, interfering with the direct path of propagation assumed in the beamforming algorithm. To avoid this problem, three different array positions surrounding the model were used. Thus, the phased array was mounted in the ceiling of the wind tunnel close to the truck as indicated in Figure 3.10b; and in two opposite walls of the wind tunnel, i.e. the braces and door side of the model as shown in Figure 3.10a and c, respectively.

To avoid the hydrodynamic noise induced over the array microphones by the turbulence in the boundary layer of the wind tunnel, the literature shows different approaches. One of them consists of using a layer of foam and a perforated plate over the array [64]. This approach was reported to be beneficial at low frequencies. An alternative is to recess the microphones behind a stretched Kevlar cloth. This mounting technique was developed and tested at NASA Ames [61] and was used in this work. Since Kevlar is acoustically transparent, the pressure fluctuations on the microphones due to the boundary layer unsteadiness are significantly reduced while allowing the sound to propagate through the cloth. On the other hand, given the high tension applied while stretching the cloth, the Kevlar appears as a hard surface to the flow.

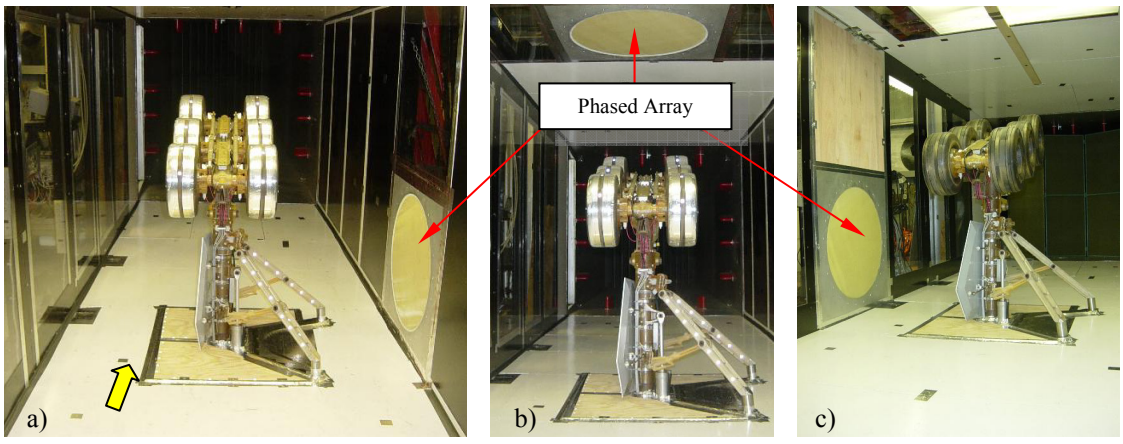

Figure 3.10: Phased array mounted on a) braces side, b) flyover, and c) door side of the landing gear model.

However, it was reported [61] that around 25 kHz the sound passing through "untensioned" Kevlar was attenuated by as much as 2dB. It was also reported that the results are affected by the incident angle of the noise relative to the Kevlar. The attenuation in the microphone response for a white noise source was also studied and is shown in Figure 3.11a. It can be observed that the attenuation can be up to 5 dB below 20 kHz. Recessing the array also could create a resonance that attenuates or amplifies the sound as a function of frequency, i.e. cavity resonance effects. However, the same work shows that recessing the array behind Kevlar reduces background noise as much as 20 dB by isolating the microphones from the turbulent boundary layer as shown in Figure 3.11b.

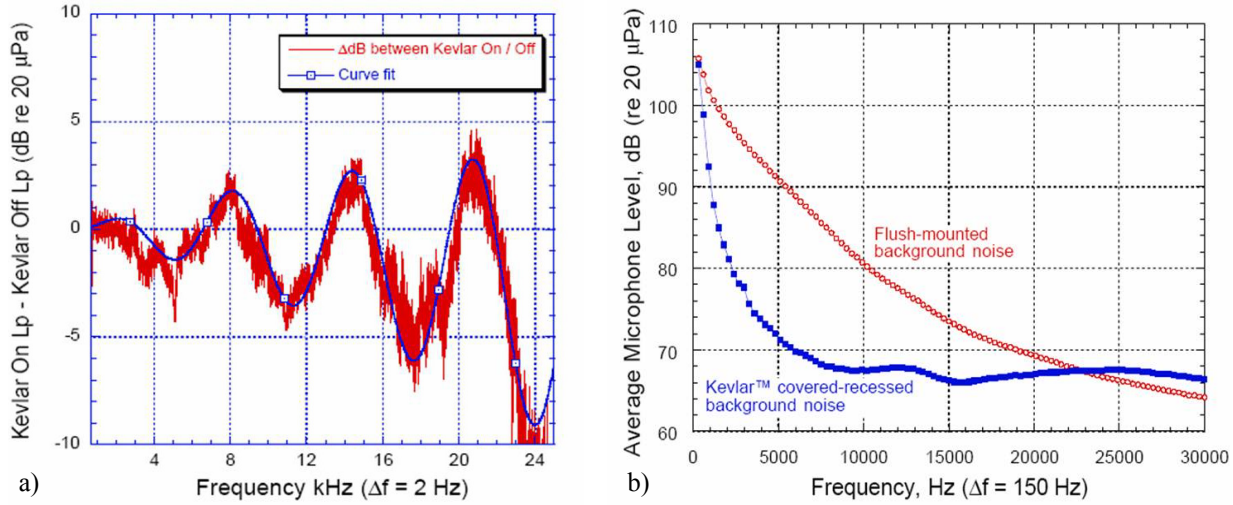

Figure 3.11: Effect of recessing the microphones behind a Kevlar cloth. a) Attenuation as a function of frequency, and b) reduction in background noise for Kevlar ON/OFF.

A schematic and pictures of the setup of the mounting of the phased array are shown in Figure 3.12. The mounting arrangement for the array was designed in such a way that it could be placed at any location in the test section.

For some experiments, the linear array was mounted in the flyover path close to the centerline of the truck, i.e. on the ceiling of the tunnel as shown in Figure 3.12. Since the microphones were flush mounted to the wind tunnel wall, they were affected by the pressure fluctuations generated by the unsteadiness in the boundary layer. The linear array was used only to determine the radiation directivity of the baseline landing gear.

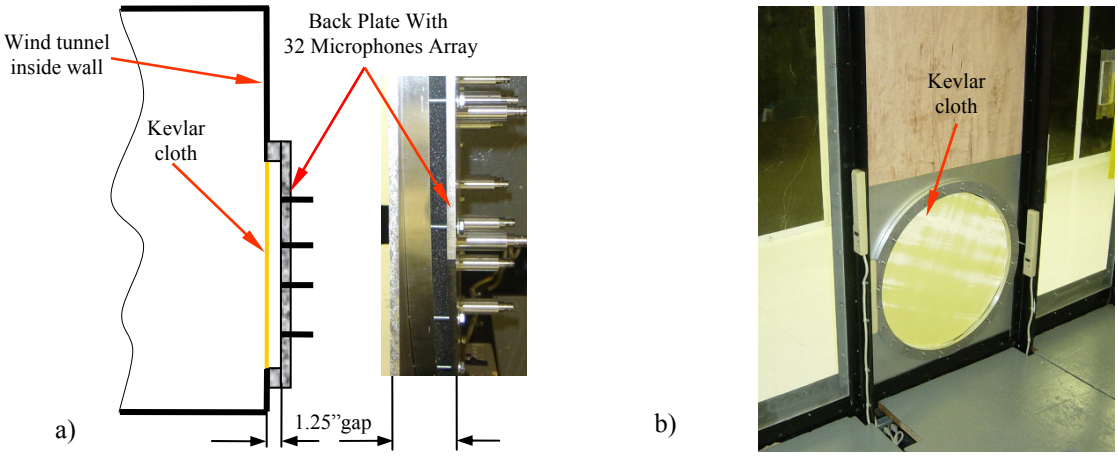

Figure 3.12: a) Wind tunnel cross-section showing a schematic of the mounting of the phased array and b) Kevlar screen mounted in the wind tunnel wall.

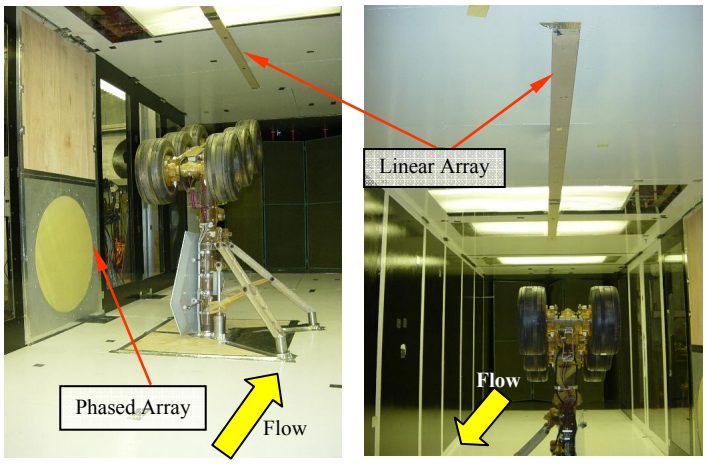

Figure 3.13: Linear array mounting in the flyover path, i.e. ceiling of the VT wind tunnel.

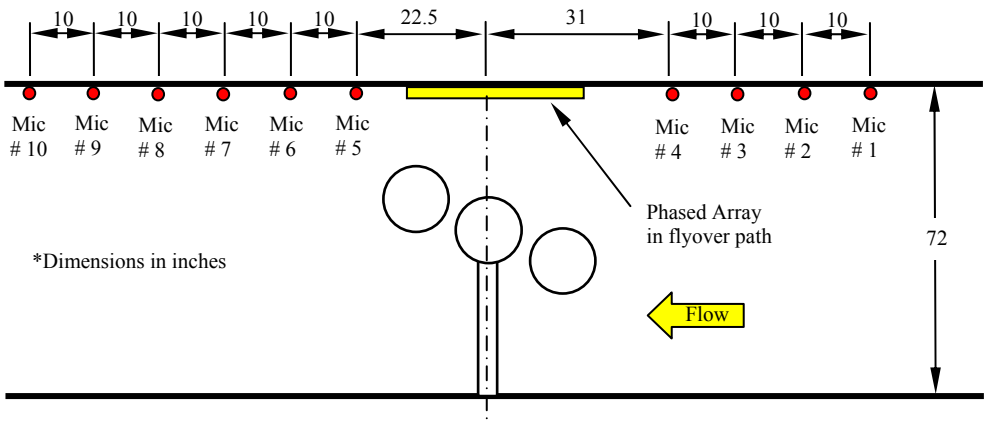

Figure 3.14: Linear array configuration for phased array on flyover path.

Since the positioning of the phased array in the flyover path interfered with the linear array mounting, the liner array was broken down in two sub arrays. Therefore, two different configurations for the linear array were used. Figure 3.14 and 3.14 show schematics of the linear and phased array installed on the walls of the wind tunnel.

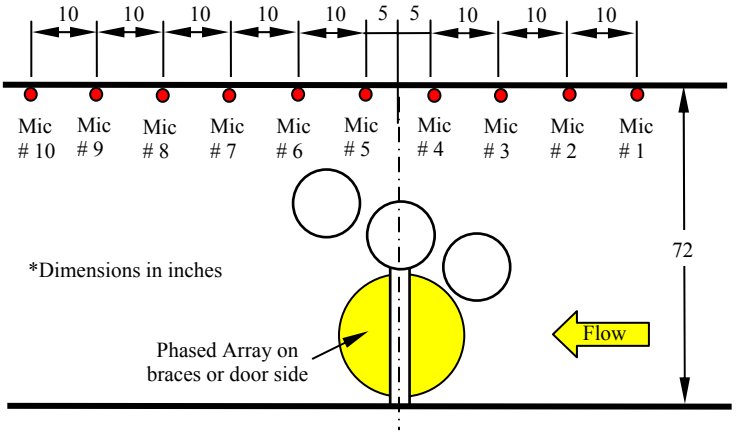

Figure 3.15: Linear array configuration for phased array on wind tunnel walls.

3.5 Preliminary Testing of the Phased Array

To evaluate the performance and capabilities of the array and the beamforming codes, a series of preliminary tests were performed. The first step was to test the array using a speaker, driven with a 10 kHz pure tone, in an arbitrary position inside the wind tunnel as shown in Figure 3.16a. The purpose of this test was to establish the capabilities and SNR of the array in a reverberant environment without flow. The beamforming result for the 32-element array shown in Figure 3.16b indicates the highest SPL for 10 kHz at the correct speaker location. In other frequencies, the mainlobe is at least 60 dB below the levels found at 10 kHz. Therefore, the results were successful in terms of frequency and spatial location of the source. The spot size was also in good agreement with the simulations.

The second preliminary test used a whistle mounted on an airfoil in the wind tunnel test section. In this configuration, the flow in the tunnel drove the whistle producing a distinct tonal signal. Due to the compact size of the whistle, it behaves as a “monopole” source. Since the frequency of the whistle depends on the flow speed, this configuration was tested at several flow

Mach numbers. The setup and beamforming results for the case at M=0.17 are shown in Figure 3.17. Once again the whistle position was successfully determined and the maximum array level was found at the 1/12th octave band #145, i.e. the whistle generated tone was at about 4.34 kHz.

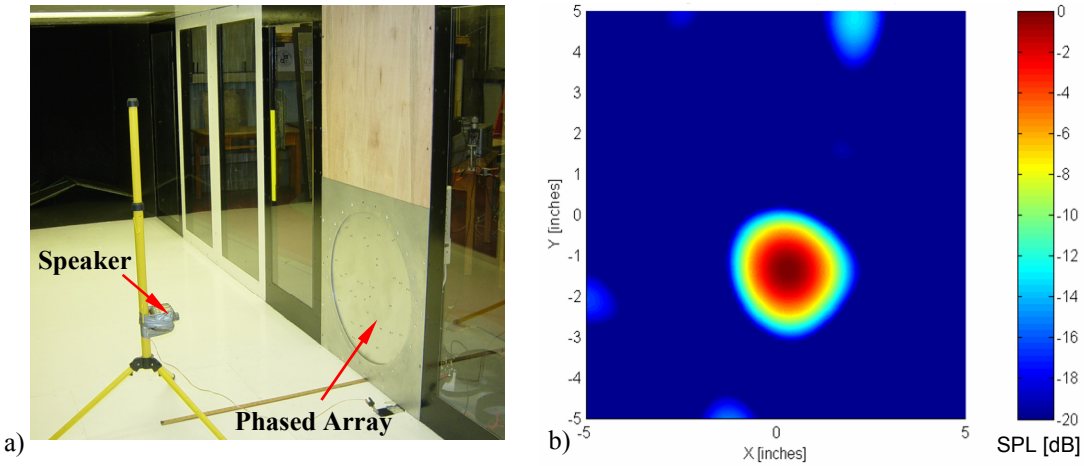

Figure 3.16: a) Test setup to evaluate no-flow performance of the array in reverberant environment using a speaker inside the wind tunnel test section, and b) beamforming results at 10 kHz showing the speaker position

The last preliminary test used the same whistle mounted on the door of the landing gear model to evaluate the performance of the system in the presence of a complex source. Figure 3.18 shows the setup and results. As in the previous test, the maximum level for the whistle was found at 4.34 kHz when the tunnel was driven at the same flow speed. The whistle position was also determined successfully.

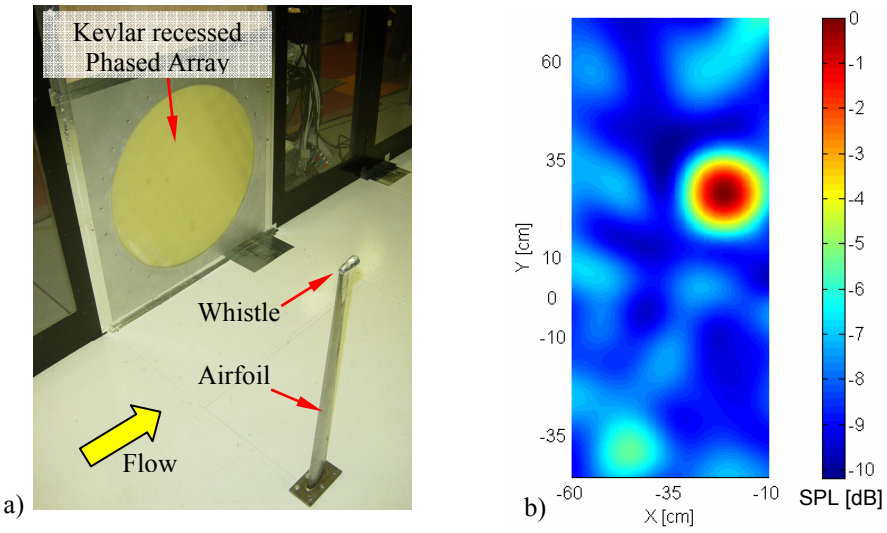

Figure 3.17: a) In-flow array testing using a whistle in the wind tunnel test section, and b) beamforming at 4.34 kHz showing the whistle position.

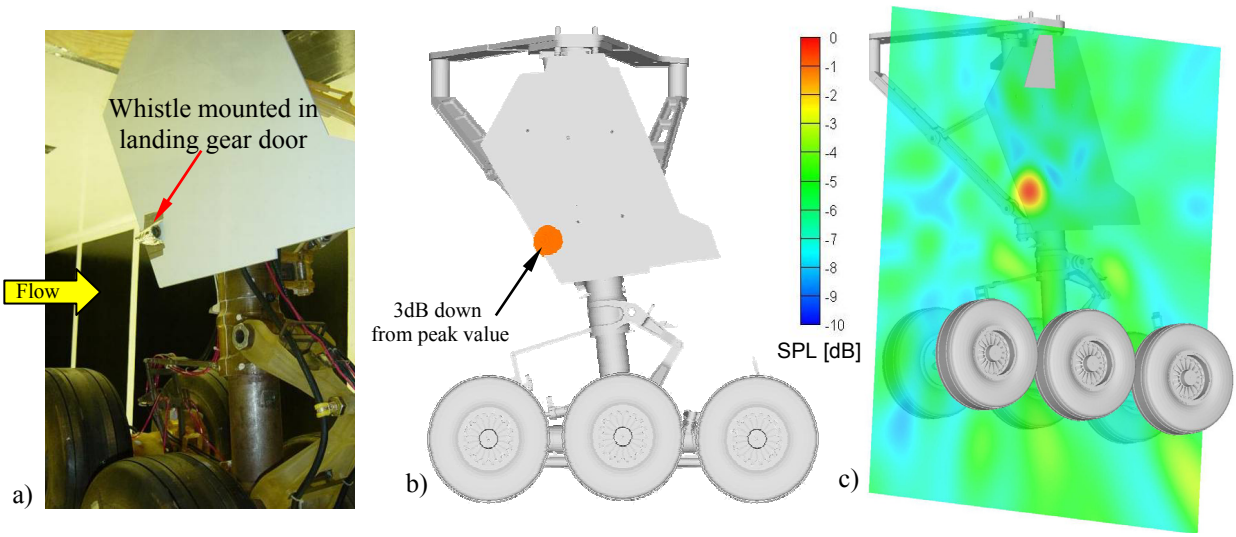

Figure 3.18: In-flow testing with complex source: a) whistle mounted in landing gear door, b) spot size and c) beamforming map at 4.34 kHz showing the whistle position.

Chapter 4

Experimental Results

This section has the main objective of describing how the phased array results were used to identify, rank, and summarize the dominant noise sources and their contribution to the flyover radiated noise from the baseline landing gear. The phased array was used for the noise source identification while the linear array data was used to determine the directivity pattern in the flyover path. The 32-element phased array shown in Figure 3.1 was used in this noise source identification phase. The effect of removing components and a repeatability study are also presented.

4.1 Noise Source Identification

For the noise source identification process, the high fidelity landing gear was tested with the phased array in the three positions as shown in Figure 3.10. The output from the beamforming over a 3D grid surrounding the model was obtained and the level and coordinates of each major noise source were tabulated. Using the “hot spots” coordinates from the beamforming maps, the landing gear components most likely responsible for those noise sources were identified. This noise source identification process is illustrated in Figure 4.1 at two different frequency bands. In this figure, the “red spot” shows the highest SPL at that particular scanning plane parallel to the phased array and the identified gear component responsible for that noise source. As can be seen, the main noise sources are the braces junction, the hydraulic valves and lines, the lock link junction, and the forward cable harness.

Since the number of noise sources found was significant, they were grouped as associated to particular gear sub-assemblies. For example, all the oleo lines and small features in the upper

part of the strut where grouped into the "Main strut-up" sub-assembly. The sub-assemblies considered for the grouping process of the noise sources are shown in Figure 4.2. By grouping noise components, it was possible to have a "clearer" picture of the relative importance of the different gear components impact on the overall noise emission. It also allows summarizing all the noise sources in a simple SPL vs. frequency plot for each array position. That is, a graph showing the maximum level at each frequency band for each sub-assembly. From these results, it was also determined that for some sub-assemblies the noise spectrum was significant only at a single 1/12th octave band. This observation was used to characterize the noise from the sub-assemblies into broadband or "tone-like" type. Note that in this study a tonal source is, thus, referred as the one that dominates at an isolated frequency band.

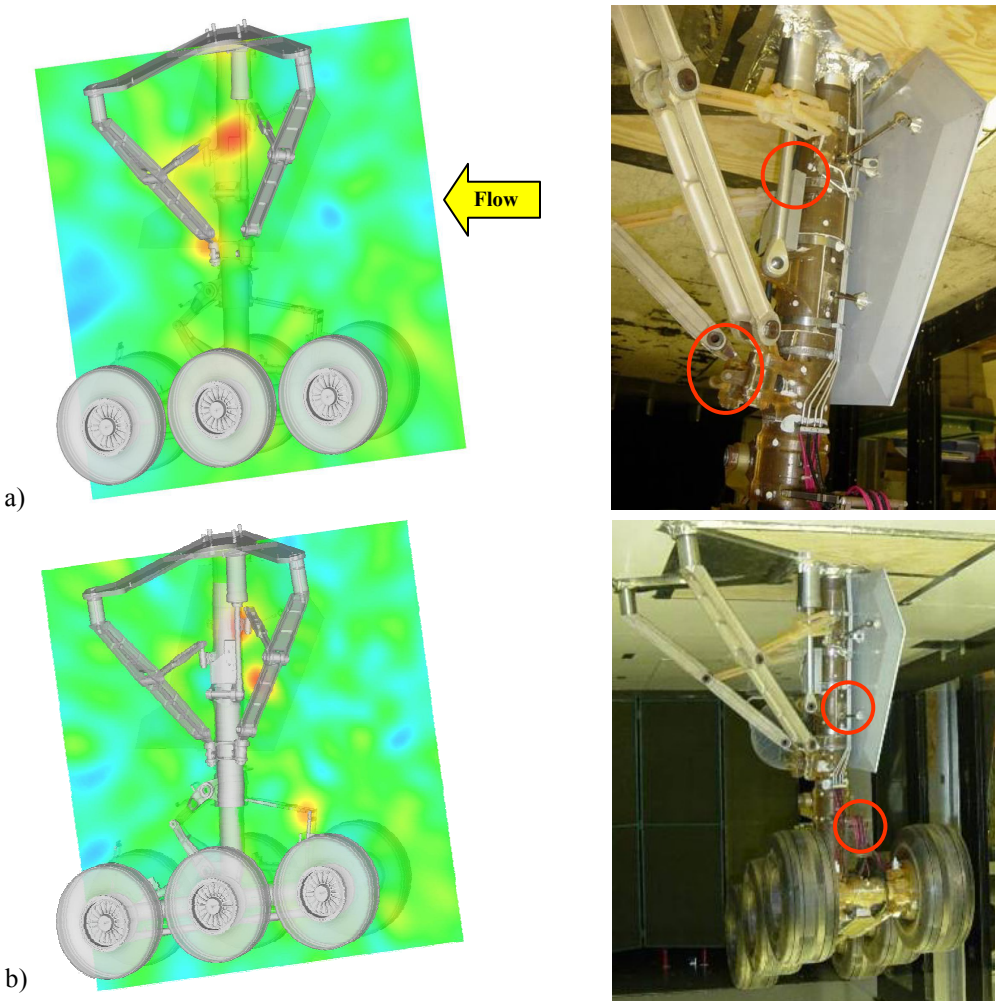

Figure 4.1: Noise source identification at a) 5.2 kHz and b) 5.8 kHz (model scale frequencies) showing the braces junction, the hydraulic valves and lines, the lock link junction, and the forward cable harness as major noise sources.

The identification of the sources, grouping into sub-assemblies, and plotting of resulting spectra was performed for all three phased array positions. The frequencies and levels were scaled to full scale using the model scale and flow Mach number corrections [3] as described in Appendix D.

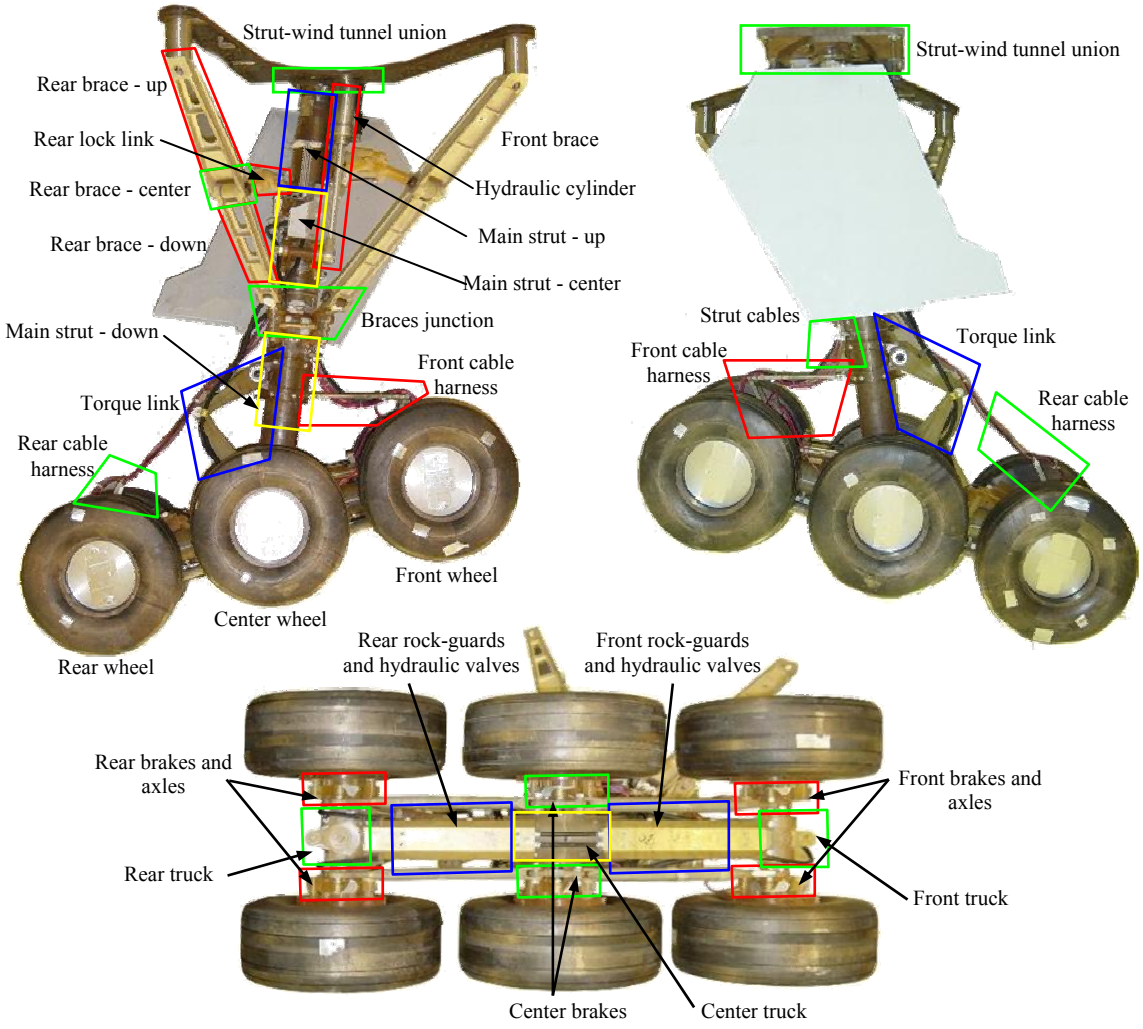

Figure 4.2: Sub-assemblies used in the noise source identification process.

4.2 Noise Source Identification – Full-Scale Frequencies

The largest number of noise sources was found with the phased array positioned on the braces side. This outcome was expected since the sources are not shielded by any particular gear component as it occurs with the other array positions, e.g. noise sources shielded by the door or

the truck. Figure 4.3 and Figure 4.4 show the results for the case of the phased array positioned on the braces side for "tonal" and "broadband" sources, respectively.

It was found that the dominant noise sources at low frequency are the braces, the strut portion close to the tunnel, and the front cable harness. At mid frequencies, the dominant sources are the strut portion close to the tunnel floor, the braces junction, the front and rear cable harnesses, and the back lock link. At high frequencies, the major noise sources are the hydraulic cylinder, the rear lock link, the brace junction, and the interface between the strut and the wind tunnel. It should be mentioned that the noise source at the interface between the strut and the wind tunnel might be lower since the source is close to a reflective source, and so, its image source is likely to modify the levels in that zone. It can also be seen that at the upper end of the spectrum (~5 kHz full-scale), the dominant sources are the wheels. This dominant noise source has been reported previously [19] and shown to be due to the sharp edges of the tire grooves in the model. However, testing of full-scale wheels did not show this noise source. Since this source is "artificial," it was eliminated in all subsequent tests by taping the grooves.

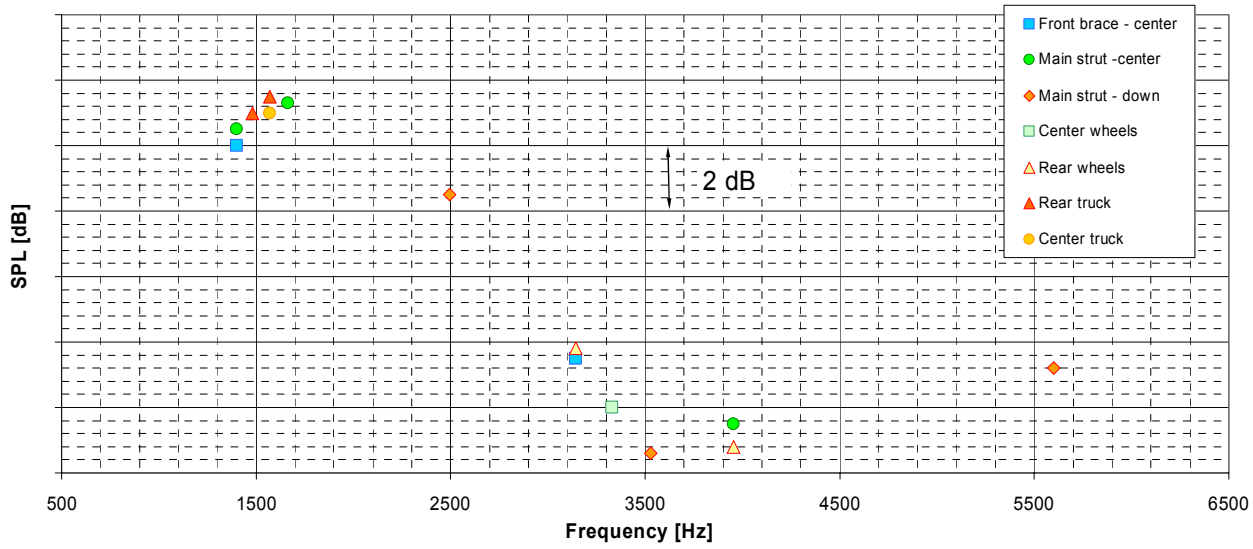

Figure 4.3: "Tonal" noise sources identified with the array on the braces side.
Results extrapolated to full scale frequencies.

With the phased array in the flyover path, most of the sources found in the strut and braces were shielded. In this sense, no assumption has been made about the capabilities of the array in "finding" noise sources behind other objects obstructing the line-of-sight to some or all the microphones in the array. Thus, only the noise sources found in the lower part of the truck or

immediately close to it were considered and tabulated. Since the same sources that appear as broadband for some frequency ranges appear also as "tonal" at other frequencies, the broadband and tonal type sources were not plotted separately in this case. The results from the array in this flyover path position are presented in Figure 4.5. For this array position, the major noise sources were found to be the hydraulic valves and oleo lines below the rock guards, the brake cylinders, axles, brake rod junctions and towing jacks. As in the previous array position, the grooves in the tires appeared as a significant noise source at high frequencies.

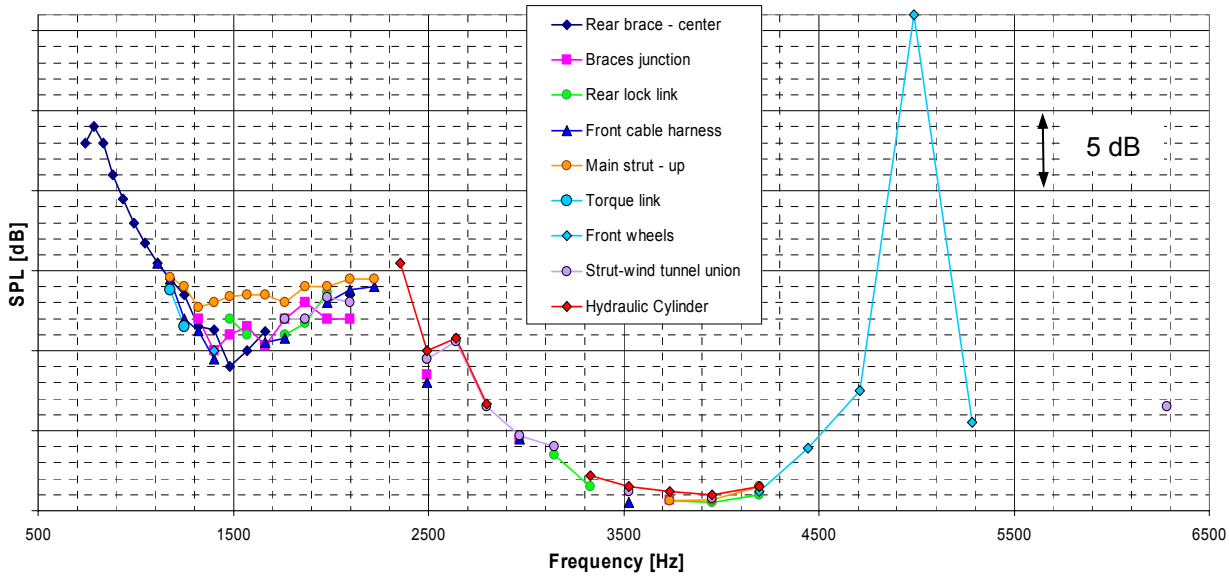

Figure 4.4: Broadband noise sources identified with the array on the braces side.
Results extrapolated to full scale frequencies

For the case of the phased array positioned on the door side, most of the noise sources found in the strut and braces were shielded by the door. However, this shielding effect was an advantage since by "hiding" the loudest noise sources it was possible to find others at lower levels and potentially relevant. As shown in Figure 4.6, it was found that at low frequencies the dominant noise sources are the torque link, the wheel hubs, and the front cable harness. At mid frequencies the noise was dominated by the torque link, rear cable harness, the oleo lines in the strut, and the gap between the door and tunnel floor. The later one related to the noise coming from the hydraulic cylinder and the strut-wind tunnel union as seen with the array on braces side. In this case, the image sources could be also important. It must be pointed out that in the actual landing gear the strut-wind tunnel interface is not present. However, the landing gear cavity was

not simulated in this test setup. At higher frequencies, the noise was again dominated by the grooves on the tires. Note that the lowest level in all these figures has been set to the same value so that results from the various array positions can be directly compared. However, the distance from the sources to the array in each case is different and the data was not corrected in this sense since the differences are not significant.

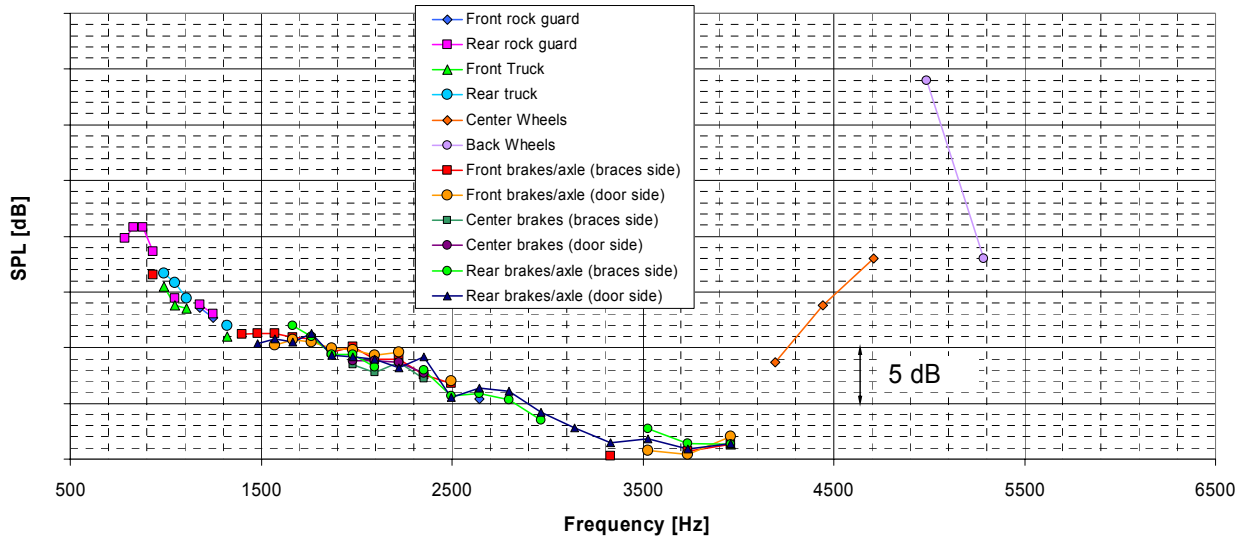

Figure 4.5: Noise sources identified with the array in the flyover path.
Results extrapolated to full scale frequencies.

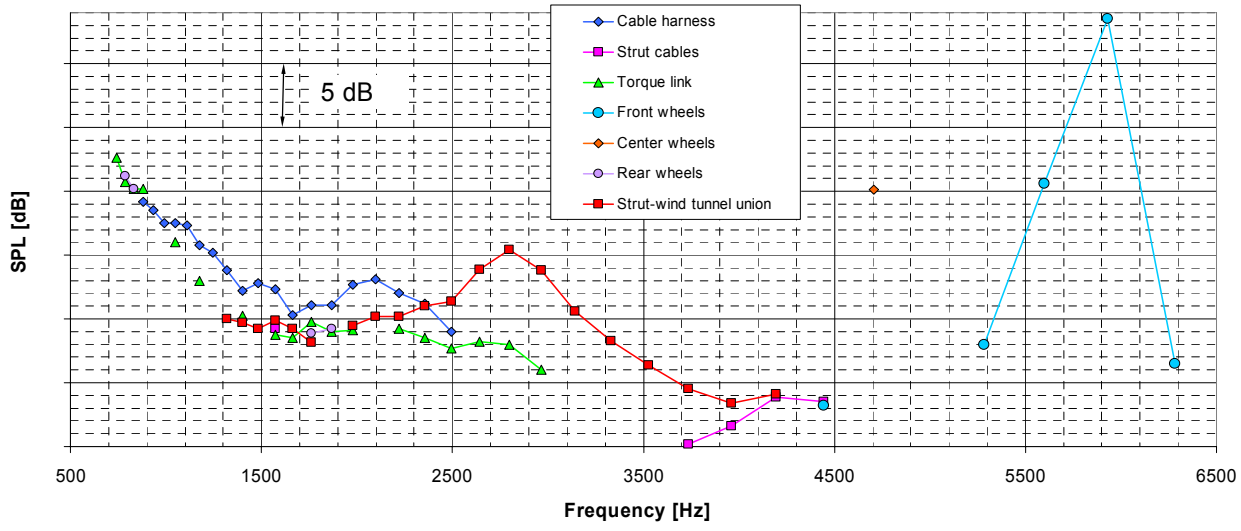

Figure 4.6: Noise sources identified with the array in the door side.
Results extrapolated to full scale frequencies.

As mentioned before, the linear array was used to determine the radiation pattern of the landing gear in the vertical plane. To this end, the levels of the microphones were adjusted to take into account distance to the model. As seen in Figure 4.7, the gear radiates about 2.5 dB more noise towards the rear observer angle.

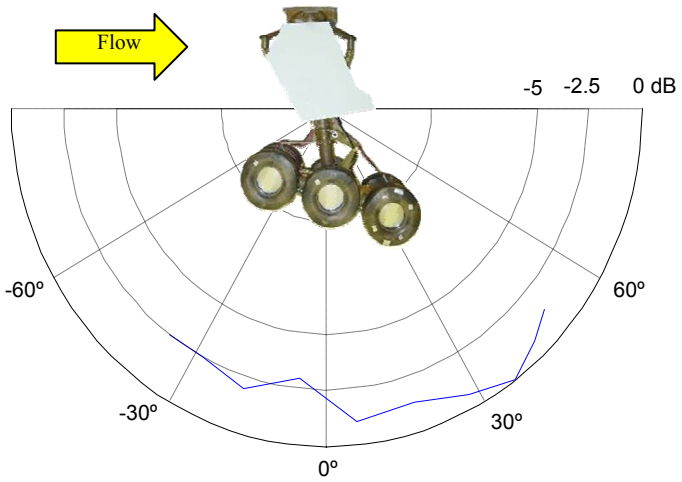

Figure 4.7: Directivity pattern obtained with linear array of microphones in the flyover path showing the rear observer angle as the direction of preference.

4.3 Repeatability of Results

After completion of the tests, the setup was removed from the wind tunnel and the data was processed and analyzed to accomplish the noise source identification task. A follow-up test entry was carried out a few months later for the same high fidelity gear configuration. This second experiment provided a unique opportunity to check for repeatability of the phased array results.

The repeatability study was performed by comparing selected noise maps focusing on the frequency bands and position of the major noise sources. Figure 4.8 shows an example of the repeatability results at the $1/12^{th}$ octave band number 151 (6.1 kHz center frequency). It can be seen that for the two test entries the position and relative level of the sources are in good agreement. The repeatability can also be assessed in terms of "global" results comparing the integrated spectra. In this sense, Figure 4.9 shows the integrated spectra for two baseline configurations taken in different test entries within a month. As can be seen, the shape of the spectra is very similar over all the frequency range. The difference in levels is less than 1 dB

over all the frequency range, thus, being very satisfactory.

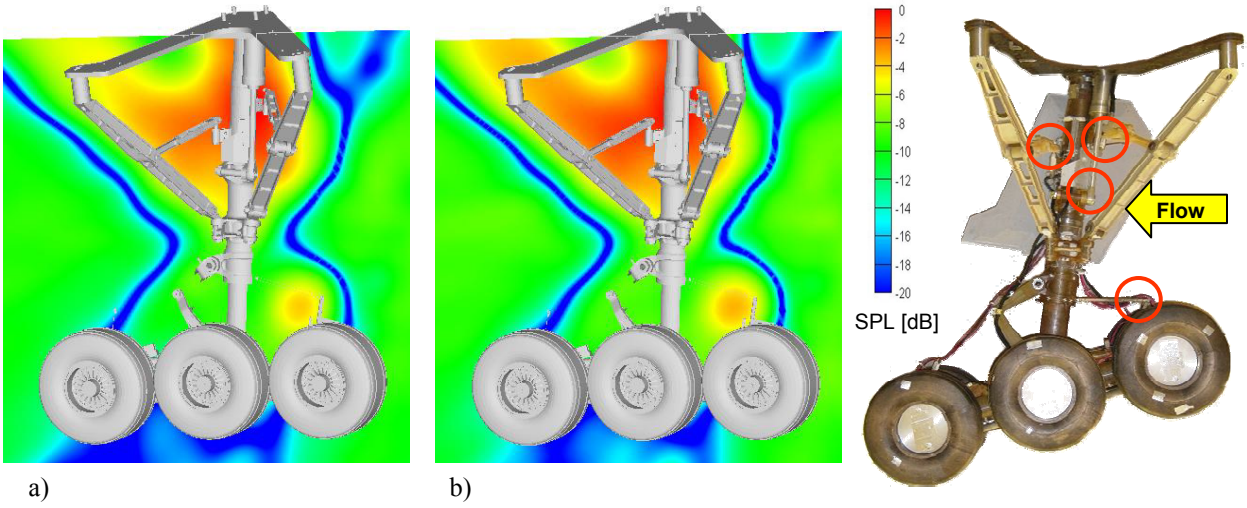

Figure 4.8: Repeatability of results comparing beamforming results from a) first test entry, and b) second test entry. Results at 6.1 kHz model scale.

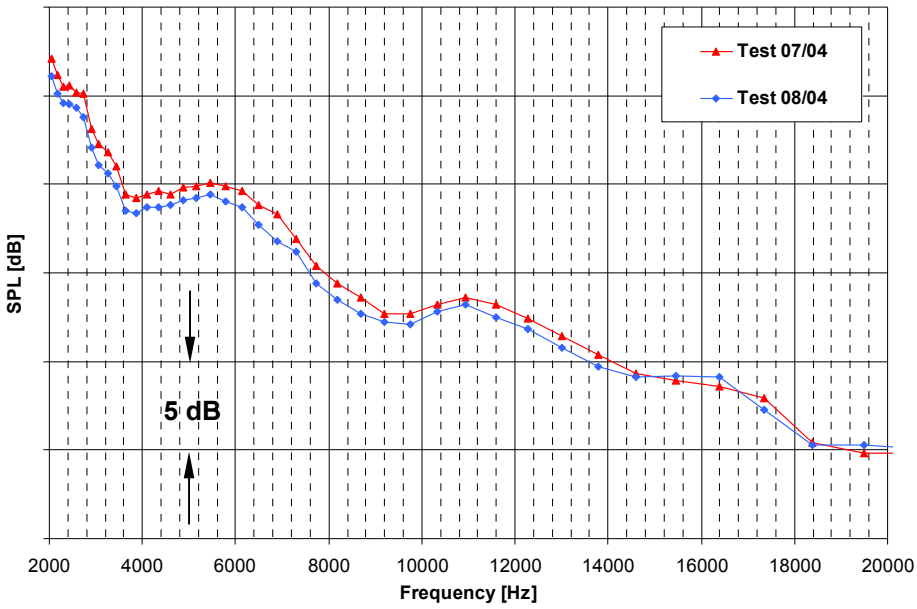

Figure 4.9: Repeatability of results comparing the integrated spectra comparison for baseline configurations in different test entries showing very good agreement in the levels.

4.4 Components Removal

Upon completion of the fully dressed landing gear configuration, a series of tests were carried out where selected gear components were removed. It was understood that in this process the flow field was affected and thus the actual noise generation mechanism might be artificially modified over other components. However, it was decided that these tests could still provide useful information. Thus, the main purpose of removing components of the model and retesting the system was to gain some insight into the noise generation mechanism as well as to determine the potential noise reduction of an "ideal" noise control device installed in the removed component. The results shown hereon are presented in model-scale frequencies.

Since from previous studies the braces were found to be one of the most significant noise sources at low frequencies, it was of particular interest to remove this component, re-test, and analyze the results. To this end, three different model configurations were tested and compared: the fully dressed landing gear, without the front brace and lock link, and without both front and rear braces and links as shown in Figure 4.10.

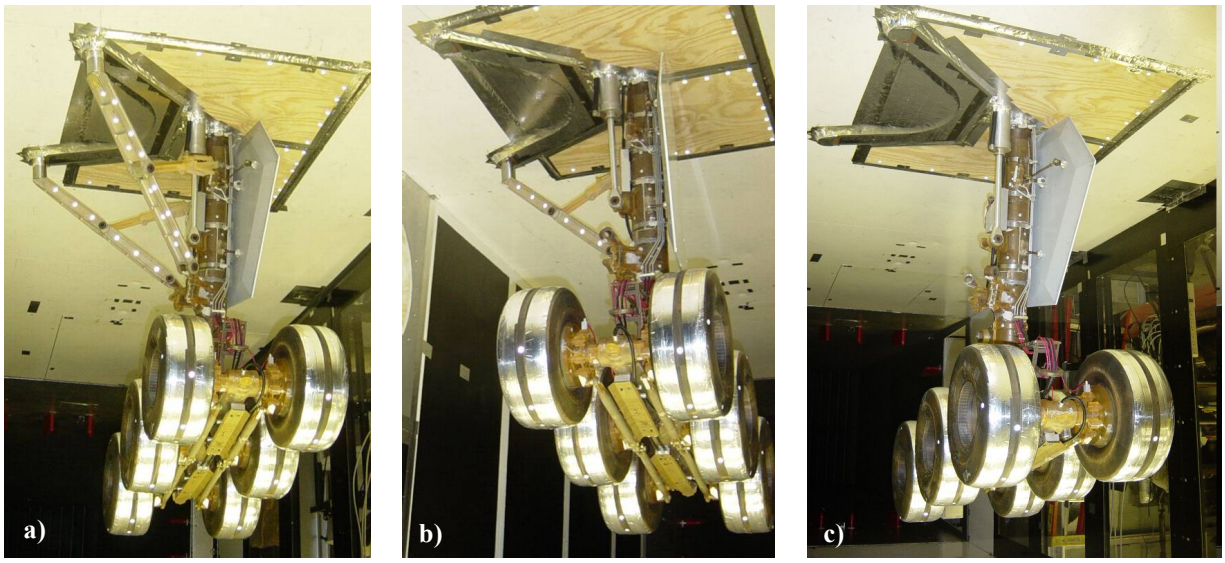

Figure 4.10: Landing gear setup for the a) fully dressed, b) without front brace and lock link, and c) without braces and links configurations for components removal study.

The beamforming results for the 1/12th octave band 133 (2.17 kHz center frequency) are shown in Figure 4.11. As can be observed, the levels of the mainlobe in the back brace were

significantly reduced when removing the front brace. This trend is observed at all the frequency bands where the noise from the braces appeared. This result suggests that the main noise generation mechanism in the back brace is the wake coming from the front brace impinging on the rear brace. It can also be noted that by removing both braces the noise source at the back brace is not present and sources that were not "visible" before start to appear in the beamforming map, i.e. source at 59.9 dB at the strut.

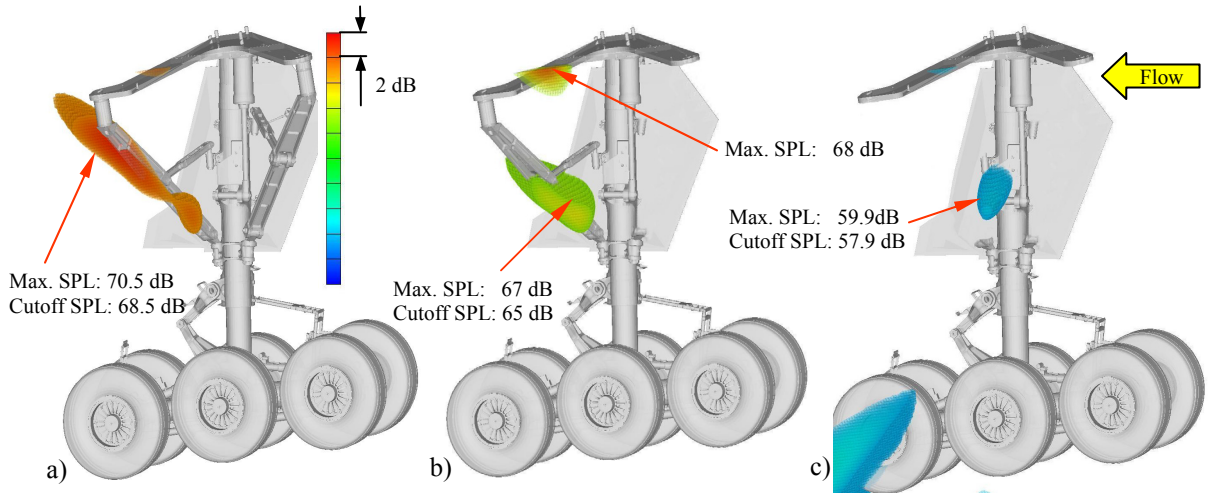

Figure 4.11: Beamforming results at 2.17 kHz center frequency for: a) fully dressed landing gear, b) without front brace and lock link, and c) without braces and links.

To evaluate the effects of removing the back lock link, three different model configurations were compared: a) the fully dressed landing gear, b) without the front brace and lock link, and c) without the front brace and both links removed, as shown in Figure 4.12.

The beamforming results at a particular frequency band are shown in Figure 4.13. It can also be observed that the back lock link shows a slight increase in levels when removing the front brace. This result suggests that the main noise generation mechanism is the flow going through its complex geometry rather than a strong interaction with the wake coming from the front brace/link. Removing the back link, the levels drops significantly and some additional sources can be seen in the strut and truck.

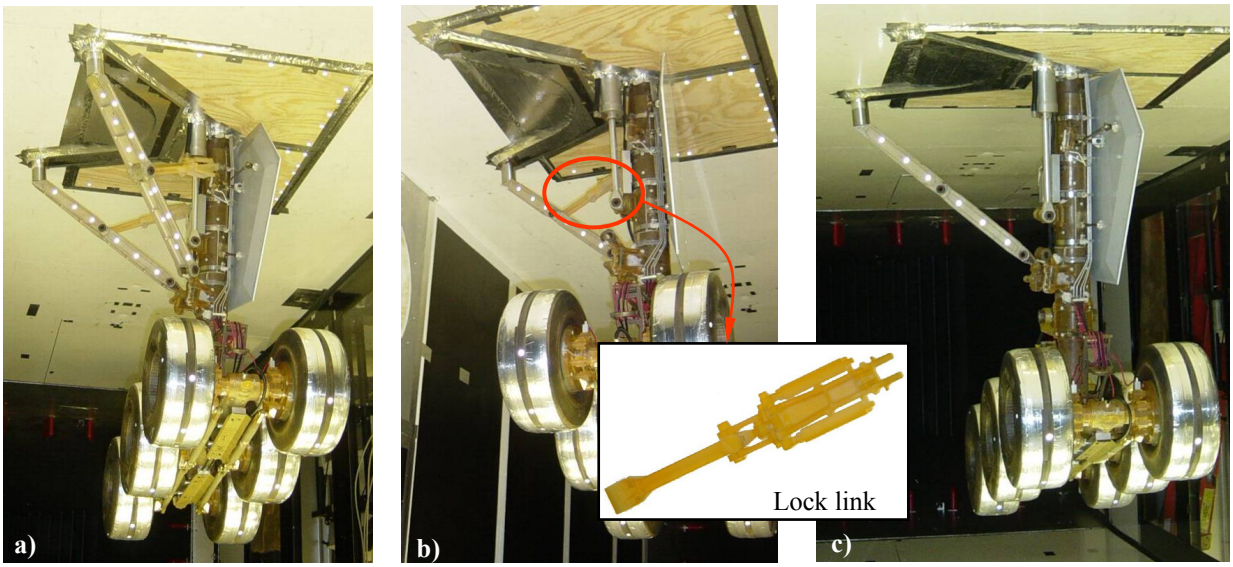

Figure 4.12: Landing gear setup for the a) fully dressed, b) without front brace and lock link, and c) without front brace and both links removed configurations for components removal study.

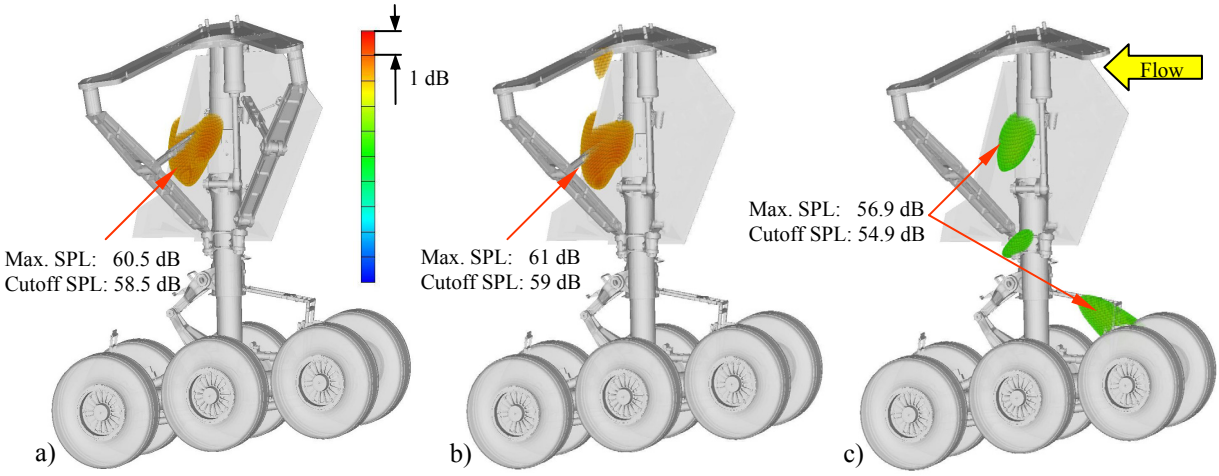

Figure 4.13: Beamforming results at 4.1 kHz for: a) fully dressed landing gear, b) without front brace and lock link, and c) without front brace and both links removed.

4.5 Summary of Results

As shown in previous sections, the landing gear presents a large number of noise sources. Furthermore, the noise associated to each component is mostly broadband. This suggests that it would be impractical to design localized noise control devices for each of identified component.

Thus, the approach used in this work to reduce the noise from the gear is to design devices that could encompass as many components as possible, i.e. a strut fairing should “hide” from the flow all the oleo lines and complexities in the main strut.

Chapter 5

Noise Control Devices

As stated before, the ultimate goal of this work was to design a series of noise control devices for a 777 main landing gear to reduce the noise emission. Aerodynamic fairings have been demonstrated to be an effective noise control approach. The fairings basically hide complex geometries from the flow and/or reduce wakes interactions. However, a lot of limitations arise for the implementation of any noise control device in a commercial aircraft. There are strict constraints about weight, dimensions, cost, maintainability, ease of inspection, and stowage (space needed when the landing gear retracts), among others. Most of these constraints were considered in the design process in order to obtain the most realistic and feasible noise control devices as possible.

The approach undertaken here was to implement a series of noise control devices to prove the concept. In a second stage, these devices were then redesigned to address the above mentioned constraints and to make their implementation practical. To this end, devices were designed for the main strut, braces, lower truck, torque link and forward cable harness. For preliminary testing of the concepts, cardboard (rigid) and speed tape were used for some of the fairings. In the second stage, the innovative concept of making fairings from ***elastic cloth membranes*** that addressed most of the system constraints was developed. These new fairing concepts were tested to demonstrate the potential noise benefits as well as to establish the feasibility of these devices for full-scale implementation.

As mentioned in chapter 3, the results shown hereon were obtained with the 63-element equal-aperture multi-arm spiral array shown in Figure 3.3. The results are presented in model scale frequencies.

5.1 Fairings Concept

As mentioned before, the novel concept developed in this work was to use elastic cloth membranes to create local aerodynamic fairings so as to hide complex geometries from the flow and/or reduce wakes interactions. The goal of these fairings was to encompass as many noise sources as possible with a single device. In this sense, the devices were focused on four main areas: the main strut, the braces, the lower truck and the cable harnesses and torque link.

For the implementation of such devices, a double-layer of elastic "lycra-like" cloth was used. This material was selected because it presented all the required properties for the concepts being developed, i.e. thin, lightweight, stretchable, and relatively strong. The noise control devices were mounted to the landing gear using Velcro for simplicity.

The proposed fairing concept offers a number of advantages as compared to previous "rigid" fairings [21]. These are:

- ***"Promising" noise reduction potential:*** as will be shown in the following sections, the noise reduction obtained with these devices is significant.
- ***Light-weight fairing:*** given the material used for the fairings, its weight is significantly reduced when compared to rigid devices.
- ***Easy to mount and remove for inspection purposes:*** since ease of inspection is a big concern, the devices should be easy to mount/unmount to inspect the landing gear.
- ***The devices do not interfere with the stowed position of the gear:*** since the wing cavity where the landing gear retracts was designed to closely fit the gear, there is little space for voluptuous fairings. However, given the small thickness of the membrane, this does not represent an issue. Furthermore, the elastic membrane offers the capability of deforming to "follow" the stowed position of the gear.
- ***No interference with the steering mechanism:*** In the particular case of a 777 landing gear, the back wheels of the gear are used to steer the aircraft. Given the flexibility of the membrane fairings, there is no interference with this mechanism. This is not true in the case of rigid fairings, where some complex mechanism should be used.
- ***Applicable to current and future landing gears:*** once the main noise sources are identified, the elastic-membranes concept can virtually be adjusted to fit any gear geometry, including the nose gear.

- ***Relatively low cost:*** this is related to two aspects. The cost of the fairing itself and the cost of "carrying" its weight during the aircraft lifetime. Since its design is lightweight, the latter one is significantly reduced. The implementation and construction cost for a full-scale fairing was not addressed in this study.

As can be seen, many of the constraints were taken into account in the design process. However, there are some unresolved issues that need to be addressed but are beyond from the scope of this work, such as material selection for resistance to working environment (i.e. interaction with oil, extreme temperatures) and sound absorbing properties to increase shielding effects and thus noise reduction, and actual mounting on the full-scale model, i.e. instead of using Velcro.

5.2 "Flight-model" Devices Implementation

As mentioned before, the final design for the strut, braces and truck fairings were accomplished using elastic cloth membranes. However, for the cable harness and torque link fairings this material was not implemented because from preliminary testing the impact on noise reduction was not expected to be significant, i.e. the final design used a rubber material.

Since the main strut presented a lot of sources at many different frequencies, the strut fairing was intended to "hide" the oleo lines and other components in the main strut from the flow. This device also eliminated the door-strut gap that was found to be a significant noise source.

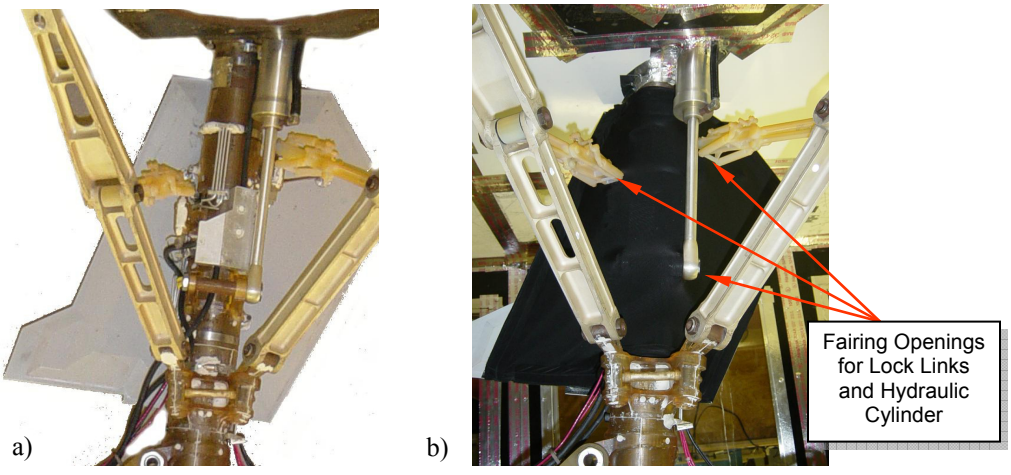

Figure 5.1: a) Baseline configuration showing the complexities in the main strut and b) strut fairing concept using elastic membranes.

Openings were created to allow the lock links and hydraulic cylinder through it as shown in Figure 5.1. In this fairing, the elastic membrane was attached to the door edges using Velcro and stretched to create a "smooth" transition, as shown in Figure 5.2.

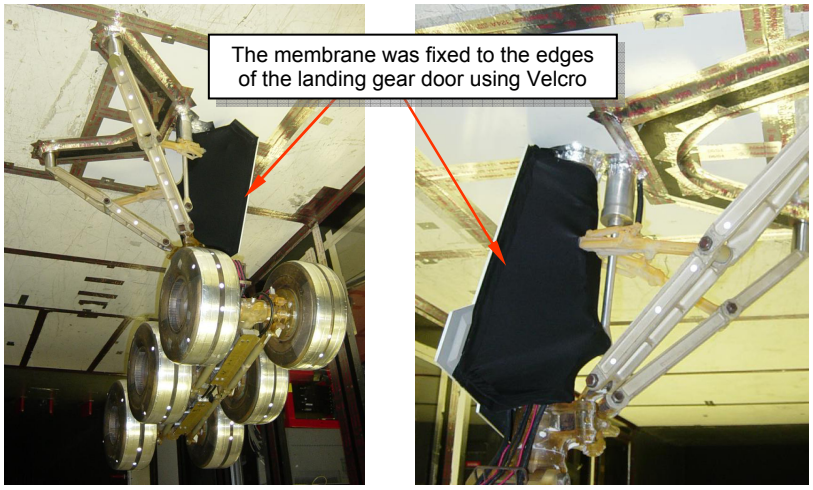

Figure 5.2: Mounting details for the strut fairing concept using elastic membranes.

In the case of the braces, the noise source ID process showed the rear brace to be the dominant noise source at low frequencies. As seen in the previous chapter, the removal of the braces aided to confirm that the noise generation mechanism was the wake generated by the up-stream brace hitting the down-stream brace, and thus generating noise. Then, the main purpose of the braces fairing was to avoid this wake interaction.

In this case, the elastic membrane was "wrapped" around the front brace, stretched around the braces, and held in place in the back of the rear brace using Velcro as shown in Figure 5.3. Openings were created to allow the lock links to go through. The braces junction, also identified as a major noise source, was also "faired" with this device as shown in Figure 5.4.

The noise control device for the lower truck was intended to hide complex geometries and streamline the air flow in that area. Shielding effects could also be a factor in noise reduction, but given the material used it is not likely to have a big impact in the results. The lower truck fairing is shown in Figure 5.5. As can be seen, the membrane was wrapped and "stitched" around the brake rods, and attached to the front and rear of the truck using Velcro. As mentioned before, the use of elastic membranes also adds the advantage of allowing the steering of the back wheels of the gear. The pictures also show that the towing hook and jack points are not "unutilized".

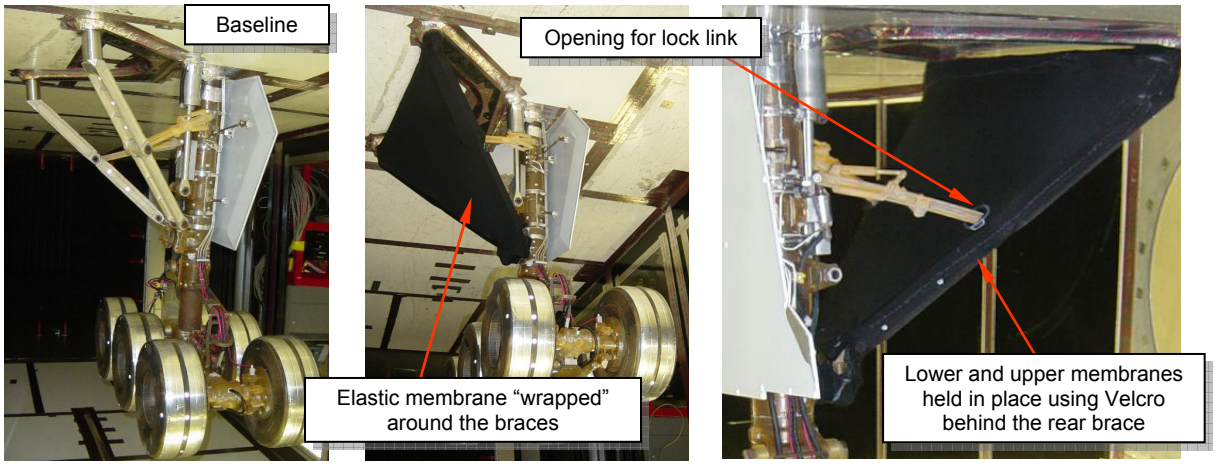

Figure 5.3: Braces fairing concept using elastic membranes

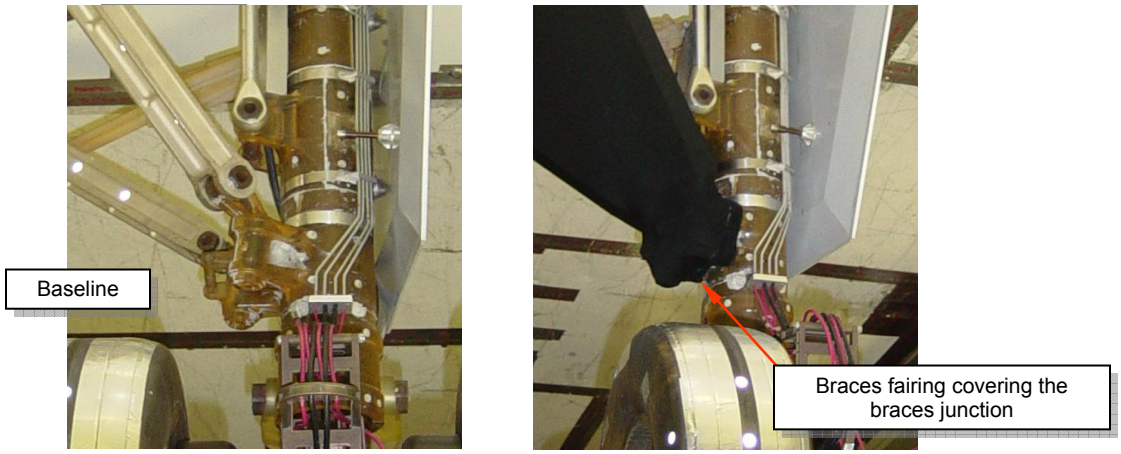

Figure 5.4: Detail of the braces fairing concept in the braces junction area.

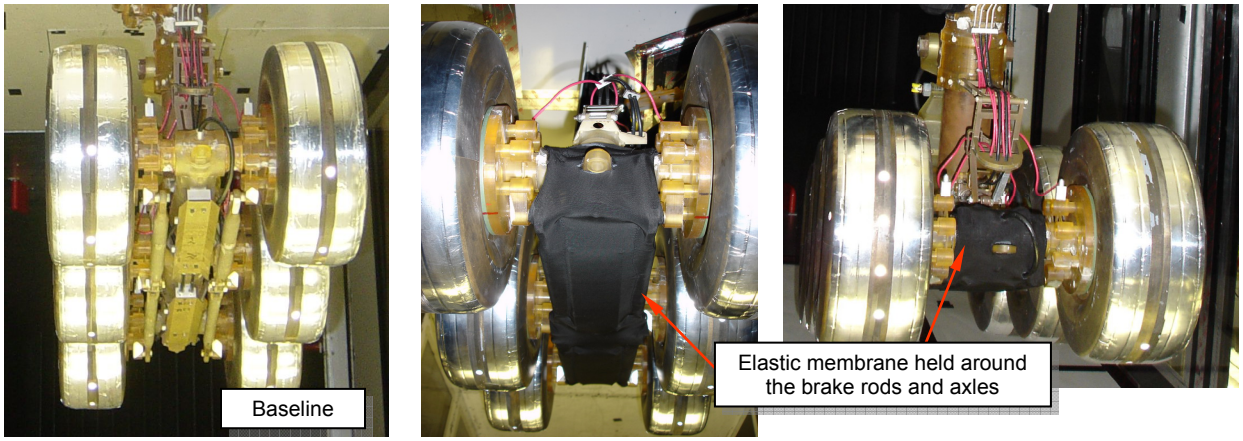

Figure 5.5: Lower truck fairing concept using elastic membranes

For the forward cable harness and the torque link, a different approach was used. Since both of these elements have parts with relative motion, the design must also account for this issue. Since the noise reduction obtained with these devices was not significant, the lycra-cloth concept was not implemented. Furthermore, the front cable harness is no longer used in the new 777-300 series. Figure 5.6 shows the rubber fairing mounted to the moving parts independently, thus allowing motion. In this case, the rubber was allowed to stretch or shrink depending on the relative position of the moving parts. To hold the elastic membranes in place, metal strips fixed to the hinge points were used.

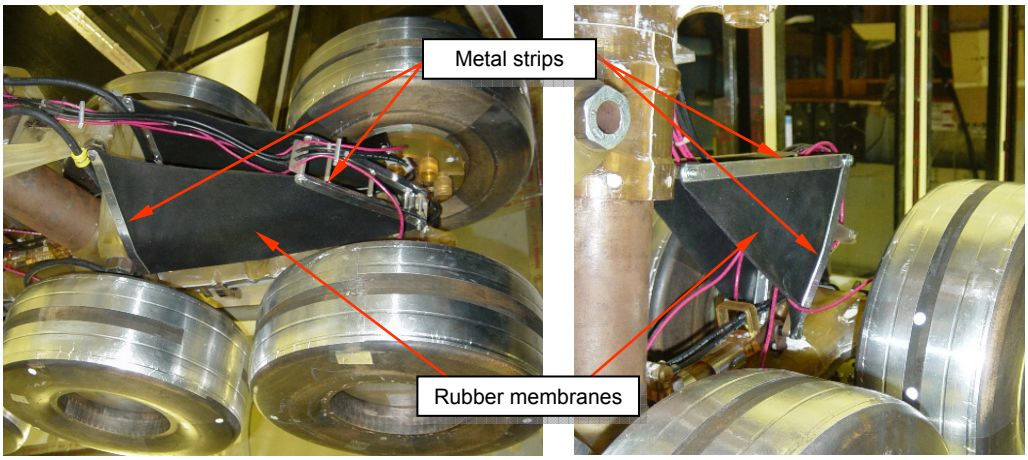

Figure 5.6: Cable harness and torque link fairings using elastic membranes, i.e. rubber.

5.3 Analysis of Results

The beamforming maps and integrated spectra results obtained with the previously introduced devices are shown next. However, only the most significant cases are shown.

5.3.1. Strut Fairing

For the elastic-cloth strut fairing, noise reduction was observed at several frequency bands. It was of particular interest to see that in some cases, the flow seems to be affected by the fairing. As a result, some components were exposed to higher flow speeds and thus, sometimes

generating more noise. This effect is shown in Figure 5.7. The lobes indicated as reflections in the figures where found to be related to image sources of the strut that appear as a consequence of having a hard-wall wind tunnel.

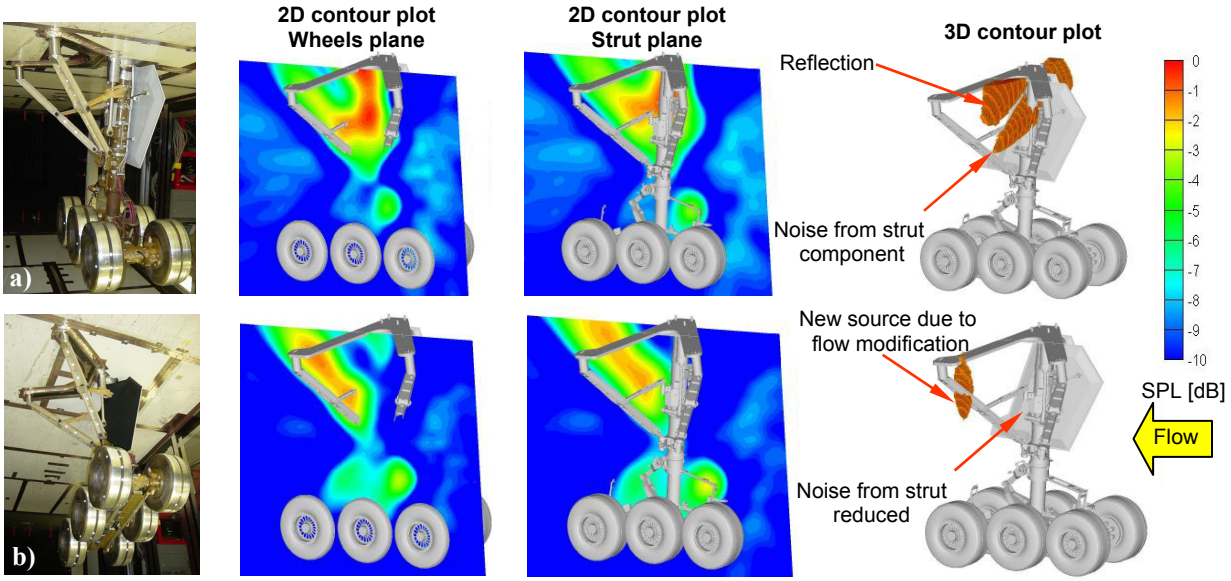

Figure 5.7: Beamforming maps at 6.1 kHz for a) baseline and b) strut fairing configurations.

5.3.2. Braces Fairing

For the braces fairing, interesting results were found. As shown in Figure 5.8, the noise levels on the braces area are significantly reduced when compared to the baseline configuration. As expected, new sources with lower relative levels can now be identified, i.e. noise from the wheels. The same significant reduction can be appreciated at every frequency band where the braces noise was present. The shielding effect on the noise sources of the strut, shown in Figure 5.9, was observed at many different bands, i.e. the braces faring affects the propagation path of sources in the main strut. Thus, a greater noise reduction could be obtained with a more "absorptive" material in this fairing, as mentioned before. The integrated spectrum is shown in Figure 5.12

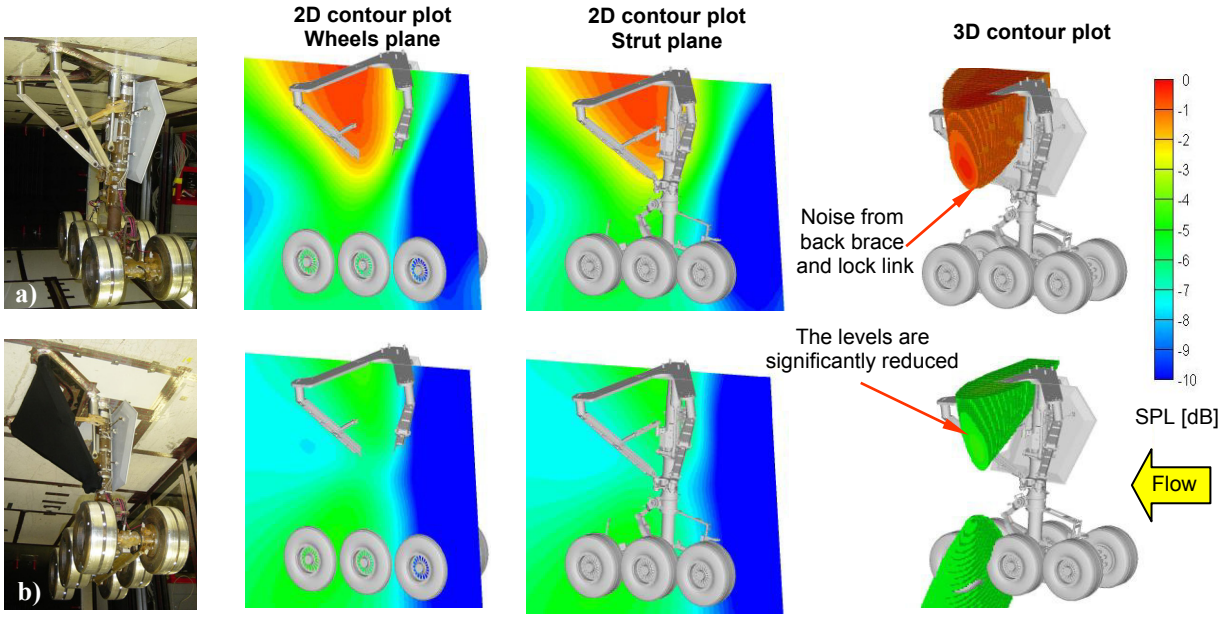

Figure 5.8: Beamforming maps at 2.3 kHz for a) baseline and b) braces fairing configurations.

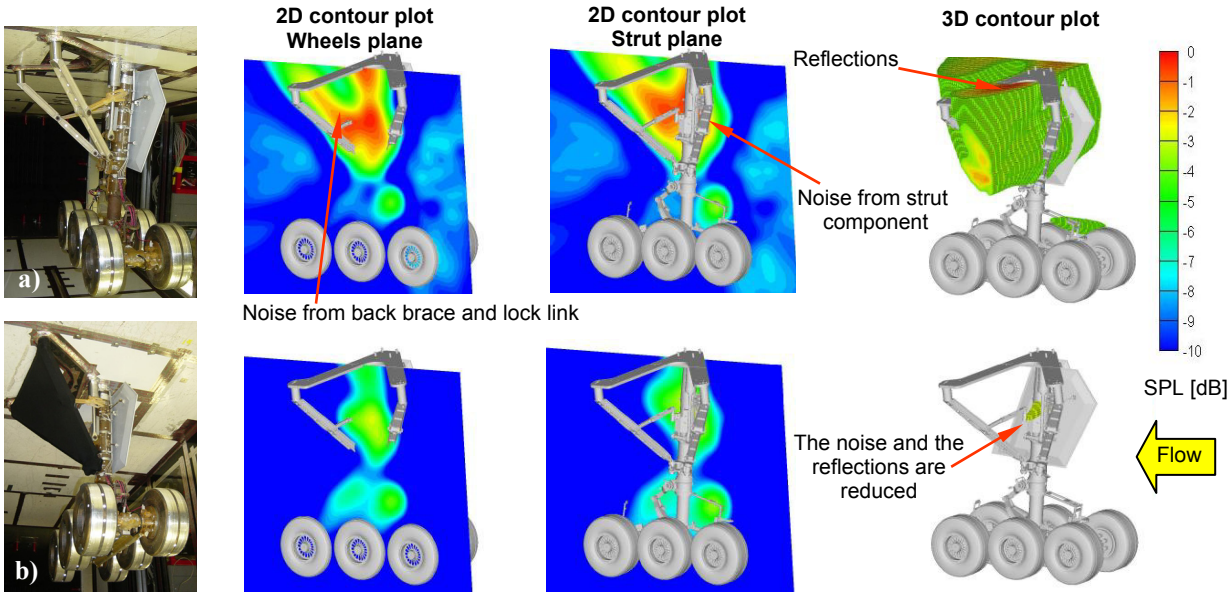

Figure 5.9: Beamforming maps at 5.8 kHz for a) baseline and b) braces fairing configurations.

5.3.3. Strut/Braces Fairings Combination

Combinations of the noise control devices were also tested. In this sense, Figure 5.10 shows the combination of the strut and braces fairings. As expected, such combination rendered better results than the devices separately. A sample comparison between baseline, braces fairing only and braces and strut fairings configurations is shown in Figure 5.11. As can be seen in this beamforming map, the noise sources are significantly reduced. Notice that the maximum levels were set to the same value in all beamforming maps for ease of visualization.

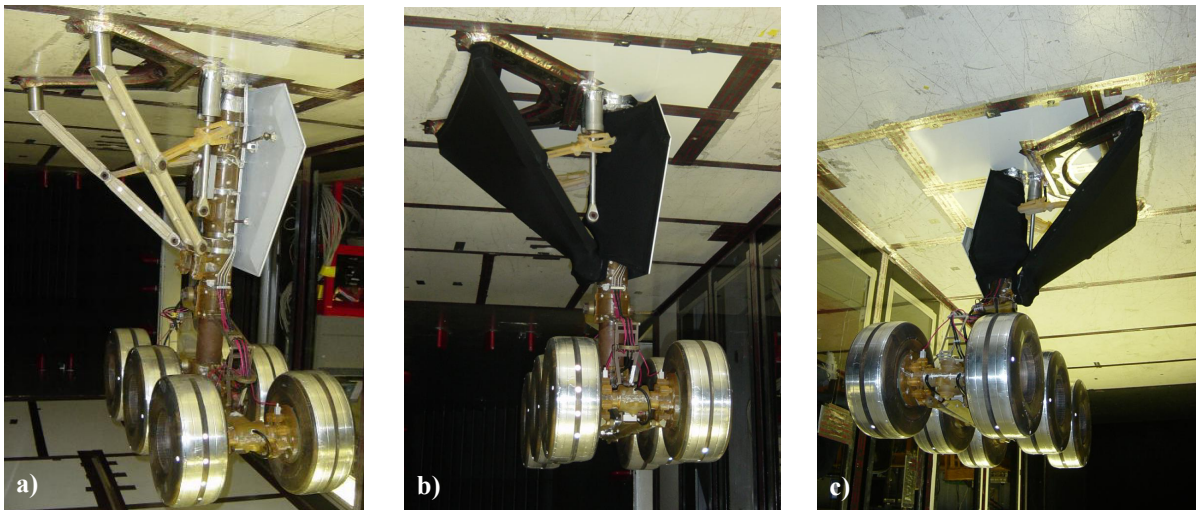

Figure 5.10: a) Baseline gear and b), c) combination of braces and strut noise control devices.

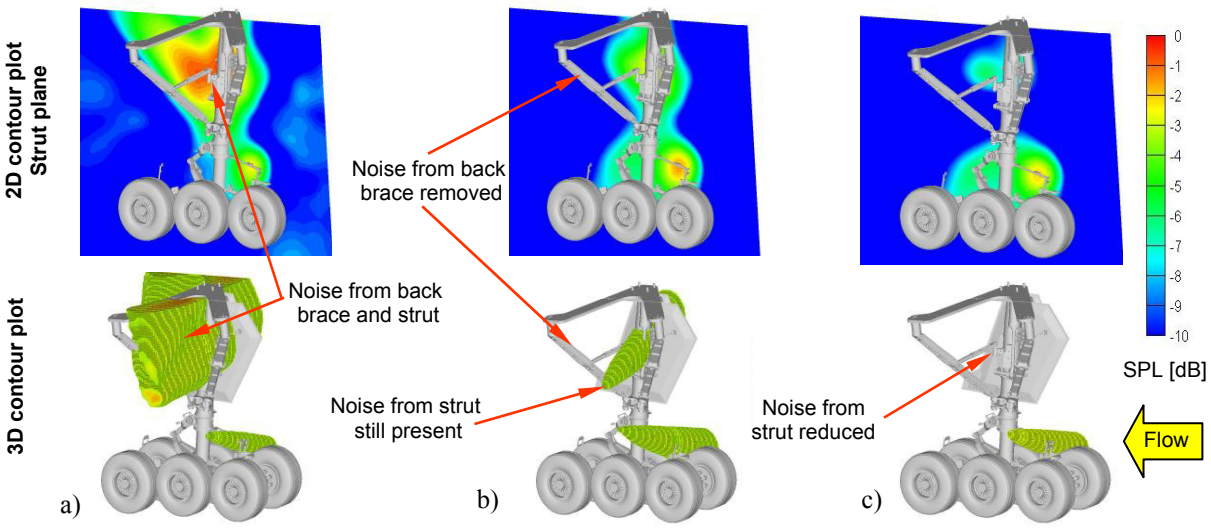

Figure 5.11: Beamforming maps at 5.2 kHz for a) baseline, b) braces fairing and c) strut and braces fairing.

As mentioned before, another way of analyzing noise reduction in a more general form is to use the integrated spectra. As explained in Chapter 2, this procedure adds the levels in the scanning grid obtained in the beamforming to obtain a full frequency range spectra. A normalization technique is used to take into account the scanning grid and array response as explained before. Also, a threshold is applied to avoid adding levels related to sidelobes. Integrated spectra for the configurations presented above are shown in Figure 5.12 and 5.13 for two different array positions, i.e. sideline and flyover.

As can be seen, significant noise reduction is obtained with the array in the sideline position over all the frequency range. In this sense, the strut fairing shows a reduction of at least 1 dB at mid frequencies, and of about 0.5 dB at high frequencies. At the low frequency end it appears to be a noise increase of about 0.5 dB, most probably related to the flow modification mentioned before. The braces fairing shows reductions of about 2 to 3 dB over all the frequency range. In the case of the combination of these two devices, the noise reduction is at least 2 dB for almost all the frequency range, with peak reductions of up to 5 or 6 dB.

In the case of the flyover array, the reduction seen with the array in the sideline configuration is not “visible”. This is due to the fact that most of the sources in the braces and the strut were shielded by the truck and thus affecting their propagation to the array, i.e. not affecting the integration output.

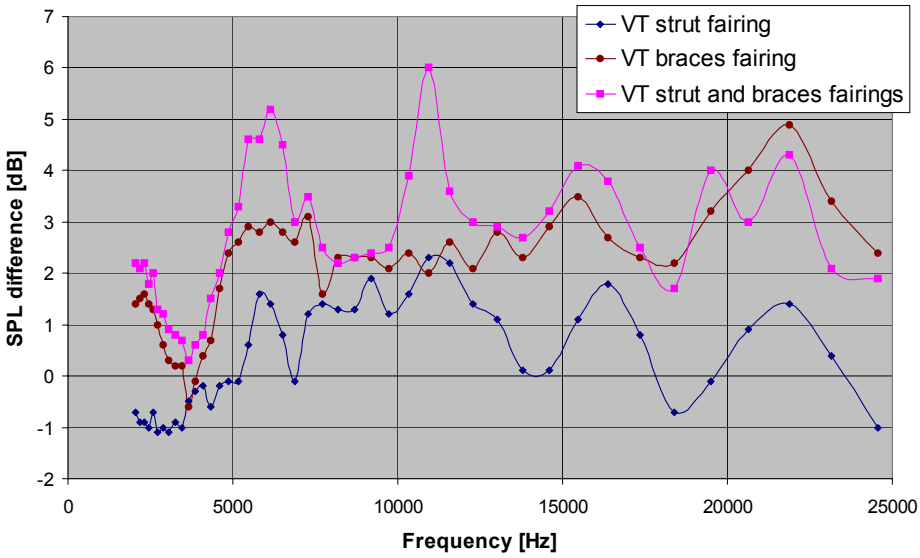

Figure 5.12: Integrated spectra difference between baseline and NCD configurations for array on braces side.

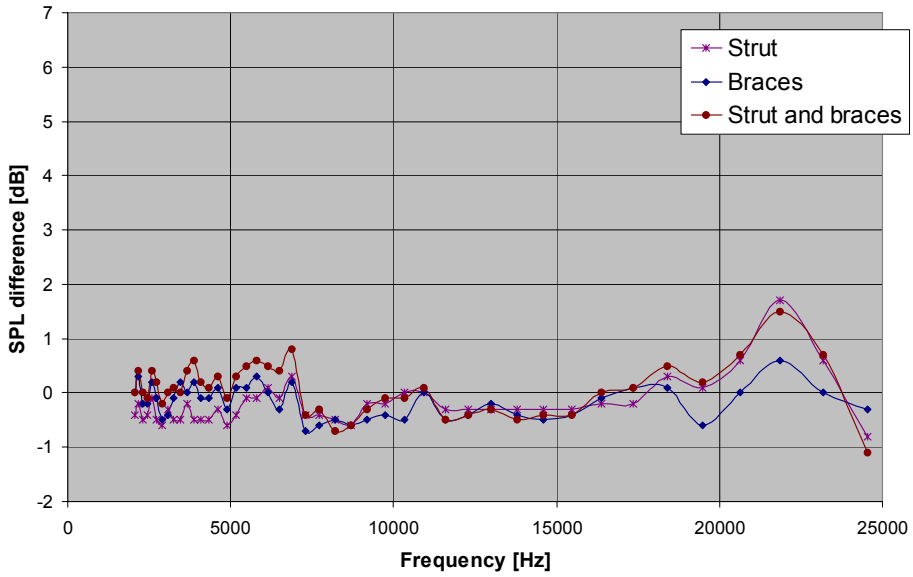

Figure 5.13: Integrated spectra difference between baseline and NCD configurations for array in flyover path.

5.3.4. Lower Truck Fairing

Beamforming results for the truck fairing are shown in Figure 5.14 and Figure 5.15 for 2 different frequency bands. The beamforming maps are presented for two different scanning planes, i.e. one passing through the front wheels axle and another at the rear wheels axle. These results were obtained with the phased array in the flyover position. As can be seen, the main noise sources that appear in the front and rear axles/brakes region are reduced significantly when compared to the baseline configuration. This trend was observed in most of the frequency bands.

The integrated spectrum for this device, when compared to the baseline configuration, shows a reduction of at least 2 dB over all the frequency range. At low frequencies, the reduction is as much as 5 dB. The integrated spectrum is shown in Figure 5.16.

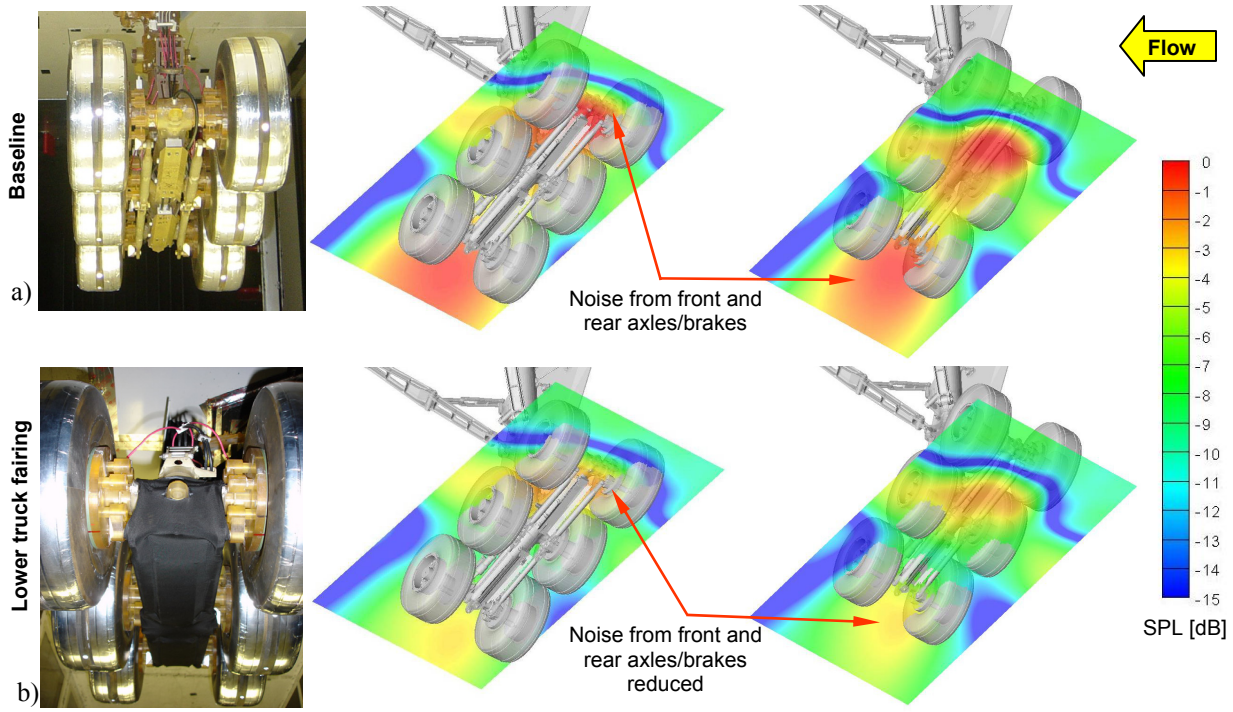

Figure 5.14: Beamforming maps at 4.3 kHz for a) baseline, and b) lower truck fairing.

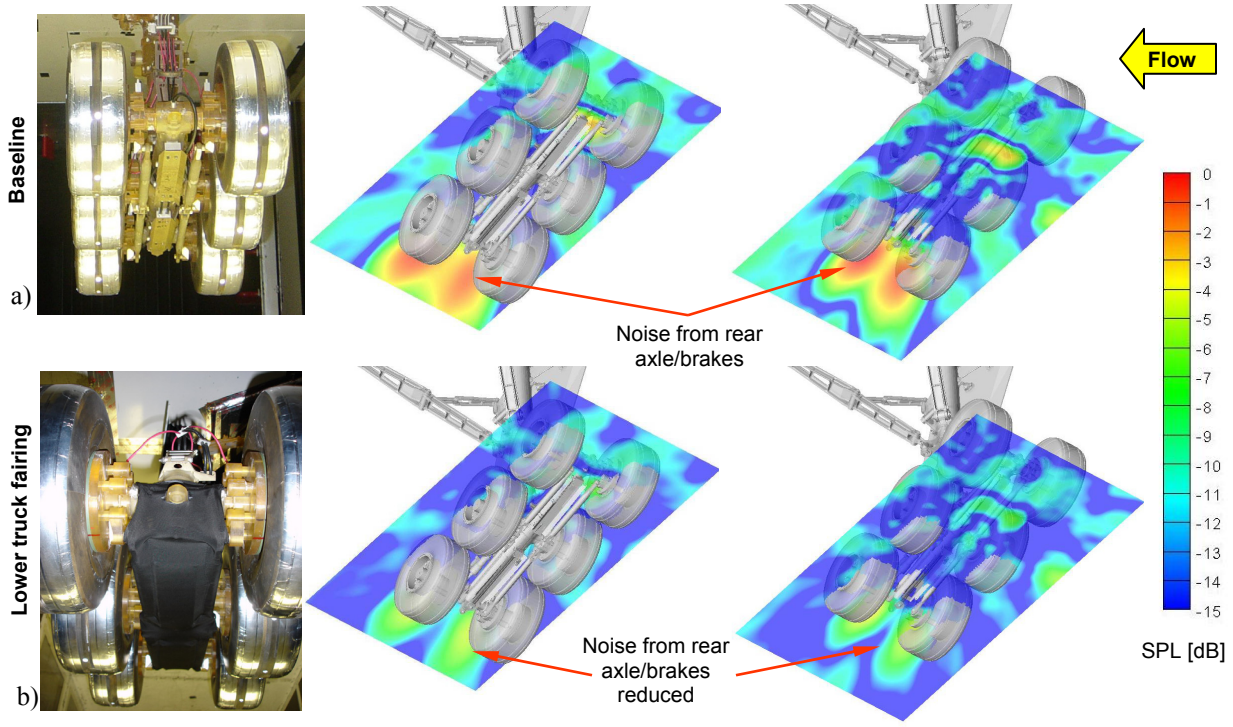

Figure 5.15: Beamforming maps at 13.8 kHz for a) baseline, and b) lower truck fairing

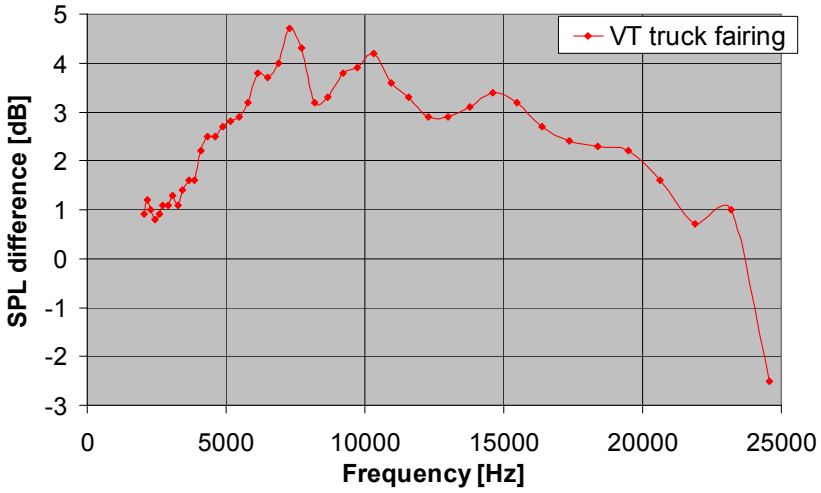

Figure 5.16: Integrated spectra difference between baseline and truck fairing configurations for array in flyover path

5.3.5. Cable Harness and Torque Link Fairings

As indicated, the elastic cloth concept was not implemented for these components. Beamforming results for the rubber concepts are shown in Figure 5.17. Since the noise levels for the cable harness are significantly lower than other sources (i.e. the braces), the results are compared to the braces fairing case in order to have "cleaner" beamforming maps. The baseline case is also shown but with different levels for ease of visualization. As can be seen the levels on the cable harness are significantly reduced. However, for same frequencies, the flow modification in the cable harness area induced higher noise levels on the down stream components, i.e. the torque link.

Two different configurations were tested for the rubber fairings: using only the cable harness fairing and using both fairings. The integrated spectra for these two configurations when compared to the baseline case are shown in Figure 5.18. It was found out that using the cable harness fairing only, the reduction at low frequencies is similar to that of using both devices. However, at high frequencies, the combination of these two devices showed a smaller noise reduction. Thus, the use of a single fairing in the cable harness seems to be more beneficial in terms of noise reduction.

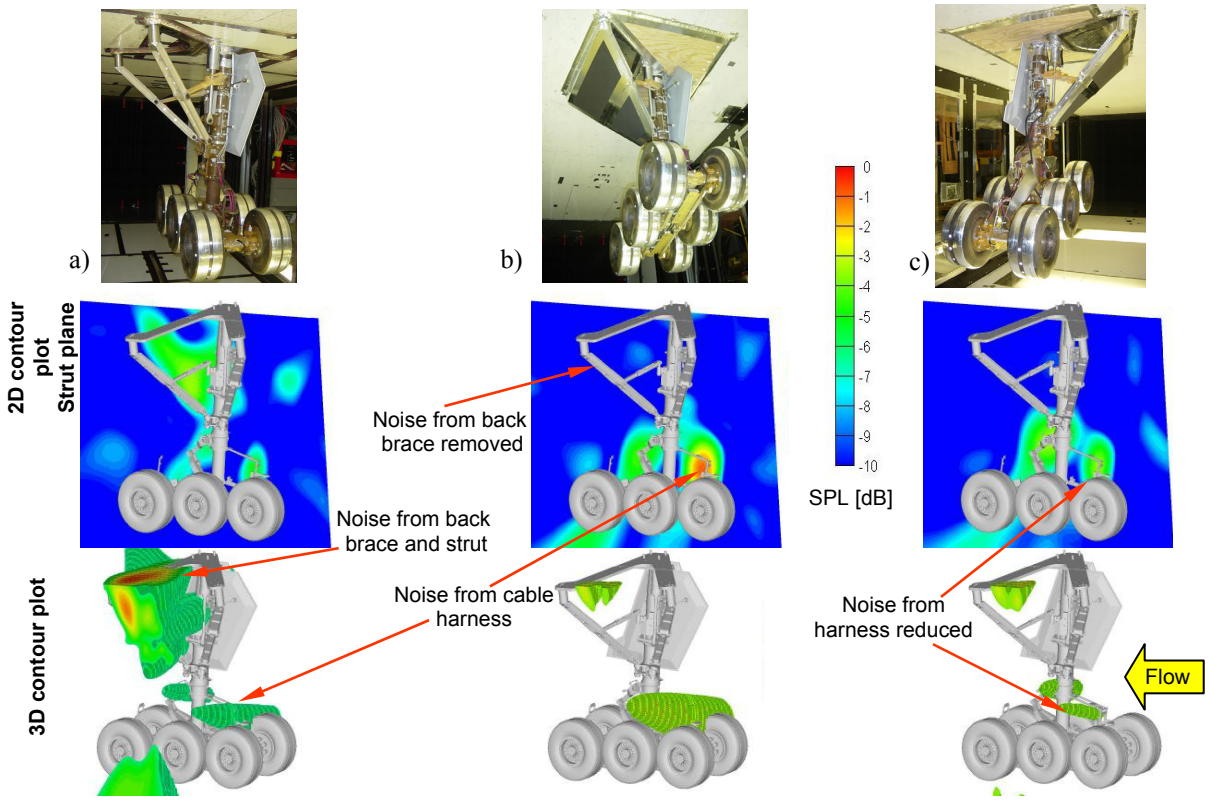

Figure 5.17: Results for cardboard fairings: a) baseline, b)braces fairing and c) braces and harnesses fairings

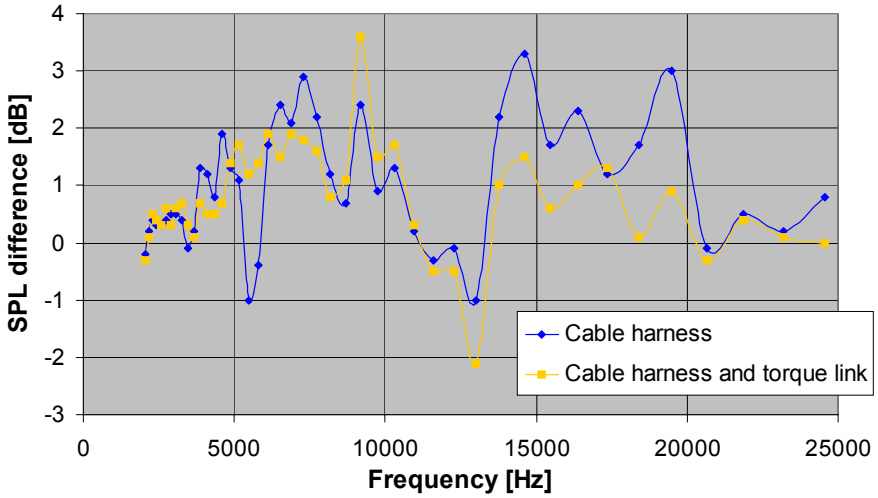

Figure 5.18: Integrated spectra difference between baseline, cable harness, and cable harness and torque link fairings configurations for array on braces side.

5.4 Additional Results

As a proof-of-concept, a series of preliminary noise control devices were implemented and tested in prior stages. This process also helped in improving the final design for the devices shown before. These initial concepts utilized rigid cardboard or elastic rubber membranes.

These preliminary concepts were also used to compare the noise reduction obtained using different materials for these devices.

In the case of the preliminary strut fairing concept, shown in Figure 5.19a, the cardboard was fixed to the edges of the landing gear door using speed tape. The braces fairing was obtained "wrapping" cardboard around them and was fixed using speed tape as shown in Figure 5.19b. To increase the absorption/shielding capacities, the gap between the upper and lower layers of cardboard was filled with foam (see Figure 5.19c). Figure 5.19d shows the rubber concept for the braces fairing. In this case the rubber was mounted to the braces using metal strips. The gap between the membranes was also filled with foam to avoid the rubber to "flap" or to have big deformations/deflections at high flow speeds due to low tension on the membrane.

For the forward cable harness and the torque link, a rigid cardboard plate was used, i.e. not allowing rotation of the truck, as shown in Figure 5.20.

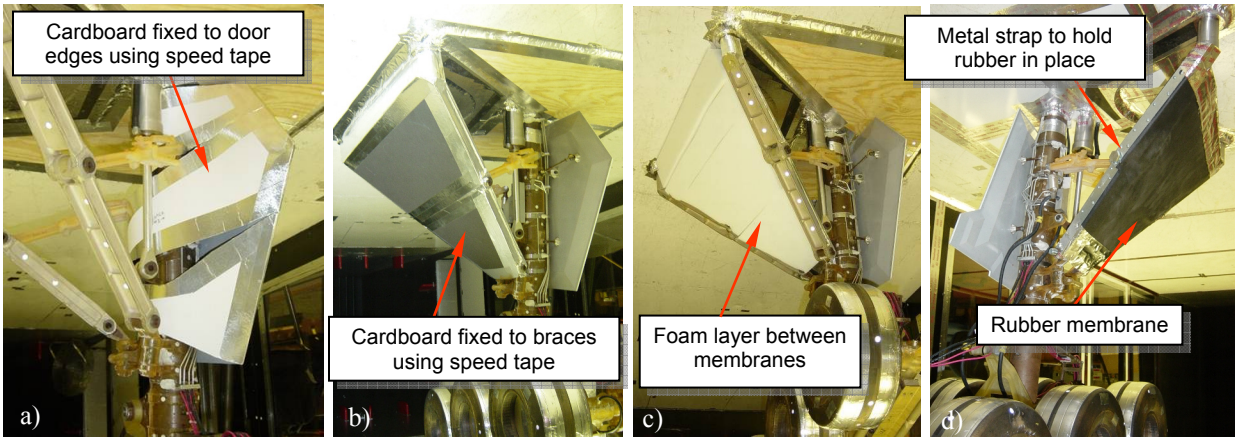

Figure 5.19: a) Strut fairing concept in cardboard. Braces fairing concept in b) cardboard with c) foam layer between upper and lower membranes, and d) rubber.

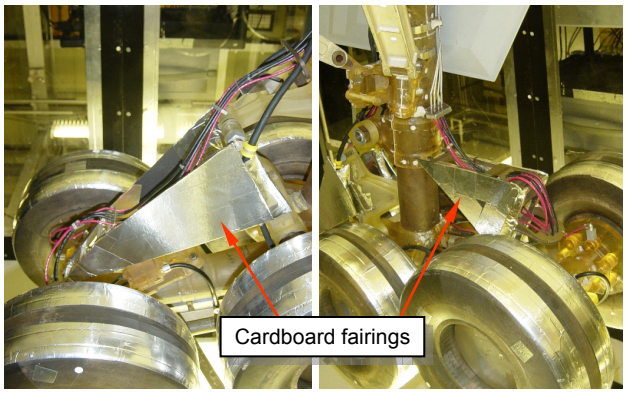

Figure 5.20: Cable harness and torque link fairings. Cardboard concepts.

5.4.1. Material Effect

As mentioned in the previous section, a very interesting result is obtained by comparing the noise reduction obtained with different materials used for the fairings. In this sense, Figure 5.21 shows the integration results for the cardboard, rubber and elastic cloth concepts of the braces fairing. As can be seen, the biggest noise reduction is obtained with the cardboard device. This suggests that deformations and oscillations of the elastic membranes reduce the efficiency of the fairing, i.e. the cardboard fairing shape is not affected by the flow speed. The difference in reduction between the rubber and cloth devices might be related to the noise absorption capabilities of the materials. Note that the rubber fairing used a foam layer between the membranes that also might have increased the absorption/shielding effects.

For the case of the lower truck fairing, a test was performed with a rigid fairing covering all the lower truck. This rigid device had the same width than the proposed elastic fairing. However, the front of the rigid fairing included a “bull-nose” type fairing extending from the lower truck to the towing hook in the form of an arc. The comparison of the results is shown in Figure 5.22. As can be seen, the reduction is surprisingly higher in the case of the elastic membrane fairing. These results suggest that most of the noise reduction is related to the flow modification rather than shielding of sources due to the material in the fairing.

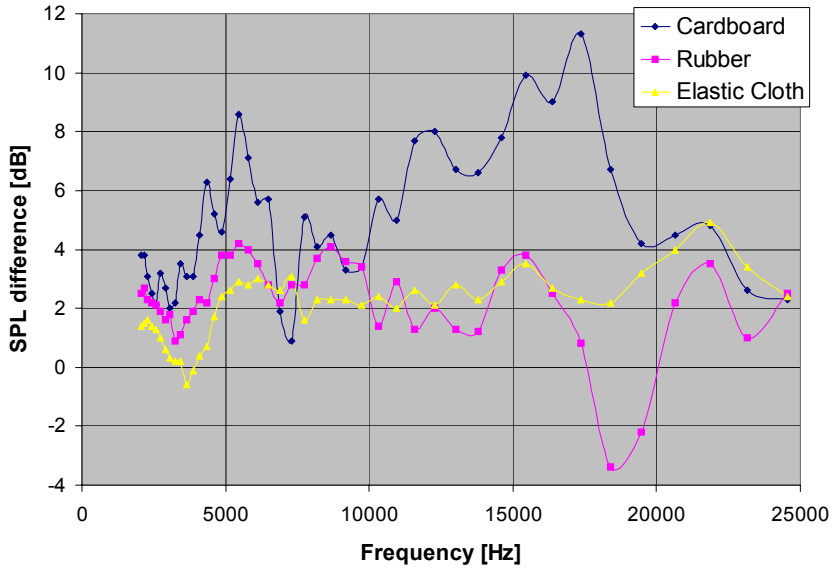

Figure 5.21: Integrated spectra difference for different braces fairing materials. Array on braces side.

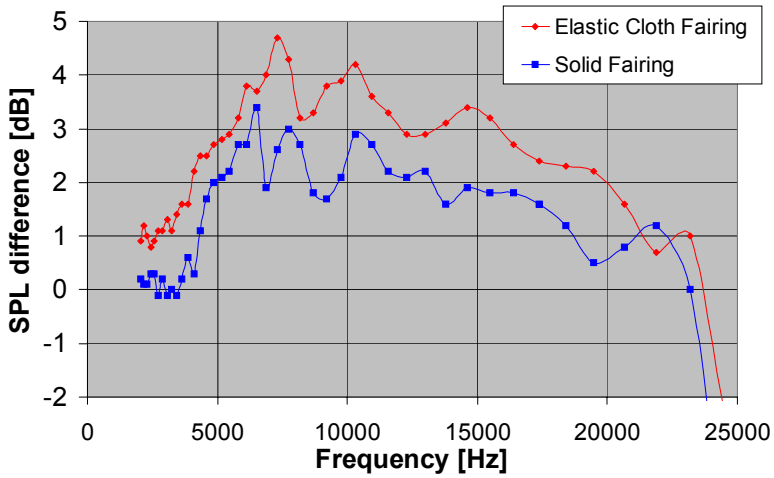

Figure 5.22: Integrated spectra difference for different truck fairing materials. Array on flyover path.

In the case of the cable harness and torque link fairings, the integrated spectra for the cardboard and rubber concepts is shown in Figure 5.23. As can be seen, the noise reduction obtained with the rubber fairing is noticeable bigger. According to the results obtained for the rubber braces fairing, this was not expected. This increase in reduction might be related to a higher tension applied to the rubber membranes that could not be achieved for the braces device due to its bigger dimensions. In this case, differences in shielding/absorption properties of the materials may also have affected the results.

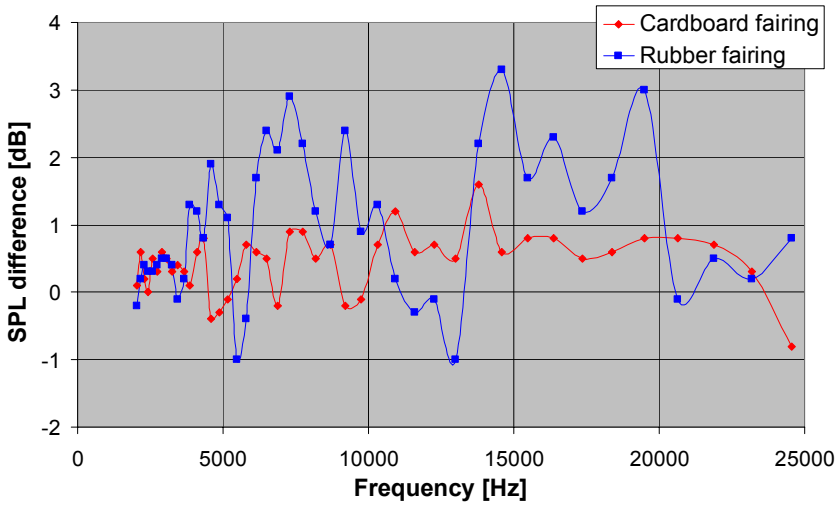

Figure 5.23: Integrated spectra for different cable harness and torque link fairings materials. Array on braces side.

5.5 Concluding Remarks

This chapter has presented a new concept in noise control devices based on elastic membranes. The localized devices designed for the braces and strut showed a significant noise reduction for the sideline array. This reduction was not quantified in the flyover path, but is expected to be smaller due to directivity effects. The elastic membrane-based lower truck fairing showed the most promising noise reduction potential in the flyover path. Further designs should be studied in order to find improvements to this design that could increase the noise reduction, i.e. extending the fairing beyond the brake rods.

Chapter 6

Post-processing of Beamforming Results

As mentioned in Chapter 1, one of the main problems in phased array measurements is to clearly identify the noise sources position and actual levels from the beamforming maps. This problem is especially true for complex sources distributions and when some of the sources are at or under the array SNR, i.e. sidelobes that can be assumed as noise sources and vice versa. The array measurements of the landing gear presented in the previous chapters is a perfect example of this situation. The interpretation of the beamforming maps had to be performed with a lot of care to properly identify the "real" noise sources.

In an effort to overcome this drawback, a new post-processing technique of the beamforming output is proposed here. The main idea is to use an "image processing-like" approach to identify the noise sources from the beamforming maps. Thus, recognizing patterns in the beamformed output and relating them to the noise sources that would produce that map. The technique is referred here as ***noise source Localization and Optimization of Array Results (LORE).***

Using this technique, the modeling of the beamforming output is obtained more accurately and unambiguously. The post-processing results at each frequency are the actual noise sources position and levels. The use of these results at every frequency of interest also allows obtaining the spectrum of a source without using integration of the maps, and thus avoiding some issues related to this technique, e.g. normalization, array size effects, grid resolution. The computational time required for the post-processing to obtain a "clear" solution seems to be reduced when compared to current techniques. Other issues present in the DAMAS approach, as position of the actual source relative to the scanning grid, are not an issue in the new approach (as long as actual source position is inside the scanning grid) [54]. Unlike DAMAS 2 and 3, the theoretical formulation is not restricted to small regions in space and can be applied to 2D or 3D cases [55]. For completeness and clarity in the derivations, some of the definitions and variables presented in previous chapters are reproduced here.

6.1 Theoretical Formulation

This section explains the theoretical formulation of the LORE technique starting with some basic definitions and derivations that will lead to the final model. The starting point in this formulation is the source-receiver model. Thus, for a microphone *j,* the frequency domain pressure can be expressed as the superposition of the sound from the sources distribution as:

$$p_j = \int C_j(\vec{x}')\, s(\vec{x}')\, d\vec{x}' \tag{6. 1}$$

where:

$s(\vec{x}')$ is the short-time Fourier transform of the amplitude for a source at $\vec{x}'$, and

$C_j(\vec{x}_s)$ is the complex array response for microphone *j*, given by the frequency domain Green's function for a source at $\vec{x}'$ in free space given as:

$$C_j(\vec{x}') = \frac{e^{-ik\left|\vec{x}'-\vec{x}_j\right|}}{4\pi\left|\vec{x}'-\vec{x}_j\right|} \tag{6. 2}$$

where:

$\vec{x}_j$ is the position of microphone *j*, and

k is the wavenumber.

Arranging the signals for all *J* microphones in a vector $\vec{p}$, the beamforming output ***power*** for a grid point at $\vec{x}$ can be written as:

$$b(\vec{x}) = \left|\vec{w}^{\dagger}(\vec{x})\,\vec{p}\right|^2 \tag{6. 3}$$

where:

$\vec{p}$ is a vector containing the signal for each of the array microphones, and

$\vec{w}(\vec{x})$ is the array weighting factor, also known as steering vector.

Thus, the signal from each array microphone is added with some weighting factor. This factor will account for corrections in the phase as well as the amplitude. In this way, the array can be "steered" to any point in space by using the adequate weights. In order to maximize the output, the steering vector is usually chosen parallel to the propagation vector $\vec{C}(\vec{x})$. Thus:

$$\vec{w}(\vec{x}) = \frac{\vec{C}(\vec{x})}{\left\|\vec{C}(\vec{x})\right\|} \tag{6. 4}$$

Replacing equation (6. 1) in equation (6. 3):

$$b(\vec{x}) = \left|\vec{w}^{\dagger}(\vec{x}) \int \vec{C}(\vec{x}') s(\vec{x}') d\vec{x}'\right|^2 \tag{6. 5}$$

If the simplest source distribution for $s(\vec{x}')$ is assumed, i.e. a single point source at $\vec{x}''$, with source strength $a(\vec{x}")$, it can be written as:

$$s(\vec{x}') = a(\vec{x}")\delta(\vec{x}' - \vec{x}'') \tag{6. 6}$$

Then, the beamformed output at $\vec{x}$ is given by:

$$b(\vec{x}) = \left|\vec{w}^{\dagger}(\vec{x}) \int \vec{C}(\vec{x}') a(\vec{x}'')\delta(\vec{x}' - \vec{x}'') d\vec{x}'\right|^2 \tag{6. 7}$$

Since $a(\vec{x}")$ does not depend on $\vec{x}'$, it can be moved out of the integral to get:

$$b(\vec{x}) = \left|\vec{w}^{\dagger}(\vec{x}) a(\vec{x}'') \int \vec{C}(\vec{x}')\delta(\vec{x}' - \vec{x}'') d\vec{x}'\right|^2 \tag{6. 8}$$

The integral in the right hand side is a convolution integral that can be solved to get:

$$\int \vec{C}(\vec{x}')\delta(\vec{x}' - \vec{x}'') d\vec{x}' = \vec{C}(\vec{x}'') \tag{6. 9}$$

Then, the beamformed output power at point $\vec{x}$ due to a single monopole at $\vec{x}''$ is given by:

$$b(\vec{x}) = \left|\vec{w}^{\dagger}(\vec{x})\vec{C}(\vec{x}'') a(\vec{x}'')\right|^2 \tag{6. 10}$$

So, for a unit source amplitude, i.e. $\left|a(\vec{x}'')\right|^2 = 1$, this last expression can be written as:

$$b(\vec{x}) = \left|\vec{w}^{\dagger}(\vec{x})\vec{C}(\vec{x}'')\right|^2 \tag{6. 11}$$

This last expression is known in the literature as the ***point spread function*** (***psf***) of the array, and is defined as:

$$psf\left(\vec{x},\vec{x}''\right)=\left|\vec{w}^{\dagger}\left(\vec{x}\right)\vec{C}\left(\vec{x}''\right)\right|^{2} \tag{6. 12}$$

Fixing $\vec{x}''$ and varying $\vec{x}$ through a scanning grid, the beamforming map that a single source at $\vec{x}''$ will produce can be obtained. Figure 6.1 shows the *psf* for the 63-element VT phased array at 5, 10 and 25 kHz. A remark is stated at this point in the sense that the same result is obtained synthesizing the signals at the microphones for a monopole source of amplitude 1 and beamforming over the desired grid.

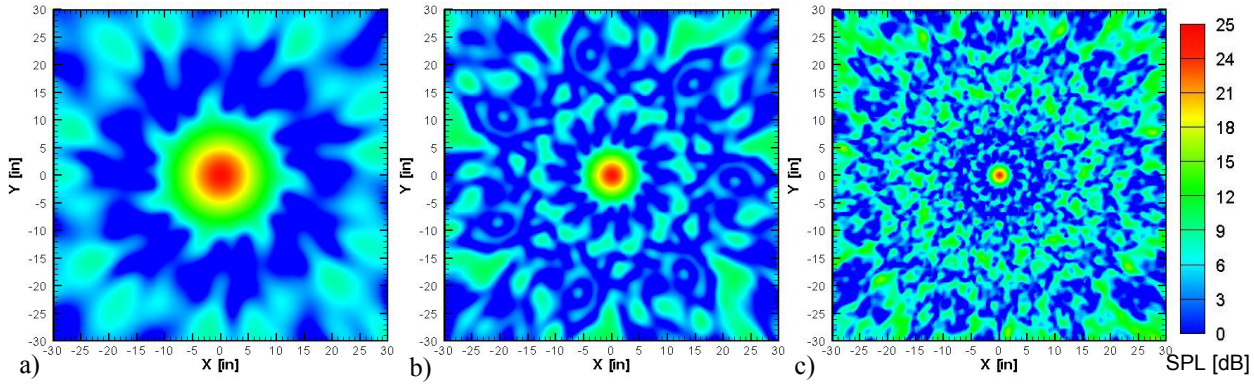

Figure 6.1: Point spread function for VT 63-element phased array at a) 5, b) 10, and c) 25 kHz.

For the purpose of developing the LORE technique, the following definition of the ***complex point spread function (cpsf)*** of the array is introduced:

$$cpsf\left(\vec{x},\vec{x}''\right)=\vec{w}^{\dagger}\left(\vec{x}\right)\vec{C}\left(\vec{x}''\right) \tag{6. 13}$$

So for a single source at $\vec{x}''$ the beamforming output $\vec{x}$ can be written as:

$$b\left(\vec{x}\right)=\left|cpsf\left(\vec{x},\vec{x}''\right)a\left(\vec{x}''\right)\right|^{2} \tag{6. 14}$$

This new definition of complex point spread function is essential for an accurate modeling in the presence of multiple noise sources. In the case of multiple monopole sources the source distribution $s\left(\vec{x}'\right)$ can be expressed as:

$$s\left(\vec{x}'\right)=\sum_{m=1}^{M}a\left(\vec{x}_{m}''\right)\delta\left(\vec{x}'-\vec{x}_{m}''\right) \tag{6. 15}$$

where:

$a(\vec{x}''_m)$ is the amplitude of the source at $\vec{x}''_m$, and

M is the number of sources.

Replacing this expression in equation (6. 5), leads to :

$$b(\vec{x}) = \left| \vec{w}^{\dagger}(\vec{x}) \int \vec{C}(\vec{x}') \left[\sum_{m=1}^{M} a(\vec{x}''_m) \delta(\vec{x}' - \vec{x}''_m) \right] d\vec{x}' \right|^2 \tag{6. 16}$$

That can be written as:

$$b(\vec{x}) = \left| \sum_{m=1}^{M} \vec{w}^{\dagger}(\vec{x}) \vec{C}(\vec{x}''_m) a(\vec{x}''_m) \right|^2 \tag{6. 17}$$

Using the definition of the ***cpsf*** **,** the beamformed output power at $\vec{x}$ is given as:

$$b(\vec{x}) = \left| \sum_{m=1}^{M} cpsf(\vec{x}, \vec{x}''_m) a(\vec{x}''_m) \right|^2 \tag{6. 18}$$

This expression is the basis for the technique proposed in this dissertation. As can be seen, the relationship between the beamformed output power and the sources amplitude is given by a non-linear equation. For the purpose of the following derivations, this equation will be further expanded. Thus, it can be written as:

$$b(\vec{x}) = \left[\sum_{m=1}^{M} cpsf(\vec{x}, \vec{x}''_m) a(\vec{x}''_m) \right]^* \sum_{m=1}^{M} cpsf(\vec{x}, \vec{x}''_m) a(\vec{x}''_m) \tag{6. 19}$$

Using the summation properties, the previous equation can be re-arranged to obtain:

$$b(\vec{x}) = \sum_{m=1}^{M} \sum_{s=1}^{M} \left[cpsf(\vec{x}, \vec{x}''_m) a(\vec{x}''_m) \right]^* cpsf(\vec{x}, \vec{x}''_s) a(\vec{x}''_s) \tag{6. 20}$$

Grouping terms that does not include cross-terms in $a(\vec{x}'')$ this last expression can be written as:

$$b(\vec{x}) = \sum_{m=1}^{M} \left| cpsf(\vec{x}, \vec{x}''_m) \right|^2 \left| a(\vec{x}''_m) \right|^2 + \sum_{m=1}^{M} \sum_{\substack{s=1 \\ s \neq m}}^{M} \left[cpsf(\vec{x}, \vec{x}''_m) a(\vec{x}''_m) \right]^* cpsf(\vec{x}, \vec{x}''_s) a(\vec{x}''_s) \tag{6. 21}$$

As can be seen, the nonlinearity in the beamforming expression gives rise to the cross terms in *a.* Thus, the assumption of incoherence between the sources is not enough to discard these cross-terms. In fact, the coherence is taken into account using the complex values for the sources

strength. As demonstrated in appendix C, the DAMAS approach neglects these terms that are essential in the modeling of the beamforming output, thus introducing errors in the model. This appendix also presents comparisons between the beamformed output, the LORE modeling, and the DAMAS modeling.

Before introducing the solution approach, it is useful to define the ***complex beamformed pressure*** as:

$$y(\vec{x}) = \sum_{m=1}^{M} cpsf(\vec{x}, \vec{x}_m'') a(\vec{x}_m'') \tag{6. 22}$$

The advantage of this form is that the equation is linear. Then, the complex beamformed pressure is related to the actual beamforming output $b(\vec{x})$ as:

$$b(\vec{x}) = |y(\vec{x})|^2 = y(\vec{x})^* y(\vec{x}) \tag{6. 23}$$

At this point, it should be clear that the similarity to "image processing" is in the sense that the beamforming maps (images) for single sources are being superimposed in ***complex form*** to obtain the actual beamforming map.

With the previous definition, the complex beamformed pressure over a set of *N* points due to *M* sources in the scanning field can be expressed as:

$$\begin{Bmatrix} y(\vec{x}_1) \\ y(\vec{x}_2) \\ \vdots \\ y(\vec{x}_N) \end{Bmatrix} = \sum_{m=1}^{M} \begin{Bmatrix} cpsf(\vec{x}_1, \vec{x}_m'') \\ cpsf(\vec{x}_2, \vec{x}_m'') \\ \vdots \\ cpsf(\vec{x}_N, \vec{x}_m'') \end{Bmatrix} a(\vec{x}_m'') \tag{6. 24}$$

This last expression can be written in matrix form to get:

$$\begin{Bmatrix} y(\vec{x}_1) \\ y(\vec{x}_2) \\ \vdots \\ y(\vec{x}_N) \end{Bmatrix} = \begin{bmatrix} cpsf(\vec{x}_1, \vec{x}_1'') & cpsf(\vec{x}_1, \vec{x}_2'') & \cdots & cpsf(\vec{x}_1, \vec{x}_M'') \\ cpsf(\vec{x}_2, \vec{x}_1'') & cpsf(\vec{x}_2, \vec{x}_2'') & \cdots & cpsf(\vec{x}_2, \vec{x}_M'') \\ \vdots & \vdots & \ddots & \vdots \\ cpsf(\vec{x}_N, \vec{x}_1'') & cpsf(\vec{x}_N, \vec{x}_2'') & \cdots & cpsf(\vec{x}_N, \vec{x}_M'') \end{bmatrix} \begin{Bmatrix} a(\vec{x}_1'') \\ a(\vec{x}_2'') \\ \vdots \\ a(\vec{x}_M'') \end{Bmatrix} \tag{6. 25}$$

Since the number of sources in the scanning field is generally unknown, the number of sources must be assumed equal to the number of scanning points, i.e. *M=N.* This will render a

square matrix in the previous equation.

It is important to note that if the sources are correlated, the source strengths ($a\left(\vec{x}_m''\right)$ for $m = 1,...,N$) must be assumed to be complex in equation (6. 25) so as to account for relative phase information. However, note that the beamforming output (power) lacks phase information and, thus, it is not possible to solve the proposed complex system of linear equations.

6.2 Solution Approach

As seen before, the modeling of the beamforming output renders a system of non-linear equation in terms of the sources amplitudes, i.e. $a\left(\vec{x}_m''\right)$ for $m = 1,...,N$. Since the size of the system is given by the number of scanning grid points *N*, the problem has a "very large" number of unknowns. To overcome this issue and solve the nonlinear problem, a new 2-step approach is proposed in this work. These steps are:

- STEP 1: ***Solve an approximated linear problem.*** Solving this approximated model will ***reduce the number of "sources"*** in the grid, i.e. only potential noise sources will have a source strength different than zero. The approach taken here finds the sources amplitude for a "linearized" model solving a least squares problem with non-negativity constraints (NNLS).

- STEP 2: ***Solve the non-linear problem using an optimization procedure***. This is accomplished by ***optimizing only the non-zero values*** obtained in Step 1. In this work, the multidimensional optimization problem was implemented using the downhill simplex method. Since a reduced number of points is being optimized, the computational time is significantly reduced if compared to optimizing the set of all grid points. Besides, it will be practically impossible to give a good starting point for the optimization procedure, i.e. the result from the least squares formulation is a good approximation to the minimum, local at least, that the optimization procedure is trying to find.

The proposed solution approach is illustrated in Figure 6.2. As can be seen, the initial point

of the procedure is the beamforming output for every single point in the grid. Solving the approximated problem in Step 1 would render a much smaller number of potential noise sources, i.e. a reduced set of nonzero grid points. Finally, the application of the optimization procedure described in Step 2 to the nonzero values from Step 1 would render only the actual noise sources levels and positions. As can be observed, the results from LORE are much "cleaner" and thus clearer than the beamforming output, i.e. sidelobes are not present and the actual levels can be recovered.

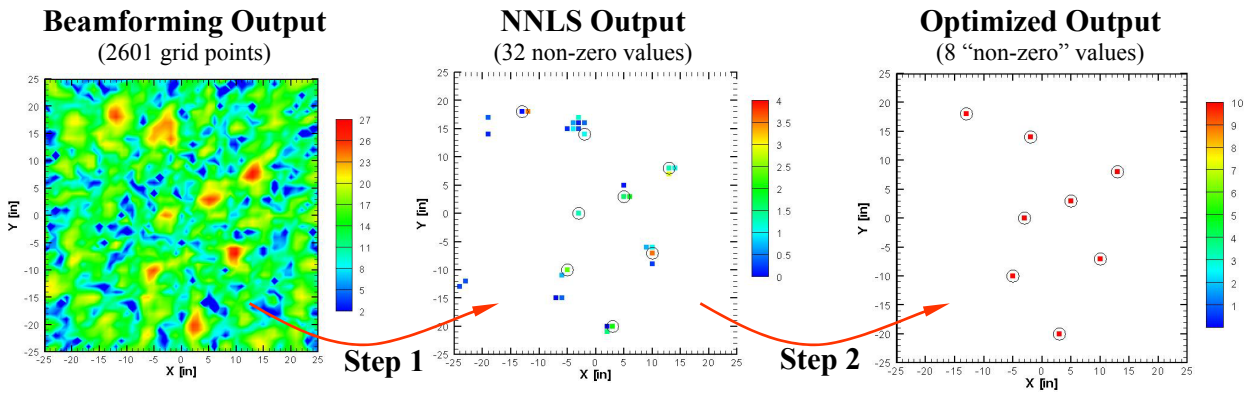

Figure 6.2: Schematic of the results obtained in the 2-steps LORE technique.

a. Solve an Approximated Linear Problem

As mentioned before, the key idea in Step 1 of the LORE technique is to discard as many grid points as possible were the amplitude is most likely to be zero. Thus, only potential noise sources are kept for the optimization procedure in Step 2. The approach is to find an approximated "linear" problem and solve it using a least squares approach.

To this end, the cross-terms $a(\vec{x}_m'')a(\vec{x}_s'')$ in equation (6. 21) are neglected, and the following linear equation is obtained:

$$b'(\vec{x}) = \sum_{m=1}^{M} \left| cpsf(\vec{x}, \vec{x}_m'') \right|^2 \left| a(\vec{x}_m'') \right|^2 \qquad (6.\ 26)$$

Note that $b'(\vec{x})$ is an "approximation" to the actual beamforming output $b(\vec{x})$. In matrix form this last expression can be written as:

$$\begin{Bmatrix} b'(\vec{x}_1) \\ b'(\vec{x}_2) \\ \vdots \\ b'(\vec{x}_N) \end{Bmatrix} = \begin{bmatrix} \left|cpsf(\vec{x}_1,\vec{x}_1'')\right|^2 & \left|cpsf(\vec{x}_1,\vec{x}_2'')\right|^2 & \cdots & \left|cpsf(\vec{x}_1,\vec{x}_N'')\right|^2 \\ \left|cpsf(\vec{x}_2,\vec{x}_1'')\right|^2 & \left|cpsf(\vec{x}_2,\vec{x}_2'')\right|^2 & \cdots & \left|cpsf(\vec{x}_2,\vec{x}_N'')\right|^2 \\ \vdots & \vdots & \ddots & \vdots \\ \left|cpsf(\vec{x}_N,\vec{x}_1'')\right|^2 & \left|cpsf(\vec{x}_N,\vec{x}_2'')\right|^2 & \cdots & \left|cpsf(\vec{x}_N,\vec{x}_N'')\right|^2 \end{bmatrix} \begin{Bmatrix} \left|a(\vec{x}_1'')\right|^2 \\ \left|a(\vec{x}_2'')\right|^2 \\ \vdots \\ \left|a(\vec{x}_N'')\right|^2 \end{Bmatrix}$$
$$= \left[\hat{\mathbf{E}}\right] \begin{Bmatrix} \left|a(\vec{x}_1'')\right|^2 \\ \left|a(\vec{x}_2'')\right|^2 \\ \vdots \\ \left|a(\vec{x}_N'')\right|^2 \end{Bmatrix} \tag{6. 27}$$

This last expression is a linear system of equations that needs to be solved to obtain the sources "power", i.e. $\left|a(\vec{x}_m'')\right|^2$; thus, a solution that is constrained to be positive.

This is physically correct because there can not be an acoustic source with negative power.

In the LORE approach, this problem is solved using a least squares (LSQ) formulation with non-negativity constraints [65]. Thus, it is posed as:

$$\min_{|\vec{a}(\vec{x}_m'')|} \frac{1}{2}\left\|\hat{\mathbf{E}}\left|\vec{a}(\vec{x}_m'')\right|^2 - \vec{b}\right\|_2^2, \quad \text{with the constraint: } \left|a(\vec{x}_m'')\right|^2 \geq 0 \tag{6. 28}$$

where the values for $\vec{b}'$ were replaced with those from the actual beamforming output $\vec{b}$.

The algorithm chosen to solve this problem is the Non-negative Least Squares (NNLS) [65] and it is explained in detail in appendix A.

It is now important to prove that using this approximation an appropriate solution is obtained to be used as a starting point for the optimization in Step 2. The key issue is to have confidence that actual noise sources are not assigned a zero value, i.e. discarding grid points related to actual noise sources. To this end, the solution from the original model shown in equation (6. 21) will be compared to the approximated one in equation (6. 26).

Using the triangle inequality property of the norms, the following relation can be expressed:

$$\left|\sum_m cpsf(\vec{x},\vec{x}_m'')\,a(\vec{x}_m'')\right|^2 \leq \sum_m \left|cpsf(\vec{x},\vec{x}_m'')\right|^2 \left|a(\vec{x}_m'')\right|^2 \tag{6. 29}$$

hence:

$$b(\vec{x}) \le b'(\vec{x}) \tag{6. 30}$$

Note that the equality holds only in the case of a single source. Since in equation (6. 28) the values for $b'(\vec{x})$ are replaced with the actual beamforming output $b(\vec{x})$, the NNLS procedure will actually find the minimum $\left|a(\vec{x}''_m)\right|^2$, $m = 1,...,N$, that satisfies:

$$b(\vec{x}_n) = \sum_{m=1}^{M} \left|cpsf(\vec{x}_n, \vec{x}''_m)\right|^2 \left|a(\vec{x}''_m)\right|^2, \quad n = 1,...,N \tag{6. 31}$$

Then, the solution from the least squares problem will be such that the sources power is always under predicted, i.e. smaller than the actual solution in order to maintain the inequality in equation (6. 30).

The fact that actual noise sources are not discarded is related to the procedure that NNLS uses to add potential variables to the set of nonzero values. Thus, the number of grid points assigned a nonzero value is usually greater than or equal to the actual number of sources.

b. Solve the non-linear problem using an optimization procedure

The next step in the LORE technique is to perform an optimization over the *NZ* non-zero values of *a* obtained from Step 1. To this end, a modification of the Nelder and Mead simplex method [66] was implemented. This method is explained in detail in appendix B.

With the results from the previous step, the system to optimize is given by N non-linear equations with *NZ* unknowns of the form shown in equation (6. 18). Thus:

$$b(\vec{x}_n) = \left|\sum_{m=1}^{NZ} cpsf(\vec{x}_n, \vec{x}''_m)\, a(\vec{x}''_m)\right|^2, \quad n = 1,...,N \tag{6. 32}$$

As mentioned before, there are no restrictions in this equation. Thus, the sources incoherence assumption is not present. To improve computational time by implementing a matrix multiplication, the expression with the complex beamformed pressures Y is used instead of the beamforming output power *b*. Thus, a tall-skinny system is obtained of the form:

$$\begin{Bmatrix} y(\vec{x}_1) \\ y(\vec{x}_2) \\ \vdots \\ y(\vec{x}_N) \end{Bmatrix} = \begin{bmatrix} cpsf(\vec{x}_1,\vec{x}_1'') & cpsf(\vec{x}_1,\vec{x}_2'') & \cdots & cpsf(\vec{x}_1,\vec{x}_{NZ}'') \\ cpsf(\vec{x}_2,\vec{x}_1'') & cpsf(\vec{x}_2,\vec{x}_2'') & \cdots & cpsf(\vec{x}_2,\vec{x}_{NZ}'') \\ \vdots & \vdots & \ddots & \vdots \\ cpsf(\vec{x}_N,\vec{x}_1'') & cpsf(\vec{x}_N,\vec{x}_2'') & \cdots & cpsf(\vec{x}_N,\vec{x}_{NZ}'') \end{bmatrix} \begin{Bmatrix} a(\vec{x}_1'') \\ a(\vec{x}_2'') \\ \vdots \\ a(\vec{x}_{NZ}'') \end{Bmatrix} \tag{6. 33}$$

where in general $N >> NZ$.

Note that if "phase" information could be obtained for the complex beamformed pressure from the beamforming output power, solving a nonlinear problem could be avoided, i.e. solving the complex system of linear equations shown in (6. 33).

At this point two choices are possible to optimize the values from step 1. The first one is to keep the incoherence assumption and optimize a system of *NZ* equations of the form:

$$\xi_n = b(\vec{x}_n) - \left| \sum_{m=1}^{NZ} cpsf(\vec{x}_n,\vec{x}_m'')\, a(\vec{x}_m'') \right|^2 \tag{6. 34}$$

where a_m are the real nonzero values obtained from the NNLS solution.

If the presence of coherent sources is "suspected", or if given the nature of the problem this is known, a more general system can be solved where $a(\vec{x}_m'')$ is complex. In this case $2 \times NZ$ values need to be optimized, i.e. corresponding to the real and complex components of $a(\vec{x}_m'')$. In both cases, the function to minimize is the norm of the total relative error given by:

$$f(\vec{b},\vec{a}) = \frac{\left(\sum_{n=1}^{N} \xi_n^2 \right)^{1/2}}{\max_i |b_i|} \tag{6. 35}$$

In order to further reduce the number of parameters to optimize in Step 2, the theoretical array SNR can be used. Thus, values of a_i that are smaller than the theoretical array SNR (or times a factor) from the maximum value can be discarded after Step 1 to reduce computational time. However, in some complex cases, this has proven to "discard" actual noise sources especially in 3D. As a consequence, the results may not be accurate. Thus, if used, it should be chosen carefully.

6.3 Estimation of Results Accuracy

To evaluate the quality of the results from LORE, it is proposed to compare a "reconstruction" to the actual beamforming map. The reconstruction of the results consists in using the amplitudes obtained with LORE and feeding them into the model of equation (6. 21) to obtain the reconstructed beamforming map. In this way, the accuracy of the results can be determined by comparing the actual and reconstructed beamforming maps. Even when visual comparison of the maps is very helpful, an automated procedure that gives a measure on how much these "images" are alike is preferred, i.e. a single numerical value giving an estimate of the accuracy of the LORE results.

In image processing, a common practice to determine if two images are similar is to use the correlation coefficient [67-[69]. If both maps are identical, the correlation will be equal to 1. If there are differences the correlation will be lower. This correlation metric is a particular case of feature detection [70,[71] where both images have the same size, i.e. same number of grid points.

Since the beamforming output in linear scale has a large range that does not allow recognizing minor differences in the maps, the comparison of the actual and reconstructed beamforming maps is performed in decibel scale, i.e. as one would compare "visually" the maps to determine if they are similar. The correlation coefficient relating the actual and reconstructed beamforming maps is then given by:

$$C = \frac{\sum_{i=1}^{N} 10\log_{10}\left(b(\vec{x}_i)\right) 10\log_{10}\left(b_R(\vec{x}_i)\right)}{\sqrt{\sum_{i=1}^{N} 10\log_{10}\left(b(\vec{x}_i)\right) \sum_{i=1}^{N} 10\log_{10}\left(b_R(\vec{x}_i)\right)}} \tag{6. 36}$$

where:

$b(\vec{x}_i)$ and $b_R(\vec{x}_i)$ are the actual and reconstructed beamforming output at point $\vec{x}_i$.

The results from LORE will be considered satisfactory if the correlation coefficient is greater than 0.9. The reconstructed maps will be shown in addition to the correlation coefficient for the cases where it is considered helpful in the understanding of the results and limitations from LORE.

6.4 Numerical Simulations in 2D

The numerical simulations presented in this section are organized in increasing level of difficulty. Thus, starting from the simplest cases and adding complexities in each step. The beamforming output was obtained by generating the time-domain signals for each microphone of the array. The time domain signals were then taken to the frequency-domain and the corresponding CSM was calculated. Conventional beamforming was then applied to a grid of 25" by 25", in a plane 36" parallel to the array. The grid resolution used was 1", thus resulting in 2601 scanning points. As seen before, this also determines the size of the system to solve in the LORE technique. Unless otherwise stated, the amplitude of the sources was set to 10. Keep in mind that the beamforming maps are in dB scale while the LORE results are given in linear scale, i.e. source amplitude. For ease of visualization a cutoff was applied to the results, i.e. values around 40 dB (amplitude) below the maximum level were not plotted. If this cutoff level is changed it is noted. The actual position of the sources is denoted using a black circle around the corresponding grid point. Red circles are used to denote "artificial" sources, i.e. grid points with amplitude not equal to zero and not associated to actual noise sources.

The computational time indicated in the following examples is shown only as a reference and was obtained using a single-processor desktop computer. No direct comparison was established with other techniques like DAMAS for the same cases; however, the time reported in the literature for a single source is in the order of minutes [54] and for some cases it was reported to be in the order of hours or days [55].

a. Single Source

The first case to analyze is the one of a single monopole source in the center of the scanning grid. As can be seen in Figure 6.3a, the beamforming map shows a clear noise source at the center of the scanning grid, while the worst sidelobe appears to be 10 dB below the mainlobe. Applying the LORE technique, the results shown in Figure 6.3b are obtained. As can be seen, the only nonzero value is at the grid point where the actual noise source is present. Its amplitude is also successfully recovered. In fact, the NNLS procedure already renders the correct value since,

as shown before, the system solved in Step 1 for a single source is a linear system. The correlation for this case is equal to 1, as expected. The time needed for this computation in a PC is less than 7 seconds.

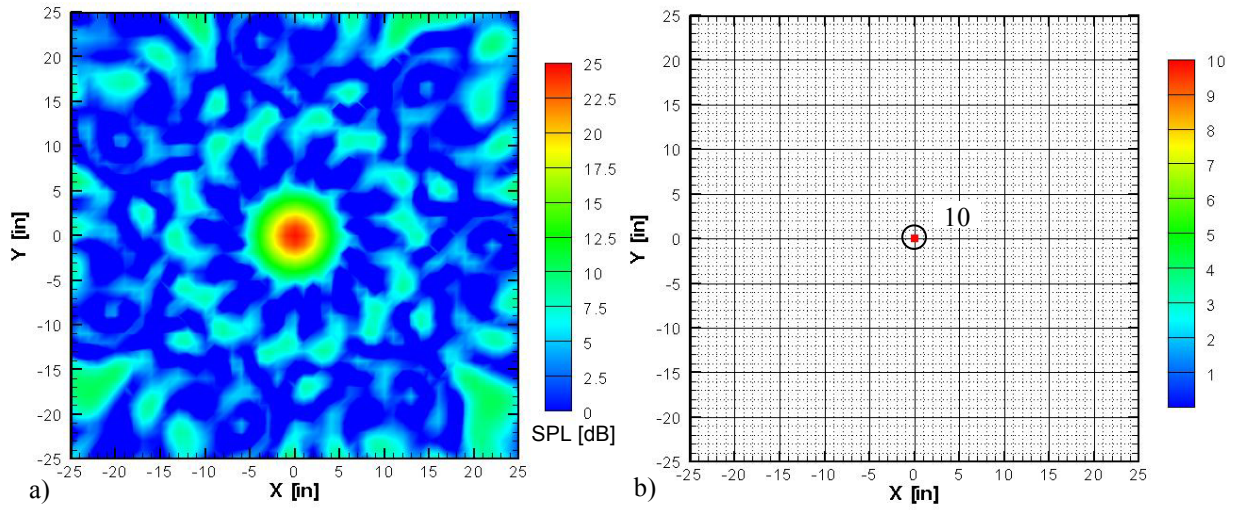

Figure 6.3: Single source simulation (10 kHz). a) Beamforming, and b) LORE results.

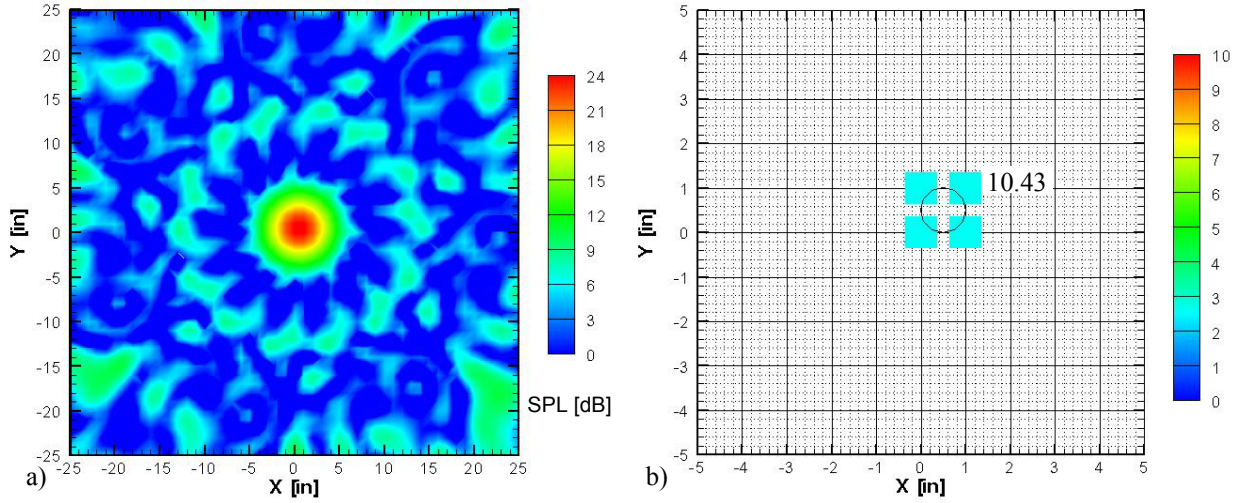

Figure 6.4: Single source between grid points (10 kHz). a) Beamforming, and b) detail of LORE results.

The second case to be analyzed is a single source which actual position is not in a grid point, i.e. at $(0.5",\ 0.5",\ 36")$, between grid points. The results are shown in Figure 6.4. Note that there are no big changes in the beamforming map when compared to the previous case. However, the maximum level is slightly lower (about 1 dB). Figure 6.4b shows a detail of the LORE results in

the region where the source is located. As can be seen, the solution renders 4 sources "around" the actual noise source position. In this case, the actual source strength is obtained by adding the values at those points. As indicated in the figure, the recovered level (10.43) is slightly higher than the actual level (10). In terms of power, this difference in amplitude is equivalent to less than 0.4 dB. The correlation factor for this case is 0.966, thus, the results are expected to have an insignificant error. The computational time for this case was only 8.5 seconds.

b. Two Close Sources

The next series of simulations show the case of 2 monopole sources separated 2", i.e. there is a scanning point in between them. The results are shown from high to low frequencies. This is related to the fact that at low frequencies the array resolution gets worst. Thus, the goal is to find at which point the results are no longer "reliable" for this technique. The fact that, as will be seen, some of the results are "poor" at low frequencies is related to the existence of "multiple" solutions that can render the same results, i.e. the solution is not unique. Remember that the system being solved is at the least ill-conditioned. Furthermore, at low frequencies the result from the NNLS might no longer be a good approximation in the sense that is not rendering an "adequate" set of initial points for the optimization. It was not studied if providing an artificial "good" starting point to the optimization will improve the results but it is expected.

Figure 6.5 shows the beamforming results for 25, 15, and 10 kHz respectively. Since the LORE results were almost the same for a wide range of frequencies, only one plot will be presented for the previous 3 cases. Thus, Figure 6.6 represents the LORE results for 2 sources 2" apart for 25, 15, and 10 kHz. As can be seen, only the 2 values corresponding to the actual noise sources position are rendered. The levels are also successfully recovered. Since the plot has a cutoff level, some "extra" points with amplitude relatively small are not shown. Thus, depending on the frequency there were 3, 1, and 1 nonzero "artificial" sources corresponding to 25, 15 and 10 kHz respectively, while the remaining grid points have a zero value. The maximum value of these grid points was 6e-5, 4e-5 and 9e-5 respectively. For all cases, the correlation factor was equal to 1. The computational time was about 6 second in each case.

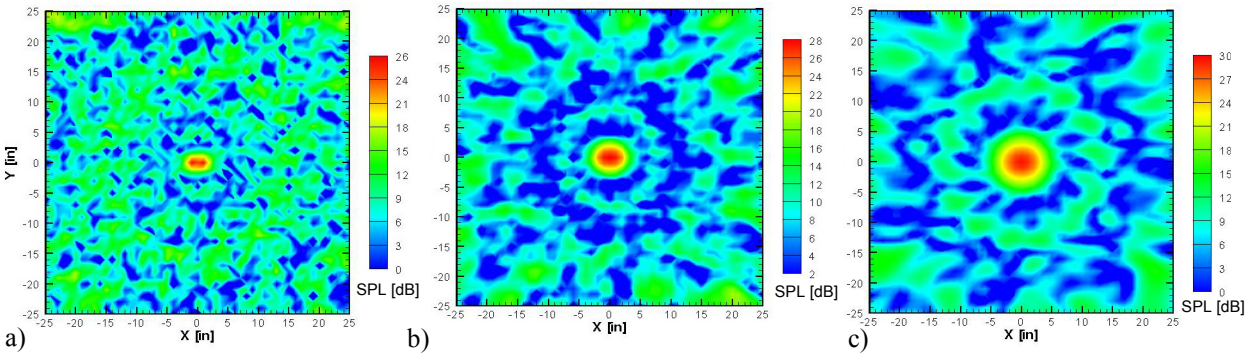

Figure 6.5: Beamforming maps for 2 sources 2" apart at a) 25, b) 15, and c) 10 kHz.

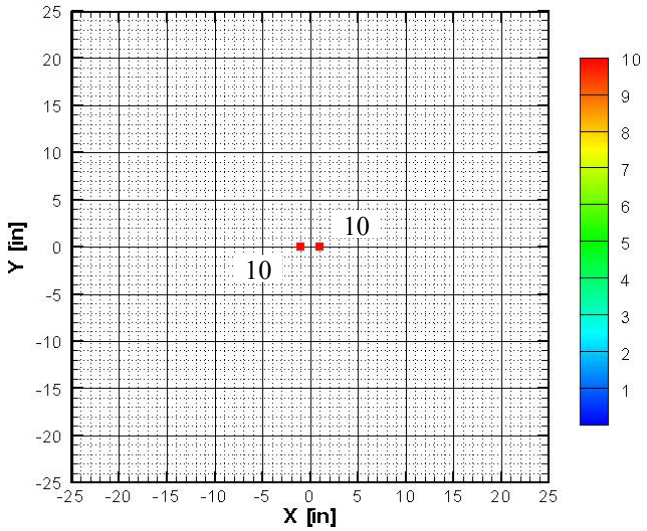

Figure 6.6: LORE results for 2 sources 2" apart.

Figure 6.7 shows the beamforming and LORE results at 5 kHz. In this case, some differences start to show up. Thus, 5 non-zero values are rendered. Two corresponding to the actual noise sources position and 3 related to the lack of resolution of the array. In this case, the two sources rendered an amplitude of 9.992 (instead of 10) and three other non-zero sources next to them. However, their amplitudes (2e-3, 1e-2 and 2e-3) are much smaller than the actual noise sources amplitude. Because of these sources, the total power recovered from the region of the noise sources is 20.00004 instead of 20. The correlation between the actual and reconstructed beamforming maps is equal to 1. Thus, at this frequency the results are still very accurate. The time required for this computation was about 11 seconds.

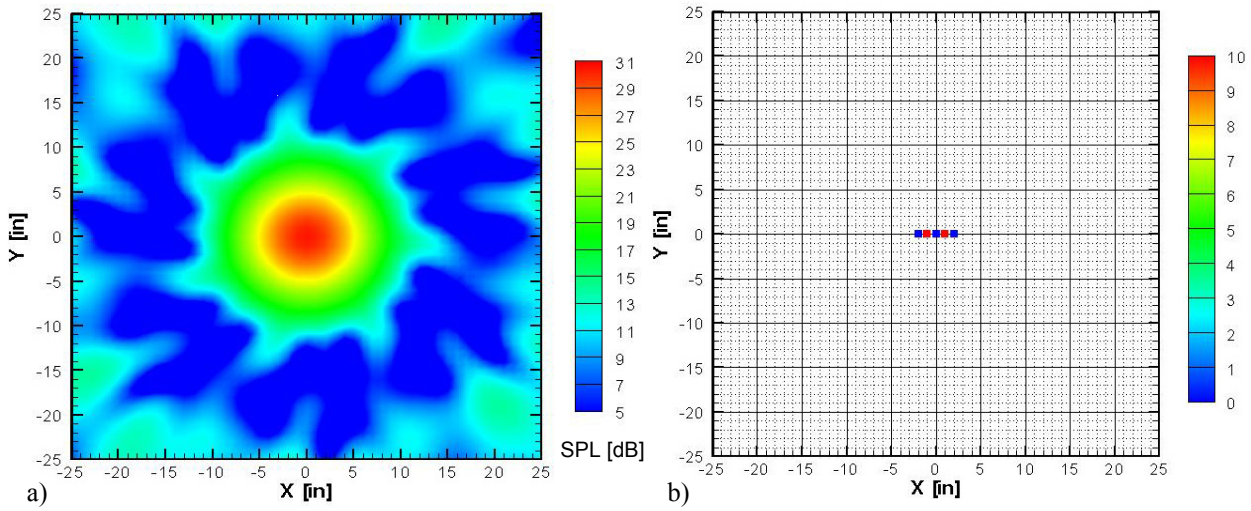

Figure 6.7: Simulation of 2 sources 2" apart at 5 kHz. a) Beamforming, and b) LORE results

As shown in Figure 6.8a, when the frequency is even lower (2.5 kHz) one can not differentiate in the beamforming map how many sources are present. However, as shown in Figure 6.8b, the post-processing still finds "some" linear distribution in the same direction than the 2 simulated sources. In this case, the correlation coefficient is equal to 1. However, the method is not able to separate the sources because the beamforming map looks very much alike the one for a single source. Thus, if these results were to be interpreted without knowing the actual sources distribution, the conclusion would probably be that there is only one source in the center. In this case, the contribution of 3 points should be added, thus rendering a total level of 20.05 instead of the actual 20, i.e. the difference is less than 0.03 dB in power.

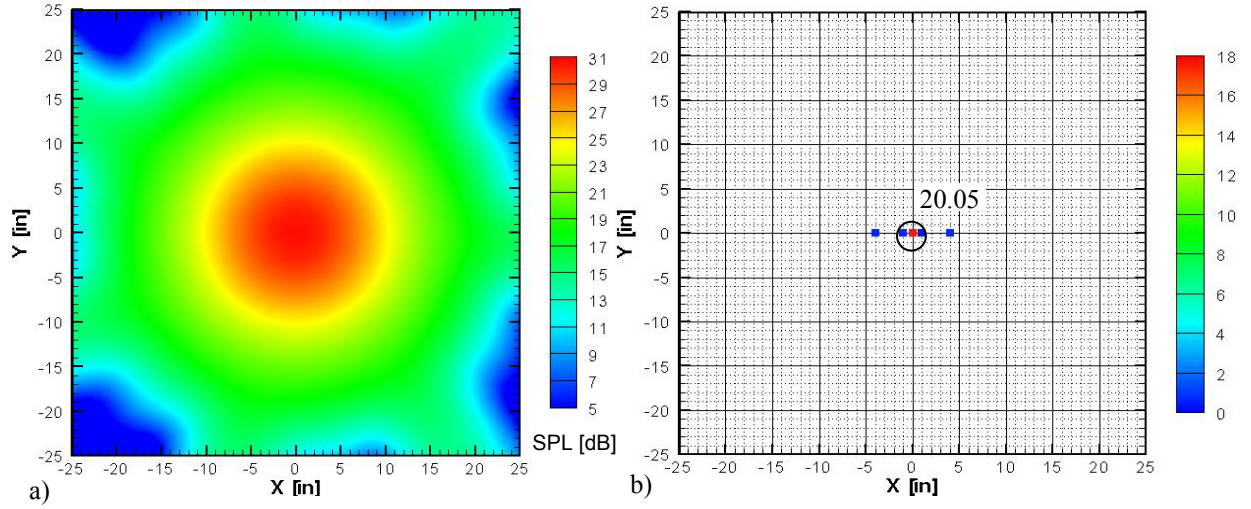

Figure 6.8: Simulation of 2 sources 2" apart at 2.5 kHz. a) Beamforming, and b) LORE results.

For this simulation, there are 5 other grid points with nonzero amplitude, the maximum of them being about 9e-5. The addition of all these "extra" sources is 1.1e-4, i.e. the power is more than 100 dB below the sources levels. The computational time in this case was 11.5 seconds.

c. Effect of a Second Source Outside the Scanning Grid

A problem that was reported in the literature [54] is that when there are sources at or outside the grid boundaries the actual levels are not recovered correctly. In this sense, the following results show the simulations obtained with a source at the center of the scanning grid and a second one at or outside the grid boundaries. The effect of an "extra" source in such configurations is analyzed.

Figure 6.9a shows the beamforming when the second source is exactly at a grid point in the right boundary of the grid, i.e. at (25", 0", 36"). As can be seen in Figure 6.9b, the sources position and levels are correctly recovered. In this case, four nonzero values other than the actual noise sources are present. The highest value of those points is 1e-4, and their sum is 1.7e-4, thus, well below the level of the sources. The correlation is equal to 1 and the computational time 8.6 seconds.

If the second source is now placed 1" outside the scanning grid, i.e. at (26", 0", 36"), the beamforming output renders the map shown in Figure 6.10a. In this case, LORE is still capable of identifying a source in the boundary. From these results it would be concluded that there is a source at the boundary with a lower level than the source at the center. In real life, the size of the scanning grid would be increased until it includes a bigger region around that source. However, to see the effect mentioned before the grid will be kept the same. The output from the LORE processing is shown in Figure 6.10b. As can be seen, as a result of the second source being outside the grid, some "artificial" sources appear in places other than the actual noise sources position. However, their levels are not "insignificant" when compared to the actual noise sources levels. In this case, the source at the center has a recovered level of 8.95, and the source that appears on the boundary a level of 8.14. Remember that both sources had amplitude 10, i.e. the error in the power is about 1.8 dB. The "contaminating" sources show a maximum level of 2.24. Such value is not negligible compared to the actual sources levels, i.e. only 12 dB below the

recovered power for the source at the center. Furthermore, the total level of all the artificial sources is 8.32. In this case the correlation factor is 0.26, thus, the results should be considered incorrect. The computational time was 32.3 seconds.

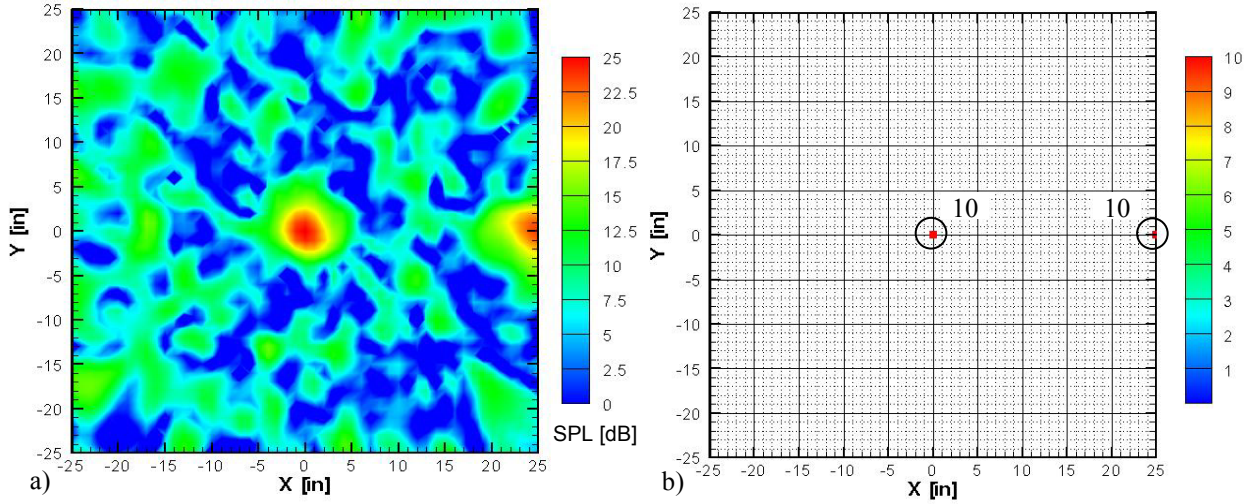

Figure 6.9: Simulation of 2 sources at 10 kHz, one at the grid boundary (25”, 0”, 36”).
a) Beamforming, and b) LORE results.

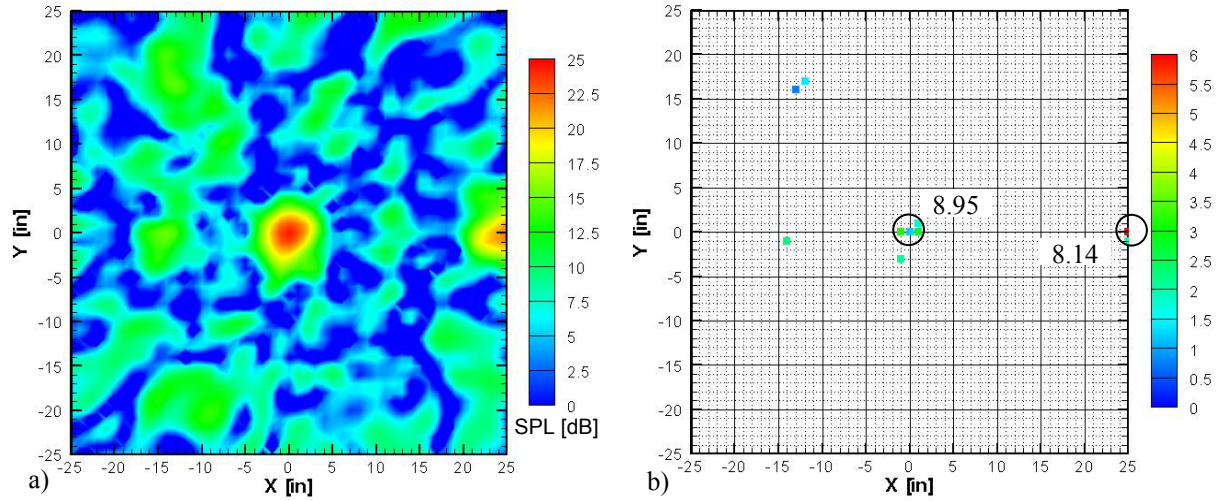

Figure 6.10: Simulation of 2 sources at 10 kHz. Second source 1” outside grid boundary (26”, 0”, 36”).
a) Beamforming, and b) LORE results.

As will be seen in the following examples, scanning a bigger grid might not be a viable solution. Thus, sometimes there could be extra sources that are too far from the region of interest. In this sense, the cases where the second source is 10”, 25” and 75” outside the scanning grid boundary are presented next.

Figure 6.11 shows that when the source is 10" outside the scanning grid, i.e. at (35", 0", 36"), many "artificial" sources appear in the LORE results. In this case, the level obtained for the center source is 11.26, about 1 dB higher in "power" than the actual level of 10. In this case, there are 31 nonzero values not associated with the source at the center. Their total level is 13.14, while the major level of such sources is 2.91, i.e. 12 dB below the source level. The reason for these "extra" sources is related to the way LORE works. It is assuming that the beamforming map is obtained as a superposition of complex beamforming maps due to sources "inside" the scanned grid. The effect of a source outside the boundaries can be graphically analyzed in the following way: if a source is present outside the boundaries of the grid being scanned, the beamforming map is "contaminated" with the sidelobes of such source. Thus, LORE will try to account for that "extra power" in the beamforming map by adding sources in the scanned grid in order to render the same beamforming output. The "contamination level" can be assessed by comparing these beamforming maps to the one obtained for a single source in Figure 6.3. As can be seen, the sidelobes structure is quite different, and thus suggesting the existence of noise sources outside the scanning grid. The correlation factor for this simulation is only 0.5927, indicating that LORE failed to find the actual sources. The computational time in this case was 179 seconds, significantly increased when compared to the previous cases. This is directly related to the number of potential noise sources that need to be optimized in Step 2 and to the fact that "noise" was introduced in the map.

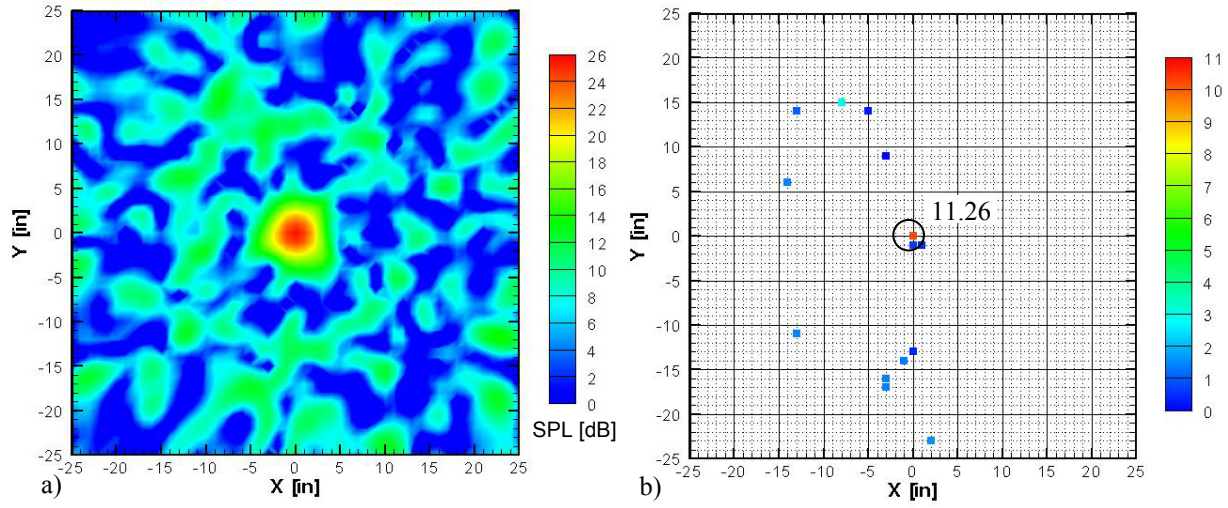

Figure 6.11: Simulation of 2 sources at 10 kHz. Second source 10" outside grid boundary (35", 0", 36"). a) Beamforming, and b) LORE results.

It would be expected that with sources relatively far from the zone of interest, the levels would be more accurately recovered and the "contamination" would also be reduced. To illustrate this, Figure 6.12 shows the results when the second source is 25" outside the grid, i.e. at (50", 0", 36"). As can be seen, the beamforming results are not yet quite similar to the one for a single source. The post-processing still shows many "extra sources" with a maximum level of 3.39 and a total level of 11.86 for the sum of the 31 of them. Thus, the total level of the contaminating sources is still of the order of the level of the actual source. In this case, the level recovered for the actual noise source is more accurate, i.e. 10.01. However, the correlation coefficient is only 0.585, indicating an erroneous result. The time required for this computation was 161 seconds.

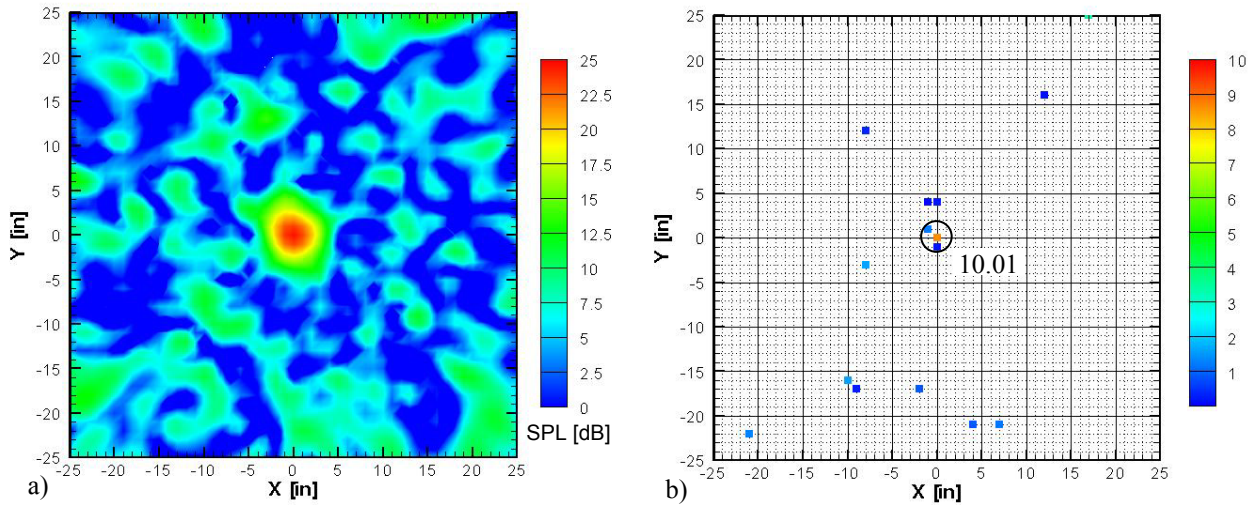

Figure 6.12: Simulation of 2 sources at 10 kHz. Second source 25" outside grid boundary (50", 0", 36"). a) Beamforming, and b) LORE results.

Finally, the case where the second source is 75" outside the boundary of the grid is presented. As seen in Figure 6.13a, the beamforming map starts to look more like the one for a single source. However, the LORE results still rendered 20 nonzero values not associated to the actual noise source. In this case, the level recovered for the actual source is 9.4. The maximum level of the artificial sources is 1.1, almost 19 dB lower than the power for the recovered source. The added level of all 20 of them is 3.88. In this case the correlation coefficient is about 0.75, suggesting an improvement from previous results, but still far from accurate. The time for this post-processing was 48.9 seconds.

These series of simulated results suggest that the presence of source outside the scanned grid will result in "artificial" sources in the LORE results. The number and level of such sources will depend on the levels and relative distance to the scanned grid. In the case of incoherent noise contaminating the beamforming maps, similar effects are expected.

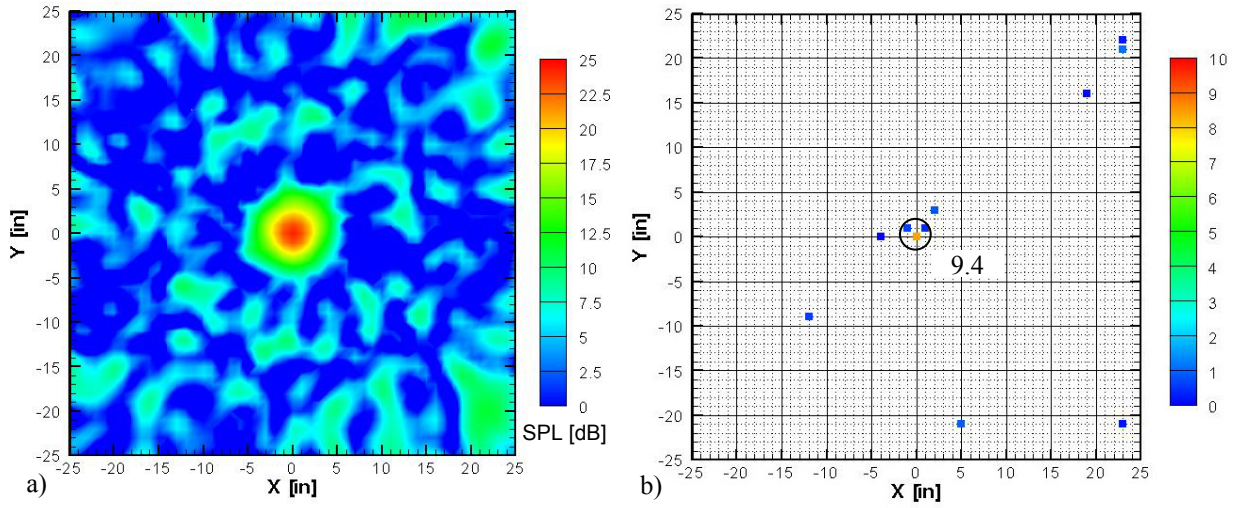

Figure 6.13: Simulation of 2 sources at 10 kHz. Second source 75" outside grid boundary (100", 0", 36"). a) Beamforming, and b) LORE results.

d. Multiple Scattered Incoherent Sources

The following section will present results for the case of multiple incoherent sources. As in the previous section, they will be presented for several frequencies in order to determine at which point the results "break down" or are no longer satisfactory. For this purpose, 8 sources with the same level (10) were simulated. Figure 6.14a shows the beamforming map for this case at 25 kHz. Note that the position of all the actual noise sources is not clear due to the presence of many sidelobes with relatively high levels. However, as can be seen in Figure 6.14b, the LORE processing successfully recovered the noise sources positions and levels. In this case, there were 21 values not associated with the actual noise sources. The highest being 3.7e-4, and their sum 1.7e-3; thus, negligible when compared to the level of an actual source, i.e. almost 75 dB lower in power. The correlation factor in this case also shows that the results are accurate, i.e. correlation equal to 1. The computational time was only 286 seconds.

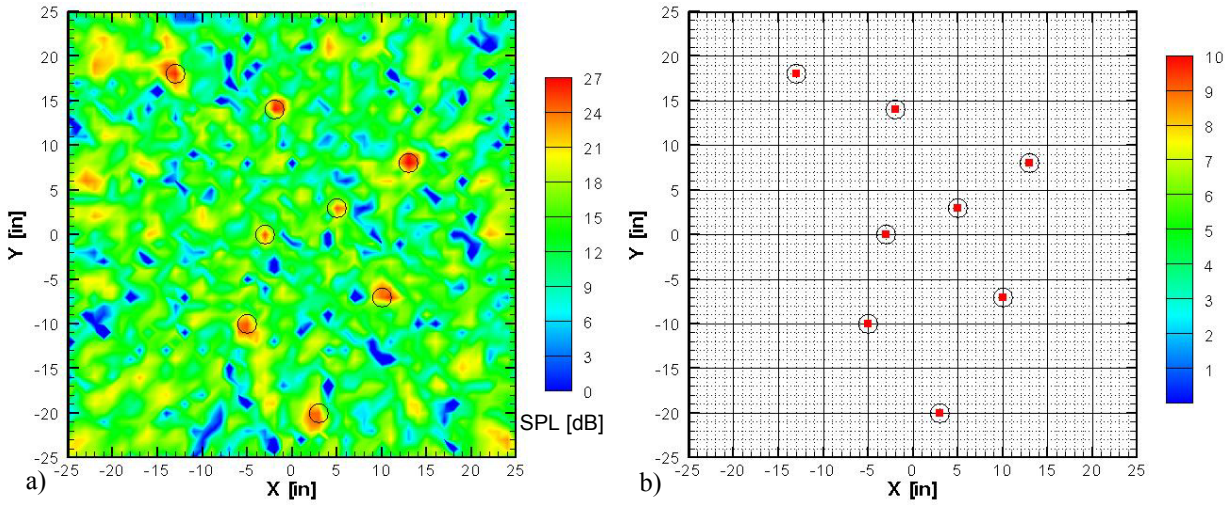

Figure 6.14: Simulation of 8 scattered incoherent sources at 25 kHz with the same amplitude.
a) Beamforming, and b) LORE results.

Moving down in frequency to 15 kHz, the results shown in Figure 6.15 are found. In this case, the levels and positions were also successfully recovered. The number of contaminating sources in this case was 22, with a maximum of 3e-3, and a sum of 1.9e-2. The correlation in this simulation was equal to 1. Thus, these results are expected to be very accurate. The time required for this post-processing was 234 seconds.

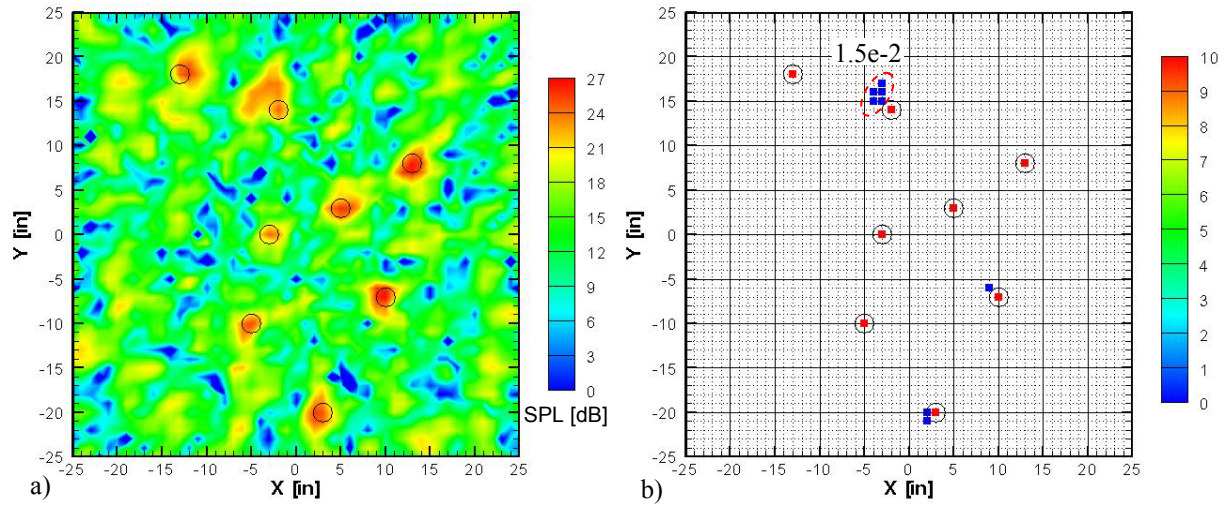

Figure 6.15: Simulation of 8 scattered incoherent sources at 15 kHz with the same amplitude.
a) Beamforming, and b) LORE results.

As mentioned before, an interesting insight can be obtained by "visually" comparing the reconstructed and actual beamforming maps. Thus, analyzing how "similar" the maps are, some

conclusions could be stated about the accuracy of the post-processing solution and the reason for eventual discrepancies. This is especially true for complex source distributions and at low frequencies as will be shown later in this chapter. In this sense, Figure 6.16 shows the comparison between the actual and reconstructed beamforming maps for the previous case. As can be seen, there are no noticeable differences between the maps. This was expected because the number and levels of artificial sources was not significant and the correlation factor was equal to 1.

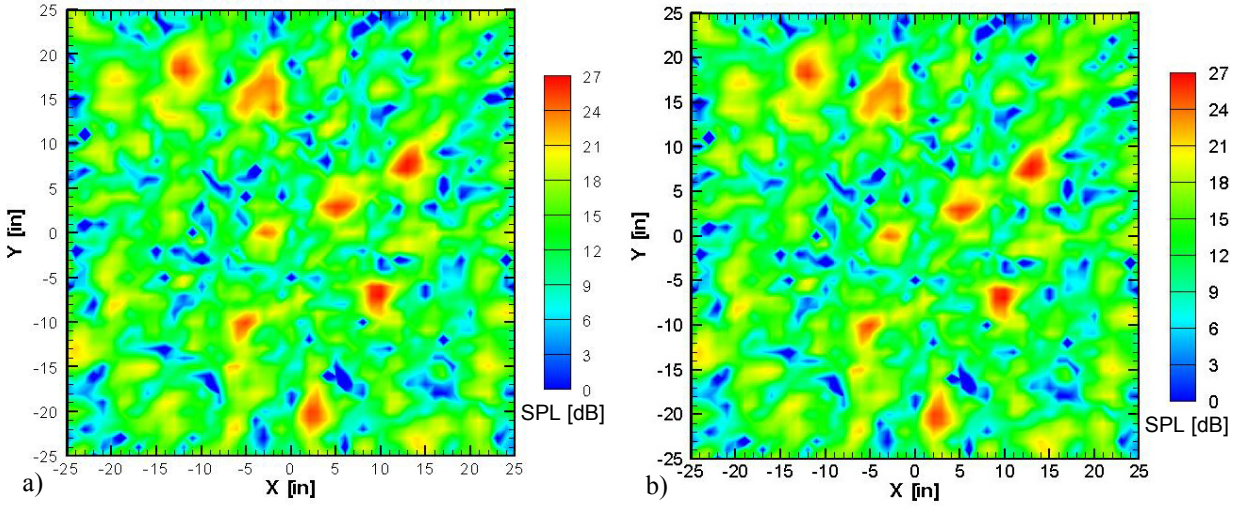

Figure 6.16: Simulation of 8 scattered incoherent sources at 15 kHz with the same amplitude. Comparison between a) beamforming, and b) reconstruction from LORE modeling.

The beamforming map for the 10 kHz case is shown in Figure 6.17a. As can be seen, the mainlobes are somewhat "shifted" from the actual noise sources position, i.e. black circles. This is especially true for the source located in the bottom of the map. This is related to the nonlinearity of the problem and was found to be dependant on the relative position of the sources, i.e. if the relative position of the sources is changed, the effects might be less drastic. As seen in Figure 6.17b, the LORE results are not rendered with the same accuracy than in the previous cases. This is related mainly to the solution from NNLS not being able to "find" a good set of starting points for the optimization procedure. However, it is expected that the correct results would be rendered if the solution to the approximated problem could provide a set with all the actual noise source positions. In this case, 28 nonzero values were rendered. Strictly speaking, only 18 of them correspond to the actual noise sources positions. Most of the levels of

the "7" sources that were recovered are "satisfactory". The reminding artificial sources have a level of 19.8 if the source not correctly recovered is taken as unsuccessful. If this case appears in real life, i.e. no knowledge of the actual positions, the source in the bottom would be treated as an actual source. Thus, the actual position would be erroneous. The maximum error on the recovered power of the sources is about 3 dB when compared to the actual level of 10. The time for this post-processing was 183 seconds.

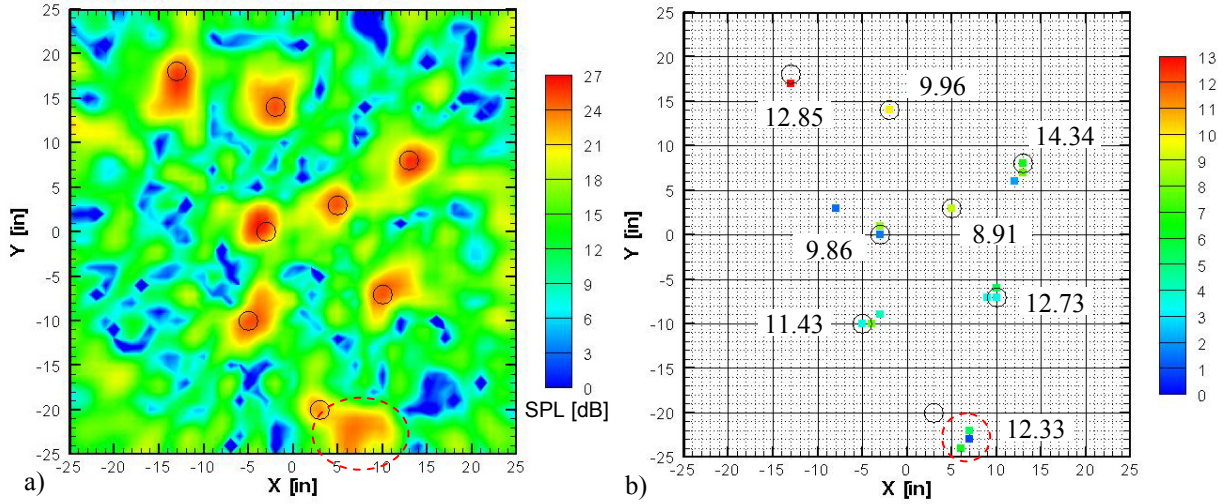

Figure 6.17: Simulation of 8 scattered incoherent sources at 10 kHz with the same amplitude. a) Beamforming, and b) LORE results.

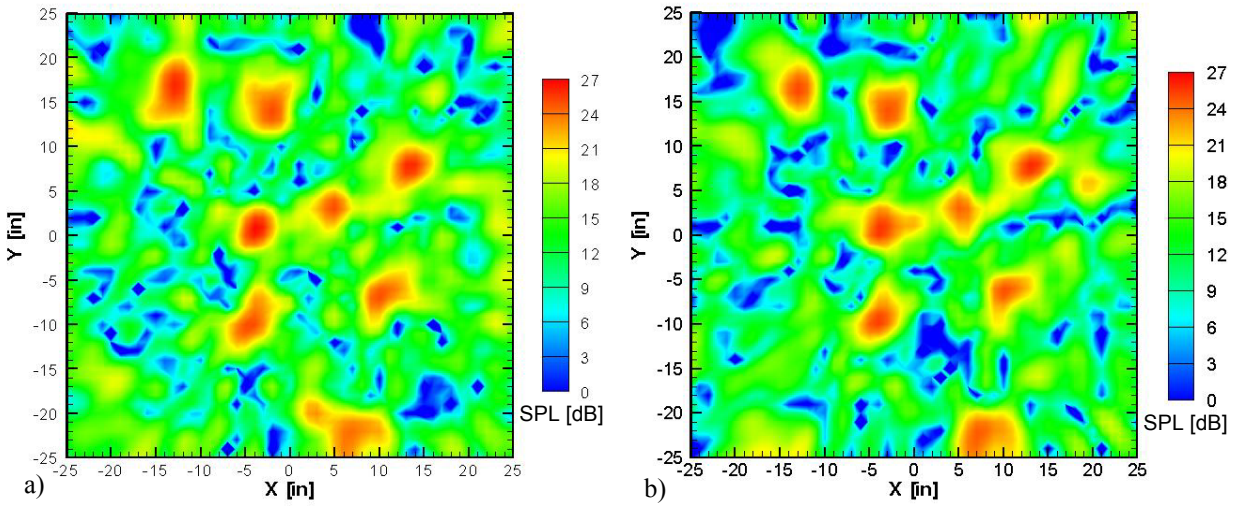

Figure 6.18: Simulation of 8 scattered incoherent sources at 10 kHz with the same amplitude. Comparison between a) beamforming, and b) reconstruction from LORE modeling.

Figure 6.18 shows the comparison between the actual and the reconstructed beamforming maps for the previous case. Unlike the cases where the results are correctly rendered, the reconstruction shows some "minor" differences. These differences in the maps also become evident in the correlation factor of 0.556 obtained for this case.

The same distribution of sources is now analyzed for a frequency of 5 kHz. As seen in Figure 6.19a, the problem of noise sources "shifting" from their actual position is even more noticeable in this beamforming map. Given this, the LORE results were not expected to be accurate in terms of position of the actual sources. Figure 6.19b shows the post-processing results for this case. As can be seen, the position of the "potential" noise sources, obtained from the NNLS procedure, is not in agreement with the actual noise sources position. Thus, at low frequencies, the effect of mainlobes shifting and the consequent "poor" solution from NNLS is more relevant. Again, performing a "blind" study of the LORE results, some source regions might be isolated and some conclusions drawn, i.e. getting some information about the sources is still possible. As shown in the plot, the total levels are "somewhat" recovered. The number of nonzero grid points in this example is 36, and the computational time was 340.5 seconds. The total level of the sources in the map is 73.8. In this case, the difference is less than 1 dB in the total power of the sources. Thus, as in previous cases, the total power in the scanning field seems to be recovered satisfactorily. The reconstruction of the beamforming map for this case is shown in Figure 6.20.

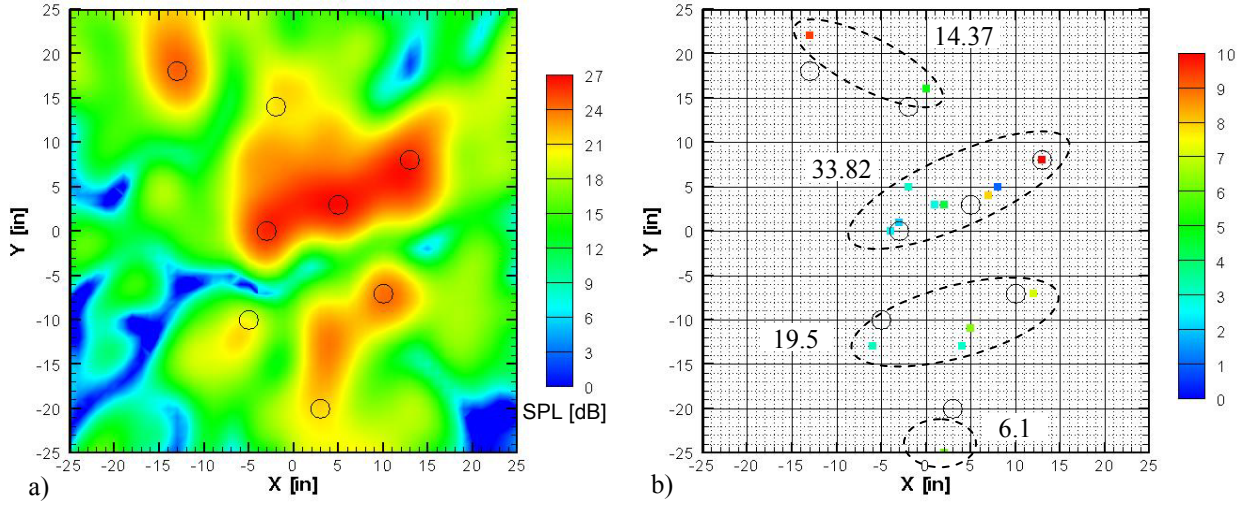

Figure 6.19: Simulation of 8 scattered incoherent sources at 5 kHz with the same amplitude.
a) Beamforming, and b) LORE results.

As can be seen, the comparison shows a relatively good reconstruction. Thus, most of the major features are captured. However, the correlation coefficient for this case is only about 0.7, indicating a poor recovery of the actual sources distribution and/or levels.

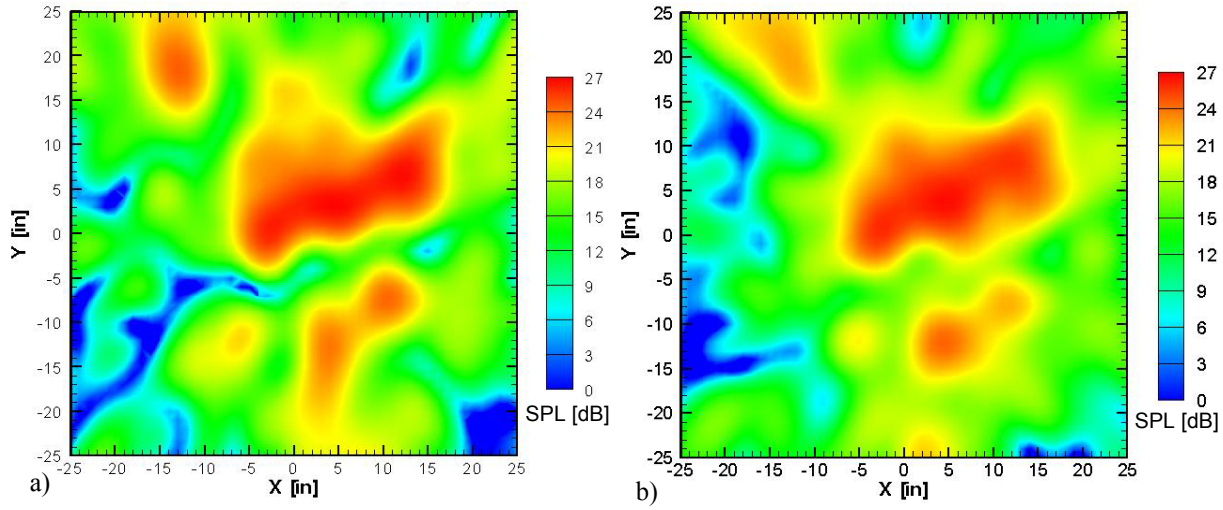

Figure 6.20: Simulation of 8 scattered incoherent sources at 5 kHz with the same amplitude. Comparison between a) beamforming, and b) reconstruction from LORE modeling.

Finally, the same sources distribution is analyzed for a frequency of 2.5 kHz. The beamforming map and post-processing are shown in Figure 6.21. In this case, the LORE results were not able to capture the total "power" in the map, i.e. total level was 46.1 instead of 80 (linear amplitude scale). The use of a bigger grid might be advantageous in this case. Thus, it is "suggested" that it is adequate to include in the map at least the region in space were all the points are within at least 6 dB from the peak value. Since this is related to the array beamwidth, the processing at low frequencies would require a bigger grid. The reconstruction of Figure 6.22 surprisingly shows very good agreement with the actual beamforming map, in agreement with the correlation factor of 0.9959 for this case. If a bigger scanning grid is used in this case, a drop in the correlation would be expected. This is related to the fact that the sidelobe structure from the actual and recovered sources will vary significantly.

It must be pointed out that, from the point of view of the author, the conclusions from LORE results are still more useful and accurate than the ones that could be drawn from the beamforming maps; especially when no information is available about the sources distribution as in the case of experimental data.

As shown in the previous set of examples, LORE is capable of rendering useful results in terms of noise source position and levels for a wide frequency range.

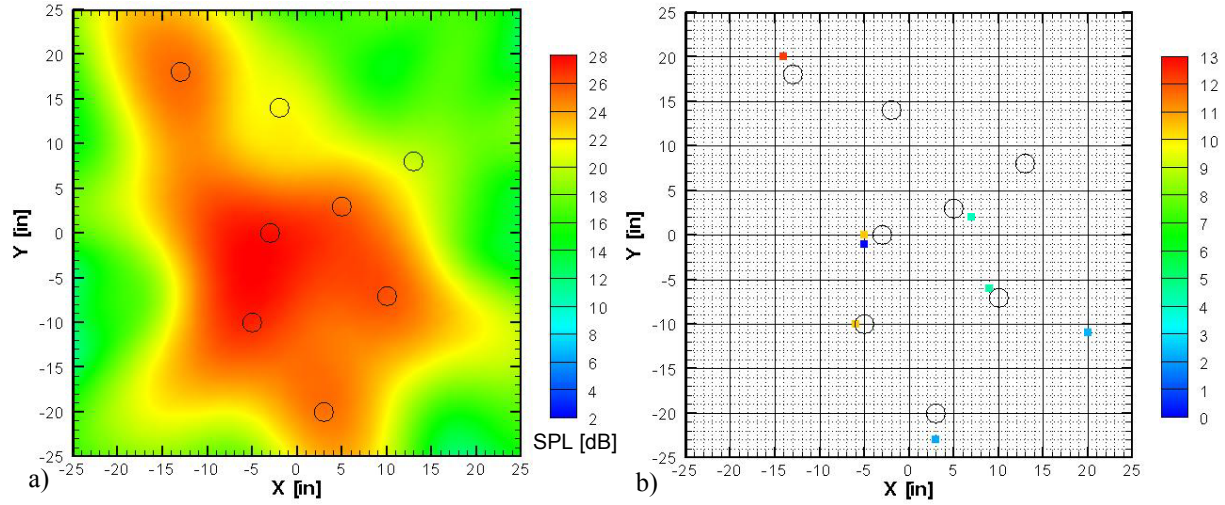

Figure 6.21: Simulation of 8 scattered incoherent sources at 2.5 kHz with the same amplitude. a) Beamforming, and b) LORE results.

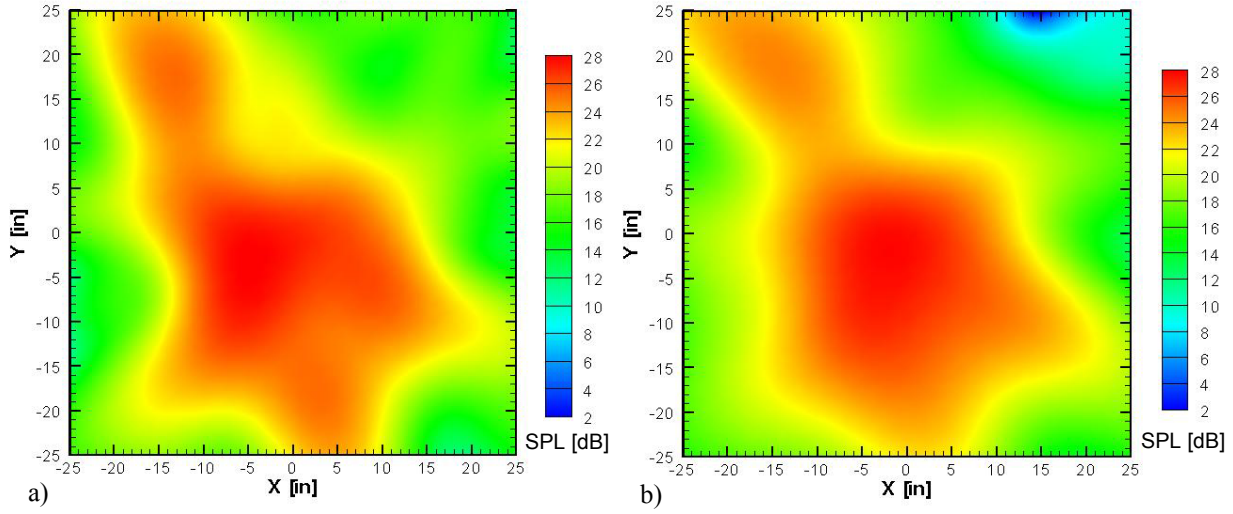

Figure 6.22: Simulation of 8 scattered incoherent sources at 2.5 kHz with the same amplitude. Comparison between a) beamforming, and b) reconstruction from LORE modeling.

The case of multiple incoherent sources with different levels will be analyzed next for 15, 10 and 5 kHz. In these simulations, 6 sources with amplitudes of 5, 6, 7, 8, 9, and 10 were used.

Figure 6.23a shows the beamforming map for 15 kHz and the sources distribution mentioned above. As can be seen, the source with amplitude 5 does not appear as a “visible” mainlobe. This

is related to the fact that its power is 6 dB below the power from the loudest noise source. In fact, some regions in the grid that are not related to actual noise sources have the same or even higher outputs than the power at that point. i.e. the sidelobes from this sources distribution are higher than the mainlobe for some actual sources. The post-processing results are presented in Figure 6.23b. As can be seen, for the quietest source the NNLS was not able to render a "potential" source in that region. Thus, without any value to optimize in that position, the source level recovered is zero. This can be related to a resolution problem, and could potentially be avoided by using a finer grid. For the remaining sources, the recovered levels are satisfactory. The actual level of the sources is indicated in the plot, i.e. (10). In this case, 25 nonzero values were optimized, where 13 of them were artificial noise sources. The maximum level of such points was 1.88, with a total of 8.29. Most of this energy is concentrated around the louder sources. The correlation coefficient in this case was 0.8587, indicating that the results are not exact. The time required for this computation was 125 seconds.

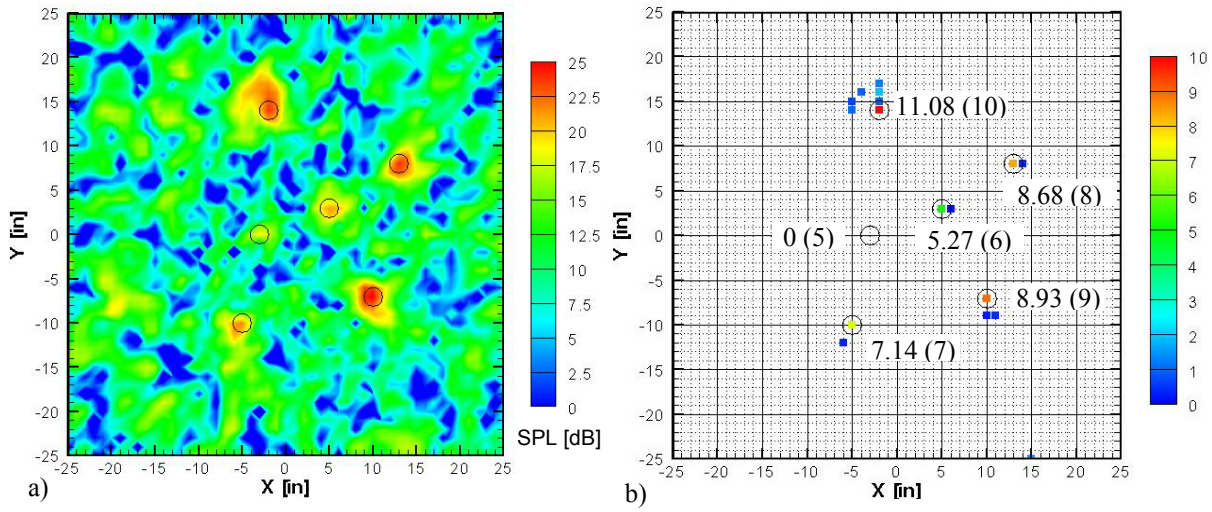

Figure 6.23: Simulation of 6 incoherent sources at 15 kHz with different amplitude.
a) Beamforming, and b) LORE results.

If the beamforming maps were to be analyzed, the 3 and 6 dB-down beamforming maps would be studied; Figure 6.24 shows such maps. From these maps it would probably be concluded that there are only 5 noise sources in the scanning field. It can also be stated that their levels are somewhat different. However, as can be seen, quantization of the levels is not accurately possible. Thus, the LORE results are very useful in these situations.

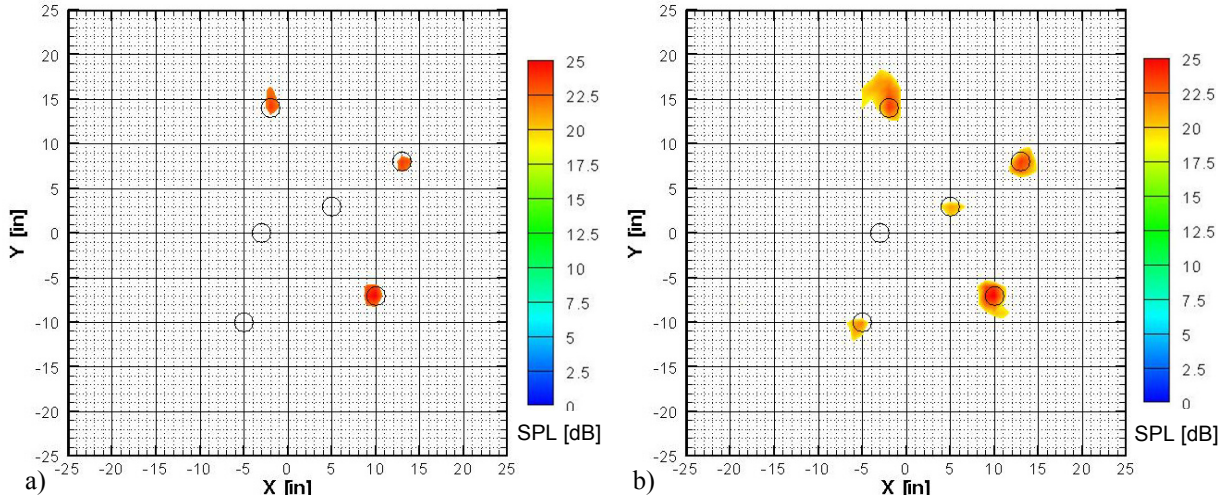

Figure 6.24: Multiple sources at 15 kHz with different levels.
Beamforming maps with a) 3 and b) 6dB down from peak value.

The same case for a frequency of 10 kHz is shown in Figure 6.25. As shown in the beamforming map, the increase in array beamwidth allows us to identify the position of all 6 sources. However, some sources are shifted from the actual position. The LORE results show a very good recovery of the levels as well as the position of all the noise sources, in agreement with the correlation factor of 0.969 for this case. The contribution of the artificial noise sources (7 out of 25 nonzero values) is much lower than in the previous case, i.e. the maximum value is 0.41 and their total level is 0.57. The computational time was only 94 seconds.

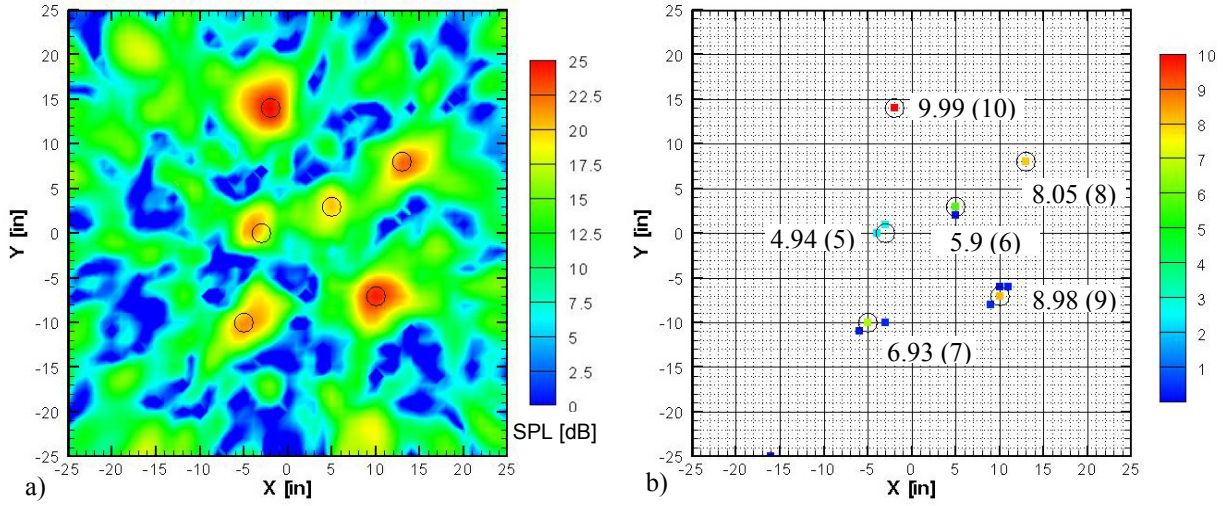

Figure 6.25: Simulation of 6 scattered incoherent sources at 10 kHz with different amplitude.
a) Beamforming, and b) LORE results.

Finally, results are shown in Figure 6.26 for the same distribution at a frequency of 5 kHz. As can be seen, for almost all the sources, the recovered levels are slightly higher. There is also an artificial noise source (circled in red) that has a level of the order of the actual noise sources. The total level of the sources including the one mentioned above is 54.8, instead of the actual 45, i.e. 1.7 dB higher in total SPL. Out of 23 nonzero values in this case, 10 of them were "artificial". However, disregarding the previously mentioned one, the maximum level of such sources is 0.27, and their total adds to 0.271. The computation took 114.4 seconds.

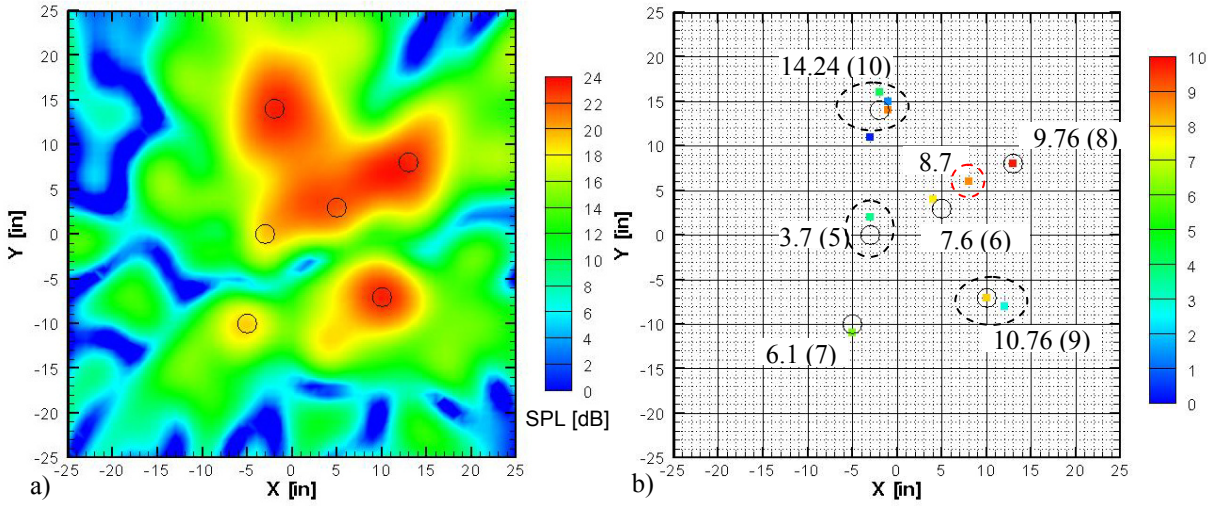

Figure 6.26: Simulation of 6 scattered incoherent sources at 5 kHz with different amplitude. a) Beamforming, and b) LORE results.

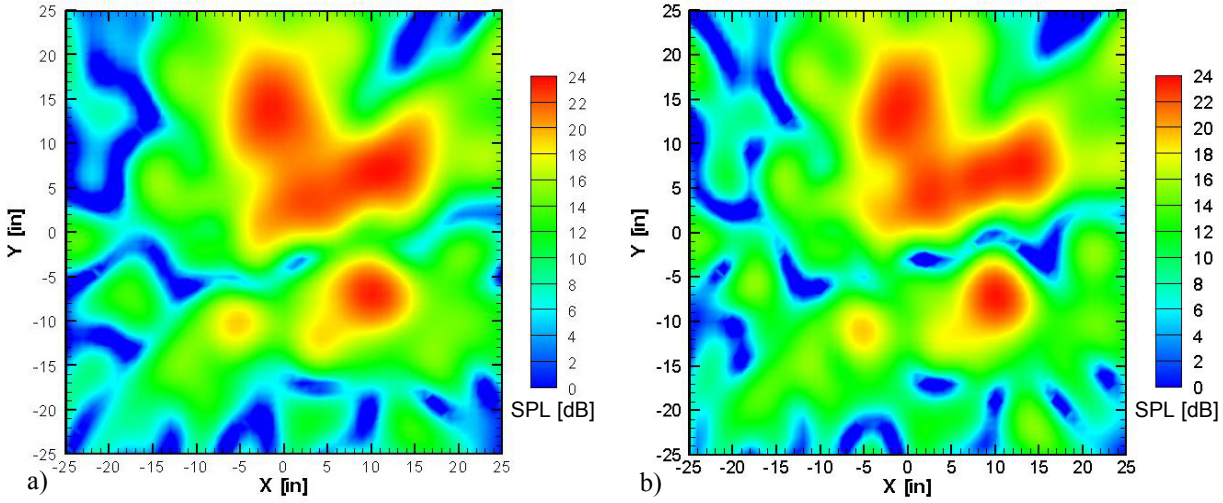

Figure 6.27: Simulation of 6 scattered incoherent sources at 5 kHz with different amplitude. Comparison between a) beamforming, and b) reconstruction from LORE modeling.

The reconstruction of the beamforming map from the LORE results in Figure 6.27 shows good agreement when compared to the actual one, i.e. the correlation coefficient is 0.867. As mentioned before, this is related to the multiplicity of solutions for this problem, i.e. there is more than one set of sources that would render the same beamforming map.

e. Line of Sources

This section will present results obtained for a linear distribution of sources. Such distribution consists of 7 sources separated 1 inch, each with amplitude 10. Since the results obtained for a wide frequency range are almost the same, they will grouped and the differences, if any, will be pointed out. Figure 6.28 shows the beamforming maps for the numerical simulations at 25, 15, and 10 kHz respectively. In all cases, the actual number of sources and levels can not be identified from the maps.

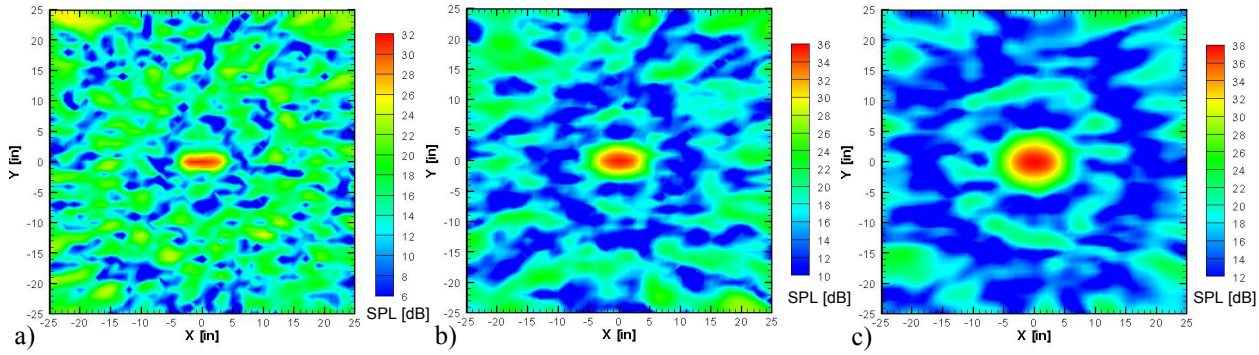

Figure 6.28: Beamforming maps for a line of 7 sources 1" apart at a) 25, b) 15, and c) 10 kHz.

The LORE results for these cases are shown in Figure 6.29a, while Figure 6.29b shows a close detail of the region of interest. In this case, as in the following examples, the black circles mark the actual position of the noise sources. As can be seen, the position and level of the sources were successfully determined. In all cases, the correlation coefficient was equal to 1. Table 6.1 shows a summary of these results.

Frequency [kHz]	Number of Nonzero Values	Sources Total Level	Max. Artificial Source Level	Total Level of Artificial Sources	Computational Time [sec]
25	17	69.99991	1.5e-4	4.3e-4	18.5
15	7	69.99989	0	0	10.1
10	7	70.00099	0	0	10.1

Table 6.1: Summary of LORE results for a line of sources.

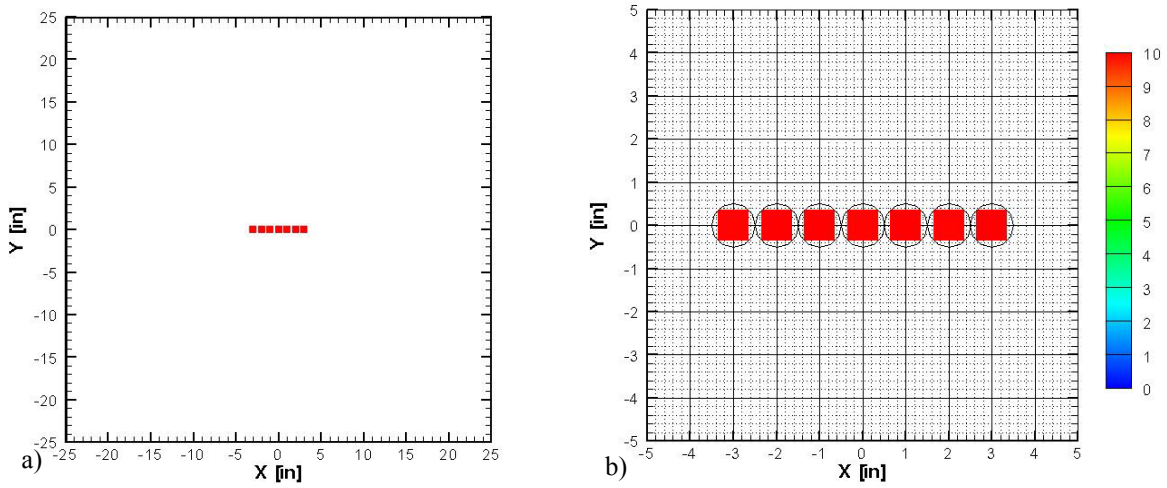

Figure 6.29: a) LORE results for a line of sources at 25, 15, and 10 kHz. b) Detail of sources region.

Moving down in frequency to 5 kHz, the results shown in Figure 6.30 are obtained. In this case, the only nonzero values in the grid are the ones corresponding to the actual position of the sources. Given the poor resolution of the array at low frequencies, the individual levels are not accurately recovered. However, the total level of the sources is 69.99273, very accurate when compared to the actual 70, and the correlation coefficient is equal to 0.9999911. This post processing was performed in 13.3 seconds.

Finally, the same case for a frequency of 2.5 kHz is presented in Figure 6.31. In this case, the beamforming map looks very similar to that of a single source or the case of two sources shown in Figure 6.8. Thus, from this map it might be concluded that there is only a single source at the center of the grid. However, the LORE result shows still show some kind of linear "spreading" of the source. The lack of resolution was expected in this case since it is an "extension" of the case of 2 sources presented before. The actual level of the sources distribution is also

successfully recovered, i.e. 70.34. There were 8 nonzero values in this post-processing, 3 of them were artificial sources, having a maximum level of 1.1e-4 and a total level of 2.8e-4. The correlation coefficient in this case was 0.999971, indicating a very good result. The computational time in this case was 21.4 seconds.

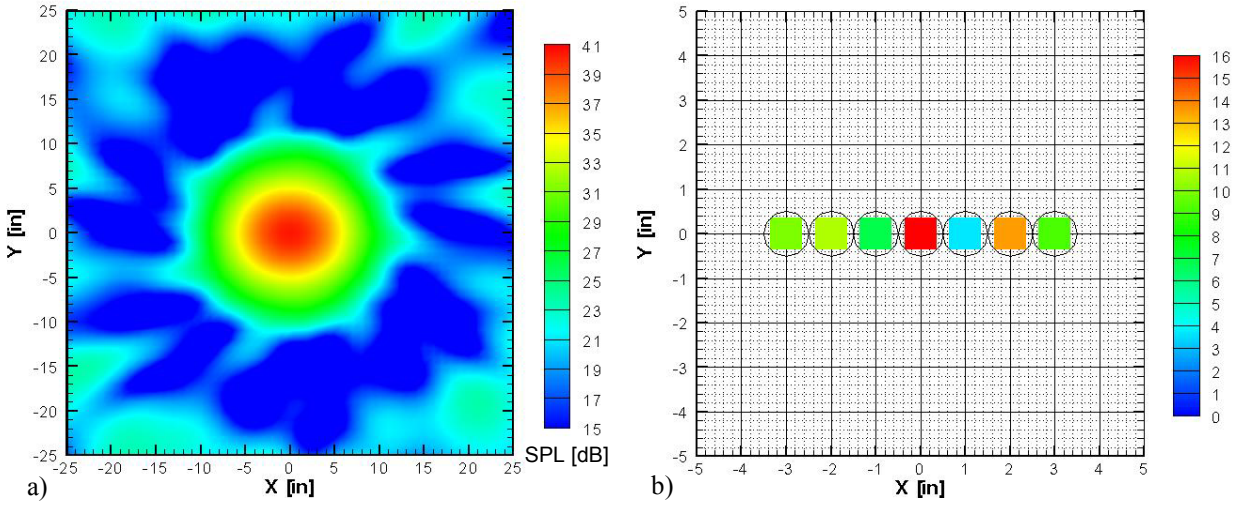

Figure 6.30: a) Beamforming map for a line of 7 sources 1" apart at 5 kHz, and b) detail of LORE results.

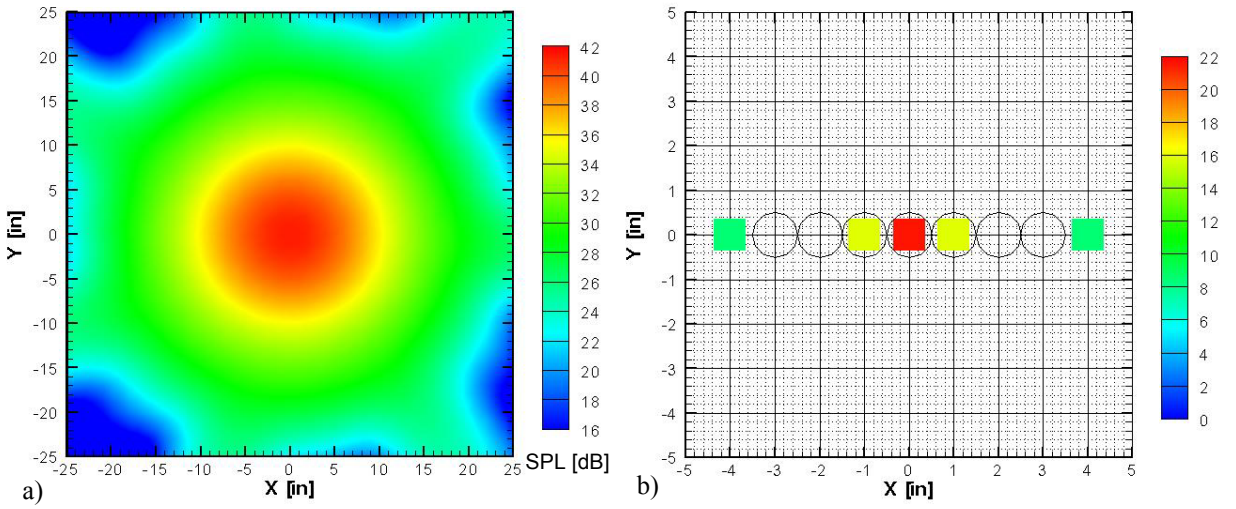

Figure 6.31: a) Beamforming map for a line of 7 sources 1" apart at 2.5 kHz, and b) detail of LORE results.

The effect of increasing the grid size was not studied in this case, but should improve the results at low frequencies. Thus, the sidelobes that would appear in a bigger beamforming map may help rendering more accurate results in some cases. This is related to the fact that the levels and positions of the sidelobes for a single source might be quite different than the ones for a source distribution like the one used in this case.

f. "Complex" Source Distributions

In this section, a complex source distribution is used to test the capabilities of the LORE technique. The distribution consists of 16 sources (with amplitude 10) in a square shape and one source in the center of such distribution with an amplitude of 25. As in the previous sections, the results are presented in descending frequency in order to determine the breakdown point.

Figure 6.32a shows the beamforming map of such noise distribution at 25 kHz. In this case, the concentration of sources in the central region renders a "confuse" map. Thus, from this map it could be concluded that a number of sources are present at the center but without any specific details. Note also that the sidelobes are only about 6 or 7 dB below the mainlobe. Thus, the SNR appears to be decreased, i.e. for a single source was about 10 dB. A detailed view of the LORE results in Figure 6.32b shows that the position of the actual noise sources, indicated with black circles, as well as their levels are successfully recovered. The NNLS procedure rendered 29 nonzero values. Of those, 10 of them are "artificial" sources away from the center region with a maximum of 1.1e-3 and adding to 3.6e-3. Thus, well below the levels of the actual sources. The correlation coefficient in this case is equal to 1. The computational time for this post processing was only 232.4 seconds.

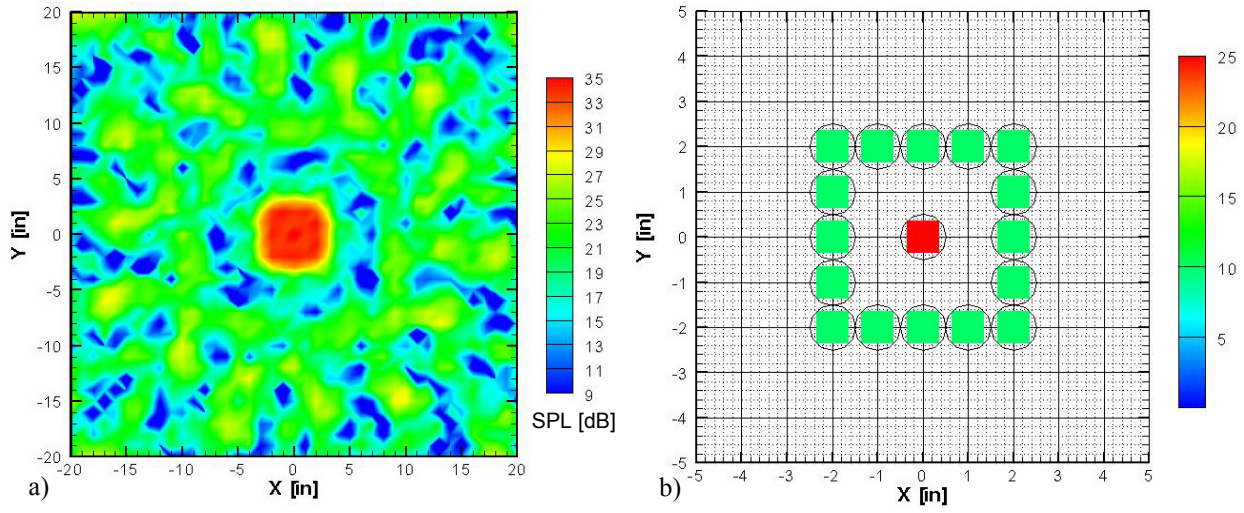

Figure 6.32: a) Beamforming map for a distribution of 17 sources at 25 kHz, and b) detail of LORE results.

The next frequency to be analyzed is 15 kHz. The results for this case are presented in Figure 6.33. Given the beamwidth, the beamforming map does not tell us much about the actual source

distribution. Also, the LORE results start to lose accuracy in terms of spatial position and actual levels, as reflected by a small drop in the correlation coefficient, i.e. about 0.978. However, the pattern and the total level (177.87) are still captured satisfactorily within 0.15 dB in power. The processing rendered 21 values which were all in the region of interest, i.e. no artificial sources. The computational time was 133.8 seconds.

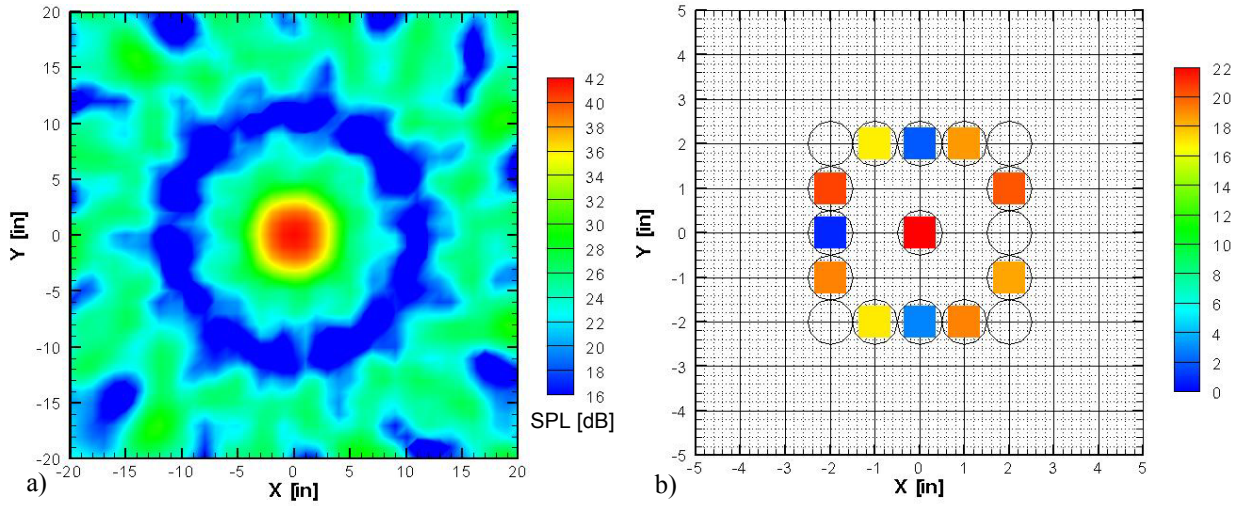

Figure 6.33: a) Beamforming map for a distribution of 17 sources at 15 kHz, and b) detail of LORE results.

For the same source distribution at 10 kHz, the results shown in Figure 6.34 are obtained. Like in the previous case, there is not much that could be said about the sources from the beamforming map. Given the complexity of the source, LORE has lost the "resolution" needed to render the actual distribution. As can be seen, the results show 4 major sources in the sides of the actual square of sources. The source in the center has "blended" with these points. The total level recovered is 175.91, about 0.4 dB difference with the actual power. In this case, 14 points had nonzero values, and as in the previous case, they were all at the center of the grid. This was expected since the NNLS will "allocate" points were the levels are higher, and in this case the maximum levels are concentrated at the center of the grid. Also keep in mind that the optimization results are "constrained" by the initial set of points rendered by the NNLS step; thus, as mentioned before better results could be obtained using a different approach in Step 1 that could render all the actual sources position. The time required for the post-processing was only 25.3 seconds.

The reconstruction of this case is shown in Figure 6.35, where the actual beamforming and the reconstruction show only minor differences in the sidelobes pattern. This suggests that even

though the actual source distribution is not being rendered, the results are very reasonable. This is also reflected in a correlation coefficient of 0.9046. Keep in mind that at this point the array performance is being "pushed". Thus, the beamwidth is an important factor when trying to identify many sources clustered in a small region.

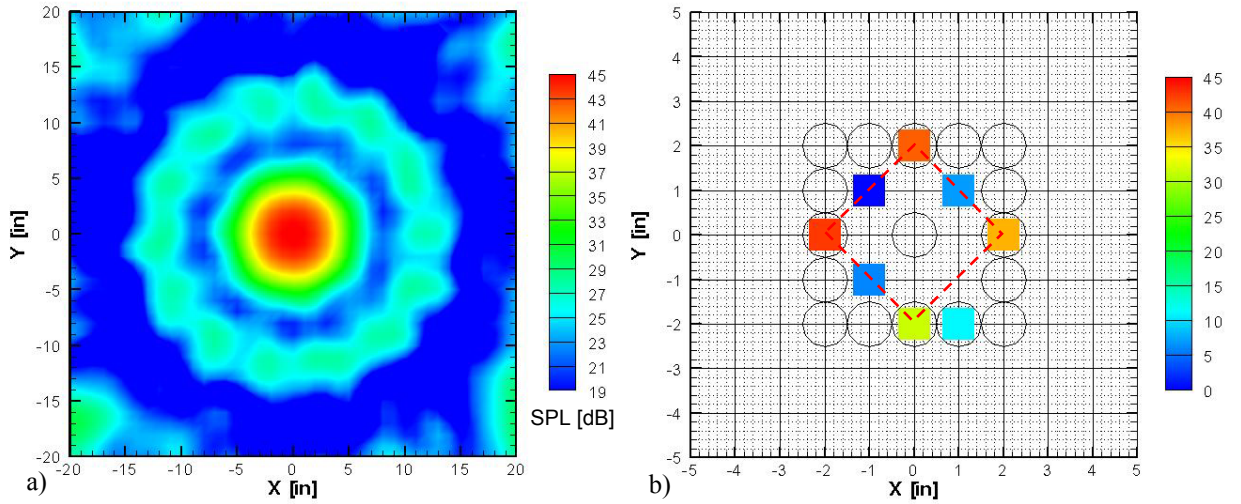

Figure 6.34: a) Beamforming map for a distribution of 17 sources at 10 kHz, and b) detail of LORE results.

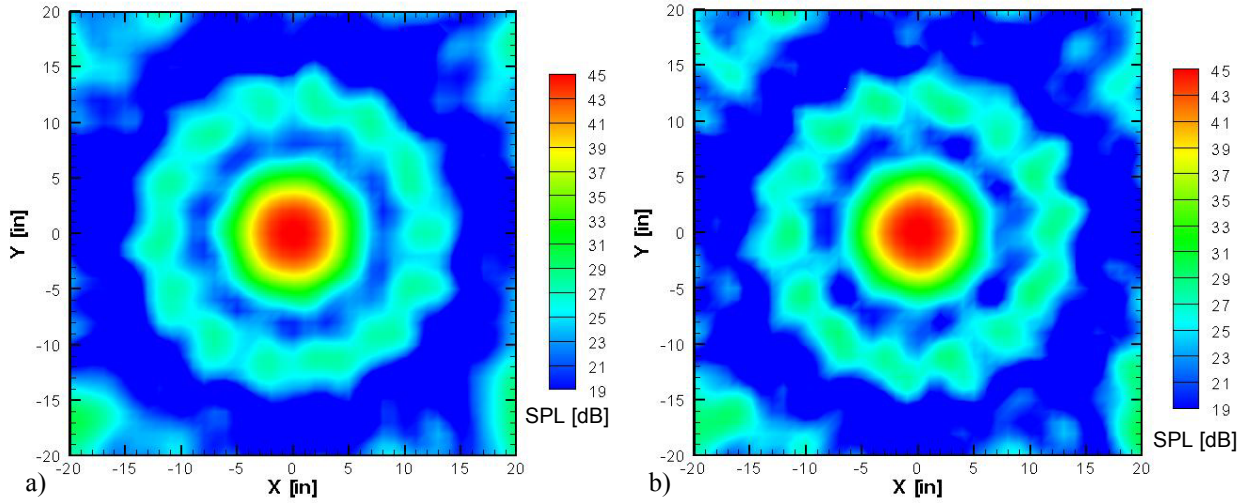

Figure 6.35: Simulation of a distribution of 17 sources at 10 kHz. Comparison between a) beamforming, and b) reconstruction from LORE modeling.

The results for 5 kHz are shown in Figure 6.36. As can be seen in the beamforming map, it looks like there is a single source at the center. However, the post-processing still gives some insight into the actual noise sources distribution. In this case, 16 nonzero values were present at

the grid center at the beginning of the optimization. However, only 7 were above the threshold at the end of the procedure, as shown in Figure 6.36b. The total level obtained was 183.7, less than 0.1 dB difference with the actual total power. Even when the actual noise source distribution is not correctly recovered, the correlation factor is 0.9991. As mentioned before this is related to the resolution of the array.

This fact that the levels are underpredicted was observed for many different distributions. Thus, when the source distribution is not correctly rendered, the difference in the total recovered level increases when moving down in frequency. The time for this processing was only 43.9 seconds.

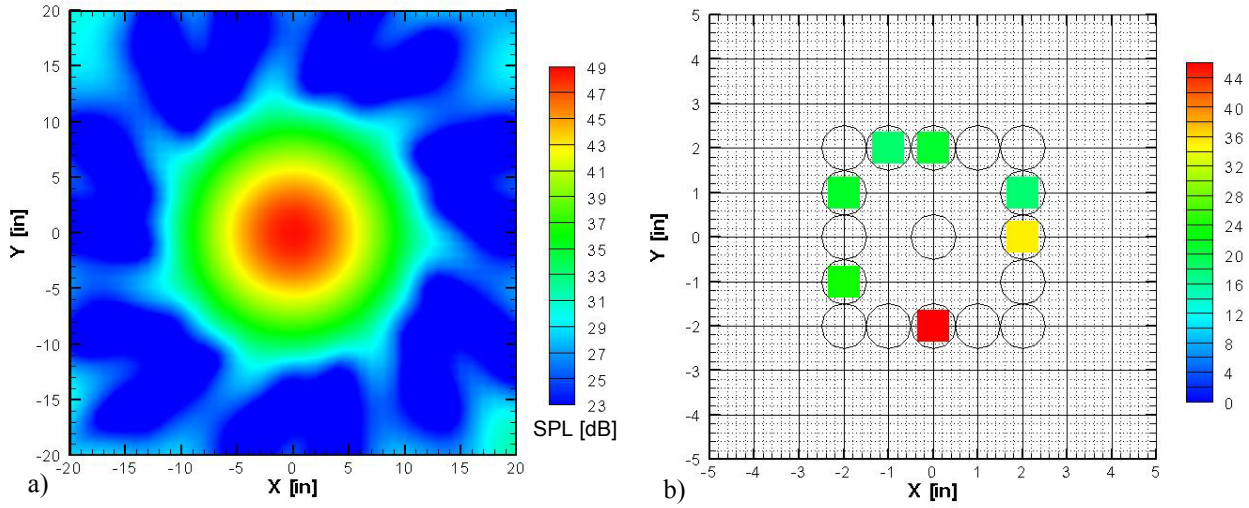

Figure 6.36: a) Beamforming map for a distribution of 17 sources at 5 kHz, and b) detail of LORE results.

g. Coherent Sources

As mentioned in the theoretical development of the LORE technique, it can be assumed that the sources are coherent and obtain significant results. Thus, even though phase information is not available in the beamforming output, the proposed modeling is able to find the relative phase between sources at the same frequency.

As will be shown next, the difference in the beamforming maps is significant when a relative phase between the sources exist. In this sense, Figure 6.37a shows the beamforming map for 2 sources with the same phase and Figure 6.37b for 2 sources with a relative phase of 180 degrees,

i.e. a dipole. In both cases, the amplitude of each source was set to 10. This difference in the maps also suggests that reconstruction from LORE could be used to determine if the incoherence assumption was correct in the first place for solving the given problem.

Solving the dipole case assuming that the sources are incoherent, the results shown in Figure 6.38a would be rendered. In this case it would be concluded that there are 2 sources with amplitudes 8.94 and 6.73. Furthermore, the results show what it seems to be a third source with amplitude of 2.24. Even considering that given the array resolution at this frequency all the nonzero grid points in the lower area correspond to the same source, the results will render 8.94 and 8.97 respectively, i.e. a difference of about 1 dB in power. However, in the case of multiple sources or for particular cases this difference could be much bigger. The correlation coefficient in this case was only 0.7969, indicating that the incoherence assumption is erroneous. The time required for this computation was 15.2 seconds.

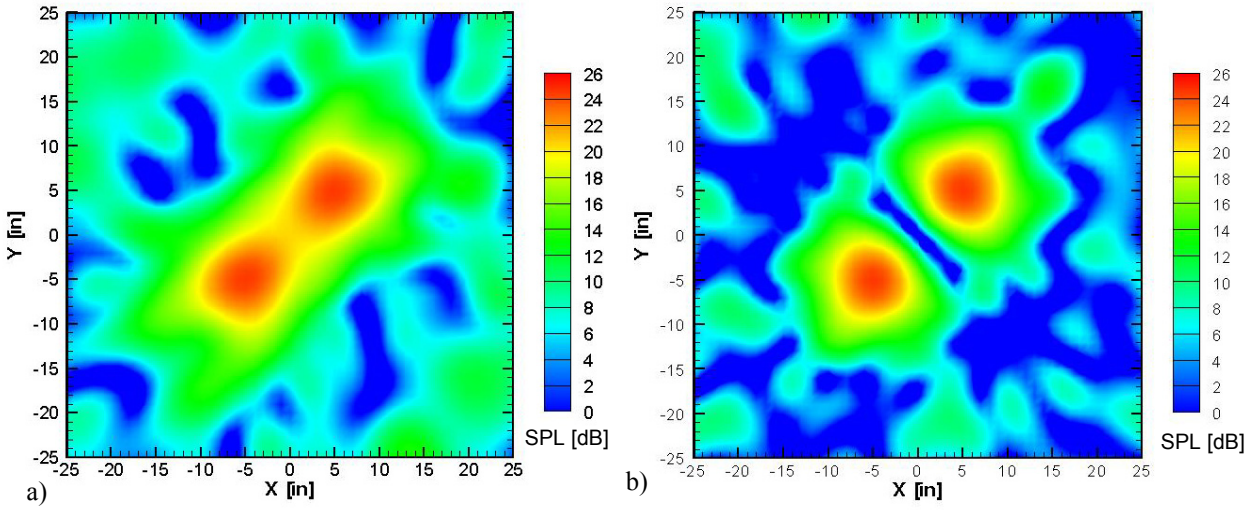

Figure 6.37: Beamforming simulation for 2 sources at 5kHz with a) no relative phase (i.e. incoherent), and b) 180° relative phase (i.e. dipole).

If no assumptions are made about the incoherence of the sources in the LORE processing, the results shown in Figure 6.38b are obtained. In this case the levels and positions are successfully recovered. Note that in both cases the optimization procedure starts with the same set of 16 points from the NNLS step. Thus, since the number of parameters to optimize is doubled, the computational time is now about 72 seconds. To obtain the total levels in the case of coherent sources, all the nonzero grid points in the source region are added in complex form.

The LORE technique also renders the phase information. In this case, the relative phase between the major sources is 179.92 degrees. The phase information is shown in Figure 6.39. As can be seen, other sources appear with a difference phase, but keep in mind that their levels are negligible when compared to the loudest ones. As expected, the correlation coefficient in this case is much closer to 1, i.e. 0.999997, indicating that the results are very accurate.

REMARK: Note that with LORE it is possible to extract ***phase*** information from the "power" in the beamforming maps.

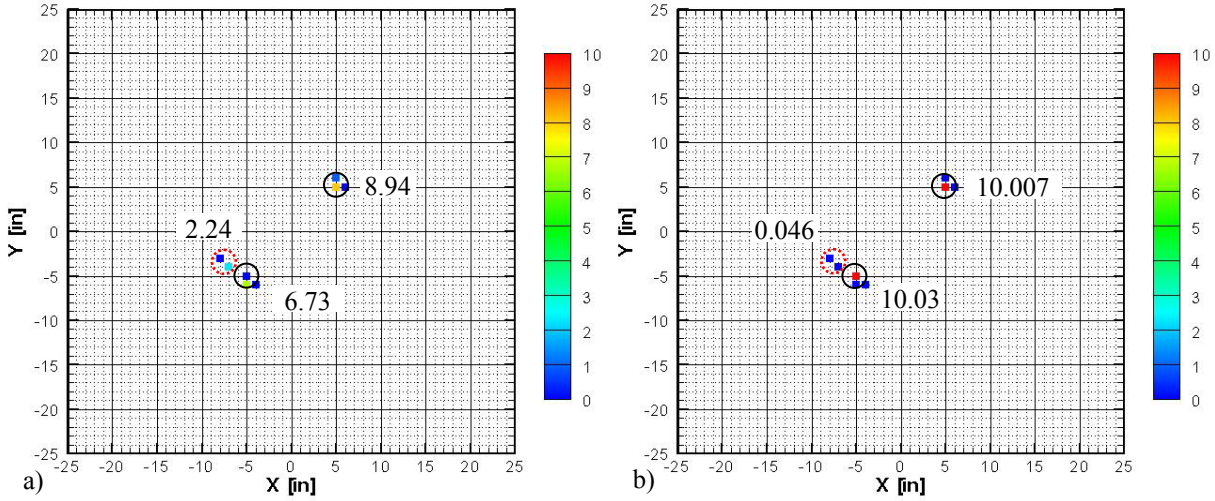

Figure 6.38: LORE results for a dipole at 5 kHz assuming a) incoherence, and b) coherence.

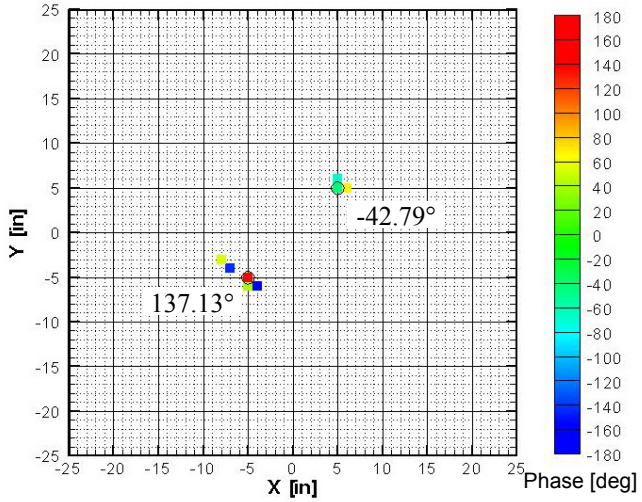

Figure 6.39: Phase information in LORE results for a dipole at 5 kHz assuming coherence.

It is interesting to analyze the case of multiple coherent sources. In particular, a linear distribution of coherent sources will be analyzed, i.e. similar to coherent trailing edge noise. Figure 6.40a shows the beamforming map for 5 coherent sources separated 2" apart. The relative phase between the sources was set to -90, -45, 0, 45 and 90 degrees respectively, from left to right. The amplitude of all sources is the same and equal to 10. As can be seen, the beamforming map looks "irregular" when compared to the results for a line of incoherent sources like in Figure 6.28. If this case is post-processed assuming that the sources are incoherent, the LORE results presented in Figure 6.40b are rendered. In this case, the results do not agree with the simulated source distribution, reflected in a low correlation coefficient of 0.62. Furthermore, there are many artificial sources, i.e. indicated with dashed red circles, with levels of the same order than the levels of the actual sources. This case is presented in order to remark the importance of not having the restriction of source incoherence.

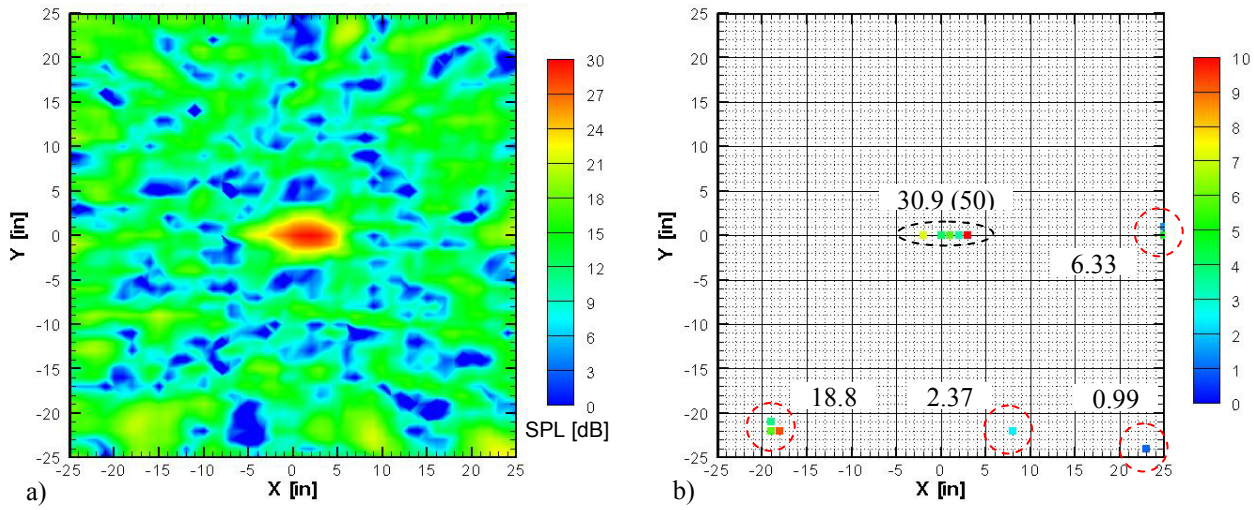

Figure 6.40: a) Beamforming simulation for multiple coherent sources with different relative phase at 15 kHz, and b) LORE results assuming incoherence.

If no assumptions are made about the coherence of the sources, LORE can render the actual levels and source positions as shown in Figure 6.41a. Note that there are some artificial sources present. However, the maximum level of such points is 1.1e-2, and they add up to 2.8e-2. Thus, well below the total level of the actual noise sources, i.e. about 65 dB in power. The actual noise sources add up to 49.975, instead of the actual 50. As shown in Figure 6.41b, sources have a phase difference of about 45 degrees with the adjacent sources; thus, in very good agreement

with the simulated sources. The accuracy of the results is also reflected in a correlation coefficient of 0.99998.

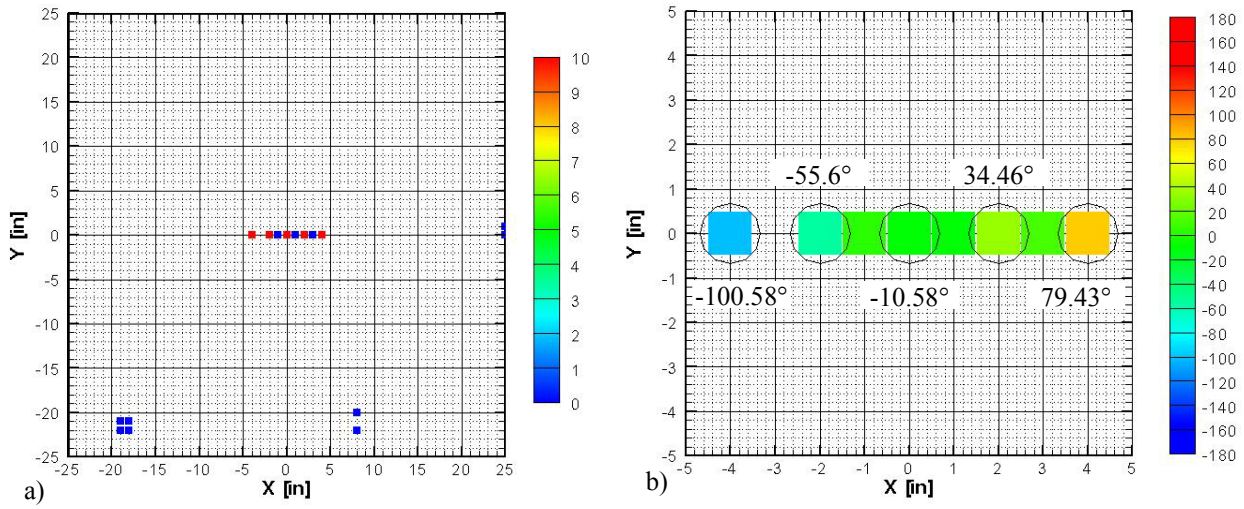

Figure 6.41: LORE results for multiple coherent sources with different relative phase at 15 kHz, a) amplitude, and b) relative phase (detail).

If there is no information regarding the coherence of the sources, or the physics of the problem does not give us any "hint" the problem can still be solved. Thus, if LORE is used assuming coherent sources and they end up being incoherent, the results will show a zero relative phase. A sample case of two incoherent sources at 15 kHz is shown in Figure 6.42. As can be seen, the levels are successfully recovered and the phase information for both sources renders the same number, i.e. no relative phase. The correlation coefficient in this case is 0.9999989.

Note that in more complex cases, the assumption of coherence may significantly increase the computational time. Furthermore, in the presence of several noise sources the results may loose accuracy. This is related to the increasing number of variables to optimize and the ill-conditioning of the matrix of *cpsf*. Keep in mind that the rank of the matrix of *cpsf* is given by the actual number of sources, while usually a larger number of "potential" sources is being minimized. In some sense, the domain in which the solution is to be found is expanded and the risk of having multiple minima is increased, i.e. multiple possible solutions.

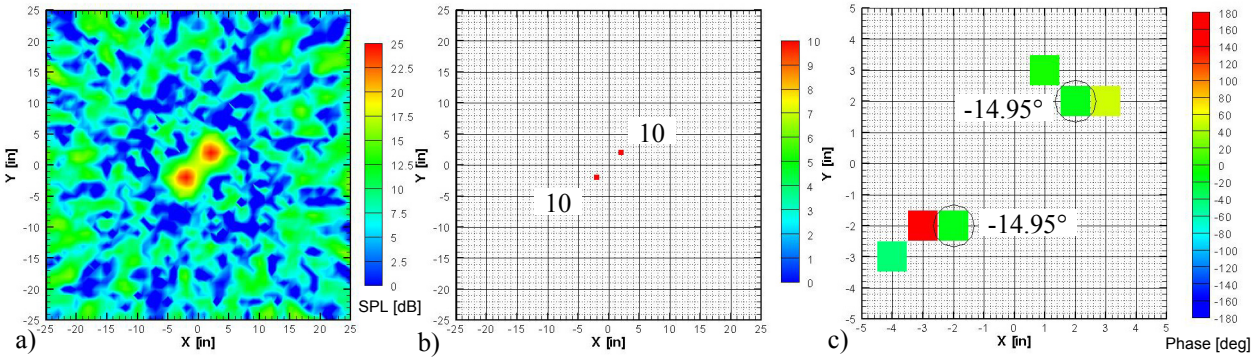

Figure 6.42: Simulation of 2 incoherent sources at 15 kHz. a) Beamforming, and b) amplitude and c) phase results in LORE assuming coherence.

6.5 Numerical Simulations in 3D

As mentioned before, the theoretical modeling developed in this work is not restricted to 2D cases. This can be proven by calculating the beamforming output for "any" 3D scanning grid and comparing to the modeling. Thus, the formulation presented in this work is not restricted to small regions in space. Some numerical simulations of 3D cases will be presented next.

In the first case, a 40-by-40-by-8 inches grid was simulated with a monopole source at the center, i.e. at (0", 0", 36"). The resolution in the XY plane was 1" and 2" in the z-direction, i.e. resulting in 8405 grid points. Figure 6.43a shows the beamforming map for a plane 36" from the array. Figure 6.43b shows a plane normal to the previous one. As can be seen, there is a lot of uncertainty in terms of position in the z-direction.

In some simple cases, a much bigger grid including all the points within 3 dB could be used to identify the position. However, for multiple sources this task gets difficult. Figure 6.43c shows the LORE results. As can be seen, the position and level of the source are successfully recovered. In this case, the correlation coefficient is equal to 1. The computational time required was 62 seconds. The increase in time, when compared to the single monopole in 2D, is mostly related to the size and the time required to read in to memory the matrix of *cpsf*.

Figure 6.44 shows the case for a monopole in a plane closer to the array, i.e. 32". Note also that it is in the boundary of the grid. Also in this case the level and position are recovered correctly and the correlation coefficient is equal to 1.

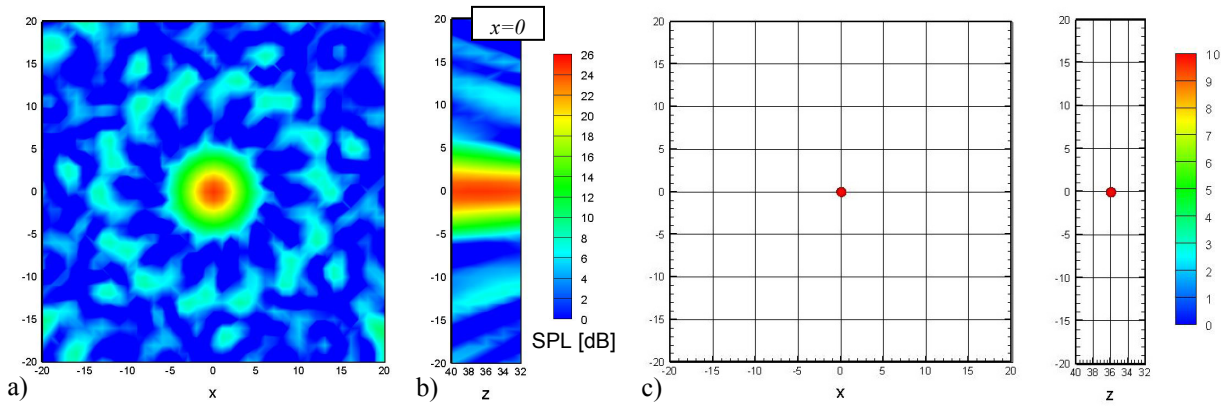

Figure 6.43: Simulation of a 15 kHz monopole at (0", 0", 36") using a 3D scanning grid.
a) Beamforming in a plane 36" parallel to the array and b) side view, and c) LORE results.

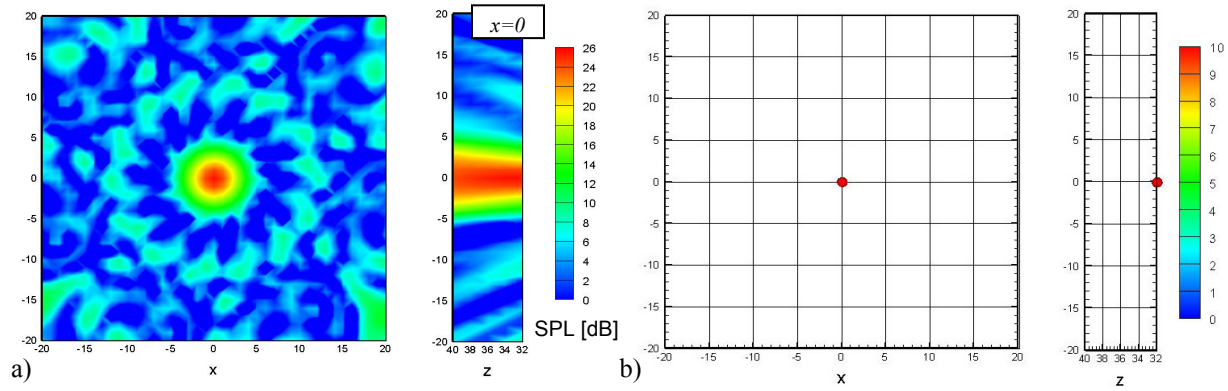

Figure 6.44: Simulation of a 15 kHz monopole at (0", 0", 32") using a 3D scanning grid.
a) Beamforming in a plane 32" parallel to the array and side view, and b) LORE results.

As is well known, the depth resolution of an array is significantly poor. Thus, the mainlobe is usually many times bigger in the Z-direction than in the XY-plane. The following cases were intended to determine the accuracy of LORE in the direction normal to the array, i.e. ability to distinguish different sources in the Z-direction.

The first case consisted of 2 monopole sources in the same line of propagation, i.e. same X and Y coordinates but different Z. The beamforming map for a plane 36" from the array is shown in Figure 6.45a. Note that the beamforming in a plane perpendicular to the previous one, shown in Figure 6.45b, does not provide information about the position or number of sources in the z-direction. Figure 6.45c shows that LORE is able to distinguish and recover the position and level of both sources. Furthermore, the correlation coefficient is equal to 1.

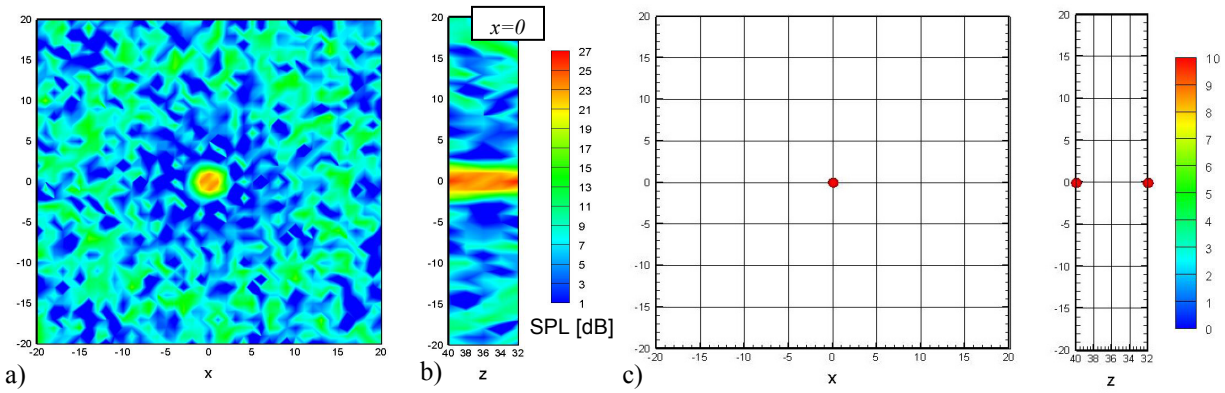

Figure 6.45: Simulation of two 25 kHz sources at (0", 0", 32") and (0", 0", 40") using a 3D scanning grid. a) Beamforming in a plane 36" parallel to the array and side view, and b) LORE results.

However, for closer sources or moving down in frequency the results get inaccurate in terms of position. In this sense, the case of 2 sources at 10 kHz and 4" apart is shown in Figure 6.46. As can be seen, the post-processing only renders a single source in between the actual ones with a level of 20. Thus, the results loose accuracy in the Z-direction much faster than in the 2D cases presented before but the total levels are still correctly recovered. However, the correlation coefficient in this case is 0.9806, indicating accurate results from LORE. Again, this is related to the poor resolution of the array in the direction perpendicular to it. This is not a problem "induced" by LORE but mostly resulting from the beamforming processing. This issue could be avoided by designing and using an array with a better resolution for all the frequencies of interest, i.e. smaller beamwidth.

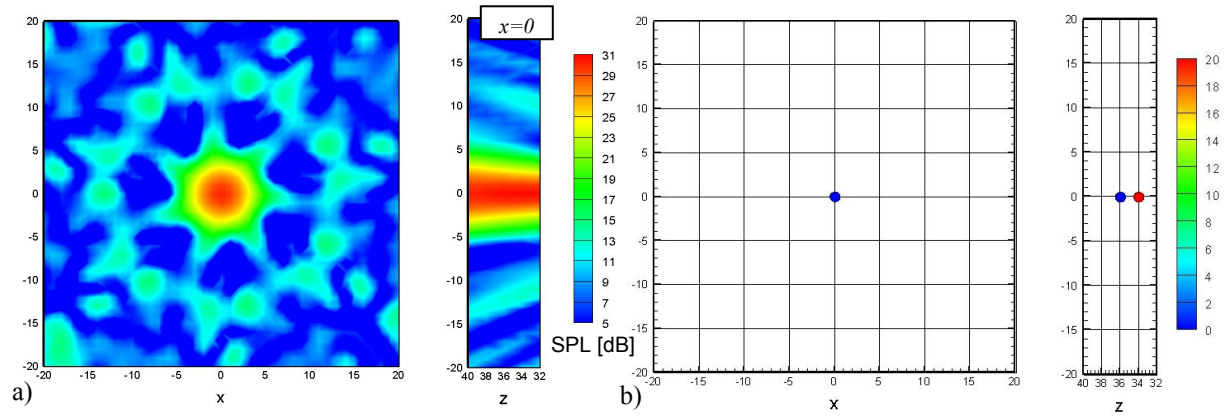

Figure 6.46: Simulation of two 10 kHz sources at (0", 0", 32") and (0", 0", 36") using a 3D scanning grid. a) Beamforming in a plane 36" parallel to the array and side view, and b) LORE results.

The case of multiple sources scattered in space is now analyzed. To this end, 4 sources with the same amplitude were numerically simulated. All sources had a different position in the Z-direction. Figure 6.47 shows 3 different beamforming maps corresponding to planes parallel to the array at 32, 36, and 40 inches respectively. As can be seen, 3 sources are clearly visible. However, the source that was farther away from the array is not "visible".

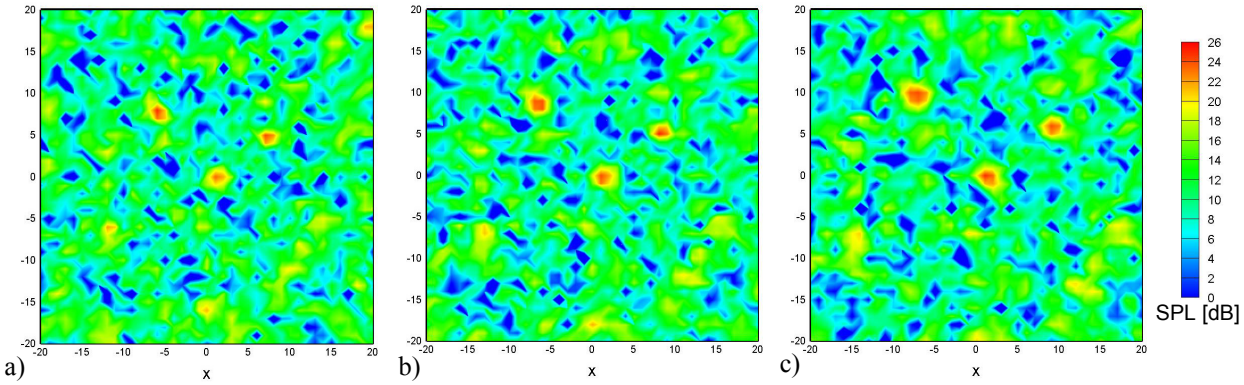

Figure 6.47: Multiple incoherent sources at 25 kHz scattered in space (3D).
Beamforming in a plane parallel to the array at a) 32", b) 36", and c) 40".

Applying the LORE technique, the sources level and position are successfully recovered. These results are shown in Figure 6.48. Note that when solving for the source amplitude, all the sources show the same value.

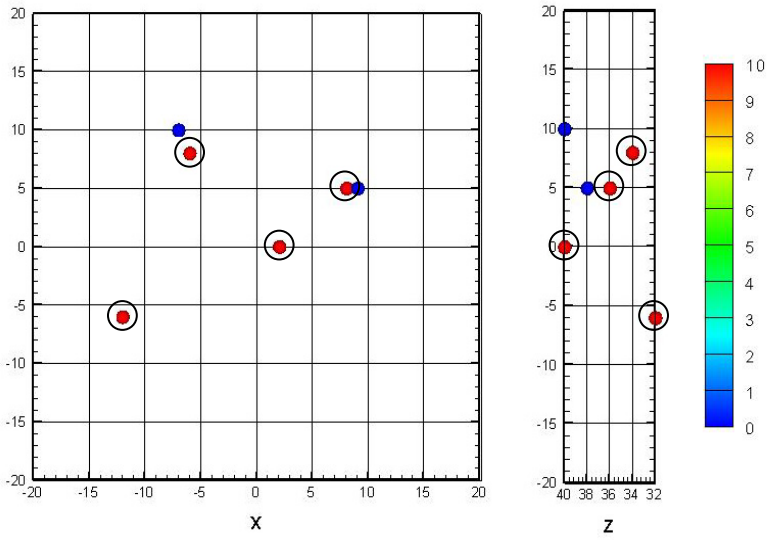

Figure 6.48: LORE results for multiple incoherent sources at 25 kHz scattered in space (3D).

If solving for the level perceived by the array this would not be true. If the levels perceived by the array are desired, the amplitude rendered from LORE should be divided by the distance to the center of the array. This is true since the propagation model used only accounts for distance in terms of decaying. The number of artificial sources in this case was 20, with a maximum of 1.5e-4, and adding to 7e-4. In this case, the correlation coefficient was equal to 1. The time required for the post-processing was about 130 seconds.

In order to follow the same methodology developed before for 2D cases, a lower frequency is analyzed. In this sense, Figure 6.49 shows the beamforming maps for the same source distribution than the previous case but at a frequency of 15 kHz. Note that in this case, given the resolution of the array, 4 sources can be identified in these maps. However, the levels and actual positions are not clearly defined. Furthermore, the analysis of the beamforming maps would lead us to the wrong conclusion that all the sources have different levels.

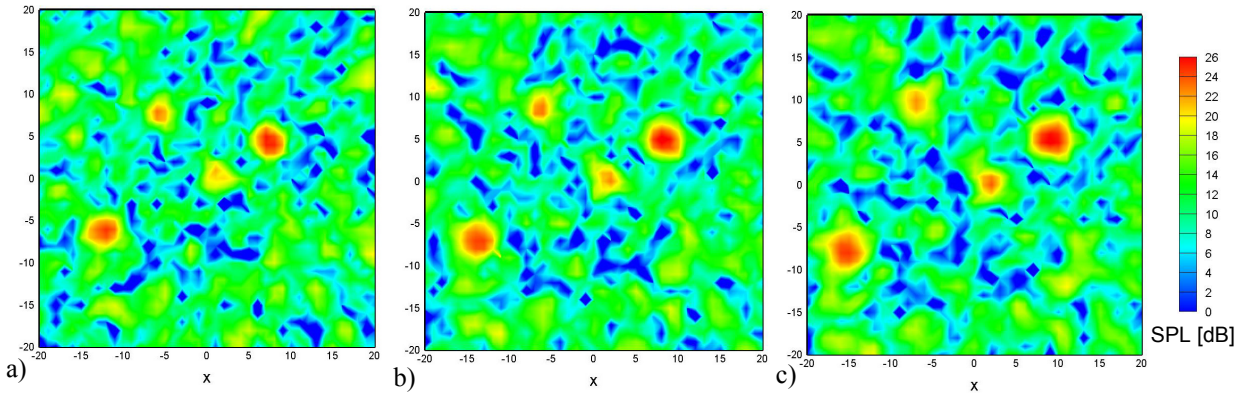

Figure 6.49: Multiple incoherent sources at 15 kHz scattered in space (3D). Beamforming in a plane parallel to the array at a) 32", b) 36", and c) 40".

Figure 6.50 shows the results of the post-processing. Again, the levels and positions are recovered successfully and the correlation coefficient is equal to 1. Note that, as in the previous case, the artificial sources have levels significantly lower than the actual sources. In this case, there were 14 artificial sources with a maximum of 1.6e-4 (96 dB difference in power) and a total of 7e-4. The computational time was only 165 seconds.

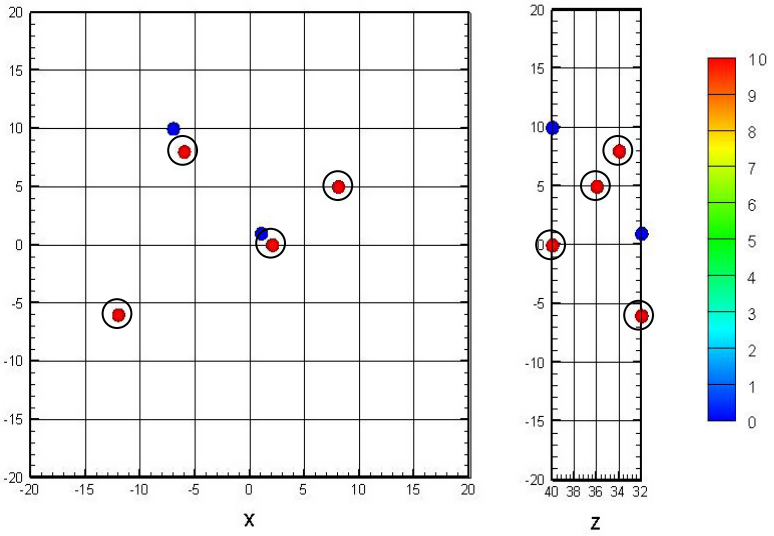

Figure 6.50: LORE results for multiple incoherent sources at 15 kHz scattered in space (3D).

The beamforming for the same case at 10 kHz is presented in Figure 6.51. As in the previous case, it is not possible to clearly identify the levels and position. At this frequency, the LORE results start to show problems, evidenced by a correlation factor of 0.88. The major problem is that the position of the sources in the z-direction is not correctly recovered, as shown in Figure 6.52. It was found that the solution to the approximated problem does not provide a good set of starting points for the optimization. i.e. the solution to the "linear" approximated problem is not as "good" as in the 2D cases.

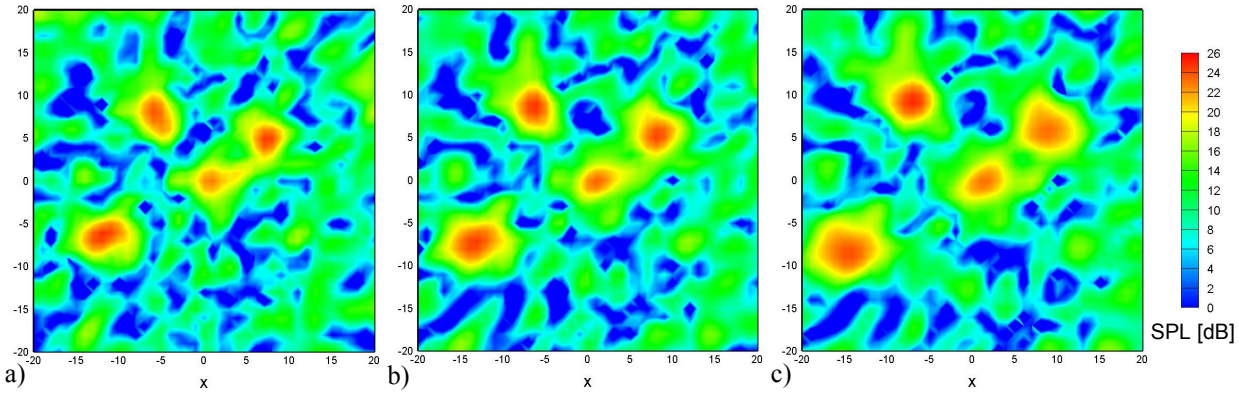

Figure 6.51: Multiple incoherent sources at 10 kHz scattered in space (3D). Beamforming in a plane parallel to the array at a) 32", b) 36", and c) 40".

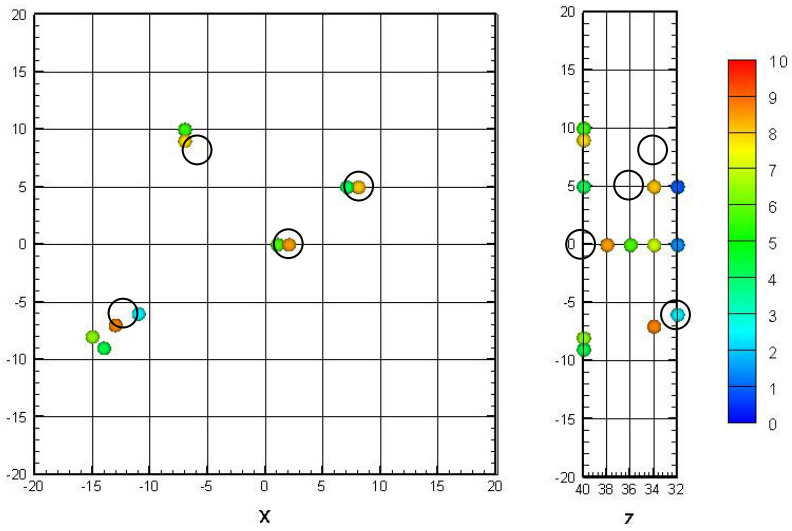

Figure 6.52: LORE results for multiple incoherent sources at 10 kHz scattered in space (3D).

Some steps were taken to try to solve this problem. In this sense, a different process was used in step 1. Thus, instead of solving the NNLS problem for the full 3D grid, the approximated solution was found for every z-plane. In this way, it is ensured that all potential grid points in each plane are included. However, the number of points to optimize is significantly increased. It was found that using this procedure the results also breakdown around the same frequency. This is mostly related with the LORE resolution in the z-direction for 2 sources as introduced before. Thus, it is not possible to determine which solution is the actual one when many sources are present in the same line of propagation. In this case, "introducing coherent sources" are introduced. Thus two sources in the same propagation direction are most likely to cancel each other or "interact". This results in total levels that are much higher than the actual sources.

It is expected that using a bigger grid in the z-direction the results would be better. This should be true since the whole mainlobe would be included for all sources in that direction. However, the computational resources needed for such processing are highly increased.

6.6 Experimental Results

It was shown in previous sections that LORE is able to successfully recover the position and actual levels of the sources in the scanning field for a wide range of frequencies. This ability is related to the accuracy of the modeling proposed in this work. However, when dealing with

experimental data, the signals are usually contaminated with noise. At the same time, this contaminating noise can be uncorrelated or "somewhat" correlated over the array. In real life, the fact that the array is not "perfect" also needs to be taken into account. Thus, since phase and positioning errors of the microphones are present, the "experimental" point spread function will depend on the calibration, i.e. response for a single source.

These factors will influence the accuracy of the results. Keep in mind that LORE relates the experimental beamforming output to the theoretical response of the array. The quality of the "expected" results from LORE can be assessed by analyzing the case of a single source in the anechoic chamber. Thus, comparing the beamforming map to the numerical simulation of a source in the same position the quality of the LORE results can be estimated. As shown before, the reconstruction from the LORE processing can also be used to determine the quality of the results.

To test the capabilities of LORE with experimental data, a series of tests were specifically conducted. The test consisted of placing multiple speakers in the VT anechoic chamber and measure using a 63-element equal aperture multi-arm spiral array [72]. The speakers were driven with different signal generators. Equipment to adjust the relative phase was also used. The array output was not calibrated in level. The test setup is shown in Figure 6.53.

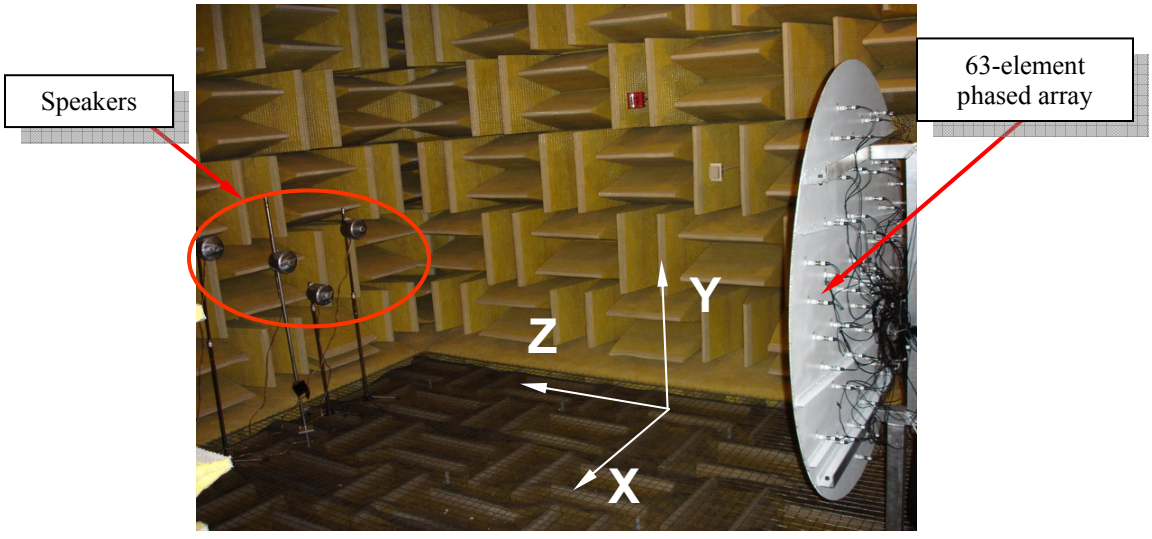

Figure 6.53: Test setup for testing LORE capabilities.

6.6.1. Experimental Results in 2D

As mentioned before, the case of a single speaker will be used to draw many conclusions about the capabilities of LORE in real life cases. For ease of visualization and interpretation, the pictures showing the configuration of the speakers is "mirrored". This is done to plot the results in the XY plane in the form indicated in Figure 6.53.

Figure 6.54a shows the configuration for a single speaker. In this case, as well in the next examples, the speakers that are ON are indicated in green and the ones that are OFF in red. Figure 6.54b shows the beamforming map at 2.2 kHz.

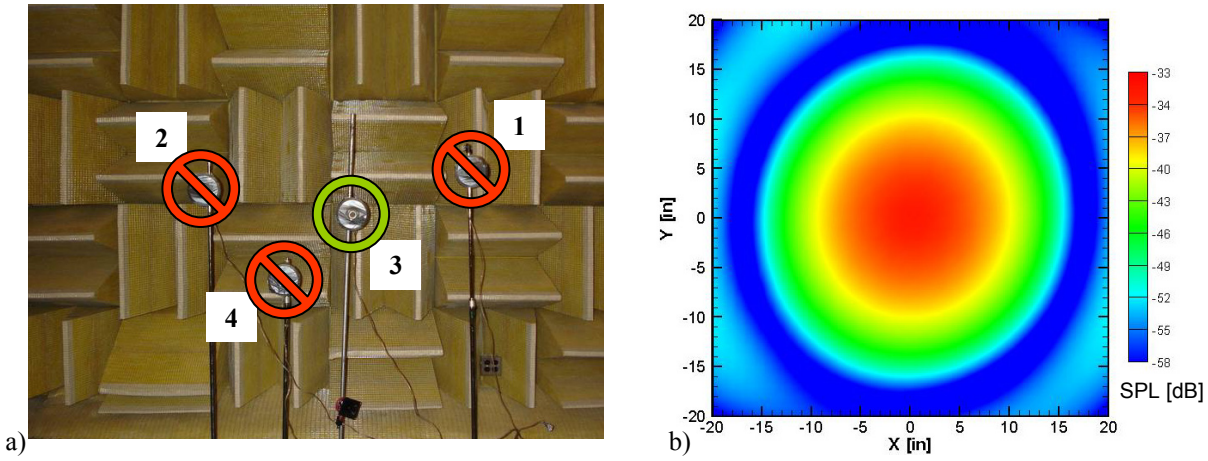

Figure 6.54: a) Speakers setup and b) beamforming map at 2.2 kHz for a single source.

Figure 6.55a shows the LORE results for a grid 20" by 20" with a grid resolution of 1". As can be seen, the method is able to recover a cluster of 3 sources at the center of the grid with a level of 4.54e-2. As seen in simulations, this kind of result would suggest that the source is not exactly at the center of the grid. Note also that there are "artificial" sources in the corners of the grid. The maximum value of such points is 6.6e-3 (about 17 dB below the speaker power), totaling 1.94e-2. The correlation coefficient in this case was 0.911, indicating a "poor" array calibration or that the actual source position is not in a grid point. The time for this computation was just 6.1 seconds.

The effect of using a "finer" grid is analyzed in Figure 6.55b. It is also used to establish the location of the source more accurately. In this case, the grid resolution is 0.5" and a detail of the center of the grid is shown. Note that the total level of the source is recovered in very good

agreement compared to the 1" grid resolution case, i.e. 4.53e-2. In this case, the artificial sources in the corners also appeared, with a maximum level of 6.7e-3 and a total of 1.94e-2. The correlation coefficient in this case was 0.916, indicating that the reason for a "low" correlation is a "poor" array calibration rather than errors induced by "missing" the actual source position. Since a bigger number of grid points is being used, the computational time is increased significantly, i.e. 92 seconds. In both cases, the number of parameters to optimize was 7.

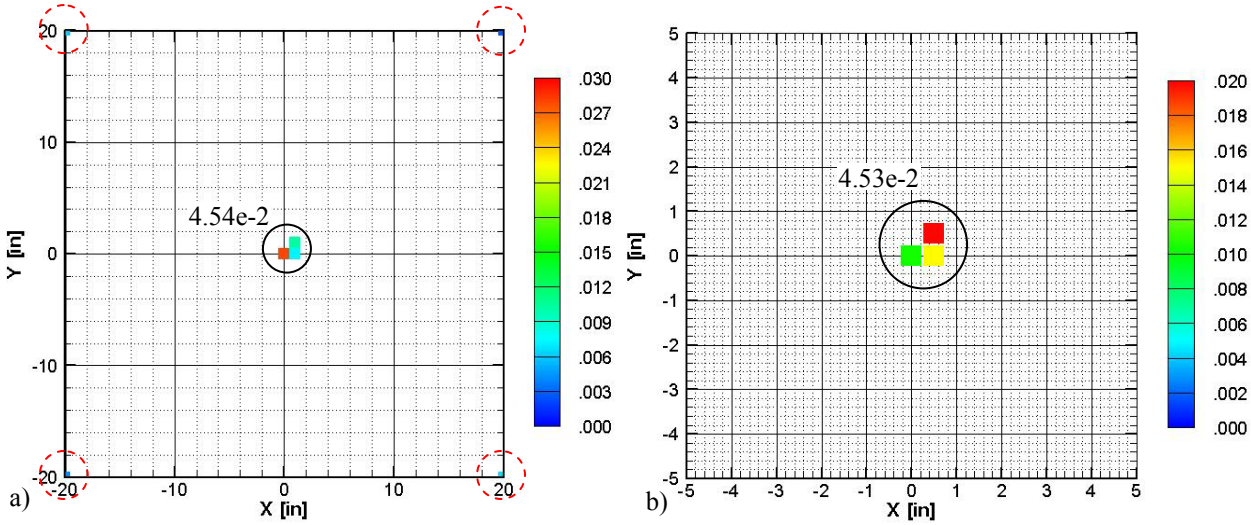

Figure 6.55: LORE results for a single speaker at 2.2 kHz using a 40" by 40" grid with a) 1" resolution, and b) 1/2" resolution (detail).

From the previous results it can be concluded that the levels are correctly recovered regardless of grid resolution. And more importantly, there is a "big compromise" between computational time and accuracy of the recovered sources position. The computational resources required are also increased significantly. This is related to the need to allocate in memory the matrix with the *cpsf*.

It is also interesting to see the effect of a bigger scanning grid. In this sense, Figure 6.56a shows the beamforming map for a 40" by 40" grid with a resolution of 1". As can be seen, the sidelobes start to appear in the map. The LORE results are presented in Figure 6.56b. Note that this is a detail of the full grid. This will allow a direct comparison with the case of a smaller grid presented before. Besides, there are no artificial sources outside this area. The recovered level of the source is in good agreement with the previous cases, i.e. about 0.17 dB. Note also that there are 2 artificial sources with a maximum of 7.3e-3 and a total of 1.1e-2, i.e. 12 dB below the

power of the speaker source. The reason for these sources will be explained next. But note that in the case of the smaller grid, Figure 6.55a, the artificial sources were in the corners of the grid. In this case, the correlation coefficient surprisingly dropped to 0.7431, indicating that the results should not be considered accurate.

The time required for this computation was 276.5 seconds. This increase in time is related to the increase in grid size and to the number of values to optimize. In this case, there were 20 nonzero values from NNLS.

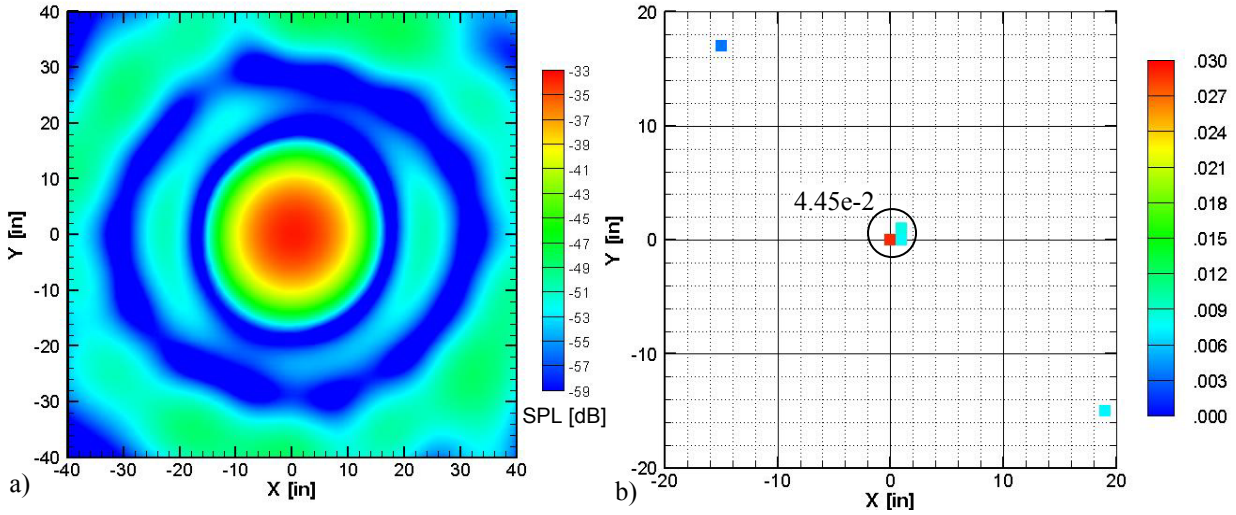

Figure 6.56: Single speaker at 2.2 kHz using a 80" by 80" grid with 1" resolution. a) Beamforming and b) LORE results (detail).

Like in the case of the numerical simulations, it is very interesting to compare the actual beamforming output with the reconstruction from the LORE results. When dealing with measured data, it is also interesting to compare the previous plots with the theoretical PSF for a single source with the same level; thus, neglecting the artificial sources. Figure 6.57 shows the comparison between the three cases. As can be seen comparing cases a and b, the effect of the artificial sources is to account for the "extra sidelobes" that appear around the mainlobe. The reason for these sidelobes in the beamforming output might be related to a "poor" calibration of the array at this particular frequency. As shown in Figure 6.57c, such sidelobes should not be present for a single source. Note also that the outer sidelobe structure is in relatively good agreement in all cases. It was interesting to find out that assuming coherence of the sources the correlation coefficient was 0.95, thus the reconstructed beamforming map looked more like the actual one of Figure 6.57a.

These results suggest that the conventional calibration procedure could be modified such that the array output matches the theoretical *psf* of the array in order to obtain more accurate results.

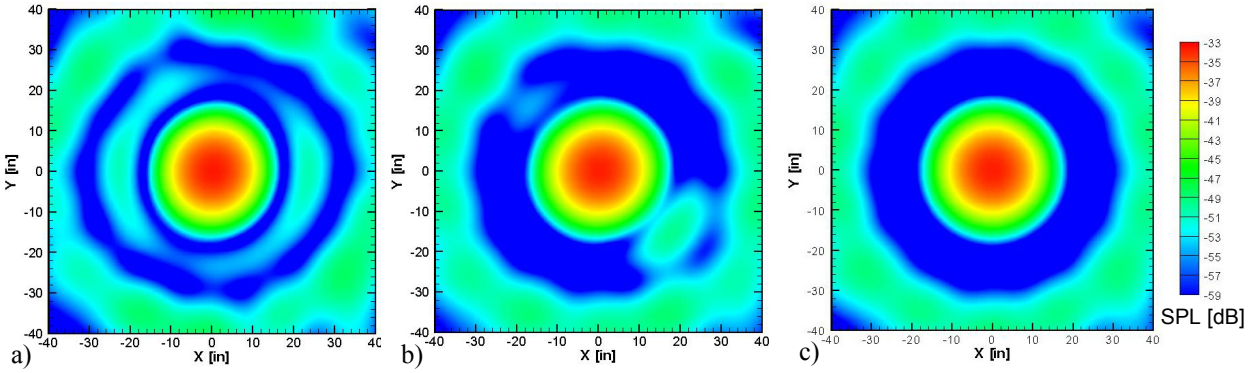

Figure 6.57: a) Actual beamforming map, b) reconstruction from LORE results, and c) PSF at 2.2 kHz.

It is also interesting to analyze the effect of applying the LORE technique to data beamformed with diagonal removal (DR). It is known that the modeling does not account for DR, but will be used to draw some conclusions. Figure 6.58a shows the beamforming for the same case of a single speaker using the 40" by 40" grid. As can be seen, due to the DR processing, the sidelobes are significantly reduced. Since the proposed technique is trying to recognize "patterns" in the beamformed data related to sidelobes levels and location, some differences are expected to show up in the results. Thus, the mainlobe size and levels will be almost the same, but the sidelobes structure will be completely different. A detailed view of the LORE result is shown in Figure 6.58b. In this case, the processing rendered only a cluster of 3 nonzero values at the center of the grid, i.e. no artificial sources. The total level recovered for the speaker is 4.32e-2, slightly smaller than the values recovered in the previous cases (about 0.25 dB in power). This is related to the fact that when diagonal removal is used, power is being "removed" from the map. In this case, the correlation coefficient was 0.933. The time required for this computation was only 45.5 seconds.

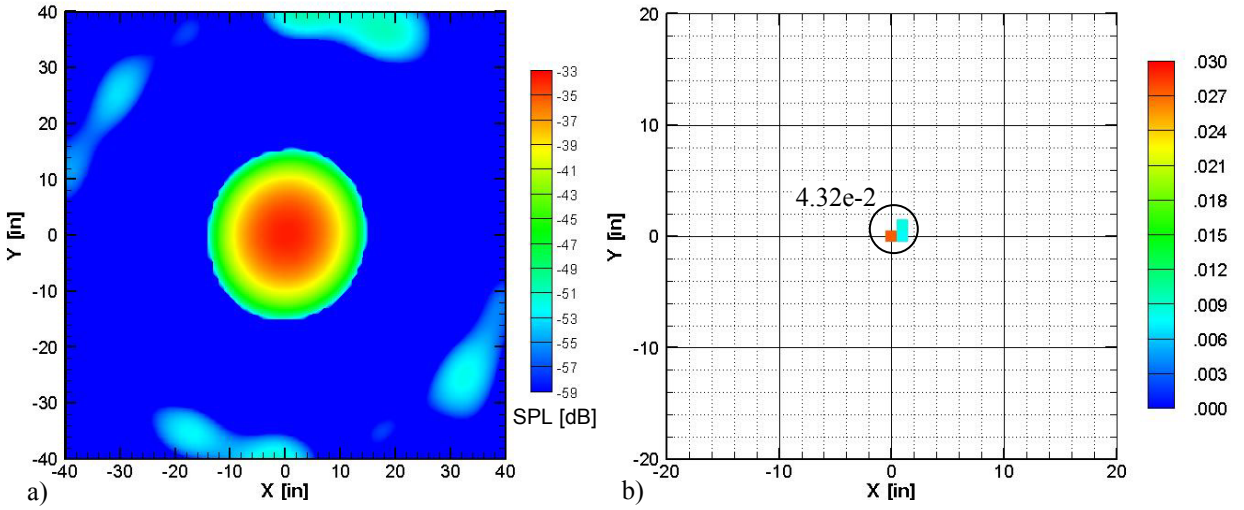

Figure 6.58: Results for a single speaker using DR beamforming. a) Beamforming at 2.2 kHz and b) LORE results.

The second test used 2 speakers driven with uncorrelated random signals, i.e. using different signal generators. The speaker's configuration is shown in Figure 6.59a. The output of both speakers was calibrated to about the same level using the device shown in Figure 6.59b, a microphone and a spectrum analyzer. Figure 6.60a shows the beamforming output. In this case, it is clear from the map that there are 2 noise sources. However, actual levels are not clear.

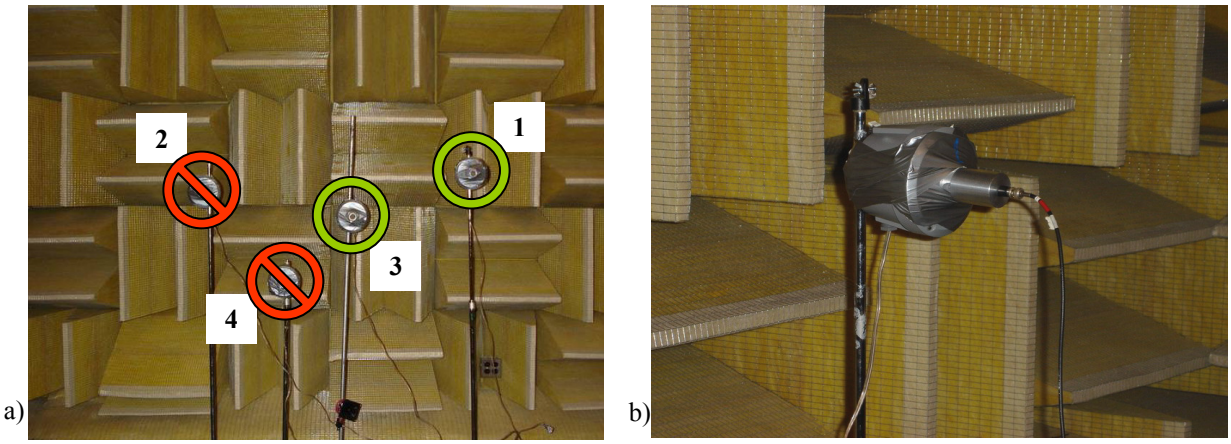

Figure 6.59: a) Speakers, and b) calibration setup for the case of 2 incoherent sources.

LORE results are presented in Figure 6.60b. As can be seen, the positions and levels of the sources are clearly recovered. Note also that there is very good agreement in terms of relative amplitude, i.e. the difference in SPL is less than 0.1 dB. Out of 9 nonzero values, 3 were related to artificial sources. The maximum level of them being 1.27e-2, almost 14 dB below the power

of the main sources, and adding up to 2.04e-2. In this case, the correlation coefficient was also equal to 0.93. The computational time was only 33.2 seconds.

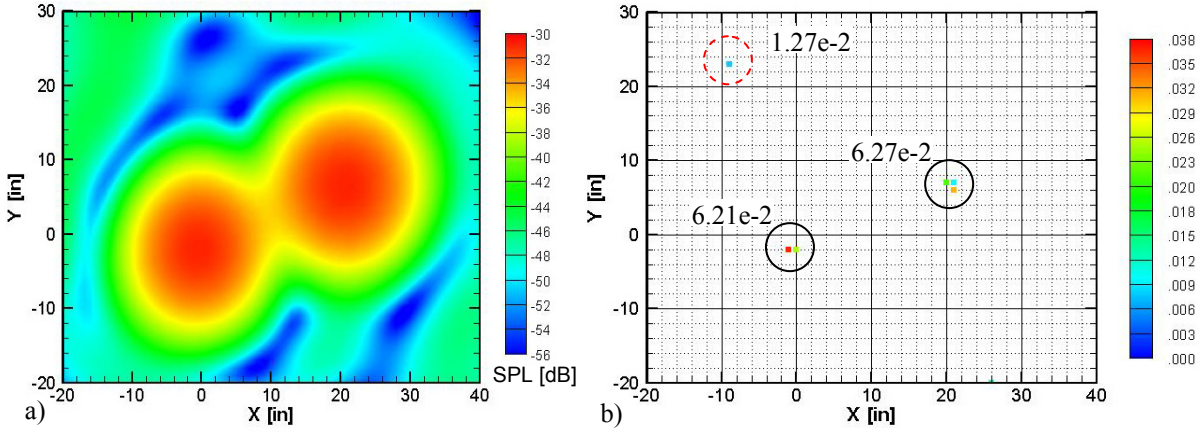

Figure 6.60: Results for 2 incoherent speakers. a) Beamforming map at 2.2 kHz, and b) LORE results.

The more complex case of 4 sources in the same plane parallel to the array is analyzed next. In this configuration, speakers 1 and 4 were driven with one signal generator, and speakers 2 and 3 with a second signal generator. However, in both cases the relative phase was adjusted using a phase shifter and measured with calibration, i.e. some sources are coherent.

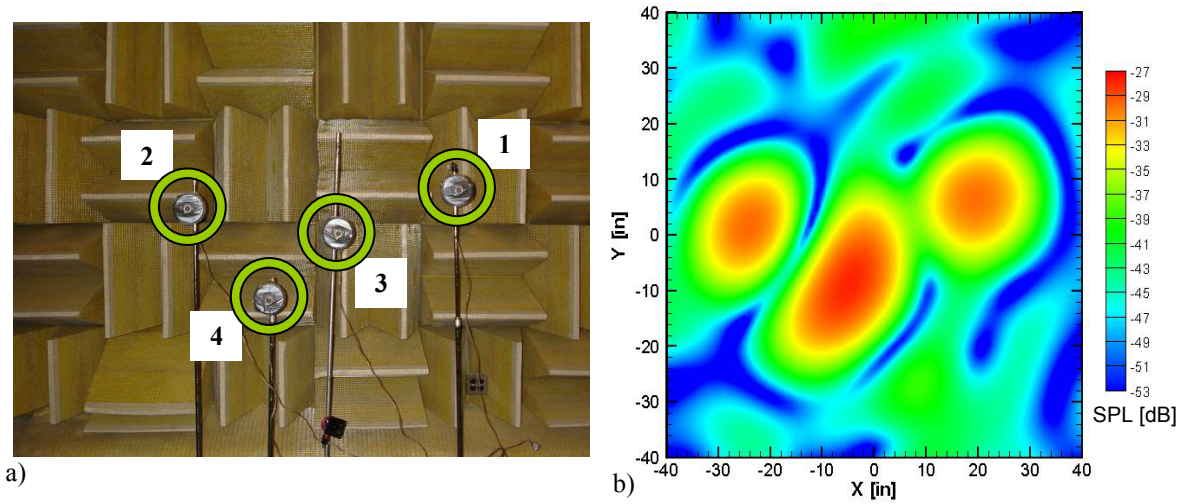

Figure 6.61: a) Speakers setup, and b) beamforming map at 2.2 kHz for multiple sources.

The post-processing results assuming incoherence are shown in Figure 6.62a. As can be seen, LORE can accurately recover the actual position of the sources. However, a correlation

coefficient of 0.75 indicates a lack of accuracy in the results. Assuming coherence, the actual positions of the sources are also recovered as shown in Figure 6.62b. In this case, the correlation coefficient is 0.9233, indicating an accurate solution. However, the levels are not in agreement with the "expected" values, i.e. the level of speaker 2 should be higher and speaker 3 should be the lowest. This difference might be related to an error in the calibration of the speakers output or a difference in the response of the speakers, i.e. the speakers were calibrated to the same level at 5 kHz, then driven with white noise and beamformed at 2.2 kHz. The post-processing time for these cases was 297 and 550 seconds respectively. In both cases, the number of "artificial" sources was zero.

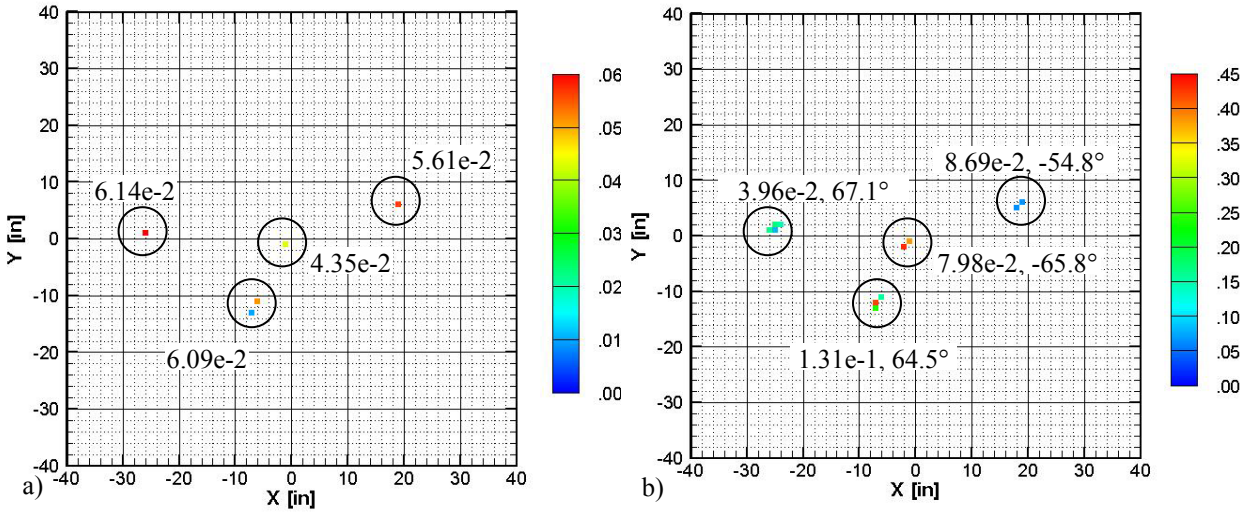

Figure 6.62: LORE results for 4 speakers assuming a) incoherent and b) coherent sources.

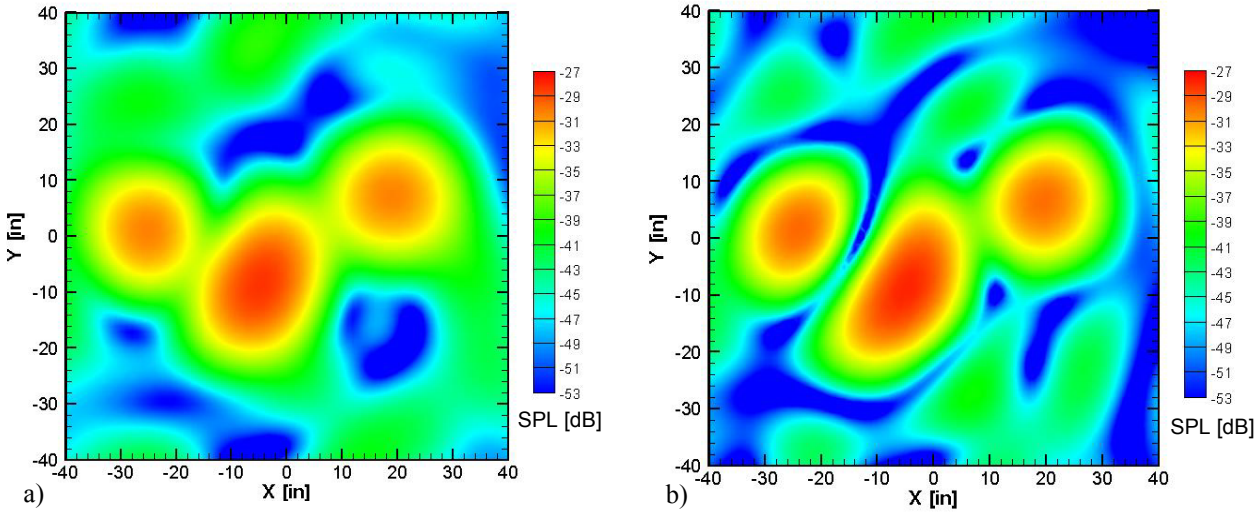

Figure 6.63: Reconstruction from LORE results for 4 speakers assuming a) incoherent and b) coherent sources.

The reconstruction for both assumptions is shown in Figure 6.63. As can be seen, the reconstruction from the coherence assumption is in very good agreement with the actual beamforming map, while the reconstruction from the incoherent results is "poor". This suggests that the sources are coherent, in agreement to the experimental setup and the correlation coefficient of 0.9233.

6.6.2. Experimental Results in 3D

Three-dimensional cases were also studied for simple configurations. The test setup consisted of staggering 4 speakers inside the chamber as shown in Figure 6.64a. In this picture, the case of 2 speakers ON is shown and will be presented first. Figure 6.64b shows the beamforming with the 3 dB down in 3D contour plot and the full contour map at a distance of 140". The same results for planes at 110" and 76" are shown in Figure 6.65b and c respectively. As can be seen in this maps, there is not much that could be said about the actual position and levels of the sources besides that one of them seems to be closer to the array.

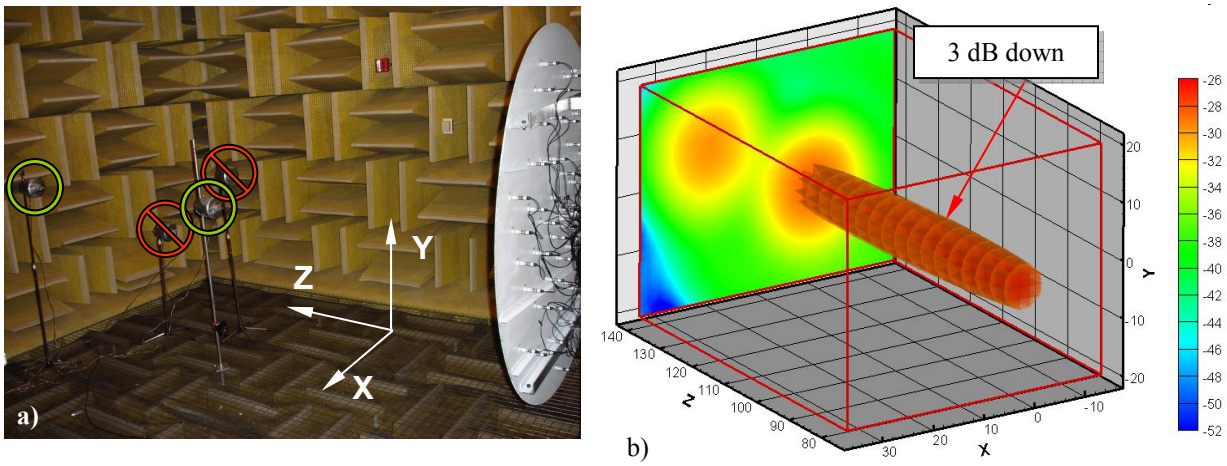

Figure 6.64: a) Test setup for 3D tests, and b) beamforming map at 2.2 kHz showing 3 dB down and levels at a plane 140" from the array

However, as seen in Figure 6.66, LORE is capable of recovering the position and levels of the actual sources. Note that there is only one artificial source with a level of 2.27e-2, thus, 7 dB below the power of the smallest source. The reason for this source might be related to the "coherence" introduced by its relative position to the source closer to the array. This "issue" was addressed in the numerical simulations for 3D cases. The reminding artificial sources (6) had

levels below 1e-6. Note also that the loudest source was closer to the array and its power was almost 6 dB higher than the one further away and LORE is still able to "find" it.

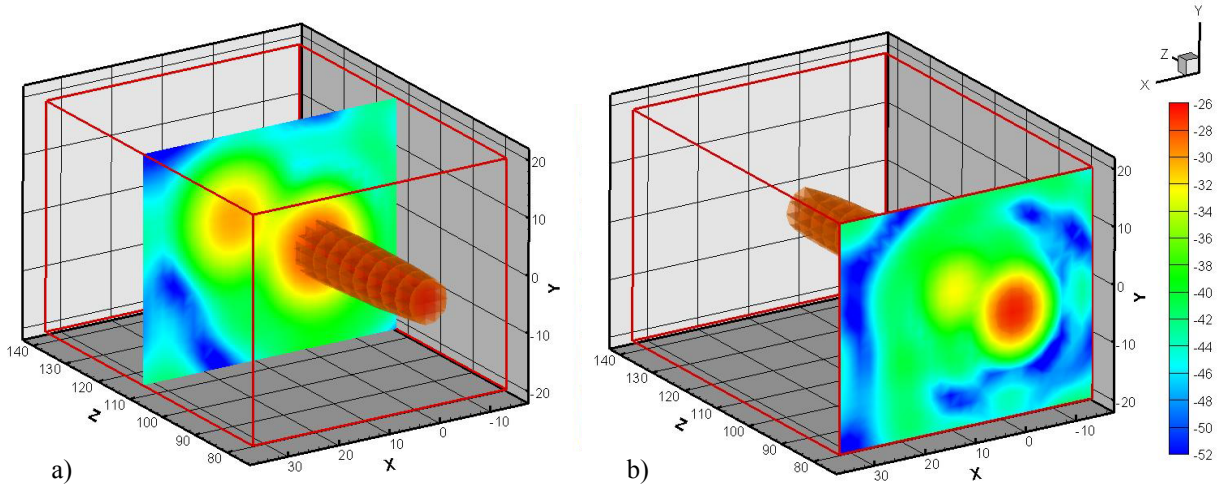

Figure 6.65: Beamforming at 2.2 kHz showing 3 dB down and levels at a plane a) 110" and b) 76" from the array

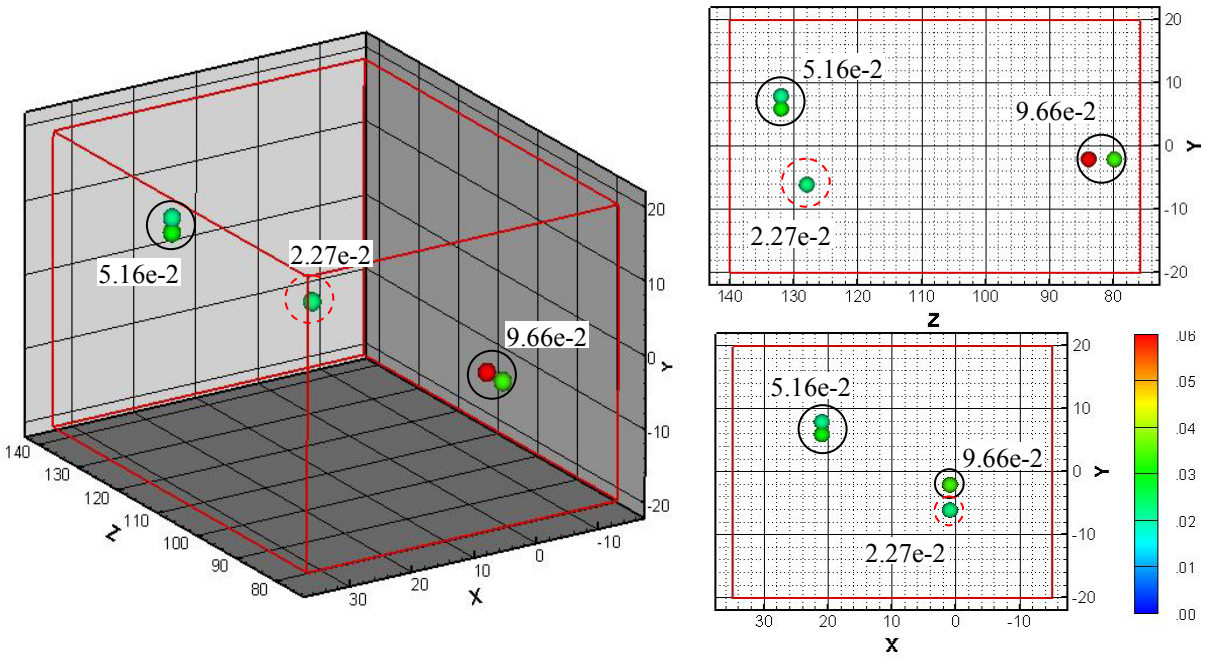

Figure 6.66: LORE results for 2 speakers in a 3D configuration

When the number of sources is increased to 4, the results are not satisfactory. In this sense, the same "errors" that appeared in the simulations at 10 kHz are obtained. Thus, the results are not satisfactory. As mentioned before, this is related to the poor depth resolution of the array at low frequencies and a "poor" calibration of the array at mid to high frequencies.

The application of LORE to multiple sources in a 3D scanning grid should be studied more rigorously but is beyond the scope of this work.

6.7 Application of LORE to Airfoil Noise

Experimental data was available for a NACA 0012 profile tested at the VT Stability Tunnel [72]. In this case, the walls of the tunnel had an acoustic treatment. The setup is shown in Figure 6.67. The 63-element phased array used in the anechoic chamber test was utilized. A schematic of the setup, including the relative position of the array with respect to the airfoil is shown in Figure 6.68.

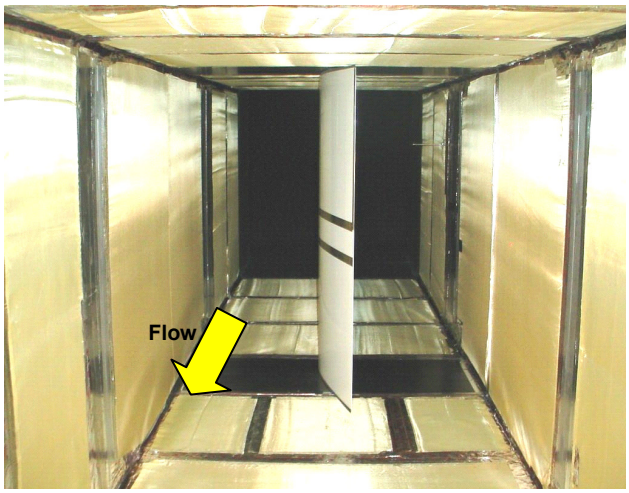

Figure 6.67: Airfoil test setup in the VT Stability Tunnel.

The results from this test will be presented with and without DR processing. Since the airfoil noise levels are too low, the DR is essential to render good results. The DR is not modeled in LORE; however, it was shown before that "useful" results can still be obtained. Thus, reconstruction showed that the mainlobes and their shape are recovered "correctly".

The case of conventional beamforming without DR is presented in Figure 6.69a. In this case, note that the scale only shows 12 dB below the peak value. This was done in order to improve visualization since background noise was significant. Figure 6.69b shows the result of the post-processing. As can be seen, a clear line of sources is found in the trailing edge of the airfoil. The total level in the trailing edge area is 0.375. Note that many artificial sources are present as a

consequence of the contamination in the map by the background noise totaling 0.266, about the same power than the airfoil noise. However, they are very scattered in comparison to the ones in the trailing edge. The computational time in this case was 44584 seconds (approx. 12.4 hours).

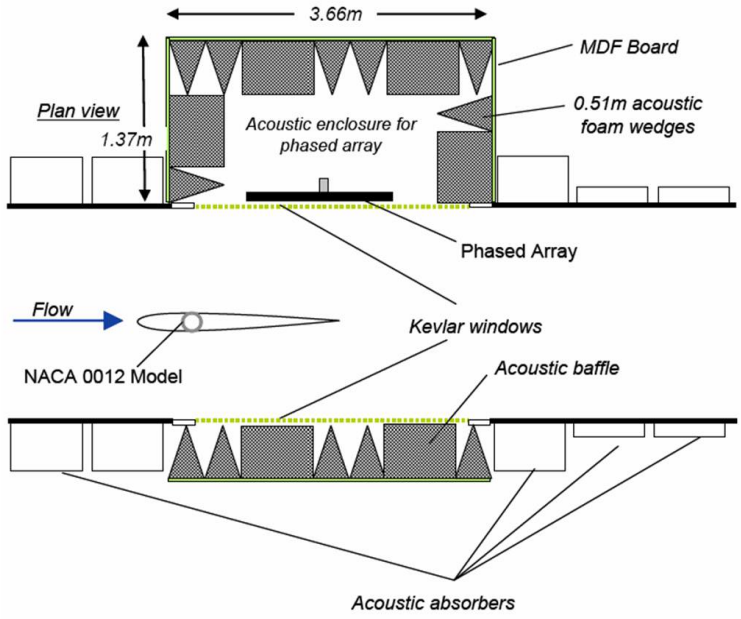

Figure 6.68: Schematic showing the relative position of the phased array and the airfoil in the test section [72]

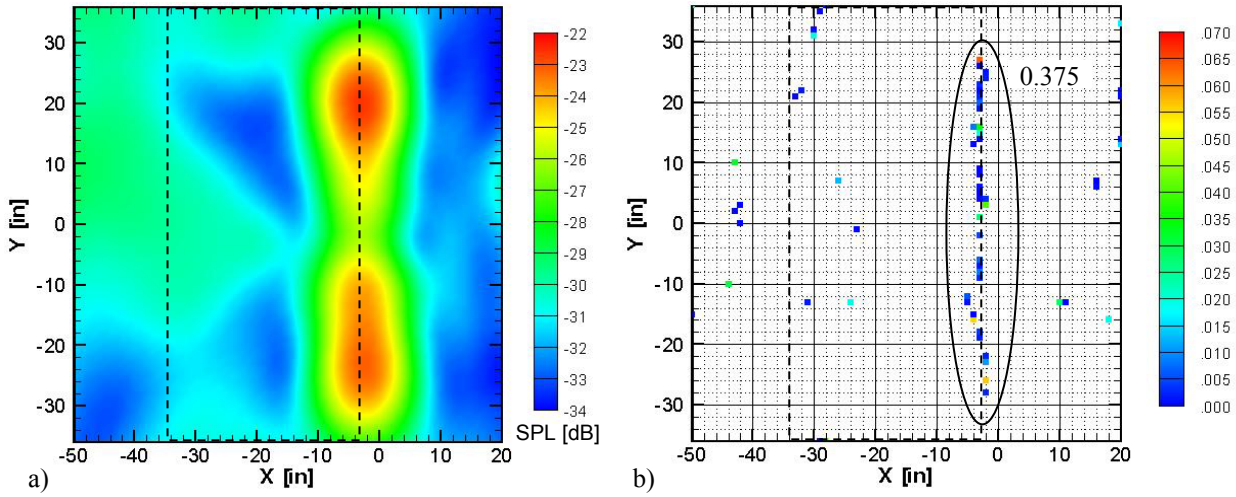

Figure 6.69: Airfoil noise a) beamforming at 1.2 kHz and b) LORE results assuming incoherent sources.

As mentioned before, the comparison between the actual beamforming and the reconstructed map may give us some insight into the accuracy of the results. In this sense, Figure 6.70 shows

the beamforming and the reconstruction from the LORE results. As can be seen, the reconstruction fairly describes the source distribution. However, the sidelobes in the map are not recovered in detail. This suggests that the background noise level is significant and/or the incoherence assumption was erroneous, in agreement with a relatively poor correlation coefficient of 0.88. In the case presented here, both statements are true since it is well known that the trailing edge sources are coherent [47]. These reasons also explain the increase in computational time.

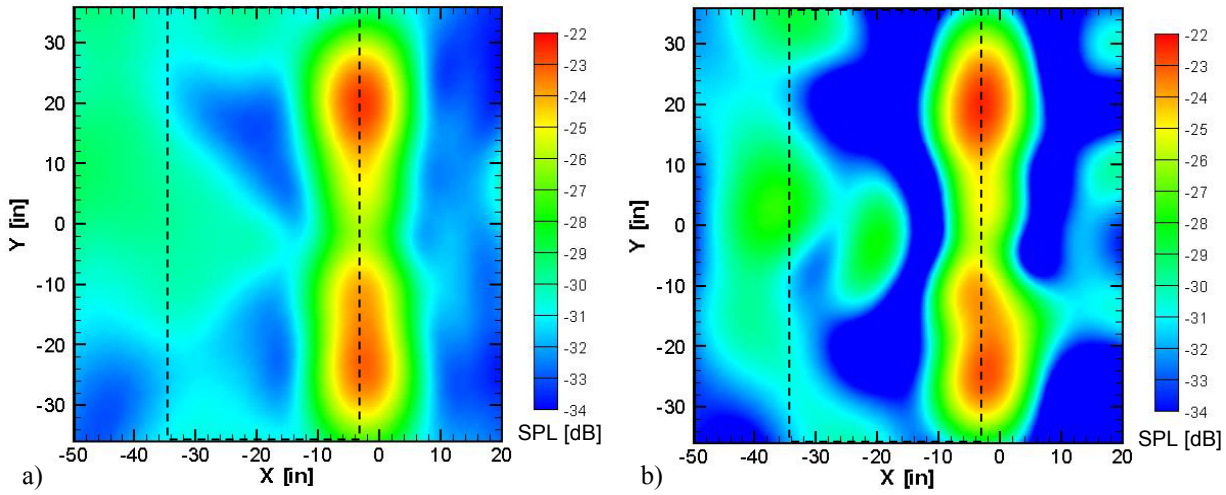

Figure 6.70: Airfoil noise a) beamforming at 1.2 kHz and b) reconstruction from LORE assuming incoherent sources.

Figure 6.71 shows the results assuming coherence. In this case the levels recovered in the trailing edge are higher, as expected. The time required for the post-processing was 18194.1 seconds (approx. 5 hours). As can be seen, the processing took less time than for the case of incoherent sources, even when the number of parameters to optimize was doubled. This is a trend that was found in cases where the sources are incorrectly assumed to be incoherent. In such cases, the solution is being "forced" to be incoherent and the optimization can not find a "clear" solution.

Reconstruction from the LORE results with the coherence assumptions shows very good agreement when compared to the actual beamforming map, as shown in Figure 6.72. This also suggests that the coherence length is nonzero, as expected. The correlation coefficient for this case was 0.9966, in agreement with the previous conclusions about accuracy.

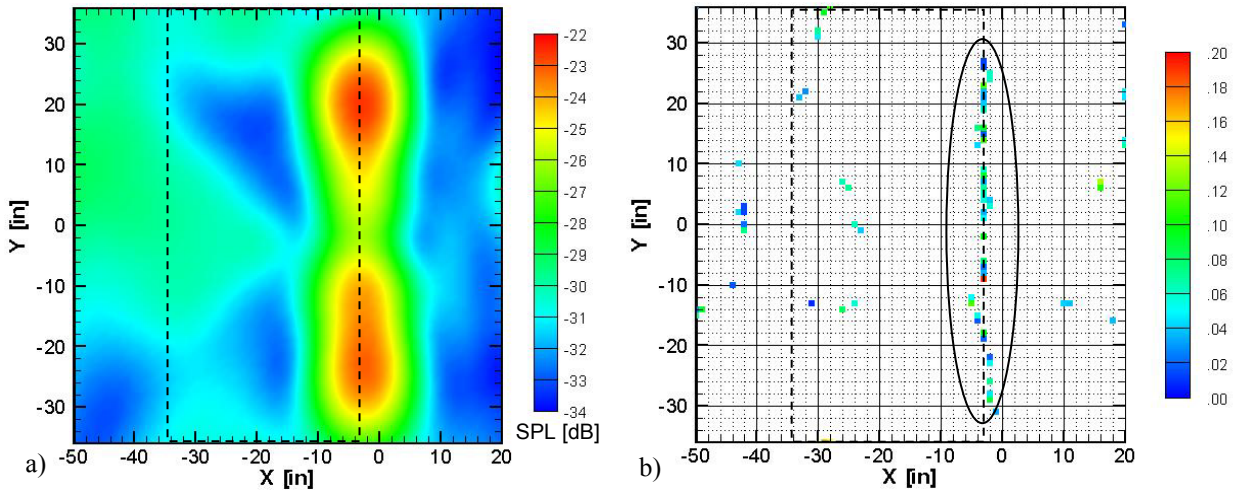

Figure 6.71: Airfoil noise a) beamforming at 1.2 kHz and b) LORE results assuming coherent sources.

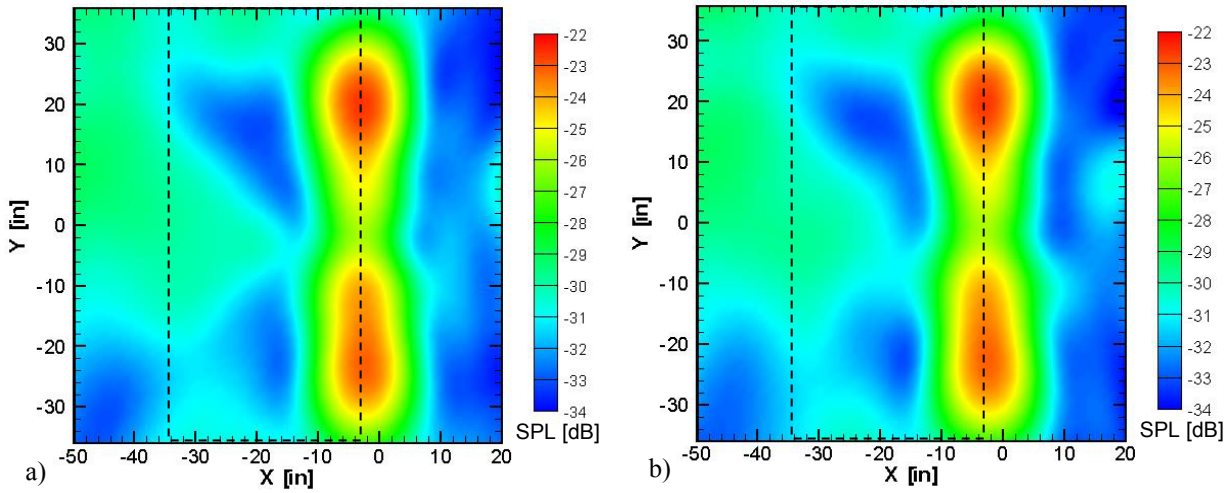

Figure 6.72: Airfoil noise a) beamforming at 1.2 kHz and b) reconstruction from LORE assuming coherent sources.

The beamforming with DR is shown in Figure 6.73a. As can be seen, all the sidelobes are removed almost completely within 12 dB from the maximum level in the map. The LORE processing rendered 13 nonzero values in this case. As seen in Figure 6.73b, 12 of them were in the trailing edge of the airfoil, adding up to 0.22. This level is lower than the obtained for the no DR processing. But note that the levels in the beamforming maps are also lower. The artificial source had a level of 4.74e-7**,** well below the actual sources level. The time required for the post-processing was only 194.3 seconds.

The reconstruction from the LORE results is shown in Figure 6.74b. In this case, the range

was changed from 12 to 20 dB in order to visualize and compare all the sidelobes. As can be seen, the reconstruction assuming incoherence is not in good agreement with the beamformed data. As stated before, this is related to the wrong assumption of incoherence of the sources in the trailing edge region.

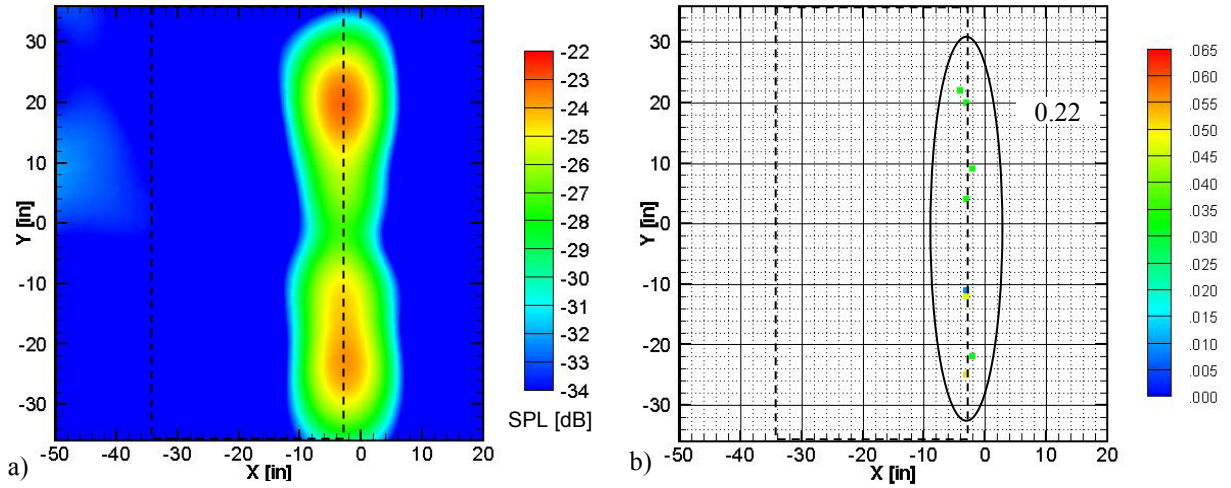

Figure 6.73: Airfoil noise a) beamforming at 1.2 kHz using DR and b) LORE results assuming incoherent sources.

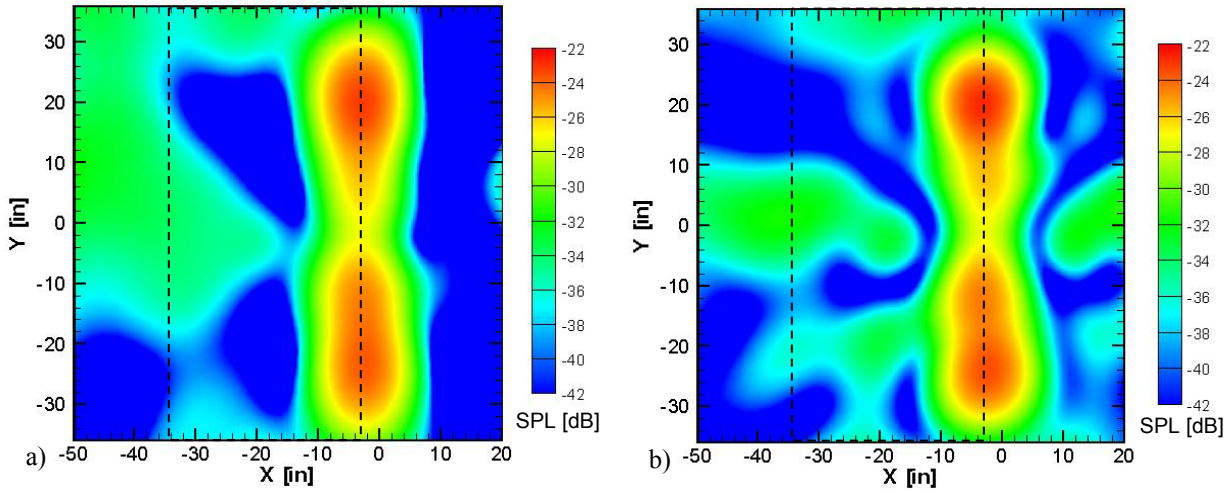

Figure 6.74: Airfoil noise a) beamforming at 1.2 kHz using DR and b) reconstruction from LORE results assuming incoherent sources.

Figure 6.75 shows the levels and relative phase obtained from LORE assuming coherent sources. The total level in this case was 0.235 (adding all the levels in complex form), slightly

higher than in the incoherent case. The level of the artificial source was slightly higher, i.e. 9.7e-3, but still well below the trailing edge noise levels. The correlation coefficient for this case was about 0.87. The time for this processing was 287 seconds; thus, higher than before since twice as much values are being optimized.

Reconstruction from these results shows very good agreement both in the trailing edge zone and the sidelobes structure. These results suggest that DR eliminates most of the sidelobes that are not related to TE sources. But most important, showing that the TE noise source has a nonzero coherence length. However, as mentioned before, the sidelobe structure should not be recovered accurately given that DR is not modeled in LORE. Thus, the results are not expected to be very accurate since the method is trying to find the sources that would render the same beamforming map "without" using DR.

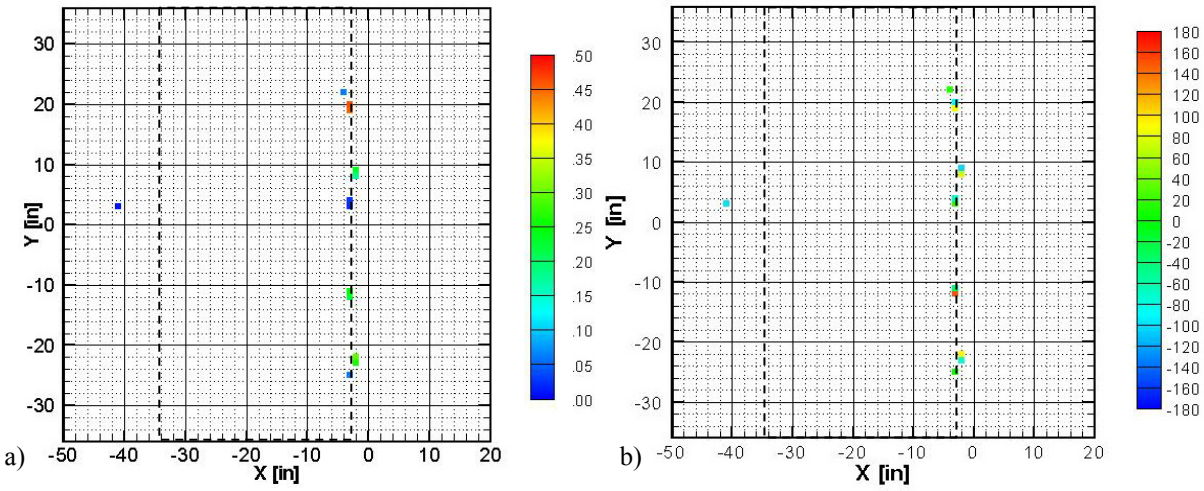

Figure 6.75: Airfoil noise at 1.2 kHz using beamforming with DR. a) Amplitude and b) phase results from LORE assuming coherent sources.

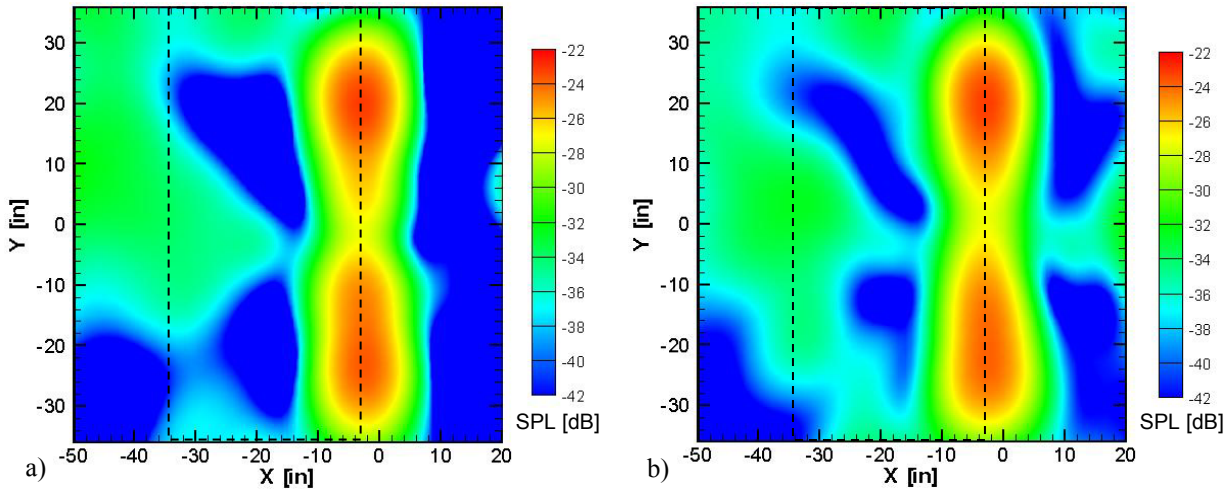

Figure 6.76: Airfoil noise a) beamforming at 1.2 kHz using DR and b) reconstruction from LORE results assuming coherent sources.

6.8 Concluding Remarks

It was demonstrated in this chapter that the non-linear modeling of the beamforming output using the complex point spread function accurately renders the actual beamforming maps. Furthermore, the LORE modeling is not restricted to incoherent sources, small regions in space.

The numerical simulations and basic experimental results shown before are promising in terms of reducing computational time and overcoming other limitations reported in currently available approaches. It was also proven that even when LORE looses accuracy, its results are easier to interpret and more "informative" than the actual beamforming maps.

However, the present work only represents the beginning of LORE. In this sense, many features can be implemented in order to improve the results accuracy and range of applicability, i.e. the "non-trivial" formulation of LORE using diagonal removal beamforming.

The application of LORE was not intended in this early stage for landing gear noise, where the reflections and high background noise difficult the accurate modeling of the beamforming output. However, landing gear noise is the ultimate goal of this technique once the modeling includes all the previously mentioned problems.

Chapter 7

Conclusions and Future Work

7.1 Conclusions

Microphone phased array measurements were used for noise source identification on a high fidelity 26%-scale 777 aircraft main landing gear model. As expected, a large number of noise sources were encountered. It was found that the back brace, rear truck, rear rock-guard sub-assemblies, torque link, front cable harness, and wheel hubs were the main contributors to the low frequency noise. At mid frequencies, the major noise sources were found to be the strut-tunnel interface, the brakes and axles, and the hydraulic cylinder. While at high frequencies, the loudest sources were the brakes and axles, the rear lock-link, and the "Main-strut cables" sub-assembly. When feasible, individual components of the landing gear model were removed and the noise field measured. By comparing to the baseline gear results, it was possible to validate the presence of specific noise sources and its contribution to the overall noise. These landing gear configurations with components removed were also used to gain insight into the noise generation mechanism for some components as well as to determine an upper bound of noise reduction for "ideal" noise control devices.

Upon completion of the noise source identification of the landing gear, the effort was focused on the development of noise control devices. As attempted by previous researchers, the approach undertaken here was to develop fairings to streamline the gear. Unlike in previous work, the fairings developed in this research were implemented using elastic membranes. This approach is a new innovative concept in the implementation of noise control devices for landing gears. These elastic fairing devices offer a number of advantages as compare to the rigid fairings. These are: "promising" noise reduction potential, light-weight fairings, easy to mount and remove for inspection purposes, the devices do not interfere with the stowed position of the gear or the steering mechanism of the back wheels, applicable to current and future landing gears, and

relatively low cost.

Using this new concept, a series of noise control devices were designed, fabricated and tested for the braces, main strut, and lower truck. Significant noise reduction was obtained with these devices. In this sense, the strut fairing showed a reduction of at least 1 dB at mid frequencies, and of about 0.5 dB at high frequencies. At the low frequency end it appears to be a noise increase of about 0.5 dB, most probably related to the flow modification mentioned before. The braces fairing showed reductions of about 2 to 3 dB over all the frequency range. In the case of the combination of these two devices, the noise reduction is at least 2 dB for almost all the frequency range, with peak reductions of up to 5 or 6 dB. For the case of the lower truck fairing, the integrated spectrum shows a reduction of at least 2 dB over all the frequency range. At low frequencies, the reduction is as much as 5 dB. Additional noise control devices were also fabricated for the cable harnesses and torque link. In these cases, a reduction of 2 to 3 dB was obtained at low and high frequencies. At mid frequencies no reduction was observed.

Since the analysis of the beamforming maps is difficult due to the presence of sidelobes and other issues described in Chapter 1, an alternative approach was developed for post-processing of phased array measurements (LORE). This approach renders maps where only the actual noise sources position and levels are shown, i.e. sidelobes are not present. The results from the post processing were found to be satisfactory for a wide range of frequencies and source complexity. This includes the case of multiple coherent sources, where the relative phase information was also recovered using LORE.

The effect of array beamwidth on the LORE results was also shown for 2D and 3D cases. In this sense, it was also proven that even when LORE looses accuracy, its results are easier to interpret and more “informative” than the actual beamforming maps.

The numerical simulations and basic experimental results presented in this work show promising results in terms of reduction of computational time and overcome of other limitations when compared to currently available approaches. These results also suggest that some advantage can be obtained if the later application of LORE is taken into account in the design of the array.

7.2 Future Work

As mentioned throughout this work, some issues are still unresolved or could be further developed, these are:

- Re-design of lower truck fairing to improve noise reduction performance,
- Test landing gear in semi-anechoic tunnel to avoid reflections and to find the differences, if any, obtained measuring with the array in the "far-field" and near field,
- Formulate LORE for diagonal removal beamforming,
- Test different multidimensional optimization procedures that could reduce the computational time or improve the results (Globalized Bounded Nelder–Mead, Powell method, others),
- Analyze phased array patterns that could give some advantage when LORE is used,
- Evaluate the possibility and advantages of using a different source model in the source receiver model, i.e. line sources instead of monopoles,
- Improve Step 1 of LORE and further analyze its implementation in 3D cases,
- Determine coherence length using LORE, and
- Perform a detailed comparison to the DAMAS approach by applying both methods to the same cases, i.e. instead of the comparison approach presented in this work.

References

[1] Operation Procedures Manual for a Boeing 767, **http://www.757.org.uk/767/sops/sop4.html** (Cited October 2005).

[2] http://www.airliners.net

[3] Stephen M. Jaeger, and Brian E. Smith, "Acoustic Measurements of a Model Semi-Span Symmetry Plane," *2nd AIAA/CEAS Aeroacoustics Conference*, State College, PA, May 1996. AIAA 96-1715

[4] Julie A. Hayes, W. Clifton Horne, Paul T. Soderman, Paul H. Bent, "Airframe Noise Characteristics of a 4.7% Scale DC-10 Model," *3rd AIAA/CEAS Aeroacoustics Conference*, Atlanta, GA, May 1997. AIAA 97-1594-CP

[5] William H. Herkes and Robert W. Stoker, "Wind Tunnel Measurements of the Airframe Noise of a High-speed Civil Transport," 36th *Aerospace Sciences Meeting and Exhibit*, Reno, NV, January 1998. AIAA 98-0472

[6] Robert W. Stoker, James R. Underbrink, Guy R. Neubert, "Investigations of Airframe Noise in Pressurized Wind Tunnels," *7th AIAA/CEAS Aeroacoustics Conference*, Maastricht, The Netherlands, May 2001. AIAA 2001-2107

[7] Robert W. Stoker, and Rahul Sen, "An Experimental Investigation of Airframe Noise Using a Model-Scale Boeing 777," *39th AIAA Aerospace Sciences Meeting and Exhibit*, Reno, NV, January 2001. AIAA 2001-0987

[8] Robert W. Stoker, Yueping Guo, and Craig Streett, "Airframe Noise Source Locations of a 777 Aircraft in Flight and Comparisons with Past Model Scale Tests," *9th AIAA/CEAS Aeroacoustics Conference and Exhibit*, Hilton Head, SC, May 2003. AIAA 2003-3232

[9] Renaud Davy, Frédéric Moens, Hugues Remy, "Aeroacoustic Behavior of a 1/11 Scale Airbus Model in the Open Anechoic Wind Tunnel CEPRA 19," *8th AIAA/CEAS Aeroacoustics Conference and Exhibit*, Breckenridge, CO, June 2002. AIAA 2002-2412

[10] L.C. Chow, K. Mau, and H. Remy, "Landing Gears and High Lift Devices Airframe Noise Research," *8th AIAA/CEAS Aeroacoustics Conference and Exhibit*, Breckenridge, CO, June 2002. AIAA 2002-2408

[11] J.F Piet , U. Michel and P. Böhning, "Localization of the Acoustic Sources of the A340 with a Large Phased Microphone array During Flight Tests," *8th AIAA/CEAS Aeroacoustics conference and Exhibit*, Breckenridge, CO, June 2002. AIAA 2002-2506

[12] F. R. Grosche, G. Schneider, and H. Stiewitt, "Wind Tunnel Experiments on Airframe Noise Sources of Transport Aircraft," *3rd AIAA/CEAS Aeroacoustics Conference*, Atlanta, GA, May 1997. AIAA-97-1642-CP

[13] Renaud Davy and Hugues Remy, "Airframe Noise Characteristics of a 1/11 Scale Airbus Model," *4th AIAA/CEAS Aeroacoustics Conference*, Toulouse, June 1998. AIAA-98-2335

[14] Werner Dobrzynski and Heino Buchholz, "Full-Scale Noise Testing on Airbus Landing Gears in the German Dutch Wind Tunnel," *3rd AIAA/CEAS Aeroacoustics Conference*, Atlanta, GA, May 1997. AIAA 97-1597-CP

[15] A. G. Munson, "A Modeling Approach to Nonpropulsive Noise," *3rd AIAA Aeroacoustics Conference*, Palo Alto, CA, July 1976. AIAA 76-525

[16] J. D. Revell, G. J. Healy, and J. S. Gibson, "Method for the Prediction of Airframe Aerodynamic Noise," *Aeroacoustics: Acoustic Wave Propagation; Aircraft Noise Prediction; Aeroacoustic Instrumentation*, Ira Schwartz, ed., AIAA, pp. 139-154, 1976.

[17] M.S. Howe, "A review of the theory of trailing edge noise," *Journal of Sound and Vibration*, vol.61, pp.437-465, 1978

[18] Robert W. Stoker, "Using Microphone Phased Arrays to Enable Low Airframe Noise Design," *41st Aerospace Sciences Meeting and Exhibit*, Reno, NV, January 2003. AIAA 2003-707

[19] Stephen M. Jaeger, Nathan J. Burnside, Paul T. Soderman, W. Clifton Horne, and Kevin D. James, "Microphone Array Assessment of an Isolated, 26%-Scale, High Fidelity Landing Gear," *8th AIAA/CEAS Aeroacoustics Conference and Exhibit*, Breckenridge, CO, June 2002. AIAA 2002-2410

[20] W. Dobrzynski, L. C. Chow, P. Guion, and D. Shiells, "A European Study on Landing Gear Airframe Noise Sources," *6th AIAA/CEAS Aeroacoustics Conference and Exhibit*, Lahaina, HI, June 2000. AIAA 2000-1971

[21] W. Dobrzynski, L. C. Chow, P. Guion, and D. Shiells, "Research into Landing Gear Airframe Noise Reduction," *8th AIAA/CEAS Aeroacoustics Conference and Exhibit*, Breckenridge, CO, June 2002. AIAA 2002-2409

[22] David P. Lockard, Mehdi R. Khorrami, and Fei Li, "Aeroacoustic Analysis of a Simplified Landing Gear," *9th AIAA/CEAS Aeroacoustics Conference and Exhibit*, Hilton Head, SC, May 2003. AIAA 2003-3111

[23] J. E. Ffowcs Williams, and D.L. Hawkings, "Sound generation by turbulence and surfaces in arbitrary motion," *Philosophical Transactions for the Royal Society of London. Series A, Mathematical and Physical Sciences*, Volume 264, Issue 1151, pp. 321-342.

[24] Guo Y. P., "A Model for Slat Noise Generation," *3rd AIAA/CEAS Aeroacoustics Conference*, Atlanta, GA, May 1997. AIAA 97-1647

[25] Guo Y. P., "Application of Ffowcs Williams/Hawkings Equation to Two Dimensional Problems," *Journal of Fluid Mechanics,* 403, pp. 201-221, 2000.

[26] Guo Y. P., "A discrete vortex model for slat noise prediction," *7th AIAA/CEAS Aeroacoustics Conference*, Maastricht, The Netherlands, May 2001. AIAA 2001-2157

[27] M.G. Smith and L.C. Chow, "Validation of a Prediction model for Aerodynamic Noise from Aircraft Landing Gear," *8th AIAA/CEAS Aeroacoustics Conference and Exhibit*, Breckenridge, CO, May 2002. AIAA 2002-2581

[28] M.G. Smith and L.C. Chow, "Prediction Method for Aerodynamic Noise from Aircraft Landing Gear," *4th AIAA/CEAS Aeroacoustics Conference*, Toulouse, France, June 1998. AIAA 98-2228

[29] L. Lopes, K. Brentner, P. Morris, G. Lilley, and D. Lockhard, "Complex Landing Gear Noise Prediction Using a Simple Toolkit," *43rd AIAA Aerospace Sciences Meeting and Exhibit*, Reno, NV, January 2005. AIAA 2005-1202

[30] S. J. Pietrzko, and R. F. Hofmann, "Mathematical Modeling of Aircraft Noise Based on Identified Directivity Patterns," *2nd AIAA/CEAS Aeroacoustics Conference*, State College, PA, May 1996. AIAA 96-1768

[31] Yueping Guo, "A Statistical Model for Landing Gear Noise Prediction," *9th AIAA/CEAS Aeroacoustics Conference and Exhibit*, Hilton Head, SC, May 2003. AIAA 2003-3227

[32] Y. P. Guo & K. J. Yamamoto, and R. W. Stoker, "A Component Based Empirical Model for Airframe Noise Prediction," *8th AIAA/CEAS Aeroacoustics Conference and Exhibit*, Breckenridge, CO, May 2002. AIAA 2002-2574

[33] K. Elmer, J. Wat, B. Shivashankara, J. P. Clarke, K. Tong, J. Brown, A. Warren, "Community Noise Reduction Using Continuous Descent Approach: A Demonstration Flight

Test at Louisville," 9th *AIAA/CEAS Aeroacoustics Conference and Exhibit*, Hilton Head, SC, May 2003. AIAA 2003-3277

[34] Marianne Mosher, "Phased Arrays for Aeroacoustic Testing: Theoretical Development," *2nd AIAA/CEAS Aeroacoustics Conference*, State College, PA, May 1996. AIAA 1996-1713

[35] Thomas F. Brooks and William M. Humphreys, Jr., "Effect of Directional Array Size on the Measurement of Airframe Noise Components," *5th AIAA/CEAS Aeroacoustics Conference*, Bellevue, WA, May 1999. AIAA 99-1958

[36] Nobuhiro Yamazaki, Kiyoshi Nagakura, Mitsuru Ikeda, *and* Akio Sagawa, "Methods to Measure Acoustic Sources in a Closed Wind Tunnel Test Section," *11th AIAA/CEAS Aeroacoustics Conference and Exhibit*, Monterey, CA, May 2005. AIAA 2005-3003

[37] Michael E. Watts, Marianne Mosher, Michael J. Barnes, "The Microphone Array Phased Processing System (MAPPS)," *2nd AIAA/CEAS Aeroacoustics Conference*, State College, PA, May 1996. AIAA 1996-1714

[38] Sekhar Radhakrishnan and Ahmad D. Vakilit, "Acoustic Measurements and Background Noise Separation in Wind Tunnels," *5th AIAA/CEAS Aeroacoustics Conference*, Bellevue, WA, May 1999. AIAA 99-1990

[39] F.R. Grosche, H. Stiewitt, and B. Binder, "On Aero-Acoustic Measurements in Wind Tunnels by Means of a Highly Directional Microphone System," Palo Alto, 1976. AIAA 76-535.

[40] J.M. Kendall, "Airframe Noise Measurements by Acoustic Imaging," Los Angeles, 1977. AIAA-77-55

[41] R. Sen, "Interpretation of acoustic source maps made with an elliptic-mirror directional microphone system," *2nd AIAA/CEAS Aeroacoustics Conference*, State College, PA, May 1996. 1996-1712

[42] R.S. Elliot, "The Theory of Antenna Arrays," *Microwave Scanning Antennas.* R.C. Hansen, ed., Academic Press, 1966.

[43] W.S. Burdic, *Underwater Acoustic System Analysis*, Prentice-Hall, Inc., Englewood Cliffs, NJ, 1984.

[44] P.T. Soderman, and S.C. Noble, "Directional Microphone Array for Acoustic Studies of Wind Tunnel Models," *Journal of Aircraft*, pp. 169-173, 1975.

[45] T.F. Brooks, M.A. Marcolini, and D.S. Pope, "A Directional Array Approach for the Measurement of Rotor Noise Source Distributions with Controlled Spatial Resolution," *Journal of Sound and Vibration*, Volume 112, Number 1, pp. 192-197, 1987.

[46] Ralph O. Schmidt, and Raymond E. Franks, "Multiple Source DF Signal Processing: An Experimental System," *IEEE Transactions on Antennas and Propagation*, vol. AP-34. No. 3, March 1986.

[47] Stefan Oerlemans, Pieter Sijtsma, "Determination Of Absolute Levels From Phased Array Measurements Using Spatial Source Coherence," *8th AIAA/CEAS Aeroacoustics Conference and Exhibit*, Breckenridge, CO, June 2002. AIAA 2002-2464

[48] Clifton Horne, Julie A. Hayes, Stephen M. Jaeger and Srba Jovic, "Effects of Distributed Source Coherence on the Response of Phased Acoustic Arrays," *6th AIAA/CEAS Aeroacoustics Conference*, Lahaina, HI, June 2000. AIAA 2000-1935

[49] Pieter Sijtsma, and Robert W. Stoker, "Determination of Absolute Contributions of Aircraft Noise Components using Fly-Over Array Measurements," *10th AIAA/CEAS Aeroacoustics Conference and Exhibit*, Manchester, United Kingdom, May 2004. AIAA 2004-2958

[50] Stefan Oerlemans, and Pieter Sijtsma, "Acoustic Array Measurements of a 1:10.6 Scaled

Airbus A340 Model," *10th AIAA/CEAS Aeroacoustics Conference and Exhibit*, Manchester, United Kingdom, May 2004. AIAA 2004-2924

[51] S. Guidati, C. Brauer and S. Wagner, "The Reflection Canceller – Phased Array Measurements in a Reverberating Environment," *8th AIAA/CEAS Aeroacoustics Conference and Exhibit*, Breckenridge, CO, May 2002. AIAA 2002-2462

[52] Pieter Sijtsma, and Hermann Holthusen, "Corrections for Mirror Sources in Phased Array Processing Techniques," *9th AIAA/CEAS Aeroacoustics Conference and Exhibit*, Hilton Head, SC, May 2003. AIAA 2003-3196

[53] S. Guidati, G. Guidati, and S. Wagner, "Beamforming in a Reverberating Environment with the Use of Measured Steering Vectors," *7th AIAA/CEAS Aeroacoustics Conference*, Maastricht, The Netherlands, May 2001. AIAA 2001-2166

[54] Thomas F. Brooks and William M. Humphreys, Jr., *"A Deconvolution Approach for the Mapping of Acoustic Sources (DAMAS) Determined from Phased Microphone Arrays," 10th AIAA/CEAS Aeroacoustics Conference and Exhibit*, Manchester, United Kingdom, May 2004. AIAA 2004-2954

[55] Robert P. Dougherty, "Extensions of DAMAS and Benefits and Limitations of Deconvolution in Beamforming," *11th AIAA/CEAS Aeroacoustics Conference and Exhibit*, Monterey, CA, May 2005. AIAA 2005-2961

[56] Wiener, Norbert, *Extrapolation, interpolation, and smoothing of stationary time series, with engineering applications*, Technology Press of the Massachusetts Institute of Technology, 1949.

[57] Thomas F. Brooks and William M. Humphreys, Jr., "Three-Dimensional Application of DAMAS Methodology for Aeroacoustic Noise Source Definition," *11th AIAA/CEAS Aeroacoustics Conference and Exhibit*, Monterey, CA, May 2005. AIAA 2005-2960

[58] Robert P. Dougherty, "Advanced Time-domain Beamforming Techniques," *10th AIAA/CEAS Aeroacoustics Conference and Exhibit*, Manchester, United Kingdom, May 2004. AIAA 2004-2955

[59] Thomas Mueller (ed.), *Aeroacoustic Measurements*, Springer, 2002. ISBN 3-540-41757-5.

[60] Robert P. Dougherty, "Turbulent Decorrelation of Aeroacoustic Phased Arrays: Lessons from Atmospheric Science and Astronomy," *9th AIAA/CEAS Aeroacoustics Conference and Exhibit*, Hilton Head, SC, May 2003. AIAA 2003-3200

[61] Stephen M. Jaeger, W. Clifton Horne, and Christopher S. Allen, "Effect of Surface Treatment on Array Microphone Self-Noise," *6th AIAA/CEAS Aeroacoustics Conference and Exhibit*, Lahaina, HI, June 2000. AIAA-2000-1937

[62] William M. Humphreys Jr., Carl H. Gerhold, Allan J. Zuckerwar, Gregory C. Herring, and Scott M. Bartram, "Performance Analysis of a Cost-Effective Electret Condenser Microphone Directional Array," *9th AIAA/CEAS Aeroacoustics Conference and Exhibit*, Hilton Head, SC, May 2003. AIAA 2003-3195

[63] W. Clifton Horne, Kevin D. James, Thomas K. Arledge, Paul T. Soderman, Nathan Burnside, and Stephen M. Jaeger, "Measurements of 26%-scale 777 Airframe Noise in the NASA Ames 40- by 80 Foot Wind Tunnel," *11th AIAA/CEAS Aeroacoustics Conference and Exhibit*, Monterey, CA, May 2005. AIAA 2005-2810

[64] Pieter Sijtsma an Hermann Holthusen, "Source Location by Phased Array Measurements in Closed Wind Tunnel Test Sections," *5th AIAA/CEAS Aeroacoustics Conference*, Bellevue, WA, 1999. AIAA 99-1814

[65] Charles L. Lawson, and Richard J. Hanson, Solving least squares problems, Englewood Cliffs, N.J., Prentice-Hall. 1974.

[66] J.A. Nelder, and R. Mead, "A Simplex Method for Function Minimization," *Computer Journal*, vol. 7, pp. 308-313. 1965.

[67] J. L. Starck, F. Murtagh, and A. Bijaoui, "Multiresolution and Astronomical Image Processing," *Astronomical Data Analysis Software and Systems IV*, ASP Conference Series, Vol. 77, 1995.

[68] European Southern Observatory, *ESO-MIDAS User Manual*, Volume B: Data Reduction. 1998.

[69] J. L. Starck, F. Murtagh, and A. Bijaoui, "Multiresolution Support Applied to Image Filtering and Restoration," *Graphical Models and Image Processing*, Vol. 57, No. 5. 1995.

[70] B. D. Lucas and T. Kanade, "An Iterative Image Registration Technique with an Application to Stereo Vision", *IJCAI* 1981.

[71] A. Goshtasby, S. H. Gage, and J. F. Bartholic, ``A Two-Stage Cross-Correlation Approach to Template Matching", *IEEE Trans. Pattern Analysis and Machine Intelligence*, vol. 6, no. 3, pp. 374-378, 1984.

[72] Benjamin S. Smith, Hugo E. Camargo, Ricardo A. Burdisso, and William J. Devenport, "Development and Testing of a Novel Acoustic Wind Tunnel Concept," *11th AIAA/CEAS Aeroacoustics Conference and Exhibit*, Monterey, CA, May 2005. AIAA 2005-3053

[73] Anthony V. Fiacco, and Garth P. McCormick, *Nonlinear programming: Sequential unconstrained minimization techniques*. Jon Wiley, NY, 1968.

[74] Marco A. Luersen, and Rodolphe Le Riche, "Globalized Nelder–Mead Method for Engineering Optimization," *Computers and Structures 82* (2004) 2251–2260

Appendix A: Least Squares Solution

This appendix presents the algorithm used to obtain the constrained Least Squares (LS) solution to the linear system of equations posted in Step 1 of the LORE technique, given by equation (6. 28) as:

$$\min_{|\vec{a}(\vec{x}'')|} \frac{1}{2}\left\|\hat{\mathbf{E}}\left|\vec{a}\left(\vec{x}''\right)\right|^2 - \vec{b}\right\|_2^2, \quad \text{with the constraint: } \left|a\left(\vec{x}''_m\right)\right|^2 \geq 0 \tag{A. 1}$$

Thus, particular interest is placed on the non-negativity constraint to the solution and the fact that the linear system of equations being solved is rank-deficient. The rank-deficiency is related to the fact that the size of the system of equations is given by the number of grid points, while its rank is given by the number of sources in the scanning field.

The algorithm implemented in this work to solve the previous system is known as Non-negative Least Squares (NNLS) and was developed by Lawson and Hanson [65]. In order to simplify the notation in this appendix, the system $\hat{\mathbf{E}}\left|\vec{a}\left(\vec{x}''\right)\right|^2 = \vec{b}$ is re-written as:

$$Ax = b, \qquad x \geq 0 \tag{A. 2}$$

Thus, the problem is to find the solution that minimizes the norm of $Ax - b$ as:

$$\min_x \frac{1}{2}\|Ax - b\|_2^2, \quad \text{with the constraint: } x_i \geq 0 \tag{A. 3}$$

Since the NNLS algorithm uses the orthogonal decomposition of the matrix A to solve the system of equations, the solution approach to such problem will be presented first. Since in particular the QR decomposition is used in the NNLS algorithm, it will be presented for completeness but is not crucial for the understanding of the algorithm. The reason for using a QR decomposition is that the system of equations can be easily solved using backwards substitution and matrix multiplications. As will be shown later, this approach also presents the advantage of simplifying the solution procedure when the matrix A or the vector b need to be modified.

In the last section, a detailed description of the NNLS algorithm is presented.

A.1 The Least Squares Problem

As mentioned before, using orthogonal decompositions to find the solution to the least squares problem simplifies the problem and presents many advantages. The solution approach makes use of the property of the orthogonal matrices of preserving the Euclidean norm under multiplication. This is:

$$\|Qy\| = \|y\| \tag{A. 4}$$

where:

y is any *m*-vector, and

Q is any $m \times m$ orthogonal matrix, i.e. $Q^T Q = I$, where *I* is the $m \times m$ identity matrix.

In the LS formulation the Euclidean norm of $Ax - b$ is being minimized, and using the previous property the following equivalent problem can be posted:

$$\|Ax - b\| = \|Q(Ax - b)\| = \|QAx - Qb\| \tag{A. 5}$$

As shown before, this is true for any orthogonal matrix Q and any vector. Using the property of orthogonal transformations it is desired to find an orthogonal decomposition of A in the form:

$$A = HRK^T \tag{A. 6}$$

where:

A is an $m \times n$ matrix of rank *k*,

H is an $m \times m$ orthogonal matrix,

K is an $n \times n$ orthogonal matrix, and

R is an $m \times n$ matrix of the form:

$$R = \begin{bmatrix} R_{11} & 0 \\ 0 & 0 \end{bmatrix} \tag{A. 7}$$

where R_{11} is a $k \times k$ submatrix of rank *k.*

Since *H* is an orthogonal matrix, it yields:

$$H^T H = I \text{ , then } H^{-1} = H^T \tag{A. 8}$$

Multiplying both sides of $Ax = HRK^T x = b$ by H^T, it yields:

$$RK^T x = H^T b \tag{A. 9}$$

The resulting vector on the right hand side is now defined as:

$$g = H^T b = \begin{bmatrix} g_1 \\ g_2 \end{bmatrix} \begin{matrix} \}k \\ \}m-k \end{matrix} \tag{A. 10}$$

where the partitioning in the vector is to account for the rank of the system as will be shown next. A change of variables is also introduced in the form:

$$y = K^T x = \begin{bmatrix} y_1 \\ y_2 \end{bmatrix} \begin{matrix} \}k \\ \}n-k \end{matrix} \tag{A. 11}$$

Thus, the resulting system can be written as:

$$R\,y = g \tag{A. 12}$$

Furthermore, given the particular form chosen for the matrix *R* shown in equation (A. 7), this system can be further "reduced" and re-written as:

$$R_{11} y_1 = g_1 \tag{A. 13}$$

Since the matrix R_{11} is a $k \times k$ matrix of rank *k*, there is a unique solution $\tilde{y}_1$ to this system. Thus, all solutions $\hat{x}$ to the problem of minimizing $\|Ax - b\|$ are of the form:

$$\hat{x} = K \begin{bmatrix} \tilde{y}_1 \\ y_2 \end{bmatrix} \tag{A. 14}$$

where y_2 is an arbitrary vector.

Note that with this proposed decomposition, the problem of solving a system of *m* equations,

was "reduced" to one with only *k* equations as posted in equation (A. 13). Note also that y_2 is arbitrary, thus, regardless of its values the solution will satisfy the system of equations. This implies that there is an infinite number of solutions that will minimize $\|Ax-b\|$. However, the main interest is in finding the unique solution of minimum length. To find such solution it is useful to define the residual *r* in the form:

$$r = b - A\hat{x} \tag{A. 15}$$

Using equations (A. 6), (A. 10) and (A. 14) the residual can be written as:

$$r = H\begin{bmatrix} g_1 \\ g_2 \end{bmatrix} - HRK^T K\begin{bmatrix} \tilde{y}_1 \\ y_2 \end{bmatrix} = H\begin{bmatrix} g_1 \\ g_2 \end{bmatrix} - H\begin{bmatrix} R_{11} & 0 \\ 0 & 0 \end{bmatrix}\begin{bmatrix} \tilde{y}_1 \\ y_2 \end{bmatrix} \tag{A. 16}$$

and thus:

$$r = H\begin{bmatrix} g_1 \\ g_2 \end{bmatrix} - H\begin{bmatrix} g_1 \\ 0 \end{bmatrix} = H\begin{bmatrix} 0 \\ g_2 \end{bmatrix} \tag{A. 17}$$

It can be observed that the residual is always the same regardless of $\hat{x}$, since g_2 depends only on the right hand side of the original system $Ax = b$. Furthermore, the norm of the residual is given only by:

$$\|r\| = \|b - A\hat{x}\| = \|g_2\| \tag{A. 18}$$

So, the minimum residual norm is obtained when $g_2 = 0$, i.e. for $y_2 = 0$. Then, the unique solution of minimum length is given by:

$$\tilde{x} = K\begin{bmatrix} \tilde{y}_1 \\ 0 \end{bmatrix} \tag{A. 19}$$

In conclusion, with "any" orthogonal decomposition, the solution to the least squares problem of minimum length can be easily found solving a reduced problem of rank *k*. In our case, this is very important since the number of grid points is usually much bigger than the actual number of sources, i.e. $N >> k$.

It is important to remark that the minimum length solution, the set of all solutions, and the minimum value, are all unique and do not depend on the choice of the orthogonal decomposition.

A.2 The QR Decomposition

As seen before, the LS problem can be solved performing an orthogonal decomposition of the matrix *A*. Since the NNLS algorithm uses the QR decomposition, it will be presented here for completeness. However, this section can be skipped without affecting the understanding of the NNLS algorithm.

An important point proven in this section is the existence of such decomposition for any matrix. This will be proven using orthogonal transformations. The idea is to perform "small" changes to the columns of the matrix that will not affect its norm. This is accomplished by using the so called elementary orthogonal transformations. After applying a number of such elementary transformations, the desired orthogonal decomposition can be obtained.

For the particular case of the QR decomposition this can be achieved using two elementary orthogonal transformations. Such elementary transformations are explained in detail in this section.

The first one is known as Householder transformation, and it is defined as:

$$Qv = -\sigma \|v\| e_1 \tag{A. 20}$$

where:

v is an m-vector with $v \neq \vec{0}$,

$e_1 = \begin{bmatrix} 1 & 0 & \dots & 0 \end{bmatrix}^T$ is the unit vector in the 1-direction,

$$\sigma = \begin{cases} +1 & \text{if } v_1 \geq 0 \\ -1 & \text{if } v_1 < 0 \end{cases}, \text{ and} \tag{A. 21}$$

v_1 is the first component of v.

The matrix Q for the Householder transformation is obtained by:

$$Q = I_m - \frac{2uu^T}{u^T u} \tag{A. 22}$$

with I_m being the $m \times m$ identity matrix, and *u* defined as:

$$u = v + \sigma \|v\| e_1 \tag{A. 23}$$

This transformation can be viewed geometrically as a reflection in the *(m-1)*-dimensional subspace, *S*, orthogonal to the vector *u*. More strictly speaking, all the components in the vector *v* are zeroed except for one.

The second transformation is called the Givens transformation and is used to zero only one element of the vector *v*. As it will be shown, this transformation only modifies two components of a vector. The 2×2 orthogonal matrix for this transformation is defined as:

$$G = \begin{bmatrix} c & s \\ -s & c \end{bmatrix} \tag{A. 24}$$

with $c^2 + s^2 = 1$ such that:

$$Gv = \begin{bmatrix} \left(v_1^2 + v_2^2\right)^{1/2} \\ 0 \end{bmatrix} \tag{A. 25}$$

To obtain this matrix, *c* and *s* are defined as:

$$c = \frac{v_1}{\left(v_1^2 + v_2^2\right)^{1/2}} \quad , \quad s = \frac{v_2}{\left(v_1^2 + v_2^2\right)^{1/2}} \tag{A. 26}$$

As it can be seen, either $v_1 \neq 0$ or $v_2 \neq 0$ need to be satisfied. If the transformation matrix is sought to be orthogonal and symmetric, *G* can be defined as:

$$G = \begin{bmatrix} c & s \\ s & -c \end{bmatrix} \tag{A. 27}$$

with *c* and *s* as defined in equation (A. 26).

Using the transformations described above, the product of *n* Householder matrices *Q* can be

used to transform a given $m \times n$ matrix A into an upper triangular matrix. Such upper triangular matrix R is obtained as:

$$Q_1 Q_2 \ldots Q_n A = QA = R \tag{A. 28}$$

where the Q_i matrix is such that the product $Q_1 Q_2 \ldots Q_i$ will make zero all the components under the diagonal of matrix A in the first i columns.

This decomposition of a matrix as a product of an orthogonal matrix Q and an upper triangular matrix R is called QR decomposition.

If A is an $m \times n$ matrix with $m = n$ and has full rank, the orthogonal decomposition of A can be written as:

$$A = Q^T R = Q^T R I_n \tag{A. 29}$$

where the $n \times n$ identity matrix I_n is introduced in order to render the proposed orthogonal decomposition of the form $A = HRK^T$.

If A is an $m \times n$ rectangular matrix of rank m with $m < n$, the decomposition is given by:

$$A^T = Q^T R \text{ or } A = I_m R^T Q \tag{A. 30}$$

Like in the previous case this renders an orthogonal decomposition of the form $A = HRK^T$.

However, in our case $m = n$ and $Rank(A) = k < m$. Thus, the matrix R obtained using the proposed transformations is not necessarily in the form required for an orthogonal decomposition. Thus, additional transformations needs to be used to obtain the proper form of the orthogonal decomposition.

One of such additional transformations is known as permutation. The objective of this transformation is to "change" the rows order to get a decomposition of the form:

$$QAP = \begin{bmatrix} R_{k \times k} & T_{k \times (n-k)} \\ 0_{(m-k) \times k} & 0_{(m-k) \times (n-k)} \end{bmatrix} \tag{A. 31}$$

where:

Q is an $m \times m$ orthogonal matrix,

A is an $m \times n$ matrix with rank $k < n \le m$,

P is the $n \times n$ permutation matrix, and

R is a $k \times k$ upper triangular matrix of rank k.

Selecting P in such a way that the first k columns of AP are linearly independent, the elements in rows $k+1$ through m of columns $k+1$ through n of AP will be zero. Thus, an orthogonal matrix Q can be found such that QAP is upper triangular. Since the first k columns of AP are linearly independent, the same will be true of the first k columns of QAP.

The matrix QAP can be further transformed in order to get the required form of the matrix R; thus, making zero all the components in the submatrix T. This transformation is described by:

$$\left[R : T\right] W = \left[\hat{R}_{k\times k} : 0_{k\times(n-k)}\right] \tag{A. 32}$$

where:

$\left[R : T\right]$ is a $k \times n$ matrix where $rank(R) = k$,

W is an $n \times n$ orthogonal matrix, and

$\hat{R}$ is a $k \times k$ lower triangular matrix of rank k.

This can be seen as variation of the previous transformation since where the matrix T in the following expression is being zeroed:

$$\left\{\left[R : T\right] W\right\}^T = \left[\hat{R}_{k\times k} : 0_{k\times(n-k)}\right]^T \quad \text{,or} \quad W^T \begin{bmatrix} R^T \\ T^T \end{bmatrix} = \begin{bmatrix} \hat{R}_{k\times k} \\ 0_{k\times(n-k)} \end{bmatrix} \tag{A. 33}$$

in a similar way that a matrix Q would be found such that T is zeroed in the expression:

$$A = \begin{bmatrix} R_{k\times k} \\ T_{(n-k)\times k} \end{bmatrix}, \text{ then } QA = \begin{bmatrix} R_{k\times k} \\ 0_{(n-k)\times k} \end{bmatrix} \tag{A. 34}$$

Performing the orthogonal transformations shown before, this yields:

$$H^T A K = R, \qquad A = HRK^T \tag{A. 35}$$

Note that by the appropriate choice of H and K, the matrix R_{11} can be arranged to be either upper or lower triangular.

In summary, it has been shown that there are constructive procedures for producing orthogonal decompositions of the form $A = HRK^T$ in each of the cases (for *m* and *n* and the rank). In all the cases the rank *k* submatrix R_{11} is obtained in triangular form. In this way is particularly easy to compute the solution of $R_{11}y_1 = g_1$ using backwards substitution. As shown before, for some cases the matrix K^T of the decomposition is the $n \times n$ identity matrix, and in other cases, the matrix *H* is the $m \times m$ identity matrix.

A.3 Non-negative Least Squares (NNLS)

Up to this point, no constraint has been imposed to the solution from the least squares problem. This section will now describe the algorithm developed by Lawson and Hanson [65] that will enforce such restriction as presented in equation (A. 2).

In this algorithm, two sets of indexes are used, i.e. a vector $\mathcal{P}$ and a vector $\mathcal{Z}$. On algorithm termination, the variables indexed in $\mathcal{P}$ will have a value different than zero, i.e. potential noise sources, while the ones indexed in $\mathcal{Z}$ will be zero, i.e. grid points not associated to noise sources. During algorithm execution this sets will be changed until the final solution is obtained. Thus, if a variable takes a negative value the algorithm will try to make it positive or set the variable to zero and move its index from set $\mathcal{P}$ to set $\mathcal{Z}$. On algorithm termination, *x* will be the solution vector that satisfies the least squares problem:

$$A_{\mathcal{P}}x \cong b \quad \text{, with column } j \text{ of } A_{\mathcal{P}} = \begin{cases} \text{column } j \text{ of } A & \text{if } j \in \mathcal{P} \\ 0 & \text{if } j \in \mathcal{Z} \end{cases} \tag{A. 36}$$

where:

$$\begin{aligned} x_j > 0 \ , \ \ j \in \mathcal{P} \\ x_j = 0 \ , \ j \in \mathcal{Z} \end{aligned} \tag{A. 37}$$

and *w* will be the dual vector satisfying:

$$w_j = 0 \ , \ \ j \in \mathcal{P}$$
$$w_j < 0 \ , \ j \in \mathcal{Z} \tag{A. 38}$$

where the dual vector is defined as:

$$w = A^T \left(b - Ax \right) \tag{A. 39}$$

These equations are called the Kuhn-Tucker conditions, characterizing a solution vector x for the NNLS problem. The dual vector is associated with the negative gradient of $\frac{1}{2}\|Ax-b\|^2$ at $\hat{x}$, the solution to the least squares problem [73].

The block diagram of the algorithm is shown in Figure A. 1 and is described next.

The initialization of the algorithm consists in setting the solution vector x and the sets $\mathcal{P}$ and $\mathcal{Z}$ in the following way:

$$x = \vec{0} \ , \ \mathcal{P} = \{ \ \} \ , \ \mathcal{Z} = \{1, 2, ..., n\} \tag{A. 40}$$

Thus, all the variables are assumed to be zero, rendering an empty set $\mathcal{P}$.

Then, as seen in the block diagram of Figure A. 1, the NNLS algorithm consists of two loops. A main loop called A and an inner loop called B. Loop A starts with the calculation of the dual vector w, that as mentioned before is related to the gradient at point x, by:

$$w = A^T \left(b - Ax \right) \tag{A. 41}$$

After that, a stop criterion is used. If all the values $w_j \leq 0$ for $j \in \mathcal{Z}$ are negative, it means that all the gradients are positive. Thus, x is a minimum and the algorithm stops. The algorithm will also stop if the set $\mathcal{Z}$ is empty. Thus, a solution was already found where all values of x are positive and there is no reason to continue iterating. If the stopping criterion is not met, the next step of loop A is reached. In this step an index $t \in \mathcal{Z}$ is found such that $w_t = \max \left\{ w_j : j \in \mathcal{Z} \right\}$. Thus, the "direction" in which the negative gradient is bigger is determined and the algorithm will "move" along it by incorporating a new variable to the solution in the next step. It can be

proven that introducing this value in to the solution set, it will turn out to be positive [65]. Thus, the index t from the previous step is moved to the set of nonzero grid points $\mathcal{P}$.

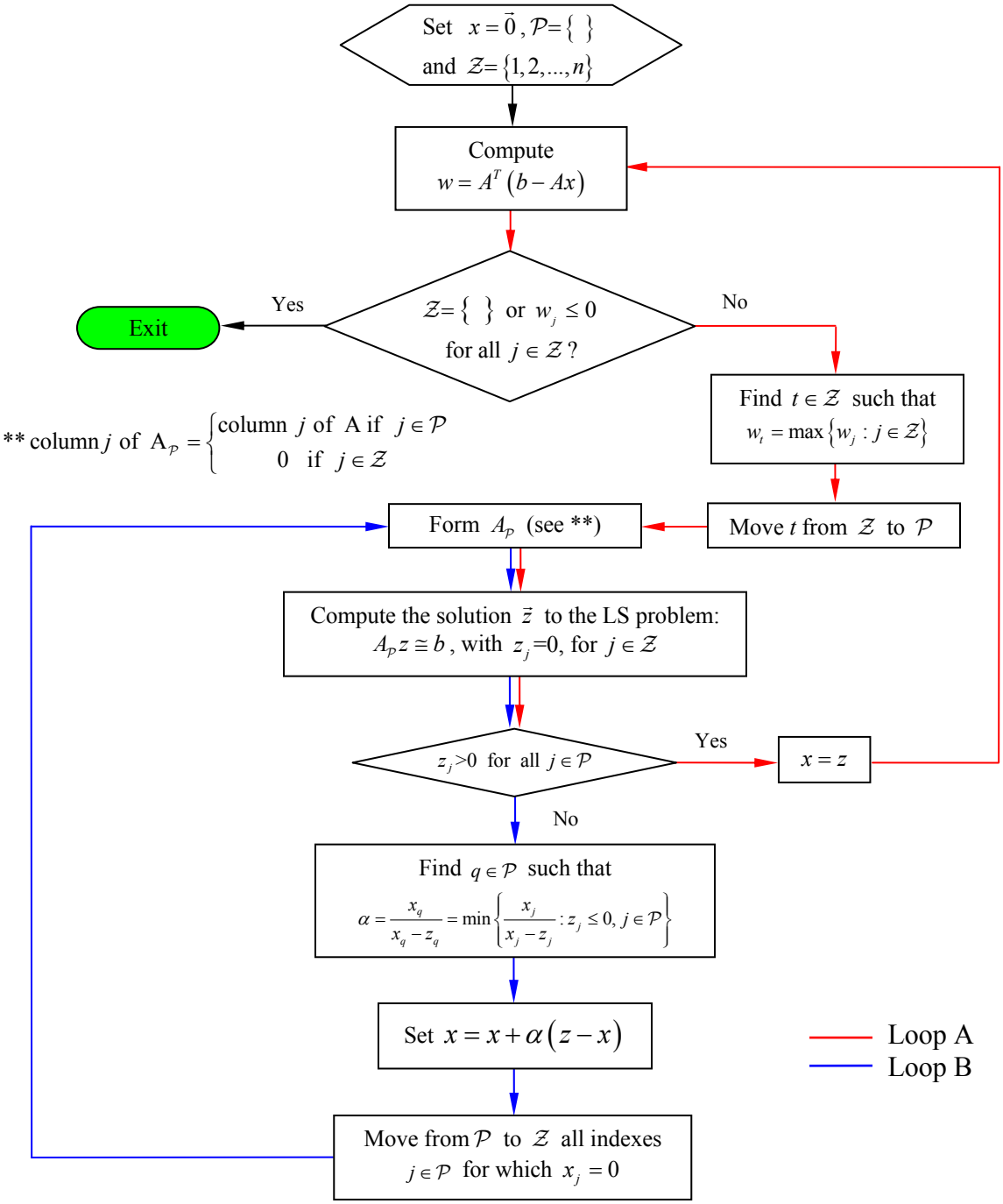

Figure A. 1: NNLS Algorithm. Block diagram.

A reduced LS problem needs to be solved in the following step, given by:

$$A_{\mathcal{P}} z \cong b \tag{A. 42}$$

where $\mathbf{A}_{\mathcal{P}}$ is the $m \times n$ matrix defined by:

$$\text{column } j \text{ of } A_{\mathcal{P}} = \begin{cases} \text{column } j \text{ of } A \text{ if } j \in \mathcal{P} \\ 0 \text{ if } j \in \mathcal{Z} \end{cases} \tag{A. 43}$$

As can be seen, a system with only the variables z_j with $j \in \mathcal{P}$ is solved. Thus, $z_j = 0$ for $j \in \mathcal{Z}$. So, the first time this problem is solved a single positive value for z_j is found. In following iterations the solution z from the previous iteration is adjusted to account for the new variable added to the set $\mathcal{P}$. At this point, the new values of z_j can be negative or positive depending on the solution found for the LS problem. If $z_j > 0$ for all $j \in \mathcal{P}$, the addition of the new variable to set $\mathcal{P}$ did not changed the values of the other variables in the set to a negative value. Thus, the algorithm will set $x = z$ and go to the beginning of loop A. Note that the purpose of loop A is to add one more variable to set $\mathcal{P}$ each time this point is reached. As mentioned in Chapter 6 this is very important in the LORE technique because this will ensure that the number of potential noise sources is as small as possible. Note also that this approach will significantly reduce the number of iterations needed to find all the potential nonzero grid points.

However, if at this step the solution renders a negative z_j, loop B needs to be repeated adjusting the solution until all $z_j > 0$, $j \in \mathcal{P}$. In order to do so, the index $q \in \mathcal{P}$ such that:

$$\alpha = \frac{x_q}{x_q - z_q} = \min\left\{ \frac{x_j}{x_j - z_j} : z_j \le 0, j \in \mathcal{P} \right\} \tag{A. 44}$$

needs to be found. This definition of the factor α is used to compute the new x in such a way that all its values are kept positive. Thus:

$$x = x + \alpha\left(z - x\right) \tag{A. 45}$$

As a result of this step, at least one value of x will be zero. Then, the indexes for which $x_j = 0$ are moved from set $\mathcal{P}$ to set $\mathcal{Z}$. The algorithm then moves to the beginning of loop B and calculates $A_{\mathcal{P}}$ taking into account the new variables or set of variables that were just added to the set of zero valued variables, i.e. moved to the set $\mathcal{Z}$. As mentioned before, this process is repeated until all $z_j > 0$ for all $j \in \mathcal{P}$.

Since every time loop B is executed at least one index is "removed" from the set $\mathcal{P}$, there is a finite number of iterations that can be performed. This number of iterations is given by the number of nonzero variables in the set $\mathcal{P}$ at the beginning of loop B. The finiteness of the number of iterations in loop A is discussed in Larson and Hansen [65].

As seen in equation (A. 42), each time $A_{\mathcal{P}}$ is defined a "reduced" LS problem needs to be solved. Thus, its QR decomposition needs to be calculated. However, advantage can be taken of the fact that $A_{\mathcal{P}}$ is the same than in the previous iteration with either the addition of a column or the removal of one or more columns. Thus, techniques that can "update" the QR decomposition based on the QR decomposition of the previous step can be used. In this way, the computational time is significantly reduced.

Appendix B: Optimization Technique

This appendix will describe the multidimensional optimization technique implemented in the LORE technique. The goal of this step is to optimize the *NZ* nonzero values obtained in Step 1 and thus, find the actual solution to the nonlinear system posted in equation (6. 21). This is accomplished by finding the minimum of a function, i.e. the total relative error in the beamforming output, with *NZ* independent variables given by equation (6. 35) as:

$$f\left(\vec{b},\vec{a}\right)=\frac{\left(\sum_{n=1}^{N}\xi_n^2\right)^{1/2}}{\max_i\left|b_i\right|} \tag{B. 1}$$

where the independent variables are nothing but the *NZ* sources amplitude $a\left(\vec{x}_m''\right)$ used to calculate the error in each grid point, ξ_n, between the beamforming output and the LORE results as given in equation (6. 34), this is:

$$\xi_n=b\left(\vec{x}_n\right)-\left|\sum_{m=1}^{NZ}cpsf\left(\vec{x}_n,\vec{x}_m''\right)a\left(\vec{x}_m''\right)\right|^2 \tag{B. 2}$$

The optimization technique implemented for this work is due to Nelder and Mead [66] and is known as *downhill simplex method*. According to recent literature [74], it is the most popular direct search method for minimizing unconstrained real functions. The method requires only function evaluations. Thus, there is no need to evaluate derivatives. The method is not very efficient in terms of the required number of function evaluations. Some other methods, like Powell's method, are most likely to be faster. However, the downhill simplex method is recommended as a "first-step" optimization technique.

Since this method needs a starting point, the *NZ* nonzero values obtained in Step 1 of LORE are used as the initial guess.

B.1 Nelder and Mead Simplex Method

As mentioned before, the solution is obtained by optimizing an equation with *NZ* nonzero "potential" noise sources starting with an initial guess. This method basically consists in comparing the function value (i.e. the "total" relative error in the beamforming output) at the $NZ+1$ vertices $\vec{P}_i$ of a simplex, where *NZ* is the dimension of the solutions space. A simplex can be described geometrically as the figure consisting in *NZ* dimensions of $NZ+1$ points (or vertices) and all their interconnecting line segments, polygonal faces, etc. In two dimensions, a simplex is a triangle. In three dimensions it is a tetrahedron, not necessarily the regular tetrahedron.

In general only simplexes that are nondegenerate are "useful", i.e., that enclose a finite inner *NZ*-dimensional volume. If any point of a nondegenerate simplex is taken as the origin, then the *NZ* other points define vector directions that span the *NZ*-dimensional vector space.

This algorithm needs a starting guess, which is an *NZ*-vector used as the first point to try. In our case, this is nothing but the solution from NNLS. The algorithm is then supposed to make its own way *downhill* through the unimaginable complexity of an *NZ*-dimensional topography, until it encounters a (local, at least) minimum.

The downhill simplex method must be started not just with a single point, but with $NZ+1$ points defining the initial simplex. To this end, we define the starting point $\vec{P}_0$, as the set of *NZ* values from Step 1, i.e. $\vec{P}_0 = \left[a(\vec{x}_1) \quad a(\vec{x}_2) \quad \ldots \quad a(\vec{x}_{NZ}) \right]$, with $a(\vec{x}_m) \neq 0$. Then, the other *NZ* points of the simplex are given by:

$$\vec{P}_i = \vec{P}_0 + \lambda \vec{e}_i, \quad i = 1, \ldots, NZ \tag{B. 3}$$

where:

$\vec{e}_i$ is the unit vector in the *i*-direction, and

λ is a constant related to the problem's characteristic length scale.

Basically, the starting simplex can be seen as a "perturbation" of the original guess in all *NZ* possible directions. Sometimes it may be convenient to setup the simplex of a given size *h*, and using directions other than the unit vectors [74], thus:

$$\vec{P}_i = \vec{P}_0 + \lambda \vec{e}_i + \sum_{\substack{k=1 \\ k \neq i}}^{N} \sigma \vec{e}_k \tag{B. 4}$$

where:

$$\begin{aligned} p &= \frac{h}{n\sqrt{2}}\left(\sqrt{n+1} + n - 1\right) \\ q &= \frac{h}{n\sqrt{2}}\left(\sqrt{n+1} - 1\right) \end{aligned} \tag{B. 5}$$

where the step λ can also be set different for each direction.

Defining f_i as the value of the function evaluated at $\vec{P}_i$, i.e. the error in the beamforming when the sources amplitude is that given by the components of $\vec{P}_i$, the following can be defined:

$$\begin{aligned} f_h &= \max_i \left(f_i\right) \\ f_l &= \min_i \left(f_i\right) \end{aligned} \tag{B. 6}$$

The centroid $\overline{P}$ is now defined as the "average" of the $\vec{P}_i$ points with $i \neq h$, thus excluding the point $\vec{P}_h$ where the function evaluation is the biggest, i.e. $f_i = f_h$, as:

$$\overline{P} = \frac{1}{N-1} \sum_{\substack{i=1 \\ i \neq h}}^{N} \vec{P}_i \tag{B. 7}$$

The idea is to change the point where the function is bigger ($\vec{P}_h$) by a point where the function evaluation is smaller than f_h; thus, minimizing on each stage of the process the maximum value of the f_i's in the simplex. To do this, the downhill simplex method uses three operations: reflection, expansion and contraction.

The reflection operation is defined as:

$$\vec{P}^* = \left(1 + \alpha\right)\overline{P} - \alpha \vec{P}_h = \overline{P} + \alpha\left(\overline{P} - \vec{P}_h\right) \tag{B. 8}$$

where α is the reflection coefficient and is a positive constant.

With this reflection, $\vec{P}^*$ is on the line joining $\vec{P}_h$ and $\overline{P}$ but in the opposite side of $\overline{P}$. If f^* lies between f_l and f_h, then $\vec{P}_h$ is replaced by $\vec{P}^*$ and a new simplex is created to start with. If $f^* < f_l$, i.e. if the reflection rendered a new minimum $\vec{P}^{**}$, the expansion of $\vec{P}^*$, is defined as:

$$\vec{P}^{**} = \gamma \vec{P}^* + (1-\gamma)\overline{P} = \overline{P} + \gamma\left(\vec{P}^* - \overline{P}\right) \tag{B. 9}$$

where γ is the expansion coefficient, with $\gamma > 1$.

Thus, moving $\vec{P}^*$ further away from the centroid $\overline{P}$. Then if $f^{**} < f_l$, $\vec{P}_h$ is replaced with $\vec{P}^{**}$ and the process is restarted. If $f^{**} > f_l$, the expansion failed and $\vec{P}_h$ needs to be replaced by $\vec{P}^*$ before restarting.

If reflecting $\vec{P}_h$ to $\vec{P}^*$ it is found that $f^* > f_i$ for all $i \neq h$, i.e. that replacing $\vec{P}_h$ by $\vec{P}^*$ leaves f^* the maximum, then a new $\vec{P}_h$ is defined to be either the old $\vec{P}_h$ or $\vec{P}^*$,which ever has the lower f value and perform a contraction operation. The contraction is defined as:

$$\vec{P}^{**} = \beta \vec{P}_h + (1-\beta)\overline{P} = \overline{P} + \beta\left(\vec{P}_h - \overline{P}\right) \tag{B. 10}$$

where β is the contraction coefficient, with $0 < \beta < 1$.

$\vec{P}^{**}$ is then accepted for $\vec{P}_h$ and the process is restarted; unless $f^{**} > \min\left(f_h, f^*\right)$, i.e. the contracted point is worse than the better of $\vec{P}_h$ and $\vec{P}^*$. For such a failed contraction all the $\vec{P}_i$'s are replaced by $\left(P_i + P_l\right)/2$ and process is restarted.

The coefficients α, β, γ give the factor by which the volume of the simplex is changed by the operations of reflection, contraction or expansion respectively. Using test functions and several values, Nelder and Mead proved that the best strategy was to set $\alpha = 1,\ \beta = 1/2,$ and $\gamma = 2$

The complete method is given as a block diagram in Figure B. 1.

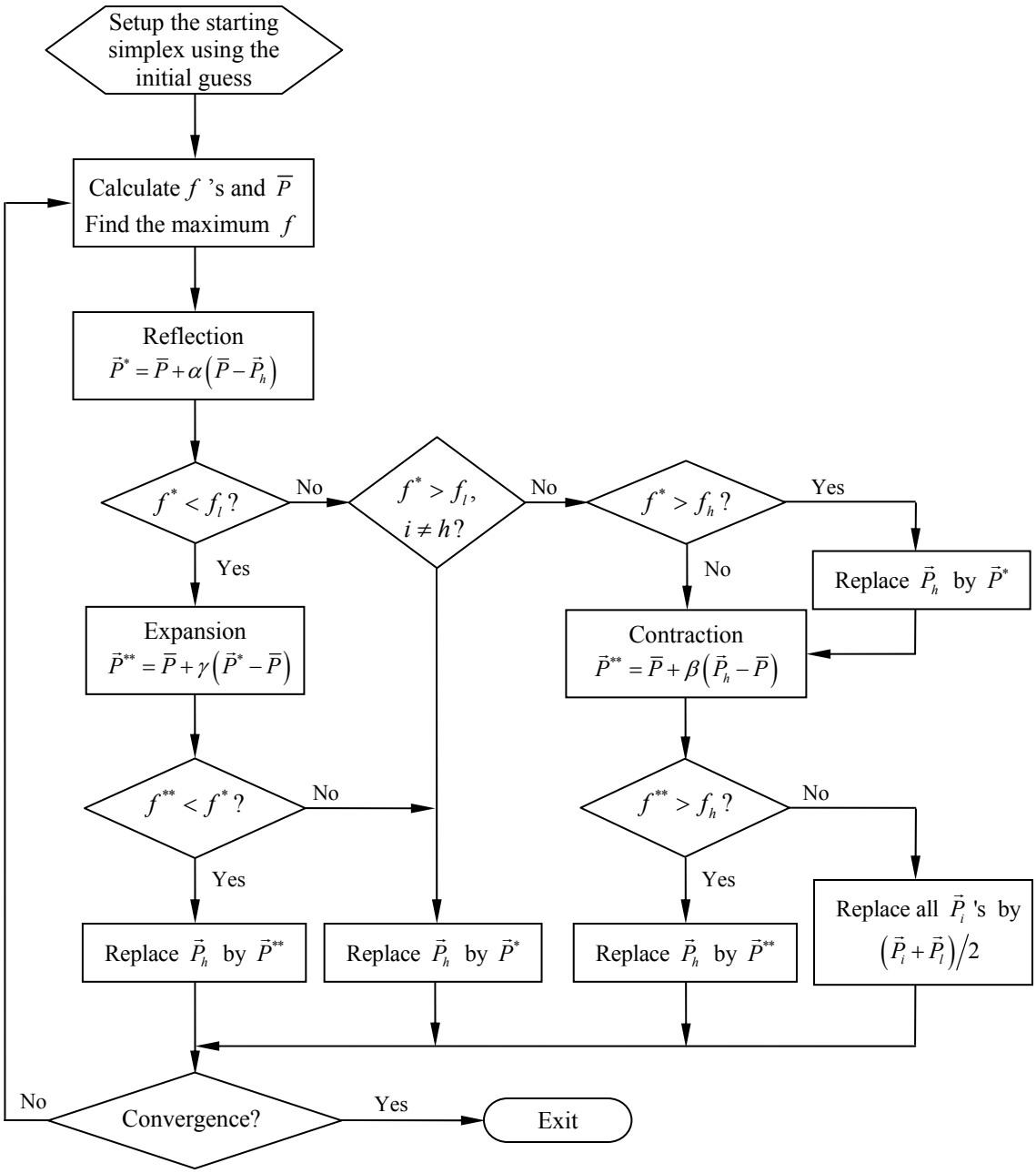

Figure B. 1: Nelder and Mead simplex method. Block diagram.

B.2 Termination Criteria

As reported in the literature [74], termination criteria in any multidimensional minimization routine is delicate. The problem is that in multiple dimensions bracketing can not be used like when trying to find the zero of a single independent variable function. Thus, a tolerance can not be required on the values of the independent variables. The criterion used for halting the procedure in the original work by Nelder and Mead uses a different approach. It is concerned with the variation in the values of the function f over the simplex rather than with changes in the values of $a(\vec{x}_m)$. The chosen criterion is to stop the process when the "standard error" of the f's falls below a pre-set value. This is:

$$\varepsilon > \sqrt{\left\{\sum_i \left(f_i - \bar{f}\right)^2 / n\right\}} \tag{B. 11}$$

where ε is a tolerance set by the user.

The success of the criterion depends on the simplex not becoming too small in relation to the curvature of the surface until the final minimum is reached. It is also possible to terminate the procedure when the vector distance moved in a step is fractionally smaller in magnitude than some tolerance.

In some cases, a single inconsistent step might fail to get anywhere and thus not rendering an actual minimum. This is an issue in most of the multidimensional minimization routines. Therefore, it is frequently a good idea to ***restart*** the minimization at the point where the potential minimum was found. In the implemented method, the restart is achieved by setting a new simplex using:

$$\vec{P}_i = \vec{P}_0 + \eta \vec{e}_i \tag{B. 12}$$

where:

η is a factor used to "expand" the simplex from the previous solution, and

$\vec{P}_0$ is the potential solution, used as one of the vertices of the new simplex.

Since the algorithm is restarted in a "small" vicinity of a claimed minimum, the number of

operations involved should not be significant. However, if the starting point was not a global or actual minimum the algorithm may find a new potential minimum. This process is performed until the solutions from consecutive restarts are the "same" within a given tolerance. Round-off errors are also overcome by this procedure.

The problem of finding local minima, instead of the actual global minimum, is related to the multiplicity of local solutions. However, implementing a global search algorithm would require much higher numerical cost. A method called Globalized Bounded Nelder–Mead (GBNM) algorithm was adapted to overcome some of the issues mentioned before. It also includes a strategy to bind the solutions from the simplex method, as will be explained in the next section. The main idea is to use different strategies for restarting the local search, i.e. using probabilistic restart. This approach was not implemented in this work but might be of interest to investigate the results.

B.3 Optimization with Bounded Variables

In the original work by Nelder and Mead, two approaches are suggested to account for bounded solutions. This is of particular interest in the LORE technique since, as mentioned before, for incoherent sources the solution is constrained to be non-negative and real. The approaches suggested by Nelder and Mead are:

1. changing the scale of the $a(\vec{x}_m'')$'s , e.g. by using the logarithm, so that negative values are excluded, or
2. modifying the function to take large positive values for all negative $a(\vec{x}_m'')$. Then, if the simplex reflects or expands over the boundaries, a contraction will keep it inside.

In both cases an actual minimum with $\vec{a}(\vec{x}'') = \vec{0}$ would be inaccessible in general, though arbitrarily close approaches could be made to it. Clearly either technique can deal with individual limitations on the range of any number of $a(\vec{x}_m'')$'s. Special care should be taken in setting the initial simplex within the permitted region.

A different approach is proposed by [74]. The idea is to bind the variables by projection, thus:

$$\begin{cases} \text{if } \left(a\left(\vec{x}''_m\right) < 0\right), \quad a\left(\vec{x}''_m\right) = 0 \\ \text{if } \left(a\left(\vec{x}''_m\right) > a\left(\vec{x}''_m\right)^{\max}\right), \quad a\left(\vec{x}''_m\right) = a\left(\vec{x}''_m\right)^{\max} \end{cases} \tag{B. 13}$$

Since the points can leave the domain either after the reflection or the expansion operation, this bounds checking should be performed after both operations. Basically, in this bounding procedure the reflection and expansion coefficients, α and γ, are changed to values other than the "optimal" $\left(\alpha = 1, \text{ and } \gamma = 2\right)$. As reported by Nelder and Mead, the use of different values for these coefficients affects the rate of convergence, and in some cases may result in convergence to false minima.

The work by Luersen and Le Riche [74] also suggests the use of specific convergence tests, based on reinitialization at the point of convergence. Basically, the simplex is tested under three criteria: smallness, flatness and degeneracy. These tests were not implemented in this work.

B.4 Approximate Number of Function Evaluations

To investigate the effect of increasing the number of variables to optimize, Nelder and Mead used a test function. They determined that the relationship between the number of variables *NZ* and the mean number of evaluations *Q* needed for convergence was well described by:

$$Q = 3.16\left(NZ + 1\right)^{2.11} \tag{B. 14}$$

However, this should be taken just as a "guess" since the maximum number of variables tested was 10, i.e. $NZ = 2\ldots10$, and the dependence with tolerance is not included in this equation.

Appendix C: The DAMAS Approach

This appendix compares the LORE modeling approach proposed in this dissertation to the DAMAS post-processing technique developed by Brooks et al. [54]. The purpose of this section is not to establish the differences between the solutions obtained for the same cases with both methods but to compare the modeling in which they are based.

To this end, two different approaches are used. The first one is purely analytical and compares the model equations used to obtain the beamforming map. The second approach uses a graphical comparison that shows the beamforming maps obtained for a number of sources with the modeling approach of both methods (LORE and DAMAS) and compare them to the beamforming maps obtained with conventional beamforming of such sources.

C.1 DAMAS Theoretical Formulation

For the analytical comparison, the formulation for DAMAS is presented and rewritten in a form that makes comparison to the LORE modeling clear. Note that extensions to DAMAS, like DAMAS2 and DAMAS3 [55] are based in the same modeling approach that will be developed in this section. Thus, the only difference is in the solution procedure that includes the use of Gaussian or Wiener filters.

As mentioned in Chapter 1, the DAMAS approach models the cross-spectral matrix (CSM) for a set of sources and obtains an inverse problem in which the power of the noise sources is solved for. Since the modeled CSM is not invertible, a Gauss-Seidel iterative scheme is used to solve the resulting system of linear equations.

The DAMAS approach is based in modeling the CSM for a single source located at $\vec{x}''$ as:

$$\hat{G}_{\text{mod}}\left(\vec{x}''\right) = X\left(\vec{x}''\right)\begin{bmatrix} \left(e_1^{-1}\right)^* e_1^{-1} & \left(e_1^{-1}\right)^* e_2^{-1} & \cdots & \left(e_1^{-1}\right)^* e_J^{-1} \\ \left(e_2^{-1}\right)^* e_1^{-1} & \left(e_2^{-1}\right)^* e_2^{-1} & & \vdots \\ \vdots & & \ddots & \vdots \\ \left(e_J^{-1}\right)^* e_1^{-1} & \cdots & \cdots & \left(e_J^{-1}\right)^* e_J^{-1} \end{bmatrix}_{\vec{x}''} \tag{C. 1}$$

where:

J is the number of microphones

$X\left(\vec{x}''\right)$ is the mean square value of the pressure per bandwidth at each microphone j normalized in level for a microphone at $r_j = r_0$,

r_j is the distance from the source to microphone j,

r_0 is the distance from the source to the center of the array, and

e_j^{-1} are inverse of the components of the steering vector given by:

$$e_j^{-1} = \frac{1}{a_j}\frac{r_0}{r_j}e^{-i2\pi f\tau_j} \tag{C. 2}$$

where a_j is a shear layer amplitude correction factor.

Note that the components of the "inverse" of the steering vector in DAMAS are equivalent to the components of the array propagation vector used in this work. The main difference is the use of the distance from the source to the center of the array r_0.

In the following step, the method assumes that there are N statistically independent sources, and models the resulting CSM as:

$$\hat{G}_{\text{mod}} = \sum_{m=1}^{N} \hat{G}_{\text{mod}}\left(\vec{x}''_m\right) \tag{C. 3}$$

In this way, the beamforming output at a point $\vec{x}''$ can be obtained with conventional beamforming as:

$$b_{\text{mod}}(\vec{x}) = \left[\frac{\hat{e}^{\dagger}\ \hat{G}_{\text{mod}}\ \hat{e}}{J^2} \right]_{\vec{x}} = \frac{\sum_m \left(\hat{e}(\vec{x})\right)^{\dagger} [\quad]_{\vec{x}''_m}\ \hat{e}(\vec{x})\, X(\vec{x}''_m)}{J^2} \tag{C. 4}$$

where:

$[\quad]_{\vec{x}''}$ are the terms expressed in equation (C. 1), and

$\hat{e}(\vec{x})$ is the steering vector for the grid point at $\vec{x}$, whose J components are given by:

$$e_j = a_j \frac{r_j}{r_0} e^{i2\pi f \tau_j} \tag{C. 5}$$

Arranging equation (C.4) in matrix form, the modeled beamforming output can be written as:

$$b_{\text{mod}} = \hat{A}\, X \tag{C. 6}$$

where the components of matrix $\hat{\mathbf{A}}$ are given by:

$$\hat{A}(\vec{x}, \vec{x}'') = \frac{\left(\hat{e}(\vec{x})\right)^{\dagger} [\quad]_{\vec{x}''}\, \hat{e}(\vec{x})}{J^2} \tag{C. 7}$$

Replacing b_{mod} with the actual beamforming output b from the test data they end up with:

$$b = \hat{A}\, X \tag{C. 8}$$

The DAMAS technique then solves for the source power $\hat{X}$ using a Gauss-Seidel iterative approach and imposing a non-negativity constraint on the results.

As mentioned before, in order to compare the DAMAS modeling with LORE it is useful to re-write the formulation given in equation (C.7) as:

$$\hat{A}(\vec{x}, \vec{x}'') = \frac{\left(\hat{e}(\vec{x})\right)^{\dagger} \left[\hat{e}^{-1}(\vec{x}'')\left(\hat{e}^{-1}(\vec{x}'')\right)^{\dagger}\right]^{T} \hat{e}(\vec{x})}{J^2} = \frac{\left[\left(\hat{e}(\vec{x})\right)^{T} \hat{e}^{-1}(\vec{x}'')\right]^{*} \left[\left(\hat{e}^{-1}(\vec{x}'')\right)^{T} \hat{e}(\vec{x})\right]}{J^2} \tag{C. 9}$$

Thus:

$$\hat{A}\left(\vec{x},\vec{x}''\right)=\frac{\left|\left(\hat{e}\left(\vec{x}\right)\right)^{\mathrm{T}}\hat{e}^{-1}\left(\vec{x}''\right)\right|^2}{J^2} \tag{C. 10}$$

Then, the DAMAS modeled beamforming output at point $\vec{x}$ for *N* sources can be written as:

$$b_{\mathrm{mod}}\left(\vec{x}\right)=\sum_{m=1}^{N}\frac{\left|\left(\hat{e}\left(\vec{x}\right)\right)^{T}\hat{e}^{-1}\left(\vec{x}''_m\right)\right|^2}{J^2}X\left(\vec{x}''_m\right) \tag{C. 11}$$

Note that $\left|\left(\hat{e}\left(\vec{x}\right)\right)^{T}\ \hat{e}^{-1}\left(\vec{x}''\right)\right|^2$ is the point spread function equivalent to the one defined in this work as $psf\left(\vec{x},\vec{x}''\right)=\left|\vec{w}^{\dagger}\left(\vec{x}\right)\vec{C}\left(\vec{x}''\right)\right|^2$.

C.2 Analytical Comparison with LORE

For the analytical comparison of both modeling approaches, it is convenient to use equation (6. 21). Thus, the LORE modeled beamforming output at a point $\vec{x}$ due to *N* sources given by:

$$b\left(\vec{x}\right)=\sum_{m=1}^{N}\left|cpsf\left(\vec{x},\vec{x}''_m\right)\right|^2\left|a\left(\vec{x}''_m\right)\right|^2+\sum_{m=1}^{N}\sum_{\substack{s=1\\ s\neq m}}^{N}\left[cpsf\left(\vec{x},\vec{x}''_m\right)a\left(\vec{x}''_m\right)\right]^{*}cpsf\left(\vec{x},\vec{x}''_s\right)a\left(\vec{x}''_s\right) \tag{C. 12}$$

where:

$cpsf\left(\vec{x},\vec{x}''_m\right)$ is the complex point spread function as defined in equation (6. 13), and

$a\left(\vec{x}''_m\right)$ is the amplitude of the source at $\vec{x}''_m$.

It is convenient at this point to note that $\left|a\left(\vec{x}''_m\right)\right|^2$ is nothing but two times the mean squared value of the source strength, i.e. $X'\left(\vec{x}''_m\right)=\left|a\left(\vec{x}''_m\right)\right|^2$. Furthermore, the relationship between the *psf* and the *cpsf* is as follows:

$$\left|cpsf\left(\vec{x},\vec{x}''_m\right)\right|^2=psf\left(\vec{x},\vec{x}''_m\right) \tag{C. 13}$$

In this way, equation (C. 12) can be written as:

$$b(\vec{x}) = \sum_{m=1}^{N} psf(\vec{x}, \vec{x}_m'') X'(\vec{x}_m'') + \sum_{m=1}^{N} \sum_{\substack{s=1 \\ s \neq m}}^{N} \left[cpsf(\vec{x}, \vec{x}_m'') a(\vec{x}_m'') \right]^* cpsf(\vec{x}, \vec{x}_s'') a(\vec{x}_s'') \quad \text{(C. 14)}$$

As can be seen, the first term in equation (C. 14) is equivalent to equation (C. 11). The relation between them would be just a factor given by the number of microphones and the differences in the definition of the steering vectors.

From this analytical comparison it can be seen that the DAMAS model discards the cross terms in equation (C. 14) under the assumption of incoherence. This assumption is not true since, as shown in Chapter 6, these terms are needed to accurately model the beamforming output even in the case of incoherent sources.

Note that this formulations are "equivalent" for the case of a single source; thus, when there are no cross-terms. Note also that for the case of multiple sources, DAMAS is equivalent to adding the beamforming maps (i.e. the *psf*'s) for each source in "absolute" value, i.e. instead of using the complex form of the *psf* like in the LORE model.

C.3 "Graphical" Comparison with LORE

In order to better visualize the effect of neglecting the cross-terms of equation (6. 21), a "visual" approach is proposed. To this end, the beamforming results for different cases are presented and compared to the modeled beamforming maps resulting from the DAMAS and LORE methods. Thus, defining a set of sources and using their strength as an input in equations (C. 11) and (C. 12) the modeled beamforming output is rendered for DAMAS and LORE respectively.

Since as mentioned before, there is a scaling factor between the formulations, the results were normalized to the maximum SPL in the map to facilitate the comparison. However, since the beamforming simulations were performed using the same definition for the steering vectors than in the LORE modeling, they rendered the same levels.

As mentioned before, for the case of a single source both modeling approaches should be equivalent. To this end, a single monopole source at the center of the grid was used as an input in both approaches and the beamforming simulation. As can be seen in Figure C. 1, there are no

major visible differences when the modeled outputs for b) LORE, and c) DAMAS are compared to a) the actual beamformed data. These results suggest that both models can accurately render the actual beamforming map for a single source, as stated in the analytical comparison.

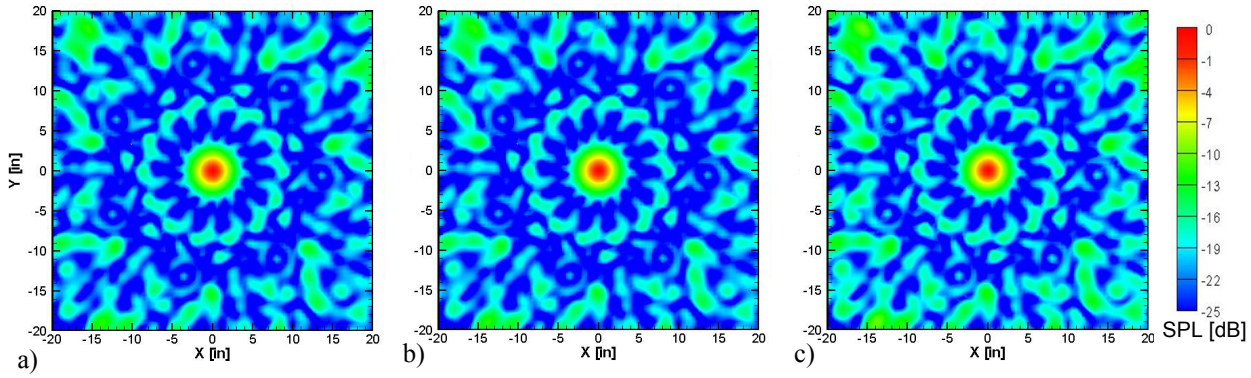

Figure C. 1: Comparison for a single source between: a) beamformed data, b) LORE and c) DAMAS modeling(15 kHz)

To see the importance of the cross-terms in the modeling, the case of two incoherent sources is analyzed next. As shown in Figure C. 2b, the LORE modeling is able to accurately render the same output than the beamforming, i.e. Figure C. 2a. However, the results from the DAMAS model shown in Figure C. 2c shows significant differences when compared to the actual beamforming map of Figure C. 2a. Thus, accounting for the "interaction" between the sources in the cross-terms significantly changes the results. As mentioned before, this discrepancy is the result of adding the point spread functions for each source without accounting for the phase information in each of them, i.e. in absolute value instead of complex form.

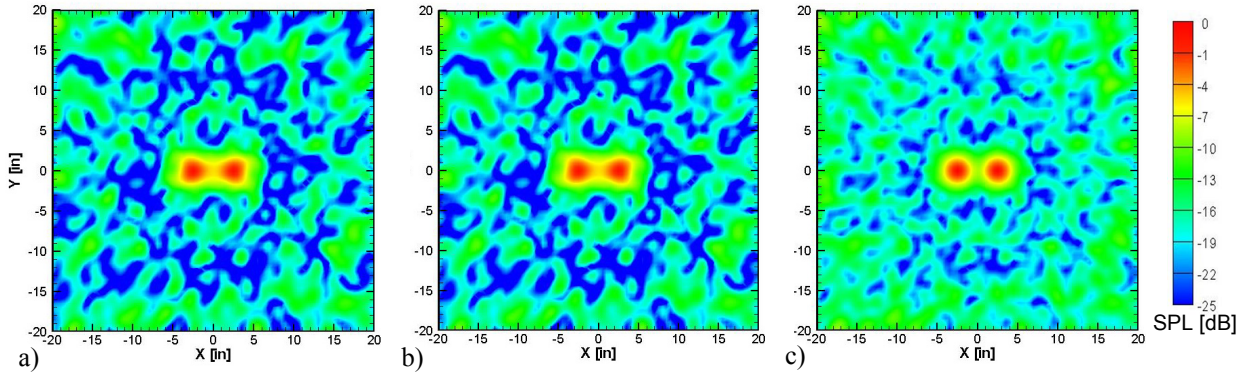

Figure C. 2: Comparison for two close sources between: a) beamformed data, b) LORE and c) DAMAS modeling (15 kHz)

The differences between the DAMAS modeling and the actual beamforming output are more noticeable for the case of multiple sources. In this sense, Figure C. 3 shows the comparison for one of the cases presented in Chapter 6, and depicted in Figure 6.33. It consisted of 16 sources with amplitude 10 in a square pattern and a source at the center of the grid with amplitude 25. As can be seen in Figure C. 3b, LORE is able to model all the features in the beamforming map, i.e. sidelobes structure and levels. However the results in Figure C. 3c, clearly show that DAMAS fails to render the actual sidelobe structure, i.e. their levels are higher than the actual ones. Note also that the sources region does not render the "actual" shape of the mainlobe in the map.

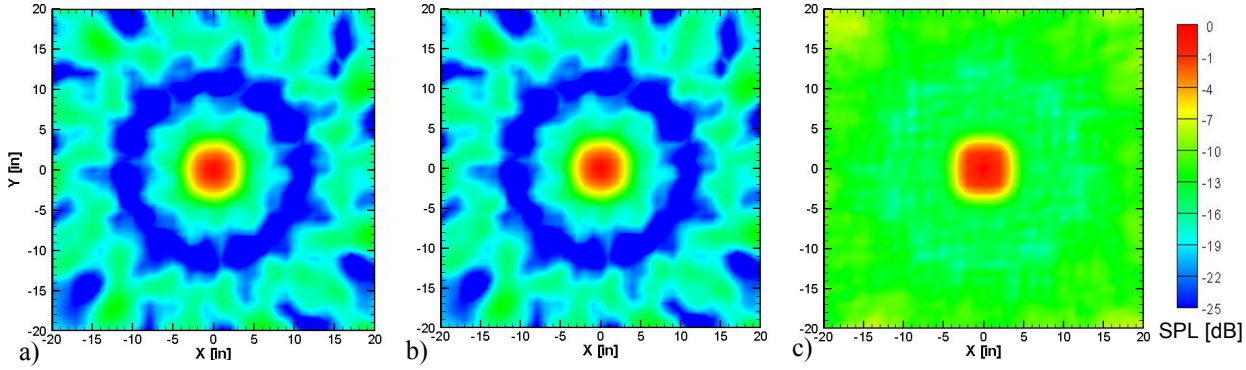

Figure C. 3: Comparison for a complex source distribution between: a) beamformed data, b) LORE and c) DAMAS modeling (15 kHz)

As mentioned before, the levels in each plot were normalized to the maximum value in the map. However, in the case of DAMAS the levels in the mainlobe will also be incorrectly higher than the actual ones as a consequence of adding the maps in "real" form. This issue was mentioned in the previous section and can also be analytically demonstrated by using the derivation leading to equation (6. 29), this is:

$$\left|\sum_m cpsf\left(\vec{x},\vec{x}_m''\right)a\left(\vec{x}_m''\right)\right|^2 \le \sum_m \left|cpsf\left(\vec{x},\vec{x}_m''\right)\right|^2 \left|a\left(\vec{x}_m''\right)\right|^2 \qquad \text{(C. 15)}$$

This last expression implies that the results from the DAMAS approach will always under-predict the actual noise sources power. Such error on the results is expected to be highly dependant on the actual sources distribution. A detailed comparison in terms of solutions to the same problem with LORE and DAMAS escapes from the purpose of this work and is proposed as future work.

Appendix D: Acoustic Results Extrapolation

In order to extrapolate the model-scale results to full-scale results, several corrections have to be applied [3]. These corrections need to account for:

- Scale factor
- Flow speed
- Distance to the model
- Strouhal frequency, and
- Frequency resolution

To this end, the scale factor *SF* is defined as:

$$SF = \frac{\text{test-scale } (ts)}{\text{desired-scale } (ds)} \tag{D. 1}$$

and the Strouhal number S_t, is defined as:

$$S_t = \frac{f\ell}{V} \tag{D. 2}$$

where:

f is the shedding or Strouhal frequency,

ℓ is a characteristic length, and

V is the free-stream flow speed.

Then, in order to maintain the Strouhal number constant at the test- and desired-scale results, the following expression needs to be satisfied:

$$\frac{f_{ds}\ell_{ds}}{V_{ds}} = \frac{f_{ts}\ell_{ts}}{V_{ts}} \tag{D. 3}$$

where:

f_{ts} is the test-scale frequency,

f_{ds} is the desired scale frequency,

V_{ts} is the free-stream velocity for the test-scale, and

V_{ds} is the free-stream velocity for the desired-scale results.

Since $\ell_{ts}/\ell_{ds} = SF$, the Strouhal-number corrected frequency can be written as:

$$f_{ds} = f_{ts}\left(SF\right)\left(\frac{V_{ds}}{V_{ts}}\right) \tag{D. 4}$$

Different corrections need to be applied to render the scaled SPL for full-scale. To take into account the scale factor between the model and full-scale results, the following correction is applied:

$$\Delta Lp_{SF} = 10\log_{10}\left(\frac{1}{SF}\right)^2 \tag{D. 5}$$

To take into account distance to the model, the following expression is used:

$$\Delta Lp_{r} = 10\log_{10}\left(\frac{r_{ts}}{r_{ds}}\right)^2 \tag{D. 6}$$

where:

r_{ts} is the test-scale distance to the model, and

r_{ds} is the distance to the model in the desired scale.

In order to account for different free-stream velocities, and remembering the dipole-like behavior of the landing gear noise, the following correction is performed:

$$\Delta Lp_{v} = 10\log_{10}\left(\frac{V_{ds}}{V_{ts}}\right)^6 \tag{D. 7}$$

Since the Strouhal-number corrected test-scale frequency may be different than the desired full-scale frequency, the correction in the levels can be obtained by:

$$\Delta Lp_{\Delta f} = 10\log_{10}\left(\frac{\Delta f'_{ds}}{\Delta f_{ds}}\right) \tag{D. 8}$$

where:

$\Delta f'_{ds} = f'_{ds}{}^{(n+1)} - f'_{ds}{}^{(n)}$: is the desired frequency resolution

$\Delta f_{ds} = f_{ds}{}^{(n+1)} - f_{ds}{}^{(n)}$: is the Strouhal-number corrected test-scale frequency resolution.

Then, the total correction for the magnitude of the sound pressure level is given by:

$$Lp_{ds} = Lp_{ts} + \Delta Lp_{SF} + \Delta Lp_r + \Delta Lp_V + \Delta Lp_{\Delta f} \quad \text{(D. 9)}$$

where:

Lp_{ds} is the desired-scale corrected sound pressure level, and

Lp_{ts} is the test-scale measured sound pressure level.

Vita

Patricio A. Ravetta was born on January 7, 1977 in Río Cuarto, Córdoba, Argentina. He attended high-school at ENET N° 1 “Ambrosio Olmos”, where he graduated with the degree of Electromechanical Technician.

In 1996 he attended the National University of Río Cuarto, where he earned the degree of Diploma Mechanical Engineer in March 2001. During his studies he was involved in research related to dynamics of MIMO mechanical systems using wavelets.

After his graduation, he started the Master’s program at the same university. His research was in the field of aeroelasticity. In particular, his work focused on the development of a numerical tool to simulate the attitude control of windmills using unsteady vortex lattice methods on delta wings. This work was performed with Dr. Sergio Preidikman as his advisor, a Virginia Tech alumnus.

In June 2002, he moved to the United States and began graduate studies in the Mechanical Engineering Department of Virginia Polytechnic Institute and State University. His main areas of research were landing gear noise, aeroacoustic testing, and phased array technologies.

In July 2005, while attending Virginia Tech, he completed his Master’s degree at the National University of Río Cuarto.

In December 2005, he completed the Ph. D. program with his dissertation focusing on landing gear noise control and the development of a post-processing technique for microphones phased arrays. This work was performed with Dr. Ricardo Burdisso and Dr. Wing Ng as his advisors.